IOWA STATE UNIVERSITY
Digital Repository

1979

Applications of pulsed nuclear magnetic resonance to chemistry: multiple-pulse NMR, cross polarization, magic-angle spinning and instrumental design

Paul DuBois Murphy
Iowa State University

Recommended Citation

7924257

MURPHY, PAUL DUBOIS
  APPLICATIONS OF PULSED NUCLEAR MAGNETIC
  RESONANCE TO CHEMISTRY: MULTIPLE-PULSE NMR,
  CROSS POLARIZATION, MAGIC-ANGLE SPINNING AND
  INSTRUMENTAL DESIGN.

  IOWA STATE UNIVERSITY, PH.D., 1979

Applications of pulsed nuclear magnetic resonance to

chemistry: Multiple-pulse NMR, cross polarization,

magic-angle spinning and instrumental design

by

Paul DuBois Murphy

A Dissertation Submitted to the

Graduate Faculty in Partial Fulfillment of

The Requirements for the Degree of

DOCTOR OF PHILOSOPHY

Department: Chemistry
Major: Physical Chemistry

Approved:

In Charge of Major Work

For the Major Department

For the Graduate College

Iowa State University
Ames, Iowa

1979

TABLE OF CONTENTS

LIST OF FIGURES

LIST OF TABLES

I. STATEMENT OF PURPOSE AND INTRODUCTION

The purpose of this work is to describe developments and applications of time-dependent techniques in Nuclear Magnetic Resonance (NMR) (1-12) to a study of: 1) the locations of ^{1}H in the hydrides of the zirconium halides, 2) signal enhancement of ^{29}Si in liquids and chemical shifts of silyl-ether model compounds and 3) the aromatic ^{13}C fractions of whole coals. Also described are 4) the design of development of instrumentation used in the above studies and 5) numerical techniques, such as digital filtering and spectral decomposition, which are used in analysis of the data of the above studies.

The general structure of this thesis is to group together work mainly concerned with the aspects of the design of equipment and computer software in Chapters II through V. Discussions of the theoretical and experimental aspects of NMR used in the current work are grouped together in Chapters VI through IX. This format has been chosen in a manner to allow those interested in theory to easily locate the appropriate portions to read, and similarly to allow those interested in the more technical aspects to easily locate material of interest.

The text has been liberally supplemented with illustrations. The author hopes that these will clarify important, and usually simple, concepts which can sometimes become obscure and abstract when described by equations or words. A brief discussion of

the themes of each of the remaining eight chapters follows.
These descriptions are intended to quickly familiarize the
reader with the body of the thesis.

Chapter II begins the first of four chapters dealing with
technical aspects. It describes how to design an NMR probe.
Four common RF matching circuits are mathematically analyzed.
Component values are shown to be easily estimated by both
equations and Design Graphs. Additional topics include
ringdown times, circuit Q's, NMR coils and power dissipation.

Chapter III describes the design and construction of a
single-coil double-resonance probe. Such probes are used in
Cross-Polarization experiments (2,3). In addition the designs
of high speed (>2.0 KHz) rotors for Magic-Angle Spinning experiments
(2,3) are also discussed.

Chapter IV describes the designs of both high and low Q
RF power amplifiers. Particular attention is focussed on the
design of the RF matching sections and circuit Q's. These
amplifiers find applications in Cross-Polarization (high Q)
experiments, and in Multiple-Pulse NMR (low Q) experiments.
Also, the designs and constructions of lumped equivalent circuits
of transmission lines are described. These circuits are shown
to act as replacements for transmission lines and to possess
favorable properties for use in Cross-Polarization experiments.

Chapter V deals with the mathematical techniques of digitally
filtering noisy data and the decomposition of overlapping NMR

absorptions into artificially resolved absorptions. Useful

properties of the Fourier Transform, as well as, those of the

lineshapes of Lorentzians and Gaussians are discussed. The

techniques described in this chapter are easily implemented

via computer programs.

Chapter VI begins the first of the four remaining Chapters

which deal with the theory and applications of NMR. Chapter VI

describes the deduction and properties of the interesting

lineshape of the NMR Powder Pattern (2, 3). Also, the technique

of numerical convolution and its use to broaden the lineshape

of the NMR Powder Pattern are discussed in some detail.

Chapter VII begins the first presentation of actual experimental

use of NMR. Measurements are made of the principal values of

the proton shielding tensors (2, 3) for the ^1H in the hydrides

of the unusual, sandwich-like and metallic salts of zirconium

chloride and zirconium bromide. The relative locations and

anisotropies of the various shielding tensors are used to infer

possible locations of the protons within the uncommon, metal-metal

double layers of these salts.

Chapter VIII details the phenomenon of the oscillatory

behavior of magnetic polarization caused by indirect, heteronuclear,

dipolar coupling between abundant (^1H) spins and rare (^{29}Si)

spins. The important consequences of this J Cross Polarization

(9, 12) in terms of improving the rapidity of acquiring good

signal-to-noise for rare spins are discussed. Finally, this technique is shown to be of great value in studies of ^{29}Si which is to be used as a probe of the environment of chemically bound oxygen in coals.

Lastly, Chapter IX describes the ^{1}H-^{13}C Cross-Polarization (8, 9) studies of many and varied whole coals. The measurements chiefly yield the fraction aromaticity, or aromatic ^{13}C content, of each coal studied.

II. THE DESIGN OF NMR PROBES

A. Introduction

A knowledge of the possible matching circuits for NMR probes (1-4) is useful and advantageous to the individual with an interest in developing novel NMR experiments. In research utilizing NMR as a tool, the key to success of the experiment frequently lies in probe design.

This Chapter presents a mathematical approach to understanding and predicting the behavior of four RF (radio frequency) matching circuits which can be used in the design of NMR probes. The technique of solving the circuit equations for unknown parameters is first developed. Then a simplified method for accurately estimating component values using Design Graphs is introduced. Finally, a visual feeling for the process of "tuning up" is portrayed through the use of graphs of ideal frequency response. Also discussed are the quality factor, Q; the NMR coil and power dissipation.

The above considerations have been applied to the construction of a compact NMR lock probe and a low Q probe for Multiple-Pulse NMR experiments.

B. Theory and Equations of the Four Circuits of NMR Probes

Useful solutions of the standard circuit-equations of four RF matching circuits will be derived. The circuits are named:

tapped parallel-tuned circuit, tapped series-tuned circuit ("Tapped" refers to the fact that the impedances of simple parallel and series resonant-circuits are tapped at an impedance, $|Z_{IN}| = Z_o$ at phase angle, $\phi_{IN} = 0.0^o$.), hybrid-tuned circuit ("Hybrid" refers to the fact that a tuning element with a transcendental frequency response, namely a cable, is used.) and finally the shorted-stub-tuned circuit (A stub is a small length of cable used as a tuning element). These names are abbreviated: TPTC, TSTC, HTC and SSTC respectively. All circuits allow a load which is composed of an inductor L, with inductive reactance, X_L, and a series resistance, R_L, to be matched to the characteristic impedance of the cable (transmission line) feeding the probe. This condition can be expressed as: $|Z_{IN}| = Z_o$ and $\phi_{IN} = 0.0^o$ at a resonant frequency, f_o. The complex number, $(|Z_{IN}|, \measuredangle \phi_{IN})$ is the input impedance looking into the probe and Z_o is the characteristic impedance (or resistance) of the cable feeding the probe. Both of these numbers are assumed real and therefore represent resistances.

All reactive elements (inductors and capacitors) and all cables are considered ideal and lossless. All ohmic losses are considered lumped into an equivalent resistance, R_L, in series with the NMR coil. The effective value of R_L can be calculated after the probe is constructed and tuned as will be shown below.

In all derivations the following definitions apply:

$$X_{C1} = (2\pi f_o \, C_{C1})^{-1} \qquad (1)$$

NMR PROBES

TAPPED PARALLEL-TUNED CIRCUIT
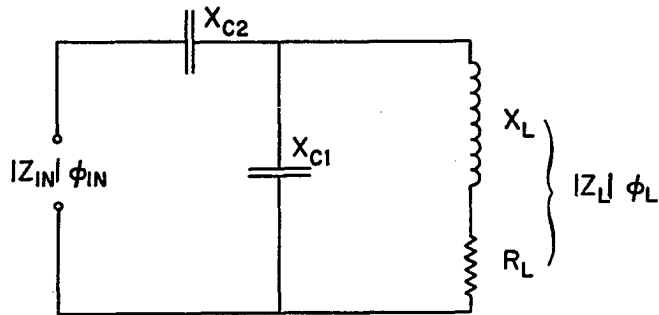
TAPPED SERIES-TUNED CIRCUIT
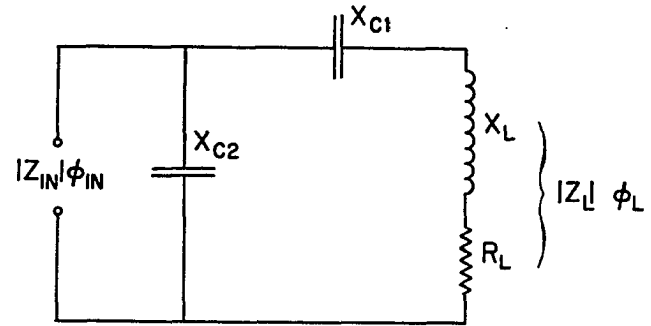
HYBRID-TUNED CIRCUIT
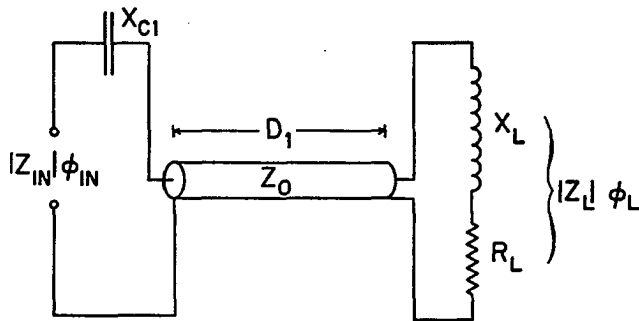
SHORTED-STUB-TUNED CIRCUIT
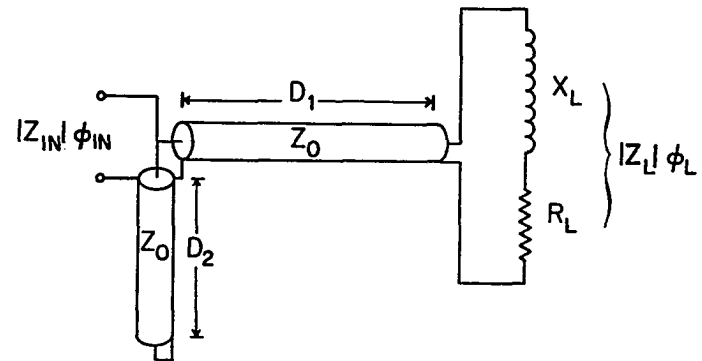
Figure 1. The circuits of four NMR probes

$$X_{C2} = (2\pi f_o \, C_{C2})^{-1} \qquad (2)$$

$$X_L = |Z_L|(\sin \phi_L) = 2\pi f_o \, L \qquad (3)$$

$$R_L = |Z_L|(\cos \phi_L) \qquad (4)$$

$$|Z_L| = \sqrt{R_L^2 + X_L^2} \qquad (5)$$

$$Q = X_L/R_L = \tan \phi_L \qquad (6)$$

X_{C1} and X_{C2} are the capacitive reactances of capacitors C_{C1} and C_{C2} at frequency, f_o. X_L is the inductive reactance of the entire load which consists of inductor, L, and series resistor, R_L. R_L is also the resistance of the entire load. Q is the quality factor of the load. Q is a measure of the ability of a circuit to store energy. Both Z_{IN} and $Y_{IN} = 1/Z_{IN}$, represent complex quantities and $|Z_{IN}|$, ϕ_{IN} represent the magnitude and phase angle of the complex number. In the laboratory, quantities such as Z_{IN} and Z_o would be read on a vector impedance meter. The equations used to calculate component values and theoretical or "ideal" frequency response are derived using the standard theory of linear-circuit analysis (5).

1. The tapped parallel-tuned circuit

The circuit diagram is shown in Figure 1. Capacitors C_{C1} and C_{C2} are used to tune a load, X_L and R_L, to an input impedance $|Z_{IN}| = Z_o$, $\phi_{IN} = 0.0^o$ at frequency f_o.

Using standard linear-circuit analysis, the input impedance, Z_{IN}, can be shown to be:

$$Z_{IN} = -jX_{C2} + \frac{X_{C1}X_L - jX_{C1}R_L}{R_L + j(X_L - X_{C1})} \tag{7}$$

The conditions:

$$\text{Real } (Z_{IN}) = Z_o$$

$$\text{Imag } (Z_{IN}) = 0.0$$

will result in $|Z_{IN}| = Z_o$, $\phi_{IN} = 0.0^\circ$ at f_o. With these conditions it can be shown that:

$$C_{C1} = \left[\frac{2\pi f_o \ (Z_o X_L + \sqrt{Z_o R_L \ (R_L^2 + X_L^2 - Z_o R_L)})}{Z_o - R_L} \right]^{-1} \tag{8}$$

$$X_{C1} = (2\pi f_o \ C_{C1})^{-1}$$

$$C_{C2} = C_{C1} \ \frac{R_L^2 + (X_{C1} - X_L)^2}{(X_{C1} - X_L)X_L - R_L^2} \tag{9a}$$

Usually the condition:

$$Q >> \frac{X_L Z_o}{X_{C1}^2}$$

is a valid approximation for most NMR probe-circuits since $X_L \sim X_{C1}$ and $Z_o < X_L$. The solutions then reduce to:

$$C_{C1} \simeq \left[\frac{2\pi f_o X_L \ (Z_o + \sqrt{Z_o R_L})}{Z_o - R_L} \right]^{-1} \tag{9b}$$

$$A = X_L \frac{(1 + \sqrt{Z_o/R_L})}{Z_o - R_L} \ , \ Q = \frac{X_L}{R_L}$$

$$C_{C2} \simeq C_{C1} \left(\frac{1 + A^2}{AQ - 1} \right) \qquad (9c)$$

Furthermore, usually both:

$$A^2 \text{ and } AQ \gg 1$$

then:

$$C_{C2} \simeq \left[\frac{2\pi f_o X_L (Z_o + \sqrt{Z_o R_L})}{R_L + \sqrt{Z_o R_L}} \right]^{-1} \qquad (9d)$$

2. The tapped series-tuned circuit

The circuit diagram is shown in Figure 1. Capacitors C_{C1} and C_{C2} are used to tune a load, X_L and R_L, to an input impedance $|Z_{IN}| = Z_o$, $\phi_{IN} = 0.0°$ at frequency f_o.

Using standard linear-circuit analysis, the input admittance, Y_{IN}, can be shown to be:

$$Y_{IN} = \frac{j}{X_{C2}} + \frac{1}{R_L + j(X_L - X_{C1})} \qquad (10)$$

The conditions:

$$\text{Real } (Y_{IN}) = 1/Z_o$$

$$\text{Imag } (Y_{IN}) = 0.0$$

will result in $|Z_{IN}| = |1/Y_{IN}| = Z_o$, $\phi_{IN} = 0.0°$ at f_o. With these conditions it can be shown that:

$$C_{C1} = \left[2\pi f_o (X_L - R_L \sqrt{\frac{Z_o}{R_L} - 1}) \right]^{-1} \qquad (11)$$

$$C_{C2} = \frac{\sqrt{\frac{Z_o}{R_L} - 1}}{2\pi f_o Z_o} \qquad (12)$$

Usually the condition:

$$Q \gg X_L / Z_o$$

is a valid approximation for most NMR probe circuits.

The solutions then reduce to:

$$C_{C1} = [2\pi f_o (X_L - \sqrt{Z_o R_L})]^{-1} \qquad (13a)$$

and:

$$C_{C2} = [2\pi f_o \sqrt{Z_o R_L}]^{-1} \qquad (13b)$$

3. The hybrid-tuned circuit

The circuit diagram is shown in Figure 1. Capacitor, C_{C1}, and transmission line, D_1, are used to tune a load, X_L and R_L, to an input impedance $|Z_{IN}| = Z_o$, $\phi_{IN} = 0.0^o$ at frequency f_o.

The impedance, Z_D, measured at the open end of a transmission line of length D in wavelengths terminated in a load, X_L and R_L, can be shown (6) to be:

$$Z_D = \frac{Z_o [(R_L + jX_L) + Z_o \tanh \gamma D]}{[Z_o + (R_L + jX_L) \tanh \gamma D]} \qquad (14)$$

$$\gamma = \alpha + j\beta, \quad \beta = 2\pi$$

Z_o (ohms) is the characteristic impedance of the transmission line, α (nepers/wavelength) is the attenuation factor and β (radians/wavelength) is the phase factor. D is the length of transmission line in wavelengths at f_o and therefore represents the length of an ideal cable with a vacuum as the "dielectric material". The length of some standard cable, D',--such as

RG58C/U--may be calculated:

$$D' = \frac{sc}{f_o} D \qquad (15)$$

where s (≤ 1.0) is the velocity factor of the cable (For RG58C/U,

s = 0.66), c is the speed of light, and D is the length of the

cable in wavelengths at frequency, f_o. The attenuation factor,

α, is frequency dependent. For small lengths of foamed

polyethylene-dielectric cable at frequencies below 100 MHz,

the assumptions that $\alpha = 0.0$ and the characteristic impedance,

Z_o, is purely resistive (i.e., a real number) are good

approximations. Furthermore if D is expressed in wavelengths

of cable at f_o then equation 14 reduces to:

$$Z_D = \frac{Z_o(R_L + jX_L) + jZ_o \tan 2\pi D}{Z_o + j(R_L + jX_L)\tan 2\pi D} \qquad (16)$$

Assuming lossless cable, $\alpha = 0$, and a purely resistive characteristic

impedance, Z_o; treating Z_D as a circuit impedance; and using

standard linear-circuit analysis, the input impedance, Z_{IN}, of

the hybrid-tuned circuit can be shown to be:

$$Z_{IN} = -jX_{C1} + \frac{Z_o[R_L + j(Z_o \tan(2\pi D_1) + X_L)]}{(Z_o - X_L \tan 2\pi D_1) + j(R_L \tan 2\pi D_1)} \qquad (17)$$

The conditions:

$$\text{Real } (Z_{IN}) = Z_o$$

$$\text{Imag } (Z_{IN}) = 0.0$$

will result in $|Z_{IN}| = Z_o$, $\phi_{IN} = 0.0^o$ at f_o. Note, here the

input impedance is tuned to the characteristic impedance

of the cable. With these conditions it can be shown that:

$$D_1 = \frac{1}{2\pi} \tan^{-1}\left(\frac{Z_o X_L - \sqrt{Z_o R_L (R_L^2 + X_L^2 + Z_o^2 - 2Z_o R_L)}}{X_L^2 + R_L^2 - Z_o R_L}\right) \quad (18)$$

$$C_{C1} = \left[\frac{2\pi f_o Z_o [X_L Z_o + (Z_o^2 - X_L^2 - R_L^2)\tan 2\pi D_1 - X_L Z_o \tan^2 2\pi D_1]}{(Z_o - X_L \tan 2\pi D_1)^2 + (R_L \tan 2\pi D_1)^2}\right]^{-1} \quad (19)$$

D_1 will be calculated in wavelengths of cable at f_o. This value can be converted to a length of cable with equation 15. Since the attenuation factor, α, will always be greater than zero, the length, D_1, will be slightly shorter and the value of C_{C1}, slightly larger than predicted with these equations.

4. The shorted-stub-tuned circuit

The circuit diagram is shown in Figure 1. Two lengths of transmission line, D_1 and D_2, are used to tune a load, X_L and R_L, to an input impedance $|Z_{IN}| = Z_o$, $\phi_{IN} = 0.0^o$, at frequency, f_o. Length D_2 is in parallel with length D_1 and its far end is shorted. Length D_2 is referred to as a shorted-stub. This design is similar to the HTC, with the stub replacing capacitor C_1. Assuming lossless cable, $\alpha = 0$, with a purely resistive characteristic impedance, Z_o, the input admittance Y_{IN} can be shown to be:

$$Y_{IN} = \frac{-j}{Z_o \tan 2\pi D_2} + \frac{(Z_o - X_L \tan 2\pi D_1) + jR_L \tan 2\pi D_1}{R_L + j[Z_o \tan(2\pi D_1) + X_L]} \quad (20)$$

The conditions:

$$\text{Real } (Y_{IN}) = 1/Z_o$$

$$\text{Imag (second term of equation 20)} > 0.0$$

$$\text{Imag } (Y_{IN}) = 0.0$$

will result in $|Z_{IN}| = |1/Y_{IN}| = Z_o$, $\phi_{IN} = 0.0^o$ at f_o. The condition, Imag (second term of equation 20) > 0.0, will yield the shorter of the two possible lengths of D_1 that are solutions. With these conditions it can be shown that:

$$D_1 = 0.5 + \frac{1}{2\pi} \tan^{-1} \left[\frac{X_L Z_o + \sqrt{Z_o R_L (Z_o^2 + X_L^2 + R_L^2 - 2 Z_o R_L)}}{Z_o R_L - Z_o^2} \right] \quad (21)$$

$$D_2 = \frac{1}{2\pi} \tan^{-1} \left[\frac{R_L^2 + (Z_o \tan(2\pi D_1) + X_L)^2}{(R_L^2 + X_L^2 - Z_o^2) \tan 2\pi D_1 + X_L Z_o (\tan^2 2\pi D_1) - X_L Z_o} \right] \quad (22)$$

D_1 and D_2 are expressed in wavelengths of cable at f_o. Since the attenuation factor, α, is greater than zero, for a highly inductive load, the length D_1 will be slightly shorter and the length, D_2, slightly longer than predicted above. Equation 15 can be used to convert wavelengths of cable into actual physical lengths.

C. Design Graphs

Figures 2, 3, 4 and 5 present Design Graphs that were drawn with a computer program (7). These curves are graphical solutions of equations 8, 9a, 11, 12, 18, 19, 21 and 22 for $|Z_{IN}| = 50.0$ ohms, $\phi_{IN} = 0.0^o$ and Q's of 57 ($\phi_L = 89.0^o$) and 19.1 ($\phi_L = 87.0^o$).
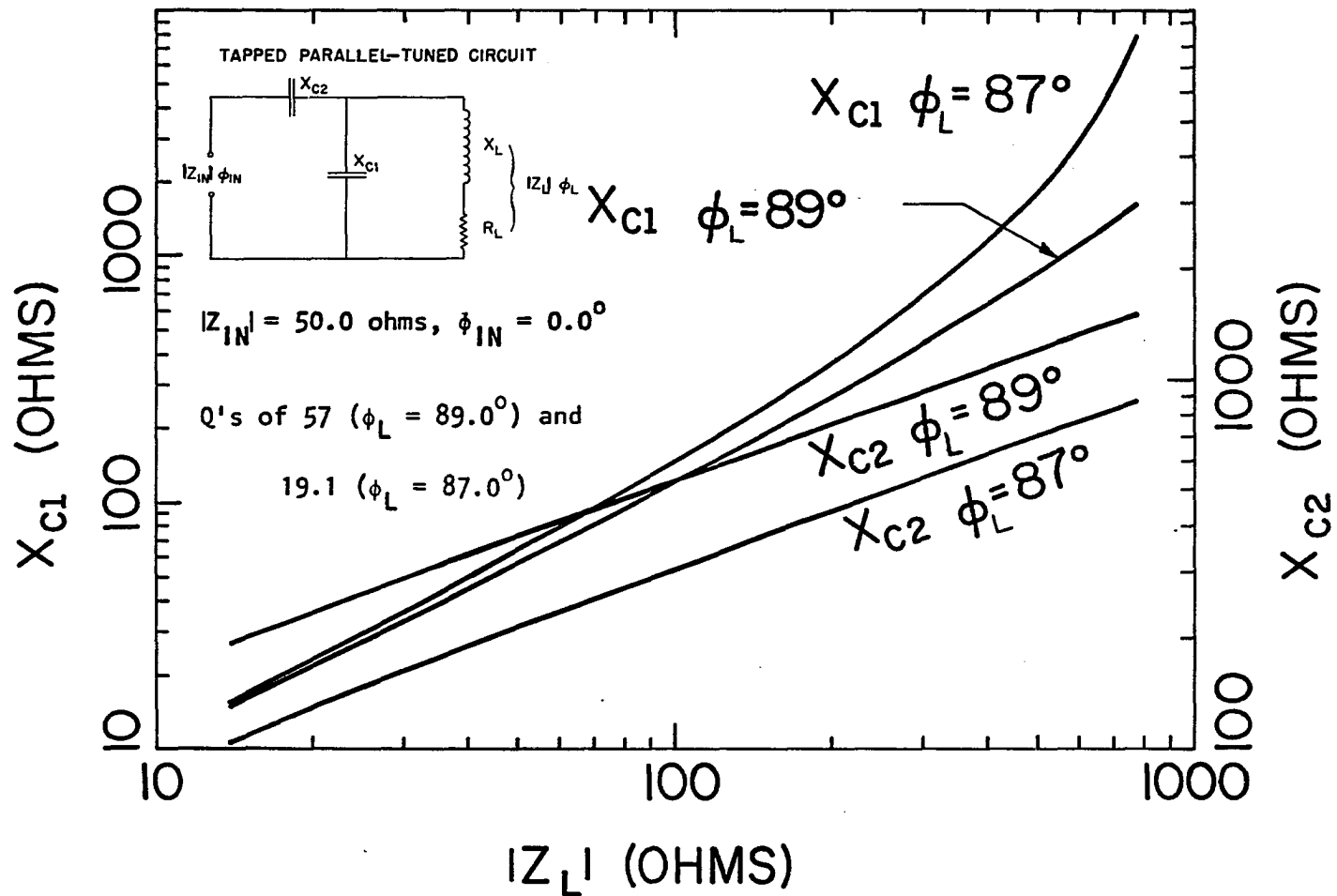
Figure 2. The Design Graph for the tapped parallel-tuned circuit

$|Z_{IN}| = 50.0$ ohms, $\phi_{IN} = 0.0°$

Q's of 57 ($\phi_L = 89.0°$) and

19.1 ($\phi_L = 87.0°$)

X_{C1} (OHMS)

X_{C2} (OHMS)

$X_{C1}\ \phi_L = 89°$

$X_{C1}\ \phi_L = 87°$

$X_{C2}\ \phi_L = 87°$

$X_{C2}\ \phi_L = 89°$

100

10

10

100

1000

$|Z_L|$ (OHMS)

TAPPED SERIES-TUNED CIRCUIT

X_{C1}

X_L

$|Z_{IN}|\ \phi_{IN}$

X_{C2}

$|Z_L|\ \phi_L$

R_L
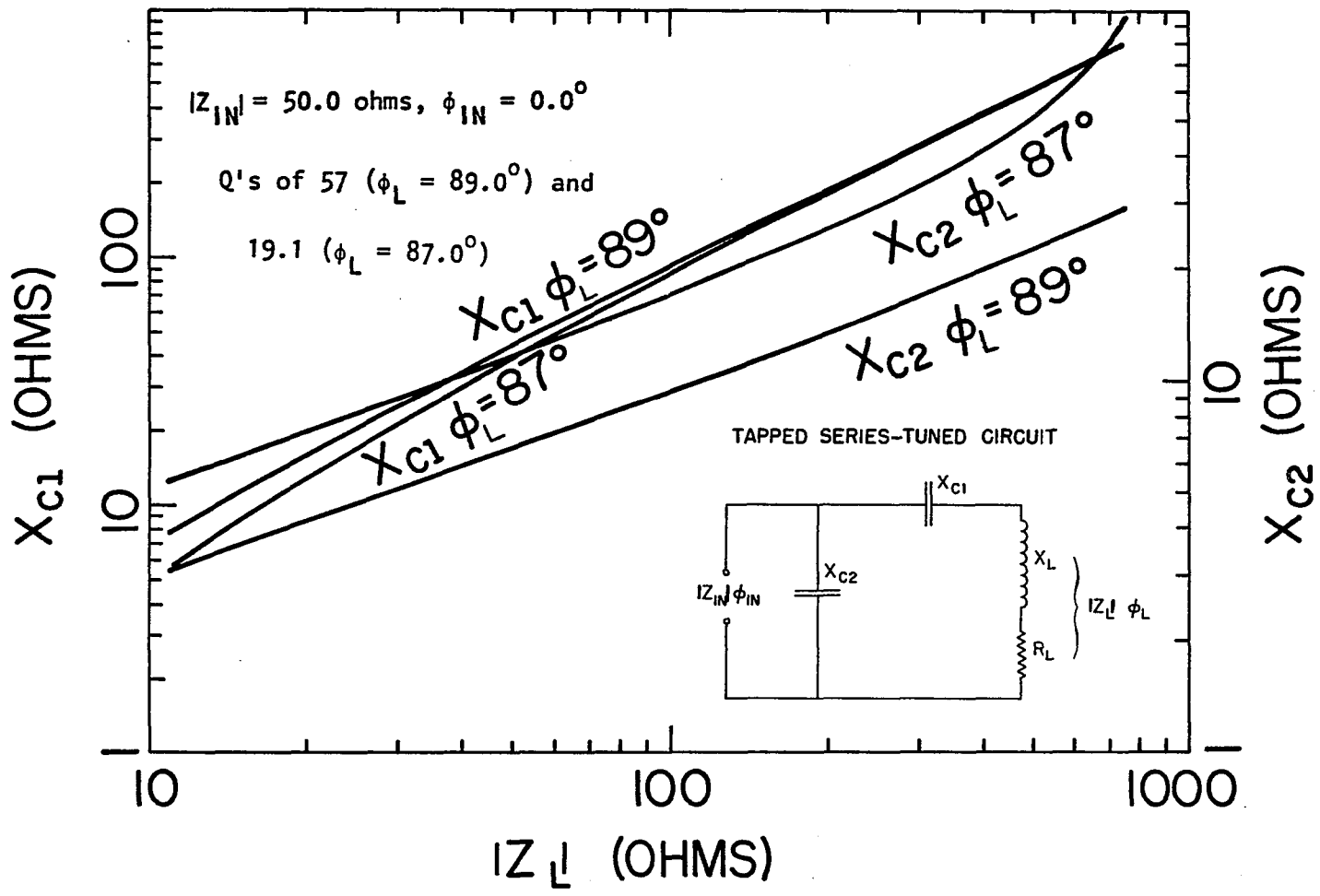
Figure 3. The Design Graph for the tapped series-tuned circuit

16
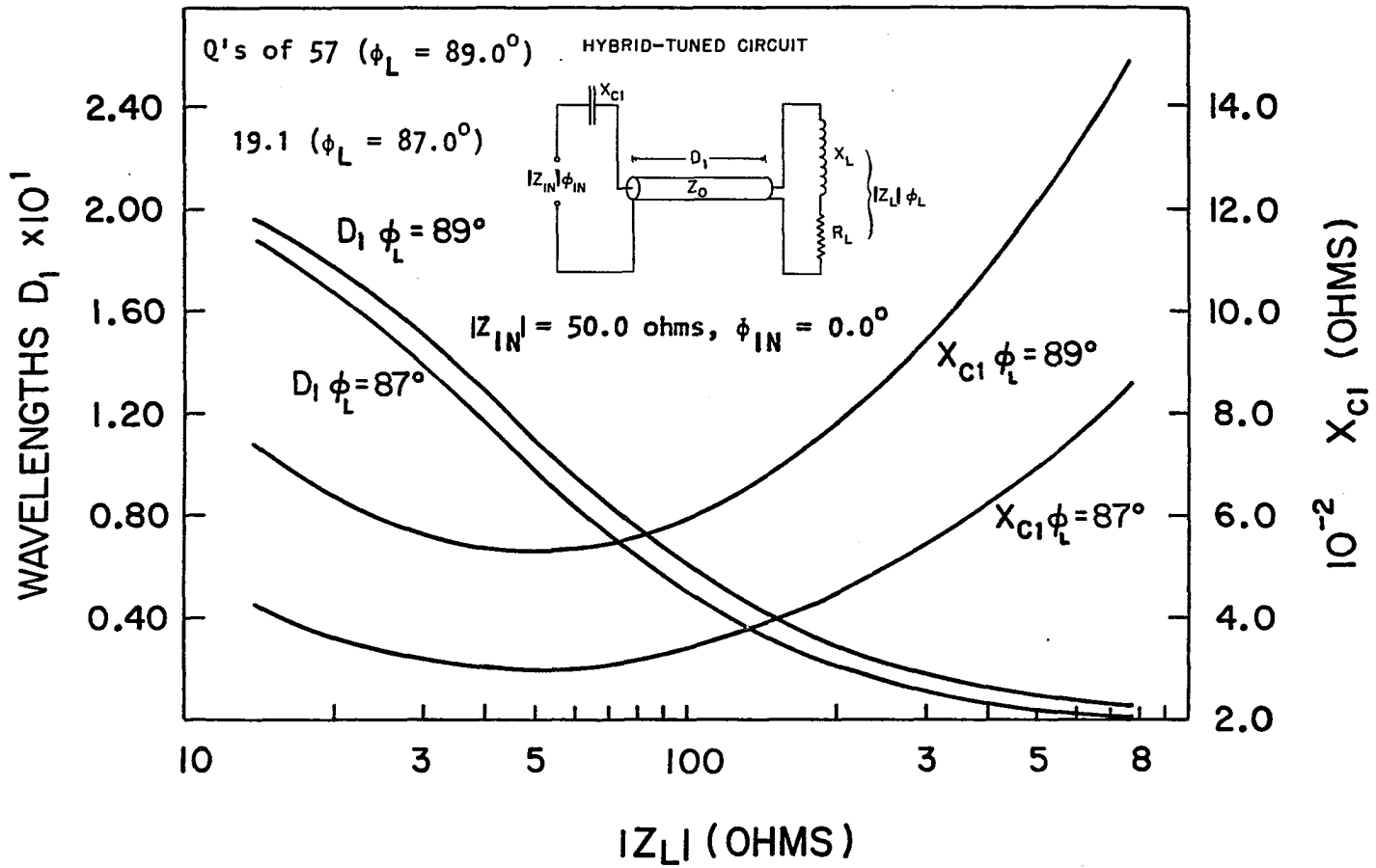
Figure 4. The Design Graph for the hybrid-tuned circuit
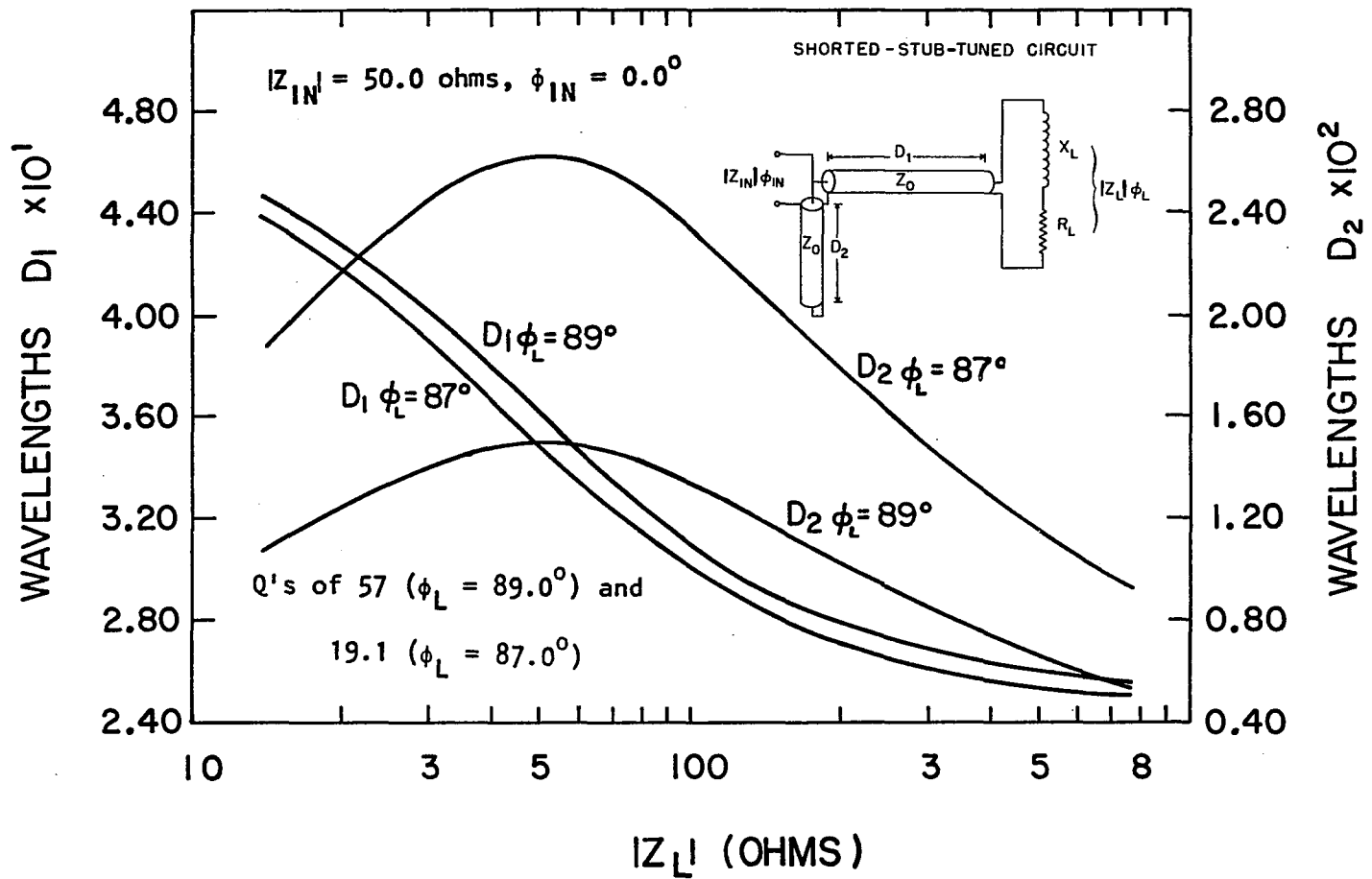
Figure 5. The Design Graph for the shorted-stub-tuned circuit

Design Graphs, which are frequency independent, provide
a graphical relationship between the impedance of the load and
the reactances and/or cable wavelengths of the tuning components.
These curves allow quick estimates for the approximate values
of the tuning components. The horizontal axis, $|Z_L| = \sqrt{X_L^2 + R_L^2}$,
represents the magnitude of the impedance of the load as would
be read on a vector impedance meter. For highly inductive
loads $|Z_L| \simeq X_L$. The vertical axes are in capacitive reactance
or wavelengths of cable. These values can be converted to
capacitance and lengths of cable using equation 1 (or 2) and
15 respectively.

Component values can be estimated rapidly and accurately
with these graphs. A comparison of calculated values with
values read from the Design Graphs is shown in Table 1. A
load which consists of a inductive reactance, $X_L = 99.9$ ohms,
and a resistance, $R_L = 5.23$ ohms, is tuned to $|Z_{IN}| = 50.0$ ohms
and $\phi_{IN} = 0.0^{\circ}$ at $f_o = 56.0$ MHz. The load impedance,
$|Z_L|$ $(|Z_L| = \sqrt{X_L^2 + R_L^2})$, is 100.0 ohms and the load Q is 19.1.
This Q corresponds to a phase angle, ϕ_L $(\phi_L = \tan^{-1}(Q))$, of
87.0°.

As one can see from this comparison, component values read
directly from the design graphs are very accurate indeed.
Unfortunately, but realistically, stray reactances and
distributed resistances are usually present in some unaccountable

Table 1. Comparison of component values for four NMR probes

obtained by equations and Design Graphs [Reactances,

X_i, in ohms, Capacitances, C_i, in pf, cable lengths,

$D_{i\lambda}$, in wavelengths, cable lengths D_i, in cm,

X_L = 99.9 ohms, R_L = 5.23 ohms, $|Z_L|$ = 100.0 ohms,

Q_L = 19.1, $|Z_{IN}|$ = 50.0 ohms, ϕ_{IN} = 0.0°, f_o = 56.0 MHz,

s = 0.66.]

CIRCUIT	EQUATIONS	DESIGN GRAPHS
TPTC		
X_{C1}	147.4	140.
C1	19.2	20.3
X_{C2}	305.5	300.
C2	9.3	9.4
TSTC		
X_{C1}	84.7	82.
C1	33.6	35.
X_{C2}	17.1	17.
C2	166.2	167.
HTC		
$D_{1\lambda}$	0.051	0.05
D_1	18.03	17.7
X_{C1}	341.8	350.
C1	8.31	8.1
SSTC		
$D_{1\lambda}$	0.301	0.30
D_1	106.4	106.
$D_{2\lambda}$	0.023	0.023
D_2	8.13	8.13

way in most circuits. The actual values of components required
to tune a given load will usually differ from the calculated
values. Therefore, one should regard equations and Design
Graphs as guides in the beginning stages of the design. The
final battle is usually won in the laboratory with a pair of
wire cutters, soldering iron and a vector impedance meter.

D. Frequency Responses

The magnitude of the input impedance, $|Z_{IN}|$, and phase angle,
ϕ_{IN}, can be obtained from the equations (7, 10, 17, and 20) of
the input impedance of each circuit. Let X_L, X_{C1}, X_{C2}, D_1 and D_2
represent the appropriate values for $|Z_{IN}| = Z_o$, $\phi_{IN} = 0.0^o$ at f_o.
The frequency dependence of these terms at any frequency, f,
can be incorporated into each equation by replacing these terms
with:

$$aX_L, \quad \frac{X_{C1}}{a}, \quad \frac{X_{C2}}{a}, \quad aD_1, \quad aD_2$$

with $a = f/f_o$. At a frequency, f, the magnitude of the input
impedance is:

$$|Z_{IN}| = \sqrt{Real^2(Z_{IN}) + Imaginary^2(Z_{IN})}$$

and the phase angle is:

$$\phi_{IN} = tan^{-1}[\frac{Imaginary(Z_{IN})}{Real(Z_{IN})}]$$

$|Z_{IN}|$ and ϕ_{IN} are the values that would be read on a vector
impedance meter as the frequency is swept. The frequency

dependent equations for each circuit are:

Tapped Parallel-Tuned Circuit

$$a = f/f_o$$

$$Z_{IN}(a) = -j\frac{X_{C2}}{a} + \frac{X_{C1}X_L - j\frac{X_{C1}R_L}{a}}{R_L + j(aX_L - \frac{X_{C1}}{a})} \tag{23}$$

Tapped Series-Tuned Circuit

$$Z_{IN} = 1/Y_{IN}, \quad a = f/f_o$$

$$Y_{IN}(a) = \frac{ja}{X_{C2}} + \frac{1}{R_L + j(aX_L - \frac{X_{C1}}{a})} \tag{24}$$

Hybrid-Tuned Circuit

$$a = f/f_o$$

$$Z_{IN}(a) = -j\frac{X_{C1}}{a} + \frac{Z_o[R_L + j(Z_o\tan(2\pi aD_1) + aX_L)]}{(Z_o - aX_L\tan(2\pi aD_1)) + j(R_L\tan(2\pi aD_1))} \tag{25}$$

Shorted-Stub-Tuned Circuit

$$Z_{IN} = 1/Y_{IN}, \quad a = f/f_o$$

$$Y_{IN}(a) = \frac{-j}{Z_o\tan(2\pi aD_2)} + \frac{(Z_o - aX_L\tan(2\pi aD_1) + jR_L\tan(2\pi aD_1))}{R_L + j(Z_o\tan(2\pi aD_1) + aX_L)} \tag{26}$$

The real and imaginary response of the above equations can be determined quite easily on the computer (7). The ideal impedance and phase responses of each circuit are shown in
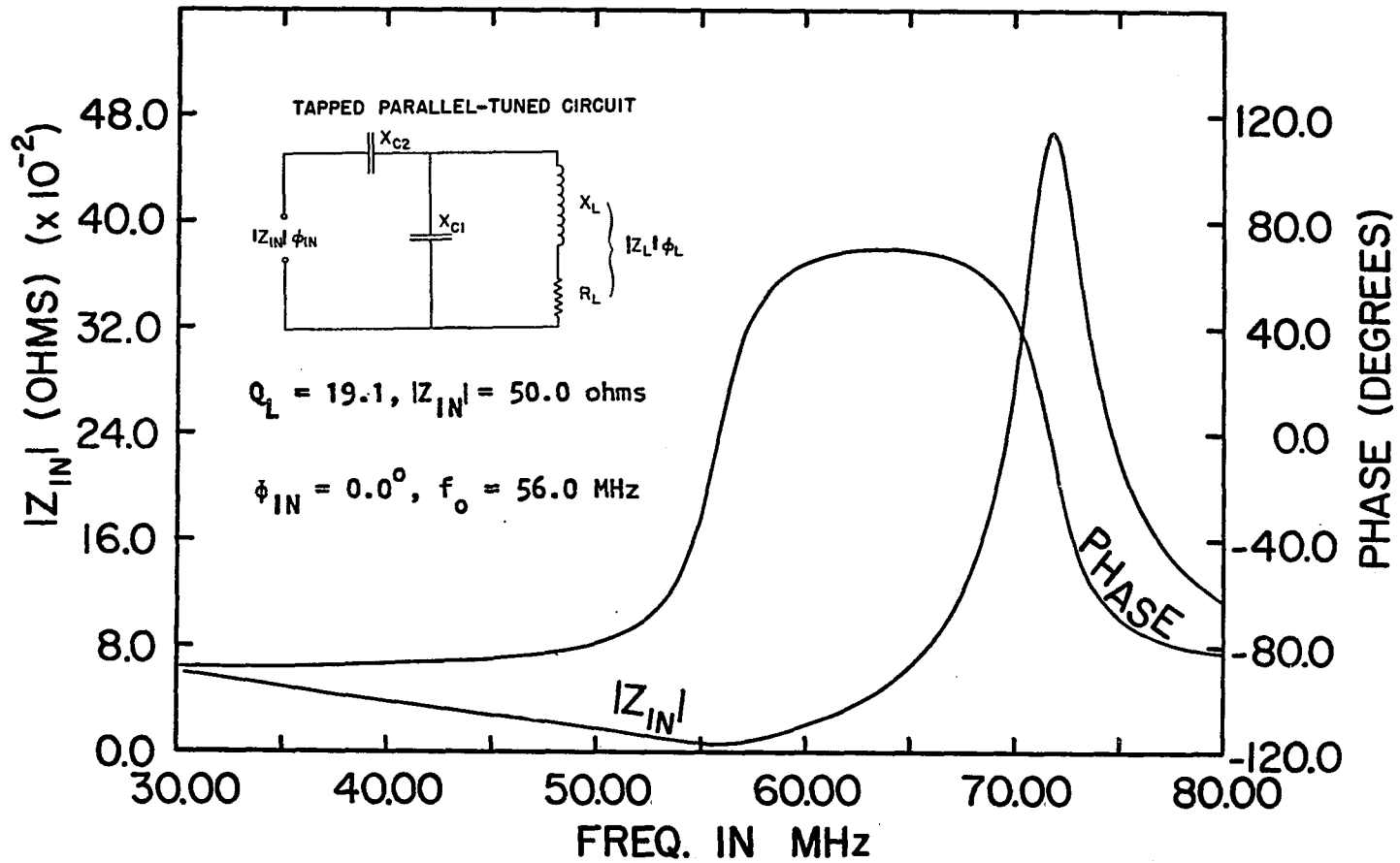
Figure 6. The frequency response of the tapped parallel-tuned circuit, Q = 19.1
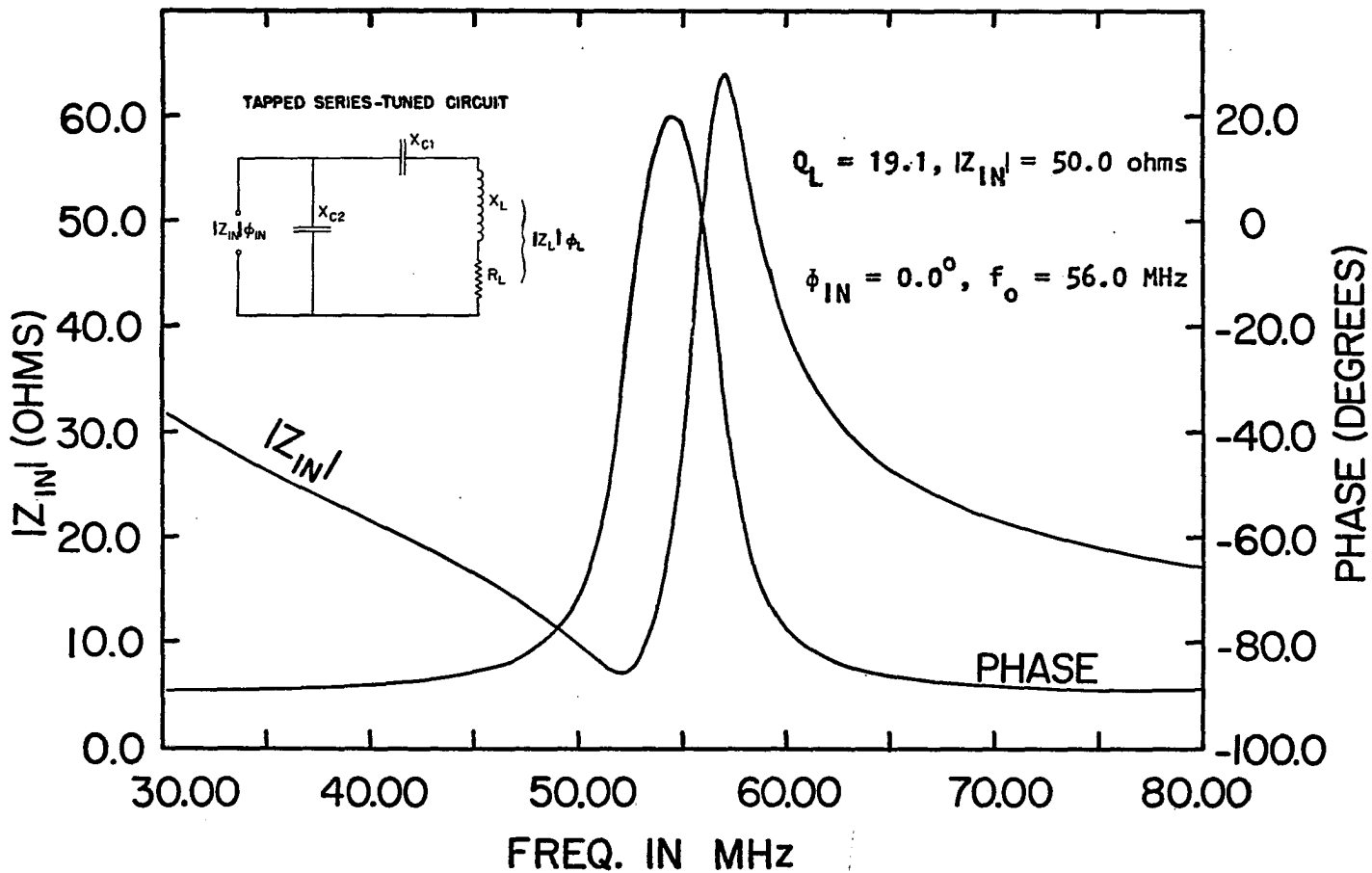
Figure 7. The frequency response of the tapped series-tuned circuit, Q = 19.1

HYBRID-TUNED CIRCUIT

$Q_L = 19.1$, $|Z_{IN}| = 50.0$ ohms

$\phi_{IN} = 0.0°$, $f_o = 56.0$ MHz

$|Z_{IN}|$

PHASE
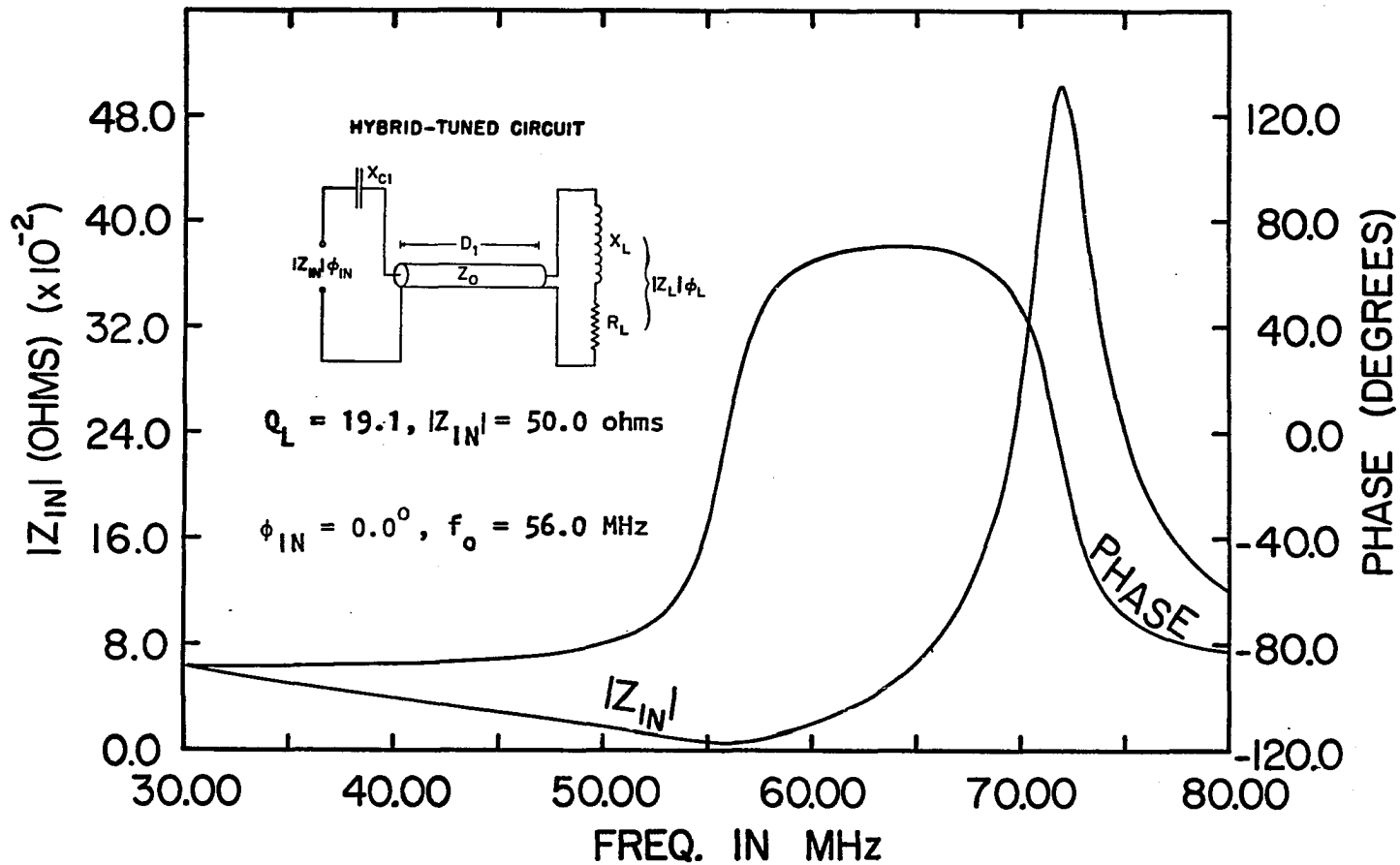
Figure 8. The frequency response of the hybrid-tuned circuit, Q = 19.1
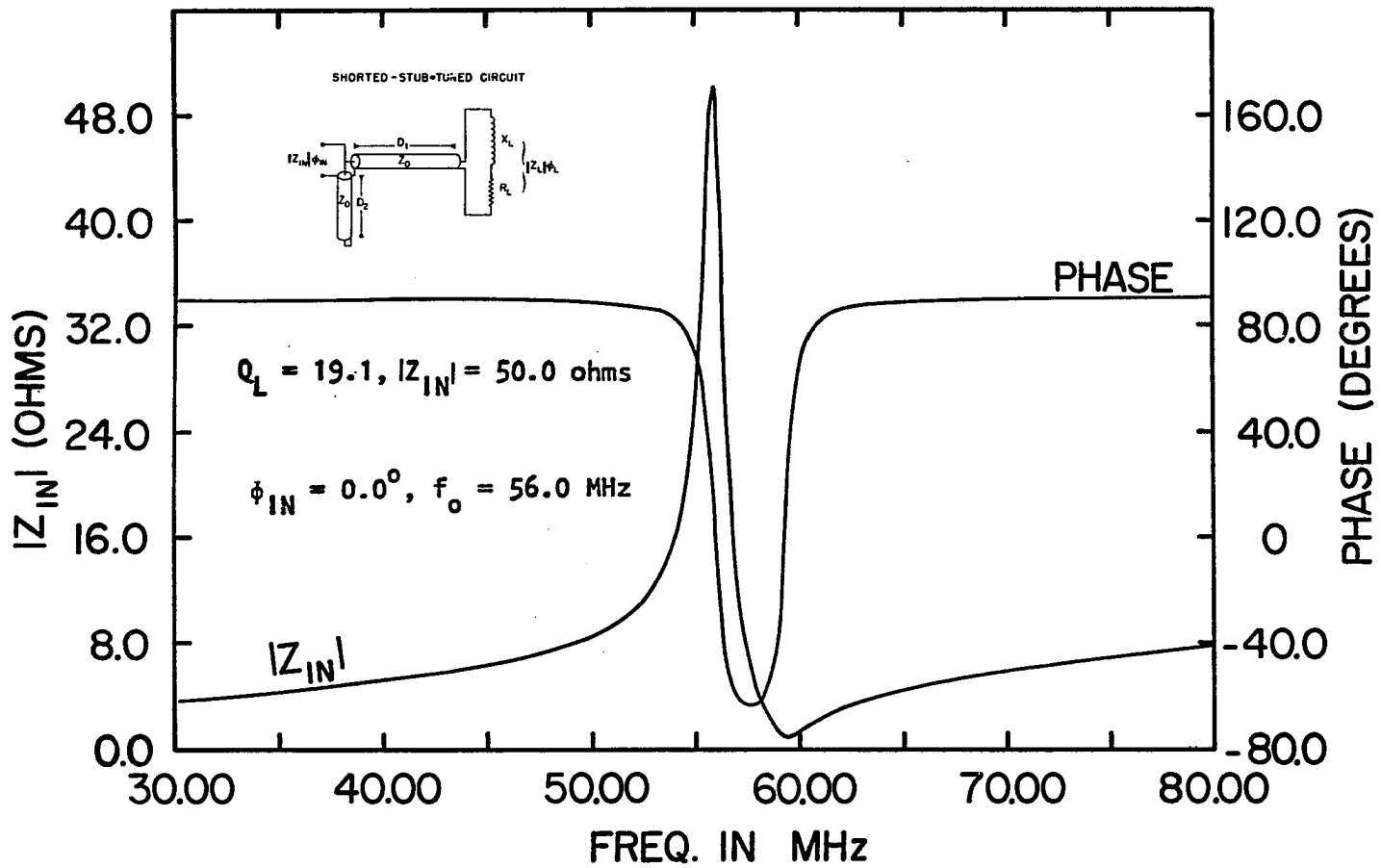
Figure 9. The frequency response of the shorted-stub-tuned circuit, Q = 19.1

Figures 6, 7, 8 and 9 respectively. Identical loads which

consist of a 0.42×10^{-6} Henry inductor in series with a 7.75

ohm resistor ($Q = 19.1$) are tuned to $|Z_{IN}| = 50.0$ ohms,

$\phi_{IN} = 0.0^\circ$ at $f_o = 56.0$ MHz. The left axis represents the

magnitude of the input impedance and the right axis represents

the phase angle of the input impedance.

These response curves allow one to visualize the behavior

that will be encountered during the "tuning up" of the probe.

For instance, after the approximate component values are installed

in a given circuit, then there should be a frequency close to

f_o where the behaviors of the impedance and phase angle are

similar to those of the appropriate response curve. Component

values are simply adjusted to bring the desired response to

f_o. If such behavior is not found, then one can be safe in

assuming that component values and/or X_L and R_L are inaccurate.

Another important use of response curves rests with their

use to judge the feasibility of attempting a specific design.

The location of low-impedance and high-impedance resonances

($\phi_{IN} = 0.0^\circ$ in both cases) can be checked in relation to the

tuning frequency. For instance, a common problem in designing

the tapped series-tuned circuit is that the low-impedance resonance

occurs slightly below the tuning frequency. This low-impedance

resonance moves farther down frequency as the Q is lowered.

However, for high enough Q's, it may interfere with the tuning

at the desired frequency. Frequency response graphs are useful in anticipating and avoiding this problem.

Interestingly, the theoretical frequency responses of both the tapped parallel-tuned and hybrid-tuned circuits are virtually identical. This behavior is not unexpected since cable D_1 is short enough to be considered as a small capacitor in parallel with the coil (i.e. almost a tapped parallel-tuned circuit) at this frequency.

E. Ringdown, Circuit Losses and Effective Q's

The quality factor, Q, of a load which consists of an ideal inductive reactance, X_L, in series with a resistance, R_L, is defined as $Q = X_L/R_L$ (6). Q is related to the ability of the circuit to store energy during one RF cycle as is shown in Chapter IV. A ringdown time, $t_r = 21 \, Q/\pi f_o$, can be considered as the approximate time required for the RF voltage across the load to exponentially decay by a factor of 10^{-9} or from 1000 volts to 1 microvolt.

The ringdown time usually places limits on the maximum allowable value of Q. When recovery time is not critical, the highest possible Q is usually desired since the signal-to-noise ratio increases with Q. In such a case, no lumped load resistance, R_L, is used. The actual, non-zero value of R_L, which limits the Q, can be considered to result from distributed losses. Probes with the fastest possible recovery times require

low Q's. In such cases, values of R_L which limit the Q are appropriately chosen.

High Q probes generally have the best RF power efficiency and reciprocally the best one-shot, signal-to-noise of the FID than do low Q probes. When a probe is finally tuned, the exact Q may be somewhat of a mystery since there are additional and distributed losses from capacitors, inductors, hookup wire, cables, etc.

An accurate method for calculating the effective Q of the entire probe-circuit is to consider all capacitors, inductors and cables as being "ideal" and to refer all losses--whatever the source--to the load resistor, R_L which is in series with the inductor. For example, the actual value of the capacitor C_{C2} which is required to tune a tapped series-tuned circuit to input impedance, $|Z_{IN}| = Z_0$, can be used to determine the effective Q for this circuit. For the TSTC the value of capacitor C_{C2} is solely determined by the resistive losses of the load, R_L (equation 12). As the resistive losses decrease (Q increases), the value of C_{C2} required to tune a fixed input impedance $|Z_{IN}| = Z_0$, increases. By rearranging equation 12, an effective Q, $Q_{eff} = \dfrac{X_L}{R_{eff}}$, $R_{eff} = R_L$, can be defined:

$$Q_{eff} = 4\pi^2 f_0^2 X_L Z_0 C_{C2}^2 + \frac{X_L}{Z_0} \qquad (27)$$

For the case where $Q_{eff} \gg \dfrac{X_L}{Z_0}$ which is usually true for most

NMR probes:

$$Q_{eff} \simeq 4\pi^2 f_o^2 X_L Z_o C_{C2}^2 \qquad (28)$$

X_L is the inductive reactance of the NMR coil measured at

frequency, f_o. However C_{C2} is the actual measured capacitance

required to tune the input impedance to Z_o, $\phi_{IN} = 0.0°$ at f_o. In

effect, the above treatment lumps all circuit losses from all

components into the load resistance, R_{eff}. Components are

now treated as lossless. Capacitance C_{C2} may now be considered

that value required to tune a circuit with load: (X_L, R_{eff} and

Q_{eff}) to ($|Z_{IN}| = Z_o$, $\phi_{IN} = 0.0°$ at f_o). Of course, all of the

capacitors including C_{C2} possess some ohmic losses. However,

to the outside world, the fictitious resistances R_{eff} $(= X_L/Q_{eff})$

appears to be in series with the inductive reactances. This

treatment is very desirable and valuable since both the H_1

field produced by the RF pulse and the induced NMR signal will

depend on Q_{eff}. A similar treatment can be applied to the

remaining three circuits:

Tapped Parallel-Tuned Circuit

$$Q_{eff} > \frac{X_L Z_o}{X_{C1}^2} \qquad X_{C1} = (2\pi f_o C_{C1})^{-1}$$

$$Q_{eff} \simeq \frac{X_L}{Z_o} (1 - 2\pi f_o X_L C_{C1})^{-2} \qquad (29)$$

Hybrid Tuned-Circuit

$$A = \tan 2\pi D_1, \qquad Q_{eff} > \frac{X_L}{Z_0\left(1 + \dfrac{1}{A^2}\right)}$$

$$Q_{eff} \simeq \frac{Z_0 X_L (1 + A^2)}{Z_0{}^2 - 2Z_0 X_L A + X_L{}^2 A^2} \qquad (30)$$

Shorted-Stub-Tuned Circuit

$$A = \tan 2\pi D_1, \qquad Q_{eff} > \frac{X_L}{Z_0(1 + A^2)}$$

$$Q_{eff} \simeq \frac{Z_0 X_L (1 + A^2)}{Z_0{}^2 A^2 + 2X_L Z_0 A + X_L{}^2} \qquad (31)$$

For the hybrid and shorted-stub-tuned circuits, D_1 is the actual measured length of cable D_1 in wavelengths at frequency, f_0. Also Z_0 is both the input impedance and the characteristic impedance of the cable. For most probes, the effective Q's are usually well above the lower limits of the inequalities for which all four equations are valid.

F. Design of the NMR Coil

The NMR coil is perhaps the most important part of the probe. The coil is usually cylindrical in shape. Its Q and the homogeniety of RF fields are very important attributes.

For an RF wave travelling on the surface of a good conductor, the distance, δ, required for that wave's amplitude to be

attenuated to e^{-1} of that on the surface is termed the depth
of penetration (6):

$$\delta = \sqrt{\frac{\rho}{\pi f_o \mu}} \tag{32}$$

ρ is the resistivity in the units of ohm-meters and f_o is the
RF frequency of the wave in Hertz. μ is the permeability of
the material and, for non-magnetic materials, it may usually
be assumed equal to $4\pi \times 10^{-7}$ Henry/meter which is the permeability
of free space, μ_o.

The resistivities of silver, copper and tin are 16, 17
and 114 nanoohm-meters respectively. For copper wire at a
frequency of 30.0 MHz, the depth of penetration is calculated
to be only 12 microns. Therefore, the properties of the coil
will be strongly influenced by the properties of the surface
of the conductor. Consequently, surfaces should be clean and
smooth. Coated wire should be used whenever possible to
prevent tarnishing.

When signal-to-noise is important, as for high Q probes,
the best possible conductors such as silver-plated copper should
be used. Although silver is only slightly less resistive than
copper, this modest improvement in Q and signal-to-noise may
lead to more rapid acquisitions of data when long time-averagings
are required.

When fast recovery is important, as for low Q probes,
tin-plated copper will result in substantially higher but
distributed losses and may improve the recovery time.

When the homogeneity of RF fields are important, both of the following properties have been found to produce good results. First, the coil's length-to-inside-diameter ratio should be at least 4/1. Second, the wire is flattened in the central region of the coil. Usually #18 or smaller gauge (i.e. larger diameter) wire is used for mechanical stability. Also, the coil may be supported by its own leads.

At higher frequencies, in order to prevent the reactance of the coil from becoming capacitive, the coil should be loosely wound i.e., the spacing between turns should be about ½ the diameter of the wire.

G. Power Dissipation in the Load Resistance

The resistance of the load resistor, R_L, is determined by the desired Q (and Q_{eff}) as explained above. The minimum wattage of this resistor depends on the average power dissipation, P_{ave}:

$$P_{ave} = \frac{n \cdot t_p}{t_{slow}} P_{pulse} \qquad (33)$$

In this equation, P_{pulse} is the RMS pulse power, t_p is the pulse width, and n is the total number of pulses in one slow clock period, t_{slow}. For example, for 400.0 RMS Watt pulses of 1.2 μsec duration and for 2048, 8-pulse sequences repeated once every 3 sec, P_{ave} will be 2.6 RMS Watts. As a precaution, a load resistor with a power rating of at least 5 Watts should be used.

H. Circuit Designs

1. Compact NMR-lock probe

The NMR-lock probe is used in conjunction with other equipment to hold or lock the laboratory magnetic field at constant value. Figure 10 shows the design of one such probe which is very compact. A hybrid-tuned circuit is used for matching.

2. Probe for Multiple-Pulse experiments

The NMR probe for Multiple-Pulse homonuclear decoupling usually requires the fastest possible recovery-times so that the shortest cycle-times can be obtained. A low Q is essential. Figure 11 shows the design of such a probe. A tapped series-tuned design is used for matching. The capacitor in series with the inductor should have a very high voltage-rating. The load resistor should have sufficient wattage to dissipate the usually-high average power.

NMR LOCK PROBE

COIL AND SHIELD
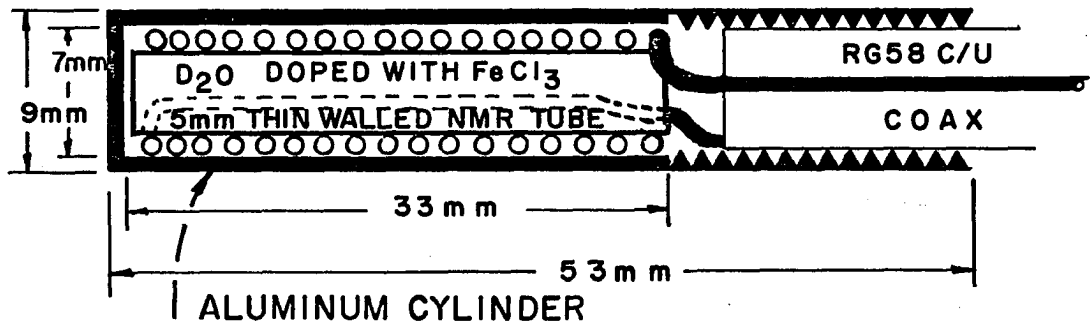
COIL: 33mm x 5mm i.d. #30 VARNISHED WIRE

$X_L = 230$ ohms $(L=4.2\mu H)$ AT $f_o=8.7$ MHz

R.F. MATCHING:
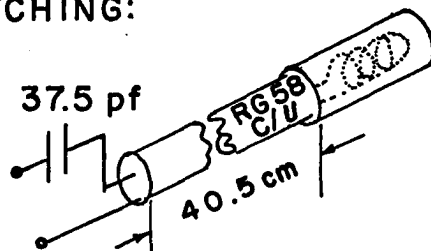
$|Z_{IN}| = 50$ ohms
$\phi_{IN} = 0°$
$f_o = 8.7$ MHz
$Q \simeq 20$

Figure 10.   The design of a compact NMR-lock probe

PROBE FOR MULTIPLE PULSE

$f_o = 56$ MHz

each: 10 ohms 2 Watts

17 turns, #18 wire

5 mm id. X 25 mm long

$|Z_{IN}| = 50$ ohms

$\phi_{IN} = 0^{\circ}$

100 pf

7 - 45 pf

FLATTENED

L = 0.36 μH

250 v

250 v

$Q_{eff} \cong 25$

6 - 35 pf 1000 v
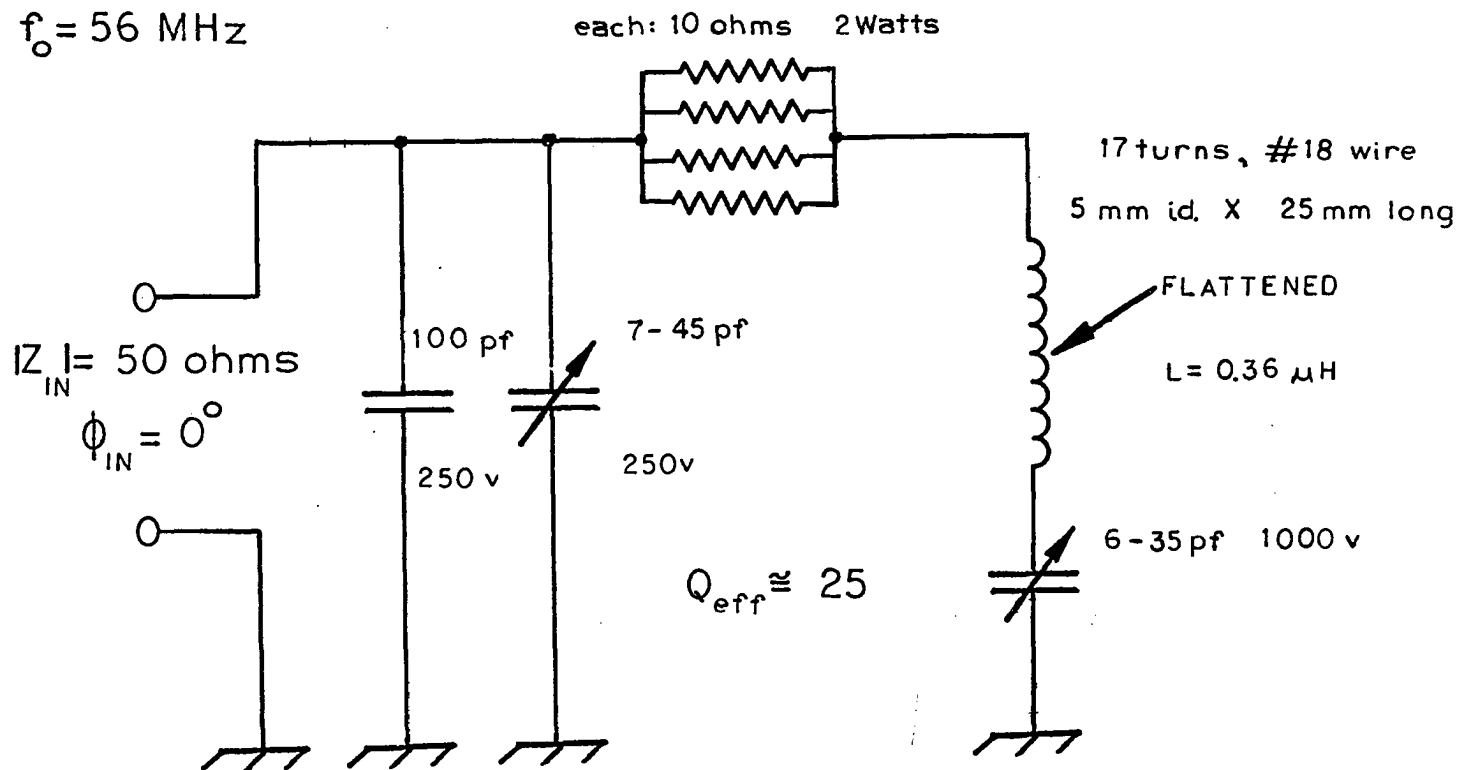
Figure 11. The design of a typical NMR probe for Multiple-Pulse, Homonuclear Decoupling

III. THE DESIGN OF A SINGLE-COIL DOUBLE-RESONANCE PROBE

A. Introduction

Recently, much interest has been directed toward the Cross-Polarization (CP) experiments (2, 3, 8) developed by Pines, Gibby and Waugh in the early 1970's. Their double-resonance technique relies upon the transfer of magnetic polarization from abundant spins such as ^1H or ^{19}F to rare spins such as ^{29}Si and ^{13}C. The rare spins (called S spins) are enhanced and observed while the abundant spins (called I spins) are decoupled.

Of course, certain conditions must be satisfied for such experiments to be successful. The most important condition, which yields maximum polarization transfer, was originally derived by Hartmann and Hahn (9) and appropriately bears their names. The Hartmann-Hahn or H-H criterion states that the frequencies of nutations, ω_i, of both the I spins and S spins caused by their respective RF fields (called H_{1i} fields) should be the same, or:

$$\omega_I = \gamma_I H_{1I} = \omega_S = \gamma_S H_{1S}$$

γ_i is the gyromagnetic ratio of the ith species. See Chapter VIII for a further discussion.

It is desirable to establish or match the H-H condition over as large a volume of the sample as possible to achieve maximum S/N in rare-spin detection.

Such desires have motivated researchers (10, 11) to design single-coil double-resonance NMR probes in which the same coil or inductor is excited simultaneously by two H_{1i} fields at widely differing frequencies.

This Chapter describes an original design of a double-resonance probe using a single coil. This design has found use in high powered, Magic-Angle Spinning (MAS) experiments (2, 3) on solids (See Chapter IX) and the much lower powered J Cross-Polarization (12) experiment on liquids (See Chapter VIII).

B. Circuit Description

The schematic diagram of the single-coil double-resonance probe is shown in Figures 12, 14 and 16. A detailed explanation of the theory behind its design and operation has been previously reported (13). Figures 13 and 15 show pictures of two actual probes.

The first probe (Figures 12 and 13) is used for combined ^1H-^{13}C Cross Polarization and high speed (>2 KHz) Magic-Angle Spinning. The last two probes (Figures 14-16) are primarily used for ^1H-^{29}Si J Cross Polarization with spinning (<200 Hz). The third probe, whose schematic diagram is shown in Figure 16, is similar to the second probe but contains a larger coil. All probes may be simply retuned at f_L to observe ^1H Cross Polarization with other rare-spin species.

$^1H - ^{13}C$ C.P. + M.A.S. PROBE
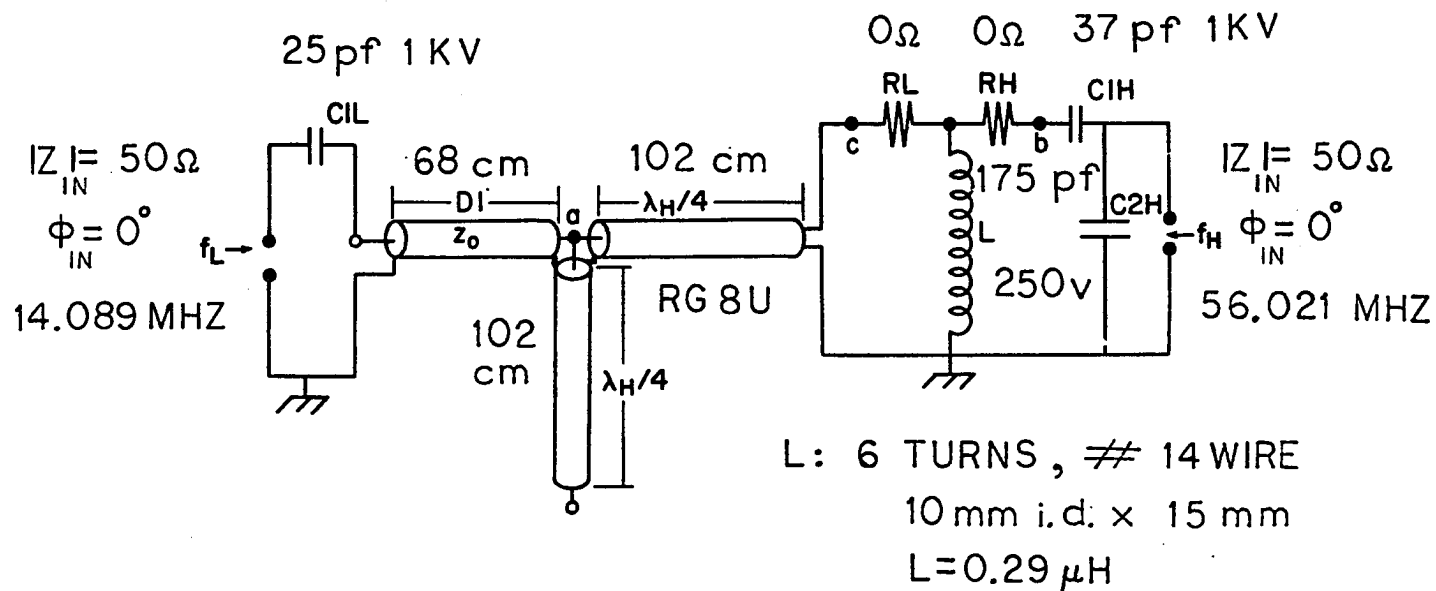
Figure 12. The circuit of a single-coil probe for ^1H-^{13}C Cross Polarization and Magic-Angle Spinning
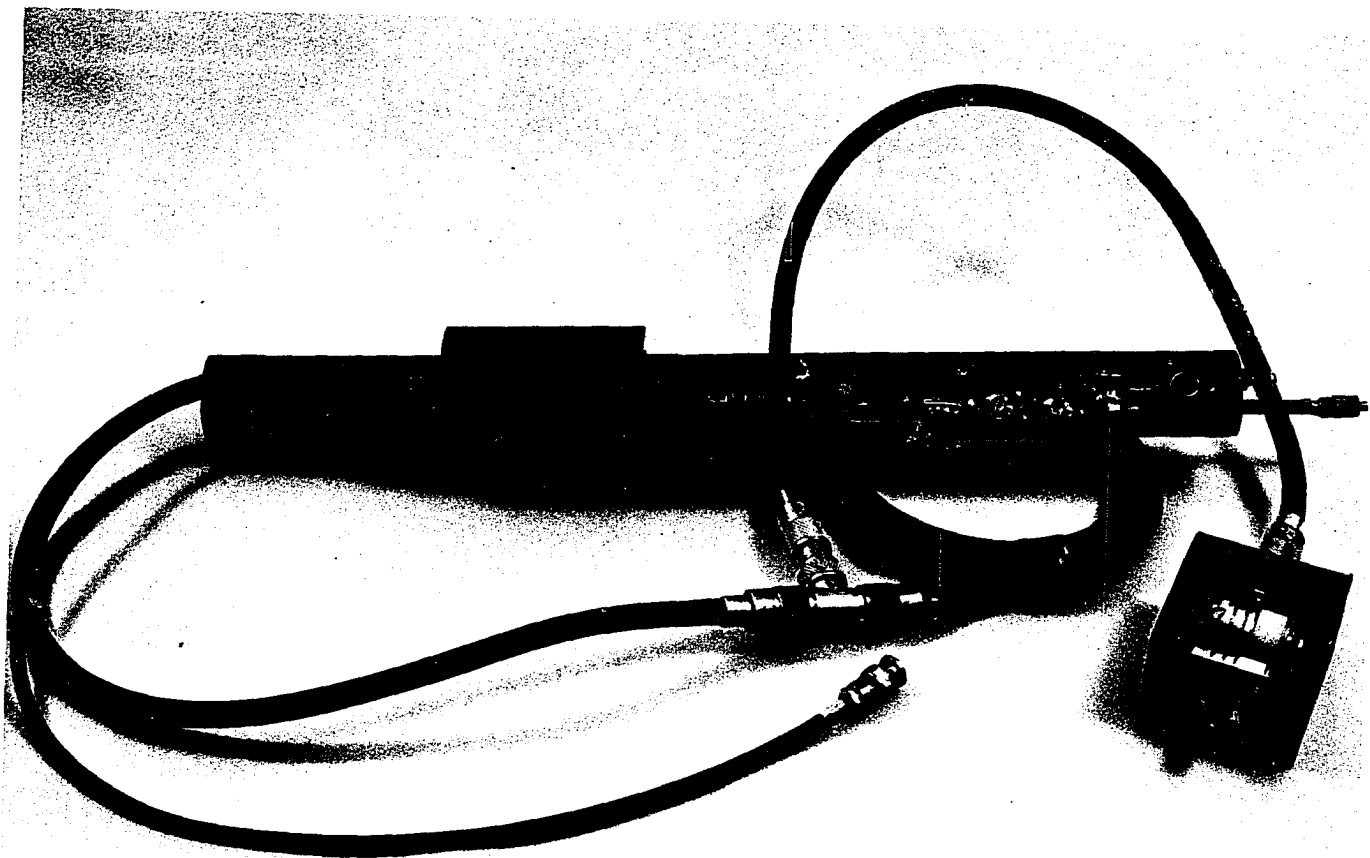
Figure 13.   A picture of the probe for ^{1}H-^{13}C Cross
Polarization and Magic-Angle Spinning

CIL

RL RH CIH

c b

D1 λH/4

Z₀ a

L

C2H

fL→ →fH

λH/4
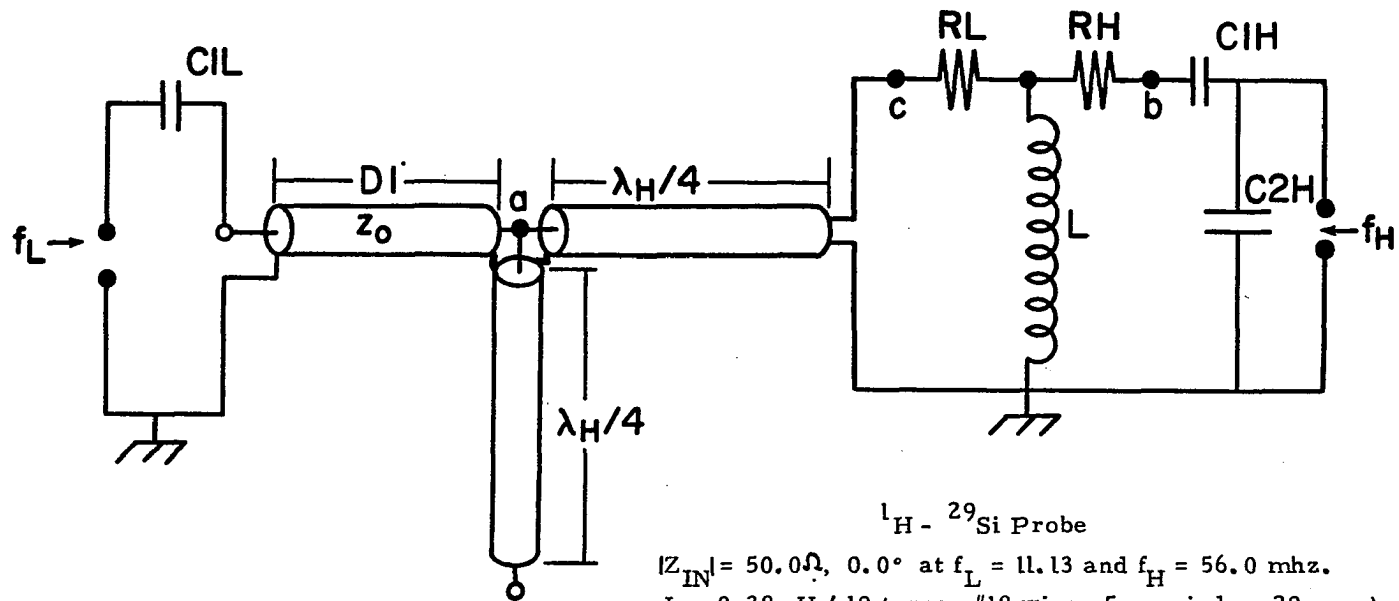
$^1H - ^{29}Si$ Probe

$|Z_{IN}| = 50.0 \Omega$, $0.0°$ at $f_L = 11.13$ and $f_H = 56.0$ mhz.

$L = 0.38$ µH (19 turns, #18 wire, 5 mm i.d. x 29 mm)

$R_{RL} = 0.0 \Omega$ and $R_{RH} = 0.0 \Omega$

$C_{C1H} = 25.8$ pf $C_{C2H} = 120.0$ pf $C_{C1L} = 46.2$ pf

$D_{D1} = 112.0$ cm $D_{\lambda H/4} = 102.0$ cm (RG 8 U)

$Q_{eff, L} = 16.4$ $Q_{eff, H} = 14.6$

Figure 14. The circuit of a single-coil (5 mm i.d.) probe for ^1H-^{29}Si J Cross Polarization
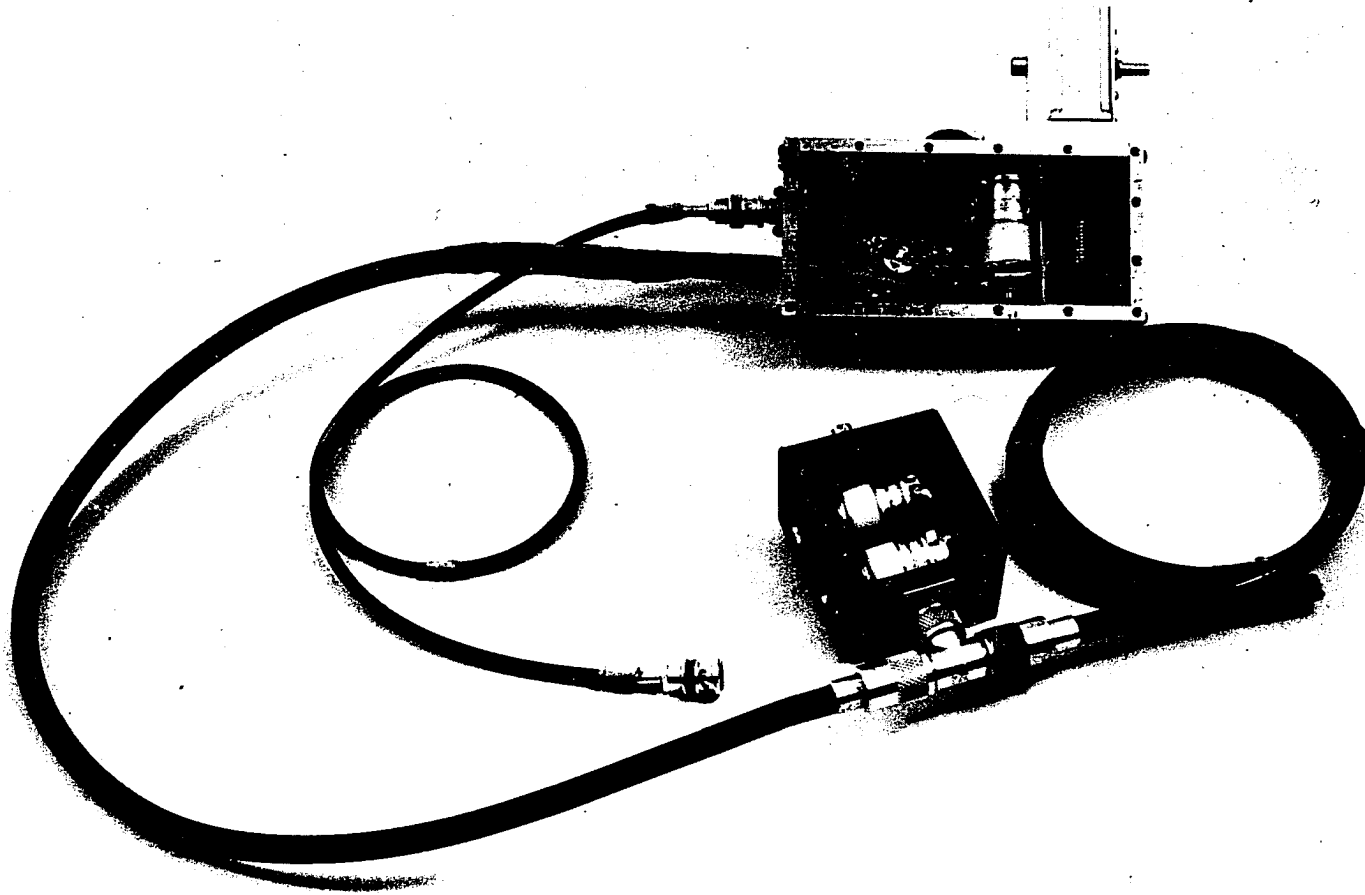
Figure 15. A picture of the probe for ^{1}H-^{29}Si J Cross
Polarization

^{1}H-^{29}Si J.C.P. PROBE
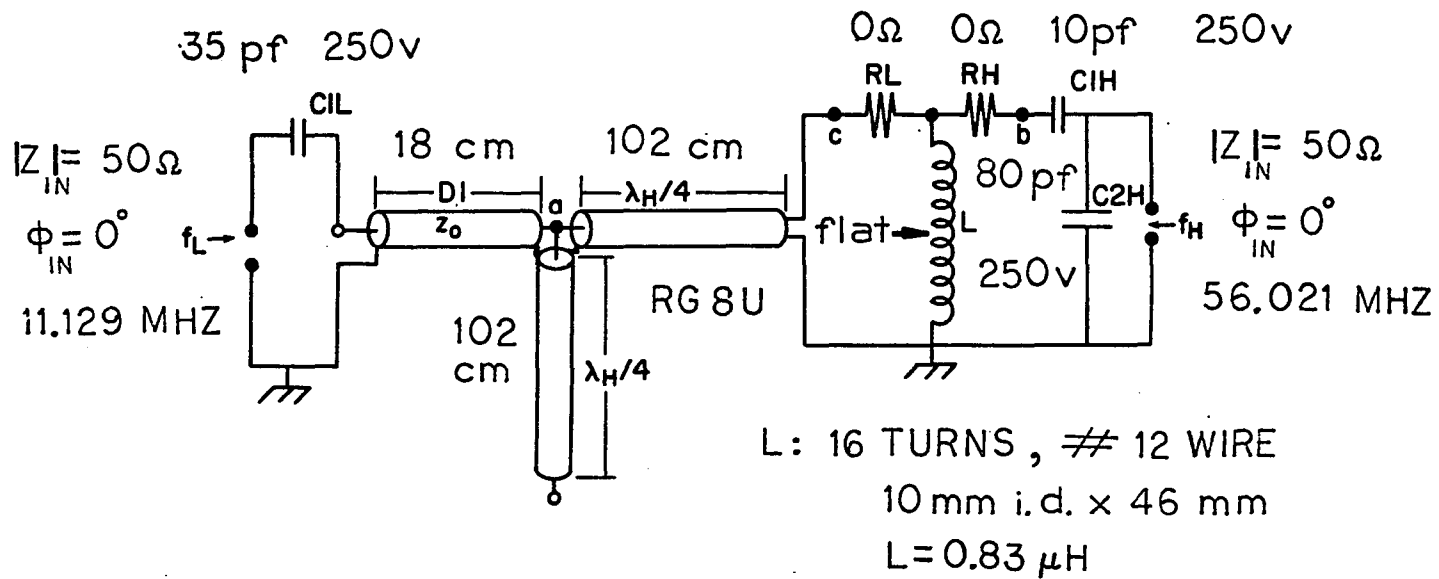
Figure 16. The circuit of a single-coil (10 mm i.d.) probe for ^{1}H-^{29}Si J Cross Polarization

There are three criteria that are important in the design of any probe used for Cross Polarization of solids with rare-spin observation. The first criterion is that adequate isolation of the high frequency, f_H, from the low frequency, f_L, is achieved. The second requires reasonably good power efficiency at both f_L and f_H. The third requires the best possible signal-to-noise ratio for rare-spin detection. The following discussions refer to the schematic diagrams of Figures 12, 14 and 16.

1. Frequency isolation

High-frequency isolation is obtained through the use of two quarterwavelengths of transmission lines, $\lambda_H/4$ at f_H. The impedance of point "a" at f_H is low but the impedance at point "c" is very high. Most of the RF energy at f_H will be effectively blocked from entering the quarterwavelength and will thus flow through the inductor to ground. Since point "a" is a low impedance at f_H, the addition of the low-frequency-tuning network, cable D1 and capacitor C1L, will have very little effect on the impedance of point "c" at f_H.

Low-frequency isolation is achieved by the large reactance of capacitor C1H at f_L. This reactance will block most of the RF energy and force it to ground through the inductor. This capacitor simultaneously serves as a tuning element at f_H.

Typical isolations of f_H measured at the input port of f_L are around -30 dB while the reciprocal isolations of f_L at the input port of f_H are approximately -15 dB.

2. Power transfer

Power is transferred into the probe at f_H by adjustment of capacitors C1H and C2H to the normal system impedance: $|Z_{IN}| = 50.0$ ohms, $\phi_{IN} = 0.0$. These capacitors form a tapped series-tuned matching network discussed in detail in Chapter II.

Similarly, power is transferred into the probe at f_L through adjustment of the length of cable D1 and the value of capacitor C1L to $|Z_{IN}| = 50.0$ ohms, $\phi_{IN} = 0.0°$. These two components form a hybrid-tuned matching network discussed in detail in Chapter II.

No design at present requires resistors RL or RH. The resistors are used to lower the Q should inadequate recovery-time pose a problem.

Typical power requirements for the probe of Figures 12 and 13 are about 100 RMS Watts at $f_H = 56.0$ MHz to establish an $H_{1I} = 10.0$ Gauss field and about 250 RMS watts at $f_L = 14.1$ MHz to establish an $H_{1S} = 40$ Gauss field. Average power requirements for the probe of Figures 14 and 15 are about 0.5 RMS Watts at $f_H = 56.0$ MHz to establish an $H_{1I} = 1.0$ Gauss field and about 1.3 RMS Watts at $f_L = 11.13$ MHz to establish an $H_{1S} = 5$ Gauss field. The probe of Figure 16 requires 9.0 and 1.6 RMS Watts to establish fields of 1 and 5 Gauss at the frequencies of 56.0 and 11.125 MHz respectively.

3. Signal-to-Noise ratio

Figure 17 shows the typical signal-to-noise obtained with one excitation (or one shot) using the three probes discussed here.

C. Probe Construction

The high-speed, MAS probe (Figure 13) was assembled and tuned in a frame previsouly described (14). The other two probes were constructed in aluminum boxes. The tuning of all probes is similar.

First, the high-frequency-isolation device which consists of the two quarterwavelengths at f_H is made. For highest Q, low loss cables such as RG8U should be used. The proper construction of this isolation network is very critical if good isolation and high power efficiency are to be achieved.

The proper length of the open quarterwavelength is established with the use of a frequency synthesizer, an oscilloscope and a three port tee (the same tee that will be used in the probe, of course). A slightly long cable is attached to one port, a signal at f_H is fed into the second port, and the third port is connected to a scope. The cable should be "snipped off" until a minimum RF signal at f_H is detected on the scope. This is the proper length of cable for an open quarterwavelength. The synthesizer and scope are now removed from the tee.

The proper length of the remaining quarterwavelength is now established. The proper length is such that a maximum

TYPICAL ONE-SHOT C.P. FID'S

BANDWIDTH: 5.0 KHZ
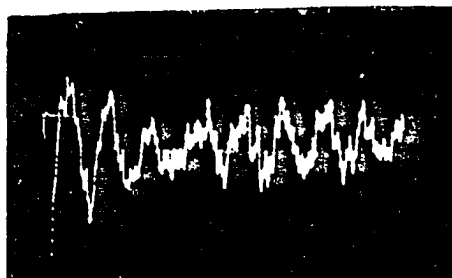
^{13}C IN ADAMANTANE
2.1 × 10^{20} SPINS
T_{CP} = 1.5 msecs
10 mm i.d. COIL
H_1: 10, 40 GAUSS
f_o = 14.089 MHZ
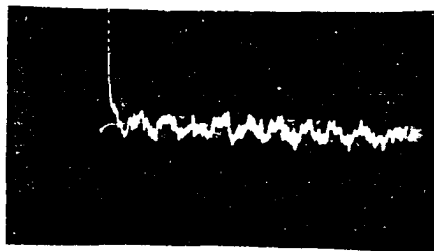
^{29}Si IN TRIETHYLSILANE
4.0 × 10^{19} SPINS
T_{CP} = 5.0 msecs
5 mm i.d. COIL
H_1: 1, 5 GAUSS
f_o = 11.129 MHZ
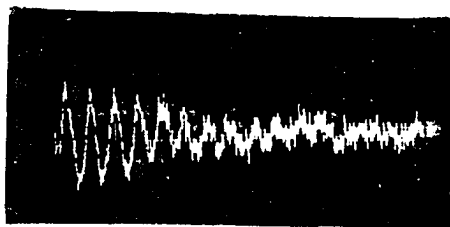
^{29}Si IN TRIETHYLSILANE
3.6 × 10^{20} SPINS
T_{CP} = 5.0 msecs
10 mm i.d. COIL
H_1: 1, 5 GAUSS
f_o = 11.129 MHZ

Figure 17. Pictures of typical one-shot C.P. FID's of rare spins

impedance at f_H occurs at the end which will eventually be connected to the NMR coil. A vector impedance meter is used to establish this length. A slightly long cable (of suitable dielectric since it will be in the magnetic field) is now connected to the tee which has the open $\lambda_H/4$ attached. This cable is "snipped off" in small chunks while one monitors the impedance of this snipped end on a vector impedance meter. The proper length occurs when a maximum impedance at zero phase angle occurs at f_H. This end is then connected from the top of the coil to ground as shown in Figures 12, 14 and 16.

Now, the initial tuning at f_H is made by first measuring the impedance, $|Z_L|$, and phase angle, ϕ_L, from the top of the coil to ground--with the f_H isolation network installed, of course. The approximate values for capacitors C1H and C2H are calculated from the equation for the tapped series-tuned circuit discussed in Chapter II. These capacitors are adjusted until $|Z_{IN}| = Z_o$, $\phi_{IN} = 0.0^O$ at f_H is obtained.

The last step is to measure the impedance, $|Z_L|$, and phase angle, ϕ_L, of point "a" to ground at f_L--with capacitors C1H and C2H installed and tuned. The equations for the hybrid-tuned circuit discussed in Chapter II are used to calculate the approximate length of D1 and capacitance of C1L. These components are then adjusted until $|Z_{IN}| = Z_o$, $\phi_{IN} = 0.0^O$ at f_L. For a properly designed probe, the addition of D1 and C1L should have very little effect on the high-frequency tuning.

Experimentally, it has been observed that the highest Q capacitors such as Polyflon (15) types should be used for capacitors C1H and C1L. Ceramic variable capacitors were found to generate enormous and horrendous broadband noise during the decoupling pulse, although the use of a ceramic variable capacitor for C2H has been found acceptable. ATC (16) type fixed ceramic capacitors have been used as padding capacitors with good results.

D. The Construction of a Stable High-Speed, Andrews-Type Rotor

This section will describe the construction of a stable rotor used for Magic-Angle Spinning at speeds of up to 2.8 KHz. This type of rotor is designed for use in the Cross-Polarization probe shown in Figure 13. Figure 18 shows a picture of one such rotor located inside the NMR coil. The connector to the air line extends from the stator to the left. The design of the stator over which the rotor spins suspended on an air bearing has been previously described (14).

The dimensions and configuration of a typical rotor designed for use with a 10 mm i.d. coil are shown in Figure 19. The rotor is machined from Kel-F rods on a lathe. Kel-F is polymerized chlorotrifluoroethylene, which machines easily. Since it contains no hydrogen, this material is well suited for use in ^{1}H-^{13}C Cross-Polarization studies.

During machining, it is very important that the sample compartment be bored out in order to insure uniformity about
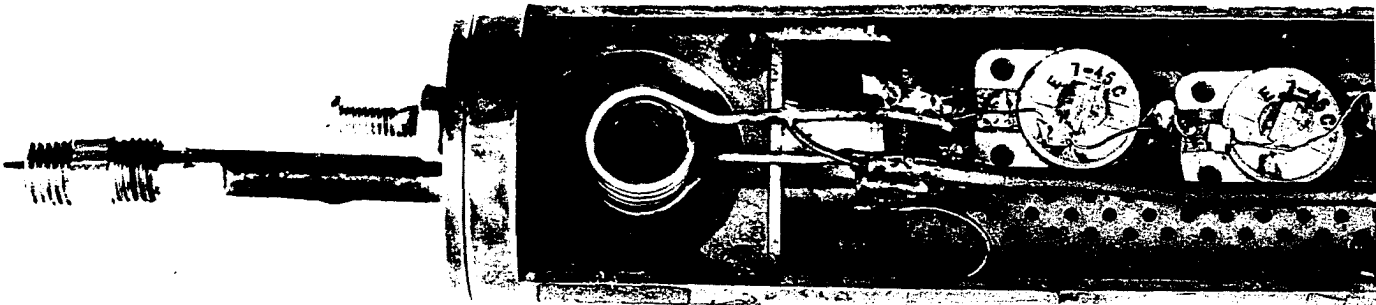
Figure 18. A picture of a high-speed rotor in a MAS probe

TYPICAL ROTOR

MATERIAL:

    KEL-F

WEIGHT:

    2.3 grams

9 mm

6 mm

12 mm

19 mm

1mm

10°

40°

17 mm
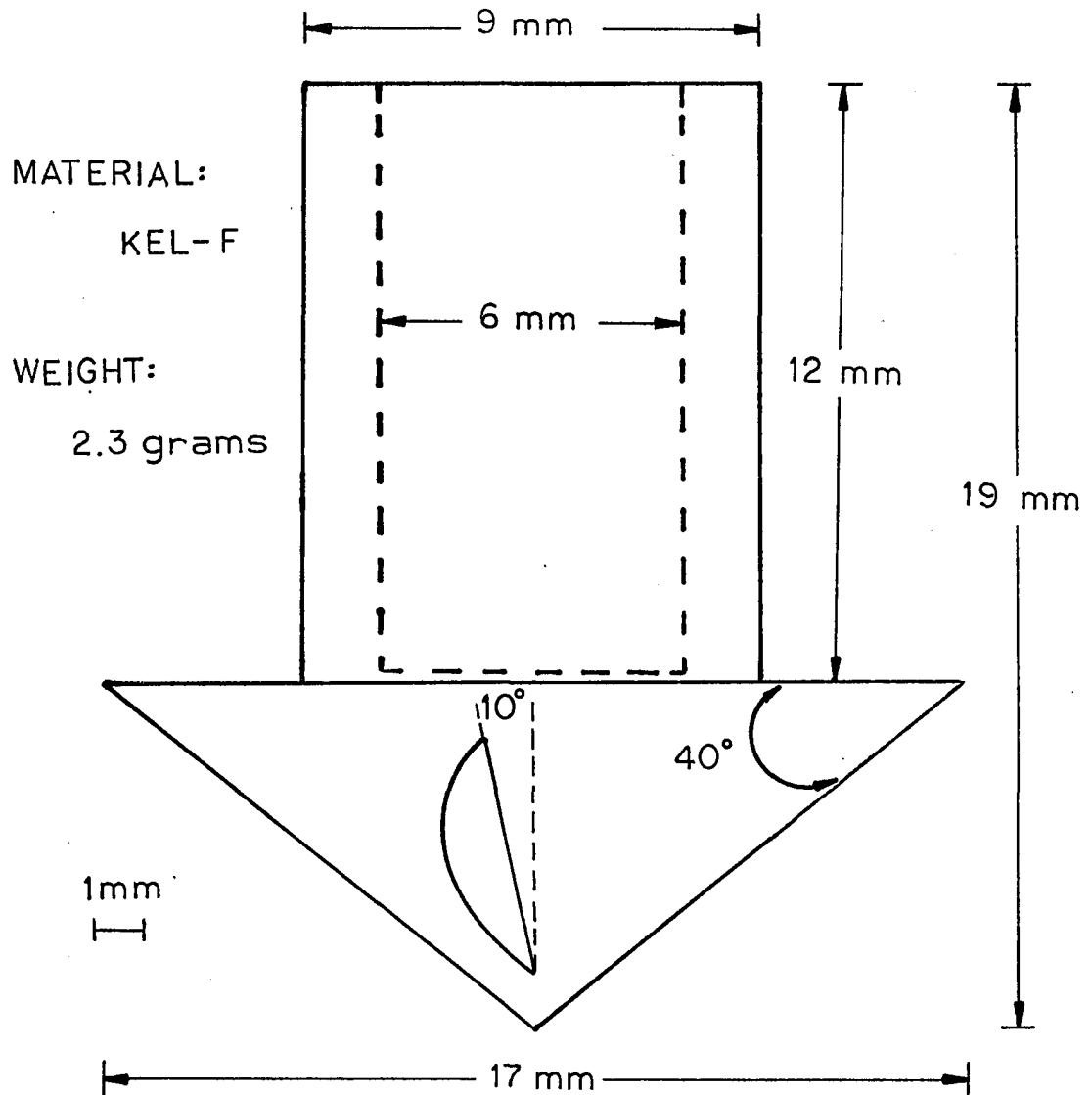
Figure 19. The dimensions of a typical high-speed rotor

the rotor axis. The flutes are slit-like cavities which catch

the stream of air and greatly increase the rotor's speed. The

flutes are cut into the base of the rotor by an end mill. For

this size of rotor 9 evenly spaced flutes have been found

sufficient to generate speeds ranging from 2.5 to 2.1 KHz with

approximately 40.0 lbs/sq. inch of air pressure. A small piece

of teflon tape firmly wedged down above the sample in the sample

well has been consistently and successfully used as a cap to

prevent sample loss while spinning.

After a rotor is machined, it may contain slight imperfections

which usually lead to instability at moderate or even relatively

slow speeds. A technique has been developed whereby the unstable

rotor can be machined to a stable configuration while it spins

in its own stator at high speeds.

First, for safety and to prevent possible damage, both by

and to, the rotor, a wire is shaped into a large loop similar

to a "bubble blower". The ring is placed aroung the neck of

the rotor (not touching, of course) and the end of the loop is

fastened to the stator. If the rotor goes unstable and decides

to rocket away from the stator, it will strike the wire loop,

bounce around and stay on the stator usually without damage

to the rotor or stator.

Next a glass rod, held in one hand is used to stabilize

the wobbling rotor. A loud whine will be heard as it gathers

speed. The pressure of the touching rod as well as the applied air pressure will determine the rotor's speed. A lathe cutting-tool is held in the free hand and the wobbling rotor is allowed to strike it near the top of the rotor--producing a machining action. A static demonstration of this process is shown in Figure 20.

With practice, one can acquire skill at machining the right places and inducing stable rotation. This technique has stabilized many unstable rotors destined for, or already in, the junk box.
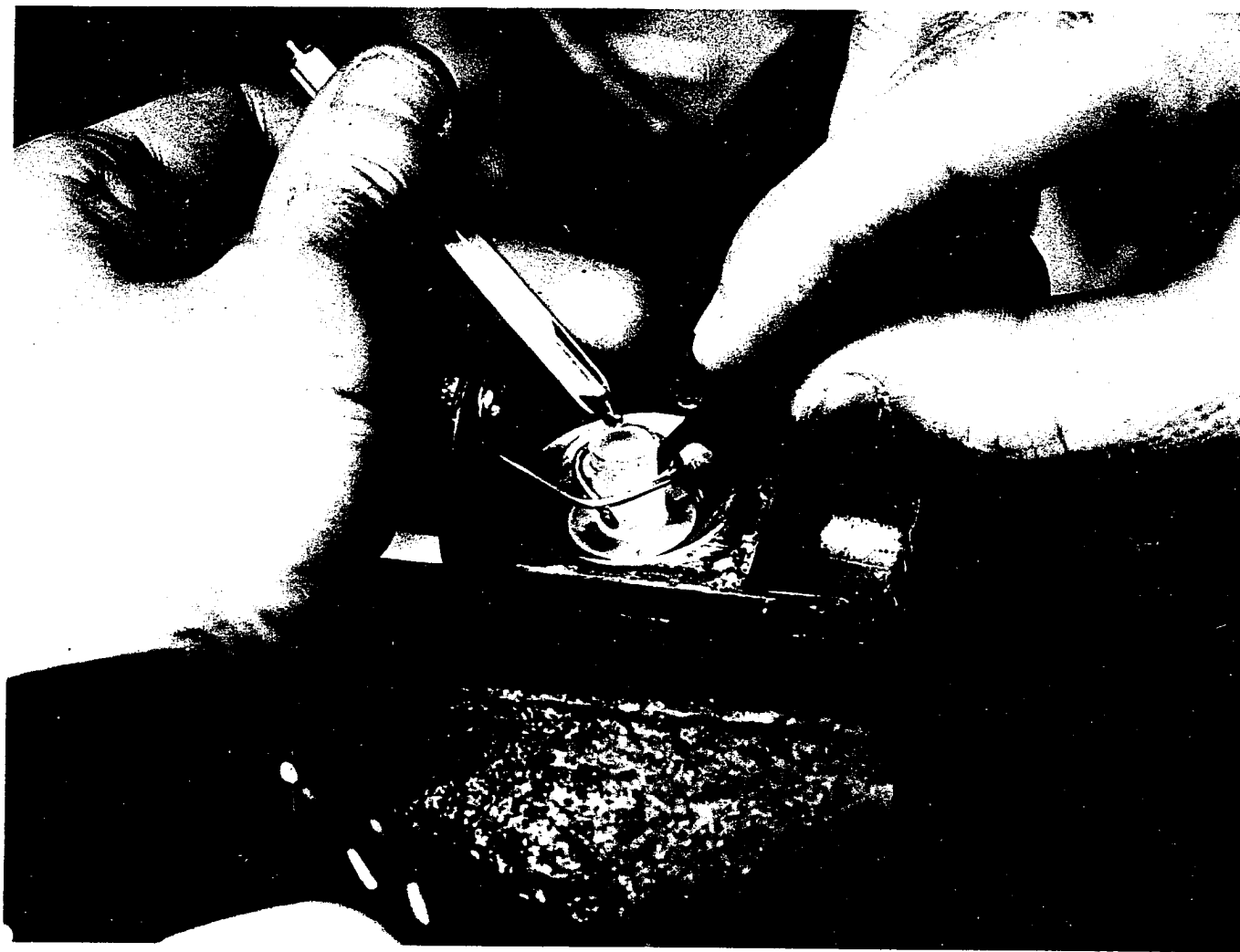
Figure 20. A demonstration of the high-speed tuning method

IV. DESIGNS OF RF POWER AMPLIFIERS AND LUMPED
EQUIVALENT CIRCUITS OF TRANSMISSION LINES

A. Introduction

The tuned RF power amplifier has many uses in pulsed NMR
(Nuclear Magnetic Resonance) (1 - 4). The high Q tuned amplifier
(17, 18) is a very convenient way of achieving narrow RF pulses
with low noise and relatively low driving power. It is useful
as a transmitter in the studies of molecular systems with long
T_2's. T_2 is the constant which characterizes the decay rate
of the Free Induction Decay (FID) of the excited nuclei. On
the other hand, the low Q tuned amplifier is suitable for use in
studies of molecular systems where T_2 is short and fast recovery
(i.e. a rapid dissipation of transient energy following the
RF pulse) is essential.

This Chapter presents the designs of two tuned amplifiers:
a high Q, 56 MHz unit which is especially useful for a high
frequency transmitter in ^1H-^{13}C double resonance NMR and NMR
of solutions and a low Q, 56 MHz unit which is useful for fast
recovery and Multiple-Pulse homonuclear decoupling experiments.
The procedure for determining the approximate values of the
components of the RF matching circuits is explained. Schematic
diagrams of the electronics of the two amplifiers are also
presented.

The last part of this Chapter discusses the lumped equivalent circuits of transmission lines and their uses as RF switches, matching devices and filters. The material of this Chapter is a slightly modified version of a Department of Energy Report (19).

B. The Q of an RF Circuit

The quality factor (6) of an RF circuit, Q, measures the ratio of the maximum energy stored, W_S, to the energy dissipated per cycle, which is the power dissipated, P_D, divided by the frequency:

$$Q = \frac{2\pi W_S}{P_D(1/f_o)} = \frac{X_L}{R_{series}} \quad \left(\simeq \frac{R_{||}}{X_L}\right) \quad (34)$$

X_L is the circuit's inductive reactance; R_{series} and $R_{||}$ are the equivalent resistances in series or parallel with X_L. All values are measured at frequency f_o. Usually the Q can be correlated with a circuit's recovery time, t_r, following an intense overload from a strong RF pulse. A low Q indicates a short recovery time; a high Q, a relatively long recovery time.

In high Q amplifiers which are designed for high efficiency, the Q is made as high as possible and the recovery time, which is usually not critical, is long--but much less than T_2. On the other hand, a low Q is purposely used in such circuits as NMR probes used in studies of solids where T_2 is usually very short and the fastest recovery essential.

For an isolated, single-port circuit, the Q can be defined as the ratio of the inductive reactance, X_L, to the effective resistance, R , in series or parallel with X_L, as shown by Equation 34. In the above notation: $X_L = 2\pi f_o L$, X_L is the inductive reactance at frequency, f_o and L represents the inductance of the inductor (coil). The time constant, $[t = Q/(\pi f_o)]$, of such a circuit measures the decay of the voltage across the inductor, L, to e^{-1} of its maximum value.

The recovery time, $[t_r = 21 Q/(\pi f_o)]$ will represent approximately a 10^{-9} decay in this voltage. For instance 1000 volts would decay to 1.0 microvolt in a time period of t_r. If the circuit were a NMR probe and since NMR signals are normally in the range of microvolts or less, after a time t_r ($t_r < T_2$) following a strong RF pulse, the NMR signal would outlive circuit transients and be detectable.

Two of the major factors which increase recovery time are probe ringdown and power-amplifier ringdown. Even when very low Q probes, matching circuits, etc. are used, the Q of the RF power amplifier itself is a major factor which may prevent extremely fast recovery. For these reasons, broadband RF power amplifiers are generally used in Multiple-Pulse experiments on solids since the shortest possible cycle times are usually needed. Broadband RF power amplifiers belong to a general class of amplifiers whose main advantages are very fast recovery and no tuning and whose disadvantages are low efficiency,

broadband noise and high cost.   Surprisingly, the low Q tuned

amplifier described in this Chapter offers relatively fast

recovery times with high efficiency, low noise and low cost.

C.   The Model of the RF Amplifier

The RF amplifier (tube, transistor, etc.) may be considered

as a "black box" which is characterized by properties usually

specified by the manufacturer.   The model of an RF amplifier

is shown in Figure 21.   The amplifier (CTI, CGP, G, and CTO)

is that of a tetrode tube to which grid, screen and plate voltages

are applied to achieve a given operating condition--in this

case: class AB_1.   Power is transferred into the ideal amplifier

by the input circuit: C2I, RI, LI and CII and is transferred

out of the amplifier by the output circuit: C1O, RO, LO and

C2O.

The tetrode tube (4CX250B) used in these designs will be

modeled as an ideal amplifier with gain, G, input capacitance,

C_{CTI}, output capacitance, C_{CTO} and control grid-plate capacitance,

C_{CGP}.   The values of C_{CTI}, C_{CTO} and C_{CGP} are usually supplied

by the manufacturer.   Both the input and output circuits are

of the tapped series-tuned design (See Chapter II) and may be

considered as forms of π-circuits.   These circuits are chosen

because they have properties similar to lumped equivalent

circuits of transmission lines (See below).   Of course, transmission

lines are broadbanded circuits.   Consequently, circuits which

TUNED AMPLIFIER DESIGN

$$x = 0, I$$
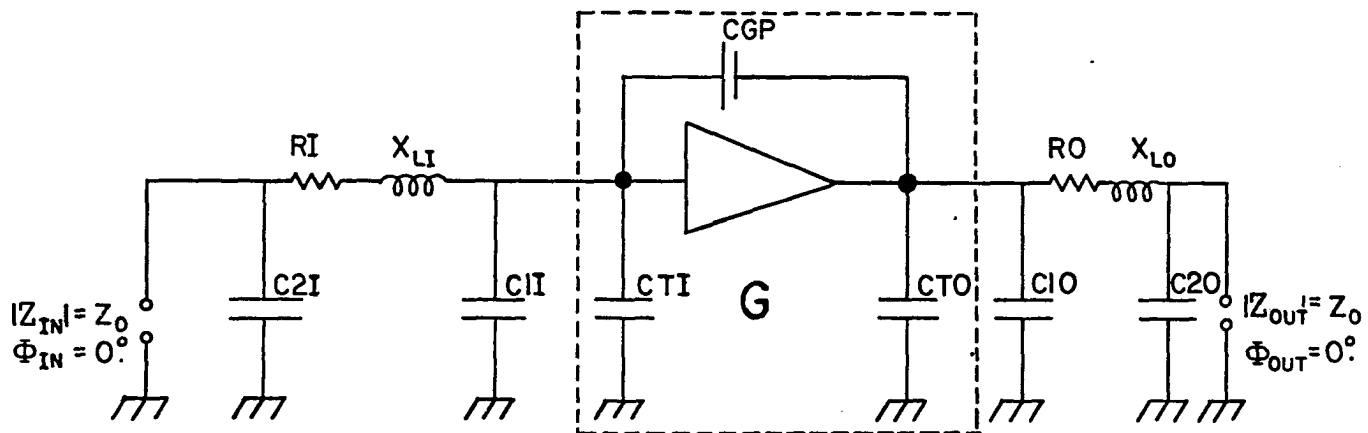
$$C_{CIX} = \left[2\pi f_o \left(X_{LX} - R_{RX} \sqrt{\frac{Z_0}{R_{RX}} - 1} \right) \right]^{-1} - C_{CTX} \qquad 1.$$

$$C_{C2X} = \frac{\sqrt{\frac{Z_0}{R_{RX}} - 1}}{2\pi f_o Z_0} \qquad 2.$$

$$C_{CGP} \ll C_{CTO} < C_{CTI} \qquad 3.$$

Figure 21.   The RF equivalent circuit of an RF power amplifier

are related to them are very desirable for rapid transfer of energy with minimum ringdown.

All losses are considered to be suitably included in resistances R_{RI} and R_{RO}. When biased AB_1, the tube will not draw cathode-control-grid current; therefore, input losses (resistance, R_{RI}) will mainly occur in the input matching circuit. During excitation, the output circuit will generate considerable RF current through the tube and the tube's resistive losses will contribute a large portion to the output losses. All output losses are considered lumped into resistance R_{RO}. The major effect of "dynamic" losses will be to increase the value of R_{RO} and thereby reduce the "static" value of C_{C2O} required for maximum power transfer.

Since the capacitors C1I and CTI are in parallel, they may be considered one capacitor, i.e., capacitor C1 of a tapped series-tuned circuit which is described in Chapter II. Capacitors CTO and C1O may be considered likewise.

Equations 1 and 2 of Figure 21 are the solutions of a standard tapped series-tuned circuit which tunes inductive reactance X_{LX} and resistance R_{RX} to $|Z_{IN}| = Z_o$ and $\phi_{IN} = 0.0^o$ at frequency, f_o. The quantities $|Z_{IN}|$ and ϕ_{IN} are in the magnitude and phase angle of the impedance that would be read on a vector impedance meter such as the Hewlett-Packard HP 4815A. Of course, the tube capacitances, C_{CTI} and C_{CTO}, will set limits on the

values of inductive reactances, X_{LI} and X_{LO}, which can be tuned

to a specific input or output impedance, Z_o.

The quantity G can be considered the actual gain of the

entire amplifier under operating conditions with all tube input

and output losses suitably included in resistances R_{RI} and R_{RO}.

The gain, G, can be measured experimentally. The actual Q's

of the input and the output circuits can be calculated (as

outlined in Chapter II) based on the actual values of X_{LI}, C_{C2I},

$|Z_{IN}|$ and X_{LO}, C_{C2O}, $|Z_{OUT}|$ under operating conditions.

D. Designs of RF Power Amplifiers

1. High Q design

For the Eimac 4CX250B tetrode, handbooks (18) list C_{CTI} =

18.5 pf, C_{CGP} = 0.04 pf and C_{CTO} = 4.7 pf. In the high Q design

the ratios: X_{LI}/R_{RI} = Q_{IN} and X_{LO}/R_{RO} = Q_{OUT} are made large. Input

inductor, LI, and output inductor, LO, are wound to be as large

as possible; however, their size should allow the use of physically

realizable capacitances for C_{CII} and C_{CIO}. At f_H = 56.020 MHz,

X_{LI} = 85 Ω and X_{LO} = 94 Ω. A Q_{IN} = Q_{OUT} = 80.0 is assumed so

that a "guess" at the values of R_{RI} and R_{RO} can be made. No

physical resistors are used in this design. These resistances

are distributed and can be considered losses in the matching

circuits, etc. Since $R_{RX} = X_{LX}/Q$, R_{RI} = 1.06 Ω and R_{RO} = 1.18 Ω.

From equations 1 and 2 of Figure 21, with $|Z_{IN}| = |Z_{OUT}| = Z_o =$ 50.0 Ω, the initial estimates are calculated in picofarads (pf): $C_{C11} = 18.0$, $C_{C21} = 386.1$ and $C_{C10} = 28.2$, $C_{C20} = 365.5$. Variable capacitors (with padding) whose tuning ranges include these values would be used.

These values are considered approximate since they are for the "static" amplifier (i.e., not under operating conditions). Under operating conditions when both DC and RF powers are applied, "dynamic" losses will be introduced (in some equivalent form) into R_{RI} and R_{RO}. The major effect of these increased losses will be to reduce the values of C_{C21} and C_{C20} required for maximum power transfer. (See equation 2 of Figure 21.)

2. Low Q design

For a low Q design, the $Q_{IN}(= X_{LI}/R_{RI})$ and $Q_{OUT} = (X_{LO}/R_{RO})$ are purposely made small relative to the high Q circuit. Of course, this will reduce power amplification so a pair of 4CX250B's are used in parallel. Note, now $C_{CTI} = 37.0$ pf, $C_{CGP} = 0.08$ pf and $C_{CTO} = 9.4$ pf. (i.e. double the values of one tube). The larger value of C_{CTI} will restrict the size of X_{LI}; however, a low Q_{IN} is desired so that a smaller X_{LI} is perfectly acceptable. Coils were wound such that $X_{LI} = 42$ Ω and $X_{LO} = 53$ Ω at $f_o = 56$ MHz.

For maximum power transfer into the amplifier, no lumped input resistor, RI, was used and a $Q_{IN} = 80.0$ was assummed--

yielding a "distributed" R_{RI} = 0.53 Ω. An R_{RO} = 1.0, 5 watt

resistor was placed in series with X_{LO} such that Q_{OUT} = 53.0.

From equations 1 and 2 of Figure 21, with $|Z_{IN}| = |Z_{OUT}|$ = 50.0 Ω,

the initial estimates are calculated in pf: C_{CII} = 40.0,

C_{C2I} = 549.0 and C_{C10} = 52.4, C_{C20} = 398.0.

Again variable capacitors (with padding) whose tuning

ranges span these values are used. Under dynamic conditions,

the actual values of C_{C2I} and C_{C20} would be smaller for reasons

discussed above.

E. Tube Biasing

Discussions of biasing (i.e. applied DC voltages) are beyond

the scope of this Chapter. The Radio Amateur's Handbook (18)

contains a good discussion of this topic. The 4CX250B tubes

are operated class AB_1 (linear amplification). This condition

is set by a grid voltage of -75.0 volts and a screen voltage

of +300.0 volts. Both of these voltages should be well-regulated.

In a tetrode, linear amplifier, both the plate and screen

voltages should be fairly constant; however, the screen voltage

is the much more critical of the two and should be well-regulated.

Likewise, the control-grid biasing voltage should also be well-

regulated to prevent unnecessary modulations which could lead

to unwanted frequencies, noise and power losses. Voltage-regulator

tubes, VR150 and VR75, are incorporated into these amplifiers to

minimize such fluctuations as shown in Figures 22 and 25.

Biasing class AB_1 will produce linear amplification. Driving power is small since the tube does not draw control-grid current. Between pulse cycles, plate current will be small (< 10.0 ma); consequently, power dissipation will be small (for pulsed operation, of course). Since these amplifiers are linear, amplitude modulated signals will not be distorted after amplification.

F. Amplifier Neutralization

A suitable phase shifting network is usually connected between the plate and control grid circuits to cancel out any "feed thru" effects which may produce unstable operations. This process is called neutralization (18). Improper neutralization can result in self oscillations, harmonics and other spurious effects.

In these designs, a small wire (representing a capacitor, C_N) is positioned near the tube. With no DC plate voltage applied, the length and position of this wire are adjusted so that there is minimum "feed through" signal at f_o in the output circuit. An oscilloscope is used to monitor the output circuit.

In the low Q design, three symmetrically placed, shorted quarterwavelengths ($\lambda/4$) of transmission line are used to suppress 60 cycle, harmonics and other noises at the output.

G. Amplifier Construction

Schematic diagrams of both the high Q and low Q amplifiers
are shown in Figures 22 and 25 respectively. Figures 23, 24,
26 and 27 show actual pictures of the two amplifiers described
in this Chapter with major components indentified.

Good design procedures usually have compact layouts
(minimum unnecessary wire). Input and output tank (i.e. tuned)
circuits should be well shielded from each other. A special
tube socket with a built-in screen bypass capacitor is available
for the 4CX250B tetrodes--although "home brew" sockets were
fabricated for these designs. The screen-grid clip was a metal
harness supported by four symmetrically placed 1500 pf capacitors
grounded to the chassis. Heater voltages should be critically
set at 6.0 VAC as overvoltages, however slight, may cause cathode
bombardment (17). The tubes should be air cooled with an
adequate blower.

H. Amplifier Performance

1. High Q design

With a DC plate voltage of 1700 volts and a driving power
of 4.6 RMS watts (pulsed operation, 2.0 μsec pulse widths), an
ouput power of 400 RMS watts was measured. The power gain, G,
is 87 (19.4 dB). Ringdown time is defined as the time for
receiver noise to predominate following the end of the pulse.
Ringdown lasted for 8 μsec.
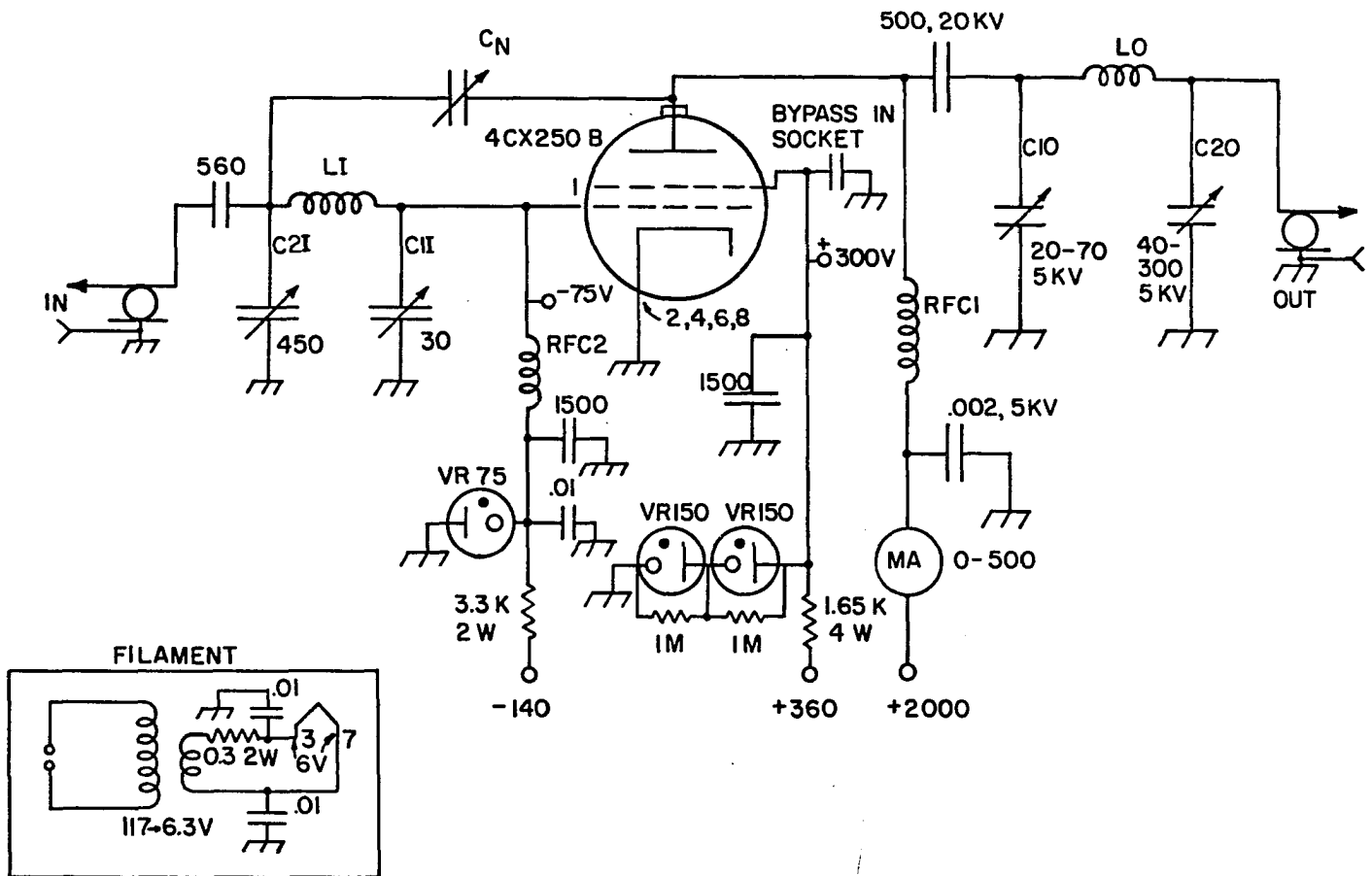
Figure 22. The schematic diagram of the high Q, RF power amplifier

66
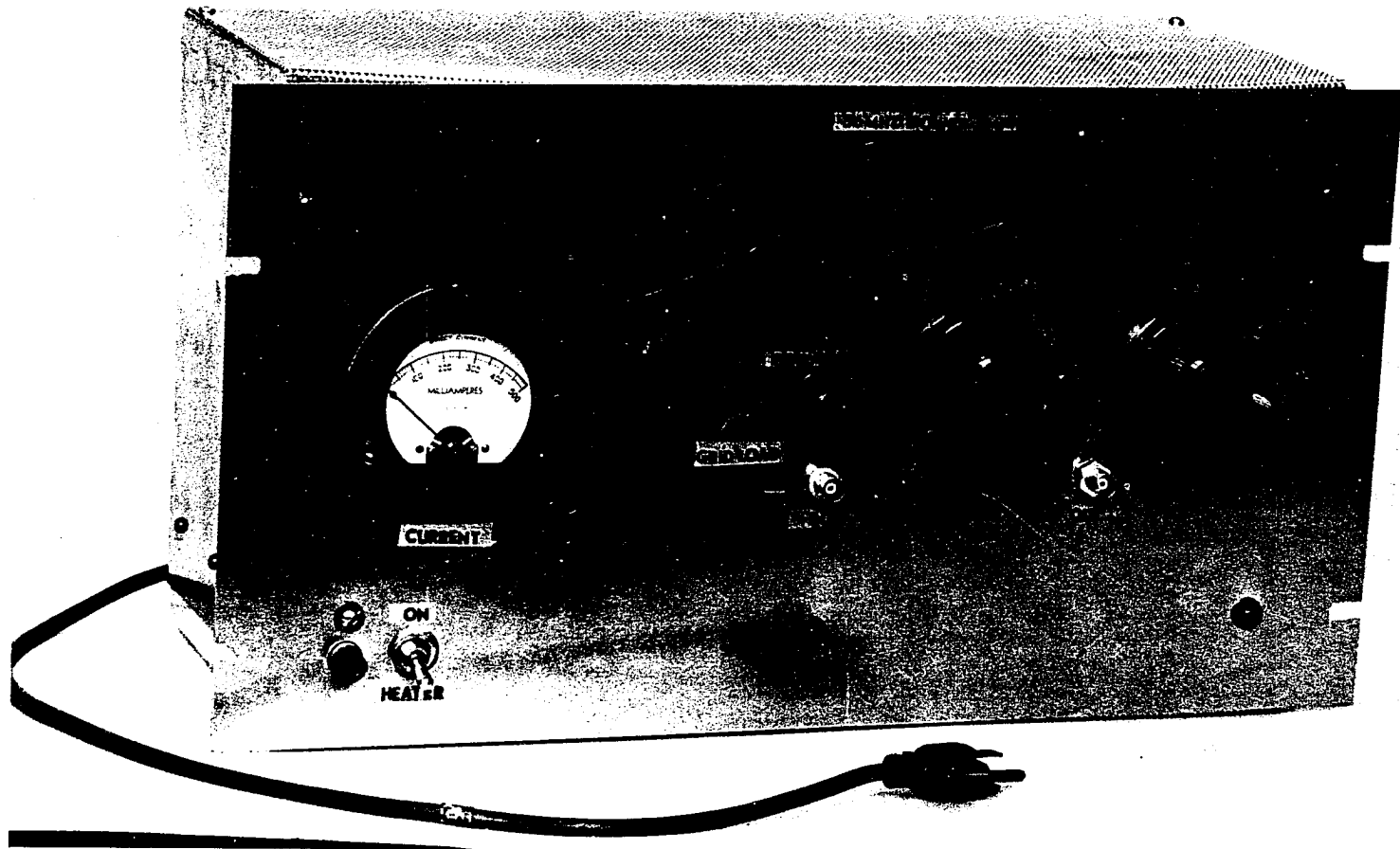
Figure 23. A front view of the high Q, RF power amplifier

VR TUBES UNDER CHASSIS
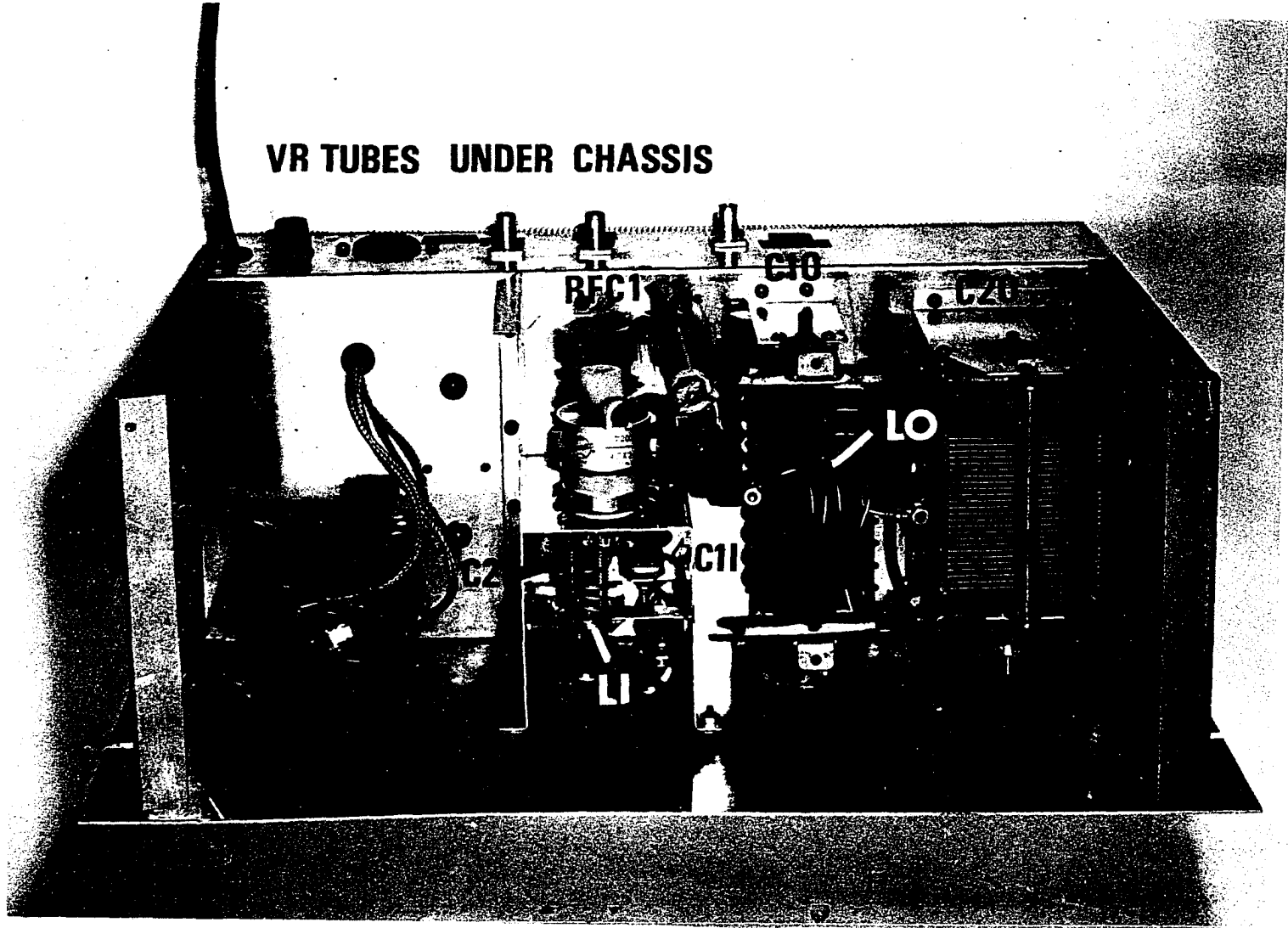
Figure 24.   A top view of the high Q, RF power amplifier
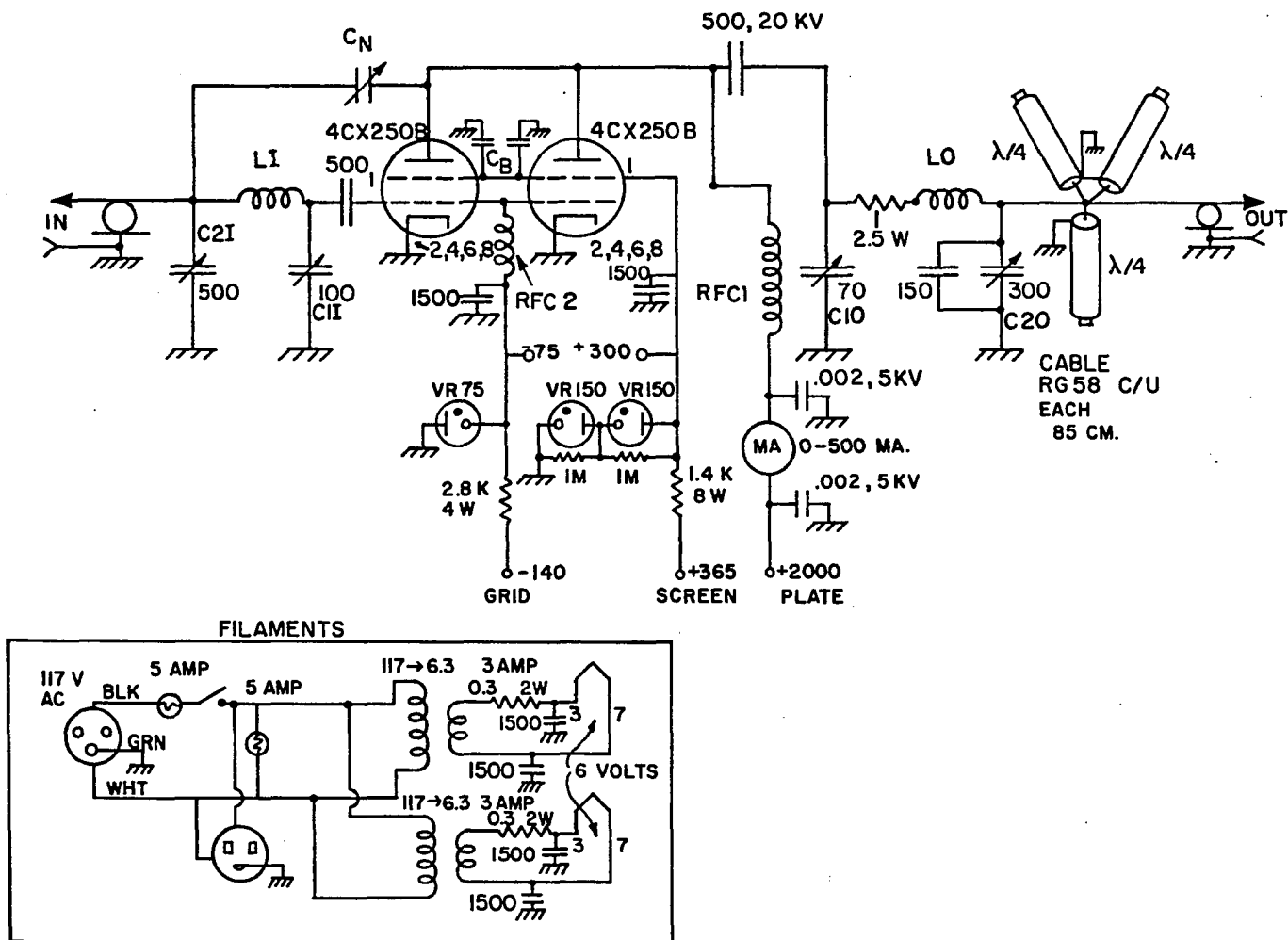
Figure 25. The schematic diagram of the low Q, RF power amplifier

69
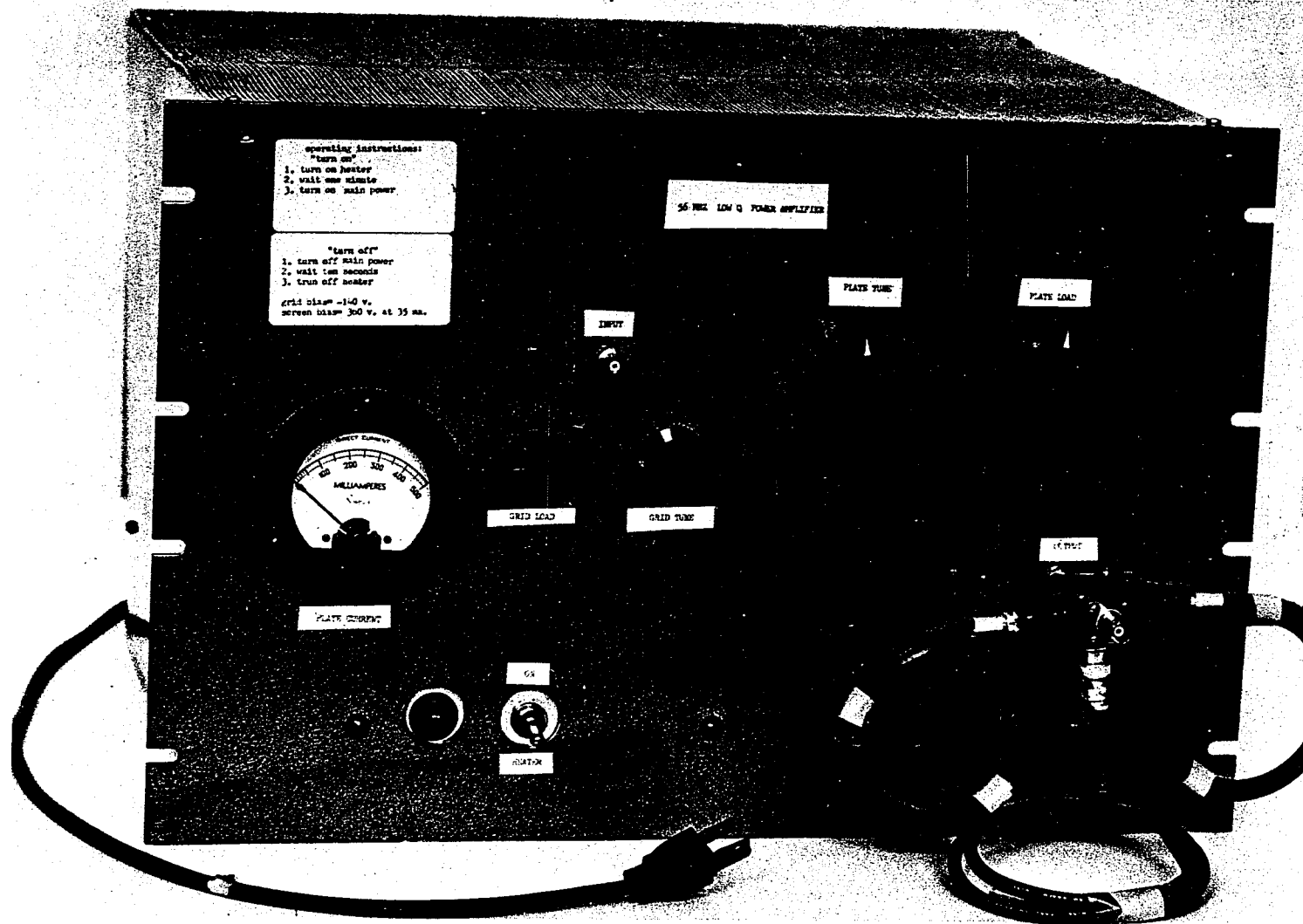
Figure 26.   A front view of the low Q, RF power amplifier
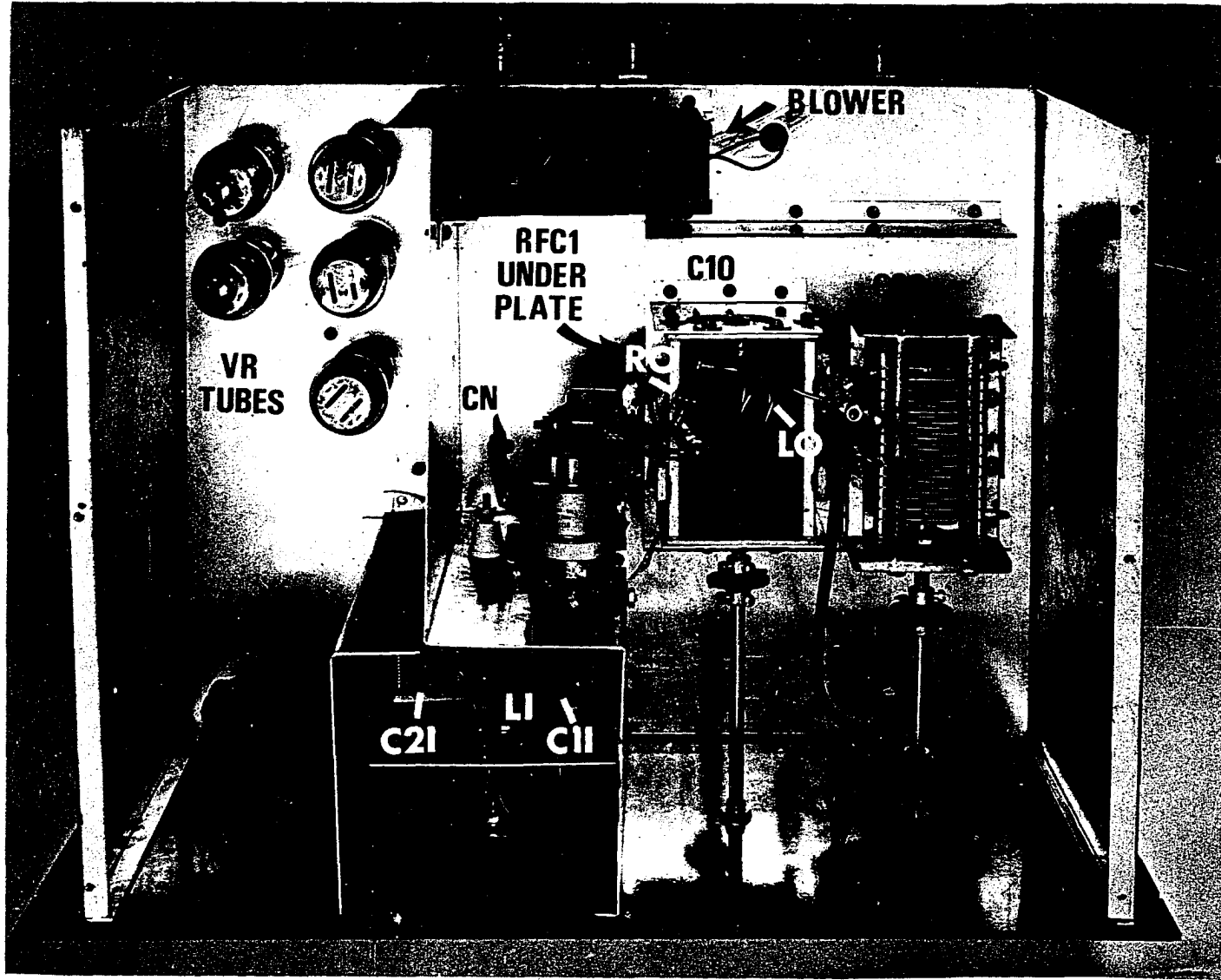
Figure 27. A top view of the low Q, RF power amplifier

In Double-Resonance experiments, this amplifier is used with a Heathkit HP-23B power supply (20) which supplies both biases and a DC high voltage of 820 volts. With this power supply, the amplifier delivered 21 msec pulses of 180 RMS watts with little droop.

2. Low Q design

With a DC plate voltage of 1700 volts and a driving power of 4.6 RMS watts (pulsed operation, 2.0 μsec pulse widths), an output power of 410 RMS watts (G = 19.5 dB) was measured. Ringdown lasted 3.9 μsec.

Operating under the MREV-8 pulse sequence (2) a cycle time as low as t_c = 24 μsec could be achieved; however, cycle times of 30 μsec produce the best (S + N)/N. These cycle times are indicative of a "viewing window", $t_c/6$, between 4 and 5 μsec wide--consistent with the measured ringdown time.

I. Lumped Equivalent Circuits of Transmission Lines

1. Introduction

The use of quarterwavelengths ($\lambda/4$) of transmission line terminated in crossed diodes is a well-known method for achieving receiver isolation and rapid switching. However, such transmission lines have convenient lengths only at relatively high frequencies (i.e. > 30 MHz). At lower frequencies cable lengths become inconveniently long. For instance, $\lambda/4$ for RG58C/U cable is

351 cm. at 14.1 MHz. These long lengths can result in noise pickup and power losses. Interestingly, the lumped π and T-equivalents of $\lambda/4$ and $3\lambda/4$ transmission lines, respectively, offer comparable rapid switching and isolation but with a compact size. Figure 28 shows a lumped $(\lambda/4)$ π-equivalent circuit for 14.1 MHz.

Transmission lines when properly terminated are very broadbanded and offer very little opposition to any signal, although attenuation usually increases with frequency. On the other hand, the lumped equivalent circuits are only "transmission-line-like" in a very narrow frequency range about their center frequency, f_o. At frequencies removed from f_o, the $(\lambda/4)$ π-equivalent bahaves like a low-pass filter and the $(3\lambda/4)$ T-equivalent, like a high-pass filter. These properties are useful since these circuits can be designed as RF switches (with the use of crossed diodes to ground) at one frequency and as filters (high or low-pass) over a second frequency range.

These remarkable circuits find use in Double-Resonance experiments where the high-frequency decoupling pulse must be suppressed to record the low-frequency NMR signal. In such experiments, the $(\lambda/4)$ π-equivalent is used for an RF switch and a low-pass filter (removes high frequencies) while the $(3\lambda/4)$ T-equivalent is used as a high-pass filter (removes low frequencies) at the output of the high-frequency power amplifier.
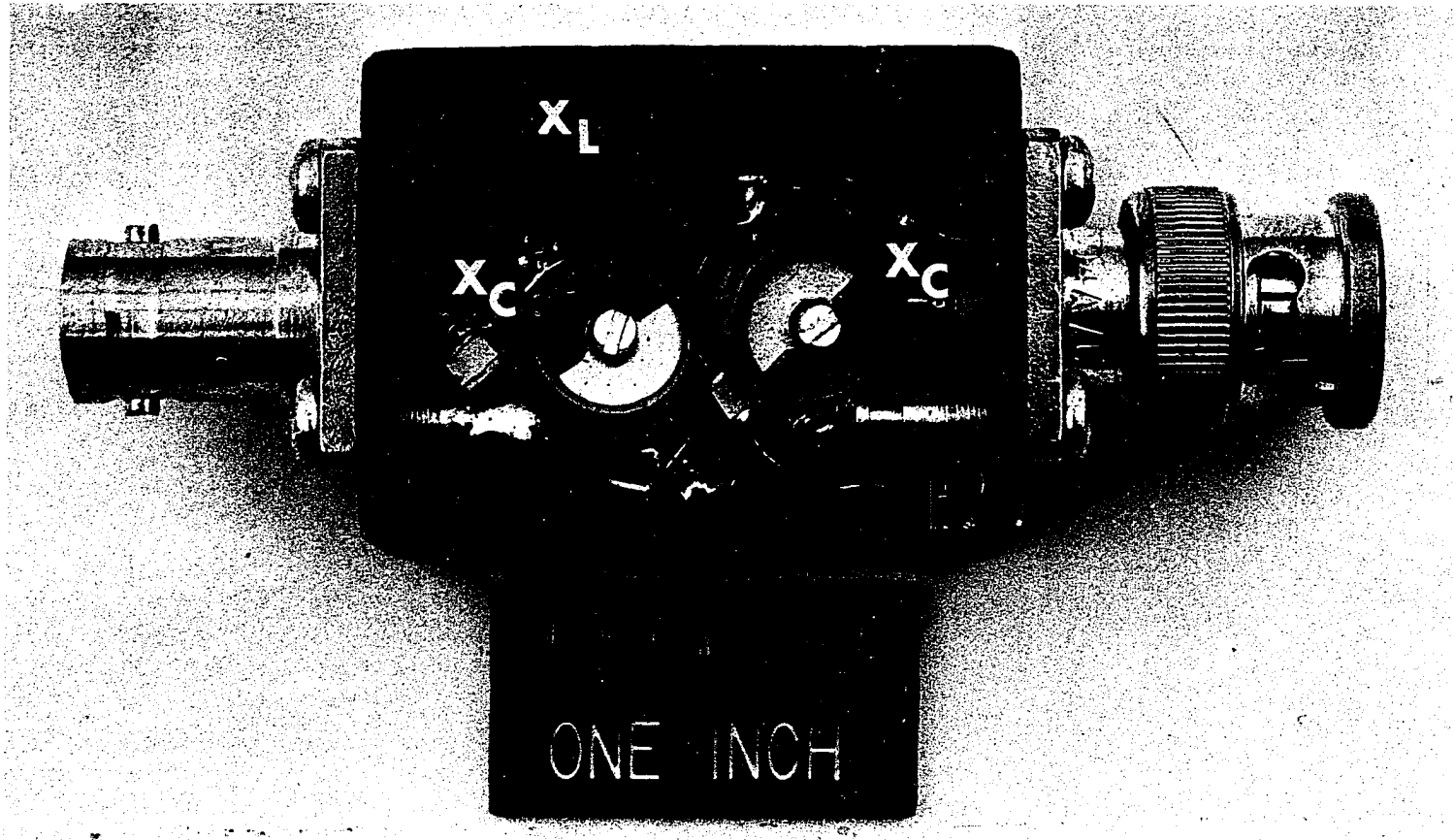
Figure 28. A picture of a lumped quarter wave at 14.1 MHz

2. Theory

The top half of Figure 29 shows the general "black box" π and T-equivalent circuits of a length, D (in wavelength at f_o), of transmission line of characteristic impedance, Z_o (6). The bottom half of Figure 29 shows the $(\lambda/4)\pi$-equivalent (D = 1/4) and $(3\lambda/4)$ T-equivalent (D = 3/4) "lumped" circuits. X_L and X_C are the inductive and capacitive reactances of the respective components. As can be seen, the values of the reactances X_C and X_L equal the characteristic impedance, Z_o, of the equivalent transmission line.

The ideal Q of the $(\lambda/4)\pi$-equivalent at f_o can be calculated in a manner similar to that of the resonant circuits. First, each port is terminated in its characteristic impedance, Z_o (purely resistive). Circuit-theory analysis shows that this termination is equivalent to placing a resistance of $R_L = Z_o$ in series with the inductive reactance. The Q of a series-resonant circuit is simply the ratio of the inductive reactance to the series resistance or $Q_{SERIES} = X_L/R_L = 1$.

The ideal Q of the $(3\lambda/4)$ T-equivalent can be calculated in similar manner except now the terminations are equivalent to placing a resistance of $R_L = Z_o$ in parallel with the inductive reactance. The Q of a parallel-resonant circuit is now the ratio of the parallel resistance to the inductive reactance or $Q_{||} = R_L/X_L = 1$ also. These low Q's are indicative of
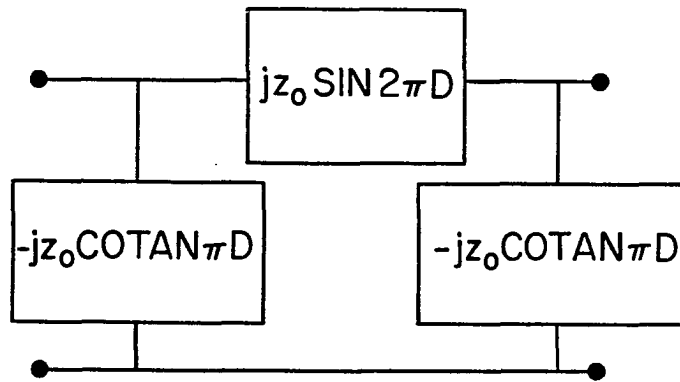
π-EQUIVALENT OF D
WAVELENGTHS OF z_0 LINE
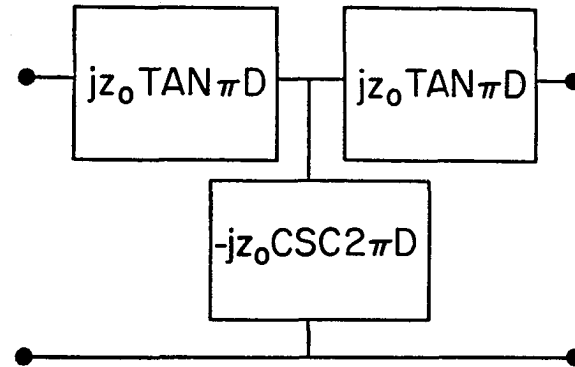
T-EQUIVALENT OF D
WAVELENGTHS OF z_0 LINE
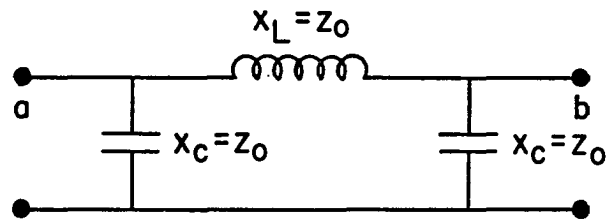
π-EQUIVALENT OF 1/4
WAVELENGTHS OF z_0 LINE
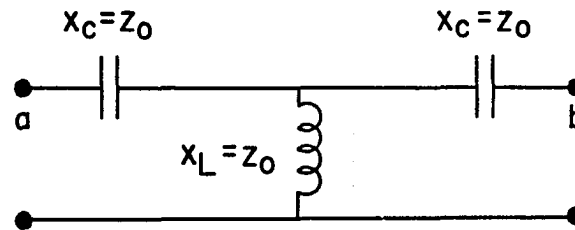
T-EQUIVALENT OF 3/4
WAVELENGTHS OF z_0 LINE

Figure 29.   The general π and T-equivalent circuits of transmission lines

relatively broadbanded frequency response and fast recovery--
which is to be expected since these circuits are supposed to
"mimic" transmission lines.

The properties of these symmetrical lumped circuits are
identical to those of $\lambda/4$ and $3\lambda/4$ wavelengths of transmission
line only at frequency f_o. Points "a" and "b" are shown in
Figure 29. If point "b" is an open circuit, then point "a"
will be a shorted circuit (i.e. will act as a low-impedance
point) and vice versa. If point "b" is terminated in Z_o (resistive),
then the impedance at point "a" will be Z_o (resistive). For all
other impedances, these circuits behave as impedance transformers,
i.e., $Z_a Z_b = Z_o^2$. At frequencies other than f_o, the $(\lambda/4)$
π-equivalent behaves like a low-pass filter and the $(3\lambda/4)$
T-equivalent, like a high-pass filter.

3. Construction and tuning

The construction and tuning of a Z_o = 50 ohm, $(\lambda/4)$ π-equivalent
lumped circuit at f_o = 14.1 MHz will be explained. First a coil
is wound such that its inductive reactance, X_L, is 50 Ω at
14.1 MHz. This inductor was 18 mm long by 6 mm wide (i.d.)
which had 14 turns of #18 enamelled copper wire. The values
of capacitances are determined by $C_C = (2\pi f_o Z_o)^{-1}$ or C_C = 226 pf.
Small ceramic variable capacitors (15-60 pf) padded with microwave-
grade fixed ceramics (16) were used. A compact assembly in a

small box (Pomona 3752) (21) was made and the completed circuit
is shown in Figure 28.

Tuning follows a repetitive procedure. A vector impedance
meter is used to measure impedances. For a $(\lambda/4)$ π-equivalent,
one port is shorted, and the capacitor at the other port is tuned
for highest impedance and vice versa. The procedure is repeated
until each port shows high impedance with the other port shorted.
For the $(3^{\lambda}/4)$ T-equivalent, the procedure is similar--only now
the capacitor near the port with the shorted circuit is tuned
for high impedance at the other port and vice versa, etc.

4. Performances

Performances were measured for the $(\lambda/4)$ π-equivalent circuit
at 14.1 and 56.0 MHz--two popular frequencies for ^{1}H-^{13}C Double
Resonance in our laboratory. The circuit was found to have
0.08 dB of insertion loss at 14.1 MHz; whereas, the loss of an
actual $\lambda/4$ of RG58 C/U was found to be 0.11 dB. When terminated
in four crossed diodes (1N914B), the 14.1 MHz RF pulse was
attenuated by approximately 40 dB. The $\lambda/4$ of cable gave about
46 dB attenuation. At 56.0 MHz, the circuit was found to have
38 dB attenuation when terminated in a 50 Ω load. Under identical
conditions, the above $\lambda/4$ of cable showed only 0.15 dB attenuation.
The circuit's large attenuation at frequencies far removed from

f_o is very useful in preventing strong decoupling pulses from overloading the front end of the receiver during Double-Resonance experiments.

V.   DIGITAL FILTERING AND DECOMPOSITION OF NMR ABSORPTION SPECTRA

A.   Introduction

This Chapter begins with a discussion of the general concepts and applications of a digital filtering technique which is a valuable method for extracting information from noisy NMR (1-4) signals.   The "mechanics" of a simple, single-pulse, NMR experiment are shown in Figure 30.   An RF pulse will nutate an equilibrium magnetization.   The disturbed spin system will return to its original equilibrium via two mechanisms: T_2 (transverse or x-y relaxation) and T_1 (longitudinal or z relaxation).

The T_2 magnetization generates a decaying signal, known as the FID, in the NMR coil.   The Fourier Transform of the FID yields the NMR spectrum.   Of course, when small samples of low abundance nuclei (such as ^{13}C in coals) are studied, such signals may be noisy.   The technique of digital filtering is also useful for establishing an accurate base line for numerical integration of such noisy signals.   A list of spin = 1/2 nuclei, percent natural abundance and Larmor frequencies is shown in Figure 31.

The process of exponential filtering or multiplication of a time signal by an exponential function (sometimes called tapering) is well-known (4).   The technique described in this Chapter combines tapering with the application of a bandpass filter.   The bandpass filter eliminates possible contributions from artifacts before the application of the exponential filter.

NUCLEAR MAGNETIC RESONANCE

FT

RF PULSE

FID

NMR SPECTRUM

NUTATION

PRECESSION

X

M

Z

Y

EQUILIBRIUM

X

M

Z

AXES

X

Z

Y

$\pi/2$ PULSE

$\bar{Y}$ PHASE

X

M

Z

HIGH RESOLUTION

S

N

MAGNET

RELAXATION
+
FID

X

T_2

Z

T_1

EQUILIBRIUM

X

M

Z
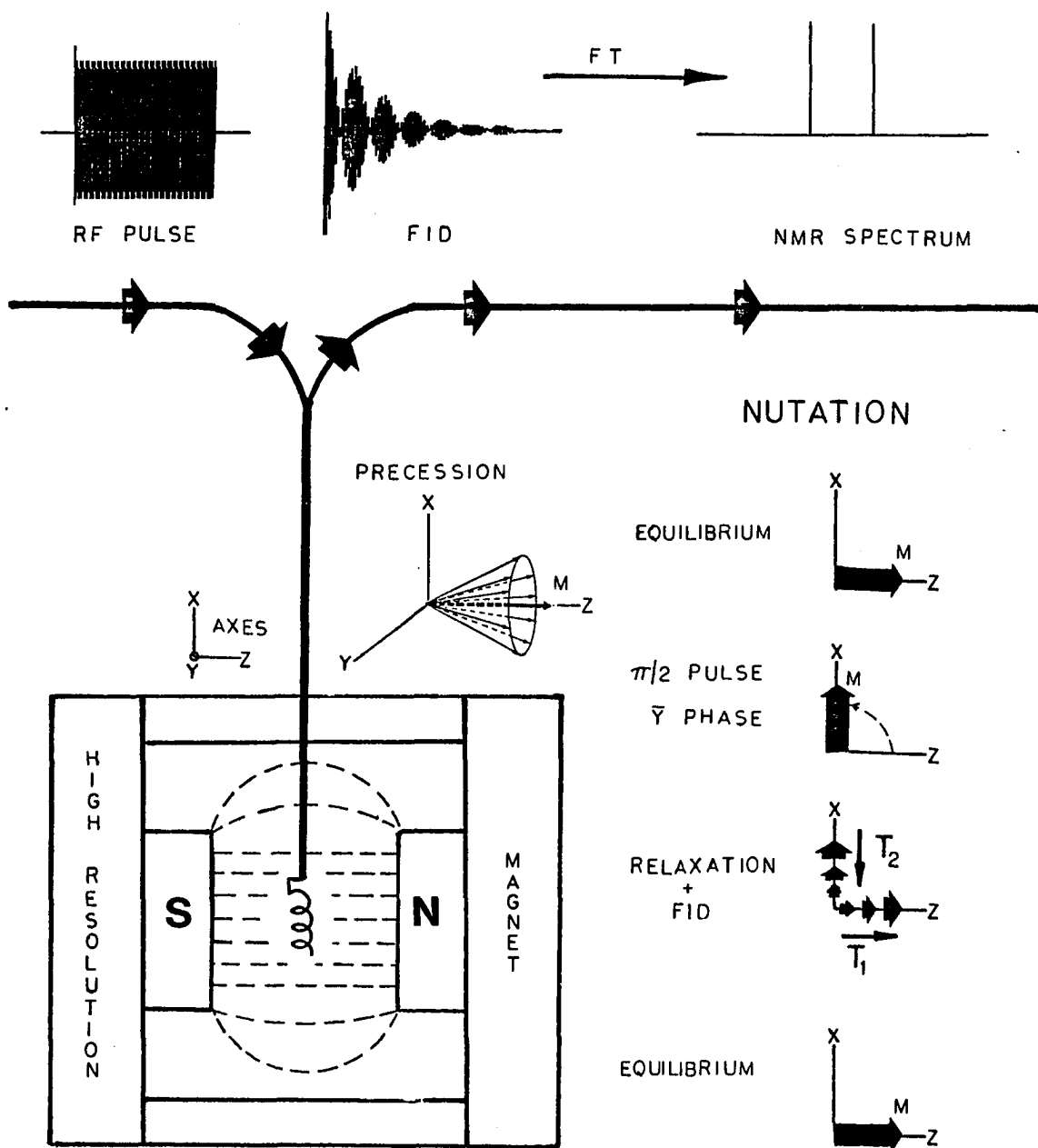
Figure 30. The flow of information in an NMR experiment

$$I = \frac{1}{2} \qquad \text{NUCLEI}$$

NUCLEUS	% NATURAL ABUNDANCE	f_o (MHz) AT H_o = 13.15 KGs
^{1}H ¢	99.98 %	56.02 MHz
ş ^{3}He	0.00013	42.68
^{13}C	1.11	14.09
ş ^{15}N ¢	0.37	5.68
^{19}F	100.0	52.70
ş ^{29}Si	4.70	11.13
^{31}P	100.0	22.68
^{57}Fe	2.21	1.82
^{77}Se	7.54	10.70
ş ^{89}Y	100.0	2.75
ş ^{103}Rh	100.0	1.76
ş ^{107}Ag	51.58	2.27
ş ^{109}Ag	48.42	2.61
ş ^{111}Cd	12.81	11.88
ş ^{113}Cd	12.30	12.42
ş ^{115}Sn	0.35	18.41
ş ^{117}Sn	7.63	19.96
ş ^{119}Sn	8.63	20.88
ş ^{123}Te	0.88	14.68
ş ^{125}Te	7.01	17.70
^{129}Xe ¢	26.34	15.50
ş ^{169}Tm	100.0	4.59
^{171}Yb ¢	14.29	9.88
^{183}W	14.24	2.30
^{187}Os ¢	1.64	1.29
^{195}Pt	33.80	12.04
^{199}Hg ¢	16.85	10.02
^{203}Tl	29.51	32.01
^{205}Tl	70.49	32.33
^{207}Pb	21.86	11.71
ş. $-\frac{1}{2}$ ¢. I≥1 ^{2}H ^{14}N ^{131}Xe ^{201}Hg ^{173}Yb ^{189}Os		

Figure 31.   Information about spin = 1/2 nuclei

Thus, greater sensitivity can be directed toward weak absorption signals, with resultant enhancement of accuracy in integrated amplitudes.

This filter is directly applied to data sets in the frequency domain through the use of numerical convolution, also herein described. Interestingly, this filtering technique can be generalized to any type of data set.

Properties of the Fourier Transform as well as properties of the Lorentzian and Gaussian lineshapes are also discussed.

Finally, this Chapter discusses the use of lineshape-fitting techniques to decompose NMR absorption spectra into Lorentzian and/or Gaussian components. This procedure is useful for applications to NMR spectra which contain overlapping absorption lines. Spectral decomposition is especially valuable in solid state NMR where areas under overlapping spectral peaks must be estimated.

The technique of digital filtering and spectral decomposition, as discussed in this Chapter, have been developed into FORTRAN computer programs which have been described in detail elsewhere (22).

B. Properties of the Fourier Transform

1. Definitions

The Fourier Transform (FT) can be regarded as a mapping operation between any two reciprocal domains. In NMR research

the domains are time and frequency (or shift). The Fourier

Transform, $G(\omega)$ of a function $g(t)$ is defined as follows:

$$G(\omega) = \int_{-\infty}^{\infty} g(t) \, e^{-j\omega t} \, dt \qquad (35)$$

The inverse Fourier Transform is given by the relation:

$$g(t) = \frac{1}{2\pi} \int_{-\infty}^{\infty} G(\omega) \, e^{jt\omega} d\omega \qquad (36)$$

The variable, ω, is the frequency in radians sec^{-1};

$\omega = 2\pi f$, where f is the more common frequency in Hertz. Lower

case letters are normally used for time functions and upper

case letters, for frequency functions. Some useful properties

of the FT are listed in Figure 32. Useful transform pairs are

listed in Figure 33. Cooper and McGillem (23), Roden (24) and

Champeney (25) have prepared more elaborate tables which show

additional FT's and properties. Also, Bloomfield (26) has

described techniques for Fourier analyses.

The exponential $e^{-j\omega t}$ is reducible via Euler's identity

to (cos ωt - j sin ωt). The cosine transform is usually called

the real transform and the negative sine transform, the imaginary

transform. The real and imaginary transforms are a quadrature

pair since they represent information separated by a -90° phase

delay in the complex plane.

Since any real (i.e. causal) time function is neither an

even nor odd function about $t = 0$, its Fourier Transform will

be complex. In common terminology used in NMR, the real part

of the transform is called the absorption and the imaginary

part, the dispersion.

FOURIER TRANSFORM RELATIONS

DESCRIPTION	TIME	FREQUENCY
DEFINITION	$g(t) = \dfrac{1}{2\pi}\displaystyle\int_{-\infty}^{\infty} G(\omega)\ e^{jt\omega}\,d\omega$	$G(\omega) = \displaystyle\int_{-\infty}^{\infty} g(t)\ e^{-j\omega t}\,dt$
INTERCHANGE	$G(t)$	$2\pi\, g(-\omega)$
REVERSAL	$g(-t)$	$G(-\omega)$
SCALING	$g(t/c)$	$c\, G(c\omega)$
DELAY	$g(t-t_o)$	$e^{-jt_o\omega}\, G(\omega)$
MODULATION	$e^{j\omega_o t}\, g(t)$	$G(\omega-\omega_o)$
TIME CONVOLUTION	$\displaystyle\int_{-\infty}^{\infty} g_1(\tau)\, g_2(t-\tau)\,d\tau$	$G_1(\omega)\, G_2(\omega)$
FREQUENCY CONVOLUTION	$g_1(t)\, g_2(t)$	$\dfrac{1}{2\pi}\displaystyle\int_{-\infty}^{\infty} G_1(\nu)\, G_2(\omega-\nu)\,d\nu$
. PARSEVAL'S THEOREM	$\displaystyle\int_{-\infty}^{\infty} g_1(t)\, g_2(t)\,dt\ =$	$\dfrac{1}{2\pi}\displaystyle\int_{-\infty}^{\infty} G_1(\omega)\, G_2(-\omega)\,d\omega$

Figure 32. Properties of the Fourier Transform
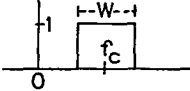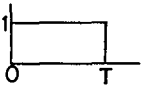
TIME	REAL [a]	IMAGINARY [b]	FULL WIDTH [d]
$\cos(2\pi f_0 t)$	$0.5\,\delta(f-f_0)$	———	0
$\sin(2\pi f_0 t)$	———	$0.5\,\delta(f-f_0)$	0
$\dfrac{2\,\sin(\pi W t)}{\pi t}\cos(2\pi f_c t)$	(box of width W centered at f_c, height 1)	———	W
(rectangle height 1, from 0 to T) [c]	$\dfrac{\sin(2\pi T f)}{2\pi f}$	$\dfrac{-\sin^2(\pi T f)}{\pi f}$	$\dfrac{0.6025}{T}$
$e^{-|t|/T_2}\cos(2\pi f_0 t)$ [c]	$\dfrac{0.5\,T_2}{1+4\pi^2 T_2^2(f-f_0)^2}$	$\dfrac{\pi T_2^2(f_0-f)}{1+4\pi^2 T_2^2(f-f_0)^2}$	$\dfrac{1}{\pi T_2}$
$e^{-0.5(t/T_2)^2}\cos(2\pi f_0 t)$ [c]	$T_2\sqrt{\dfrac{\pi}{8}}\;e^{-2\pi^2 T_2^2(f-f_0)^2}$	$-\sqrt{\dfrac{1}{2}}\,T_2\,e^{-2\pi^2 T_2^2(f-f_0)^2}\displaystyle\int_0^{\sqrt{2}\pi T_2(f-f_0)} e^{\sigma^2}\,d\sigma$	$\dfrac{\sqrt{2LN2}}{\pi T_2}$

a. $G(-(f-f_0))=G(f-f_0)$ b. $G(-(f-f_0))=-G(f-f_0)$ c. $t\geq 0.0$ d. at half height

Figure 33. Useful Fourier Transforms

2. Multiplication and convolution

An interesting and useful pair of FT operations is multiplication and convolution. When time functions are multiplied, their Fourier Transforms are convoluted. The mathematical definition is:

$$\int_{-\infty}^{\infty} n(t) \cdot l(t) \; e^{-j\omega t} \, dt \;\; = \;\; f_0 \int_{-\infty}^{\infty} N(\sigma') \; L(\sigma - \sigma') \, d\sigma' \qquad (37)$$

Here σ and σ' are used to specify a dimensionless shift-axis, $\sigma = \dfrac{\omega}{2\pi f_0}$. Reciprocally, when two frequency functions are multiplied, their inverse Fourier Transforms are convoluted.

The process of convolution is relatively easily visualized grahpically (or numerically) (24). In Figures 34 and 35, two functions $N(\sigma)$ and $L(\sigma)$ are convoluted. Numerical convolution involves a "shift and sum" mechanism which generates the convoluted function, $N(\sigma) * L(\sigma)$. This new function possesses qualities of both the original functions. In general, the width of the newly created function is closely related to the sum of the widths of the original functions and "sharp edges" are smoothed. The technique of graphical or numerical convolution is easily performed with an algorithm on a digital computer.

3. Sidelobes

All time-data sampled in time must be finite and thus can be considered as the product of some theoretical lineshape of of infinite duration multiplied by a rectangular sampling window. The Fourier Transform of this window is shown in Figure 36.

CONVOLUTION

$N(\sigma)$

$L(\sigma)$

$N(\sigma) * L(\sigma)$
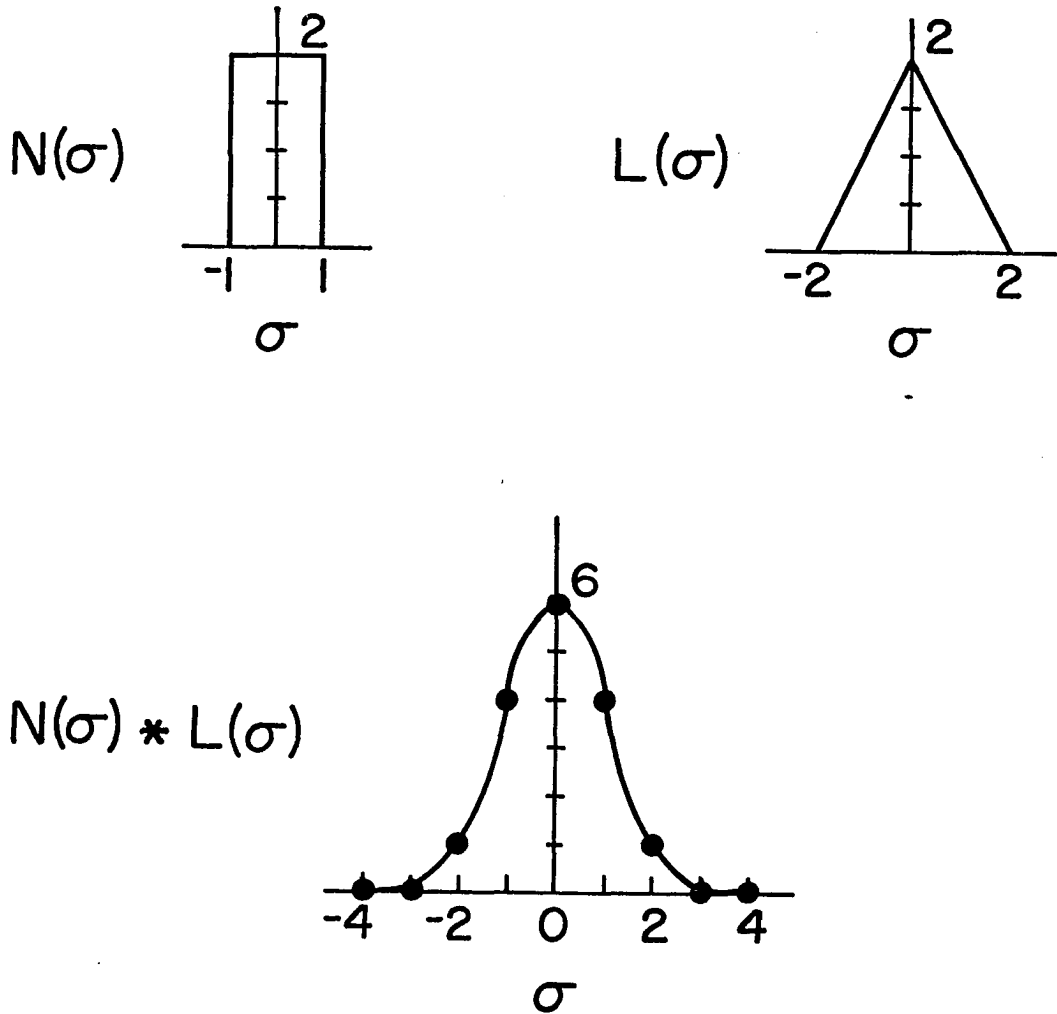
Figure 34. An example of numerical or graphical convolution

GRAPHICAL CONVOLUTION
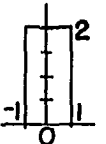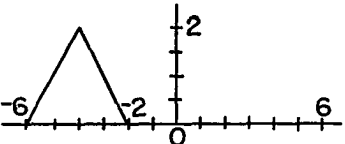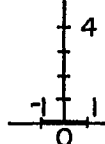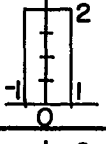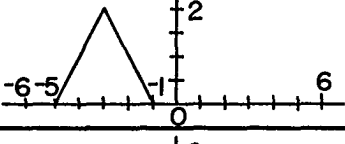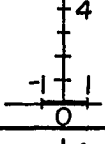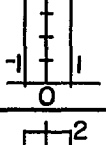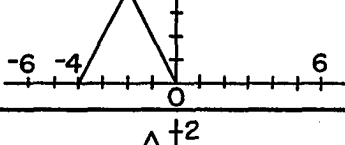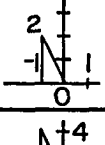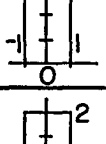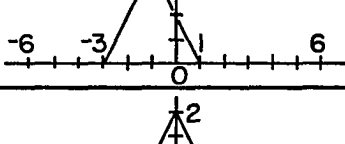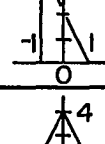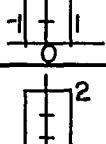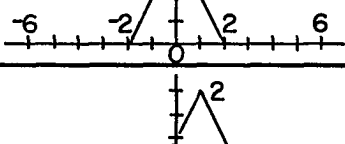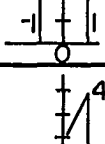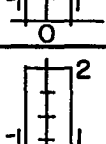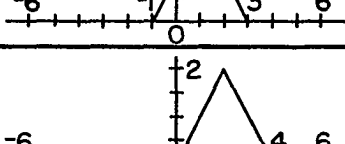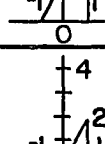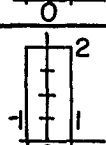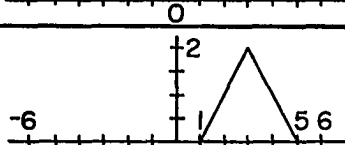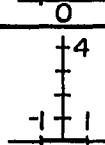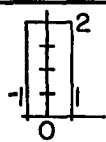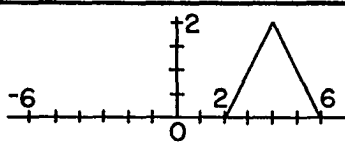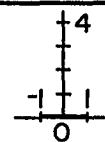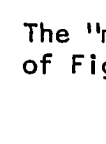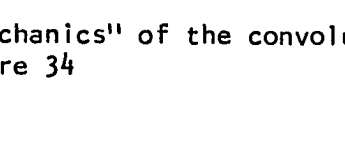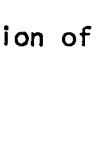
σ	$N(\sigma')$	$L(\sigma - \sigma')$	Product	Area
-4				0
-3				0
-2				1
-1				4
0				6
1				4
2				1
3				0
4				0

Figure 35. The "mechanics" of the convolution of the functions
of Figure 34
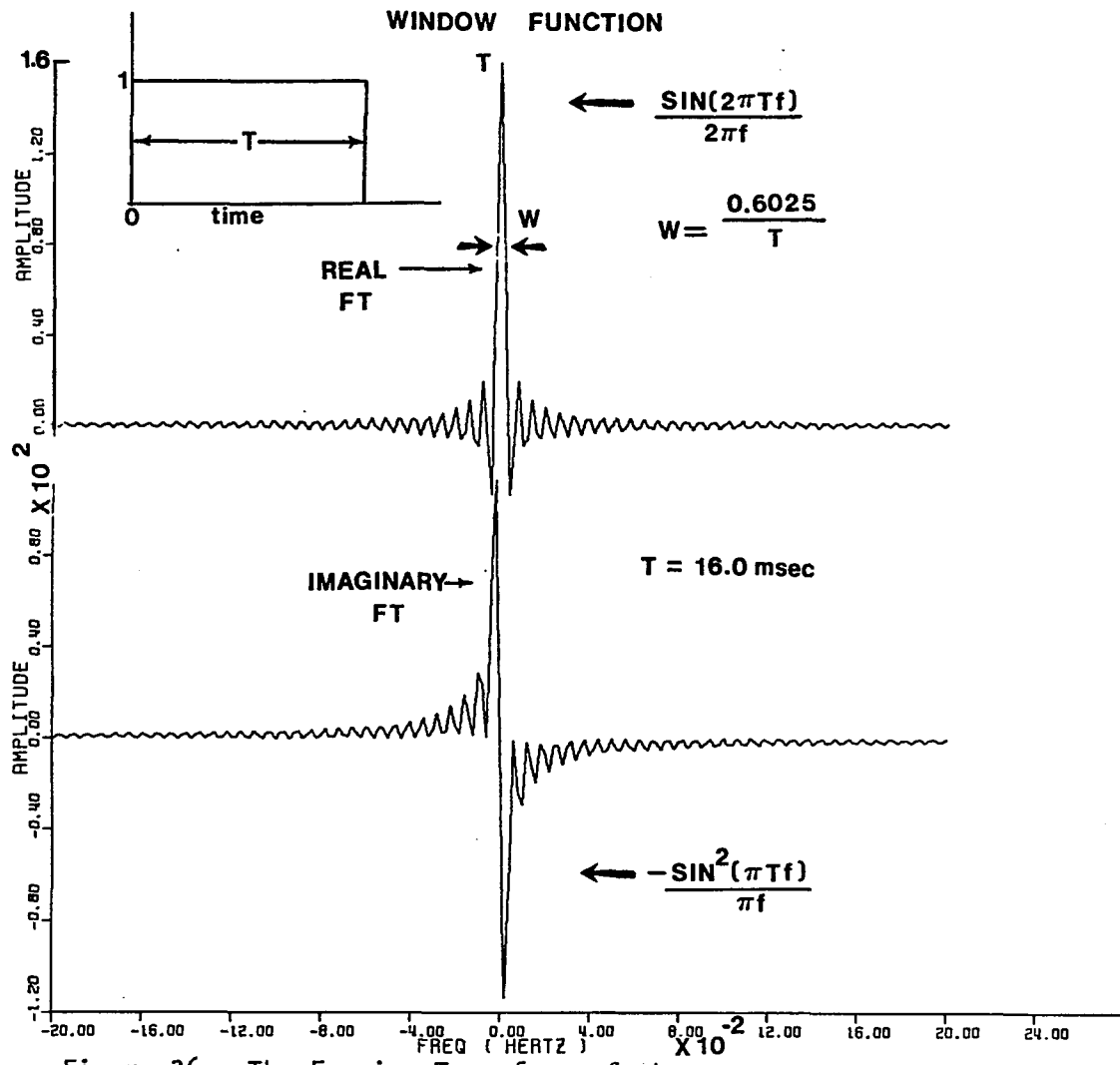
Figure 36. The Fourier Transform of the rectangular sampling window

Both the real and imaginary parts of any Fourier Transform can be generated by convoluting the theoretical real transform with the window's transforms shown in Figure 36. The width of the window must be chosen sufficiently large so that sidelobes, which are products of "windowing", are small. The imaginary transforms of both the Lorentzian and Gaussian lineshapes, shown in Figure 37 were generated in this manner.

If the length (T) of this window is made too short such that the full width of the window's real transform is comparable to the absorption line's full width:

$$\frac{0.6025}{T} \simeq \frac{1.0}{\pi T_2}$$

or:

$$T \simeq 2T_2$$

then sidelobes will start to become very apparent in the FT lineshape. Consequently the length, T, of the sampled data should always be:

$$T \gg 2T_2 \qquad (38)$$

4. <u>Relationship between initial amplitude and area</u>

Parseval's Theorem:

$$\int_{-\infty}^{\infty} g(t) \, h(t) \, dt = \int_{-\infty}^{\infty} G(f) \, H(-f) \, df \qquad (39)$$

(which can be derived by equating: $1/2\pi \int_{-\infty}^{\infty} G(\omega) \, H(\omega - \omega') \, d\omega'$ with: $\int_{-\infty}^{\infty} g(t) \, h(t) \, e^{-j\omega t} \, dt$ at $\omega = 0$) can be used to demonstrate the property that the area under any absorption (i.e. real FT) is proportional to the value of the time function at $t = 0$.

THEORETICAL   LINESHAPES

LORENTZIAN

e^{-1}

$e^{\frac{-|t|}{T_2}}\cos(2\pi f_0 t)$

T_2

AMPLITUDE

TIME (SECS) $\times 10^3$

REAL F.T.

$\times \dfrac{2}{T_2}$

unit amplitude

$\dfrac{1}{1+4\pi^2 T_2^2 (f-f_0)^2}$

$W = \dfrac{1}{\pi T_2}$

$AREA = \dfrac{\pi W}{2}$

-0.5

W

AMPLITUDE

IMAG F.T.

$\times \dfrac{1.56}{T_2}$

FREQ (HERTZ) $\times 10^{-2}$

GAUSSIAN

$e^{-0.5}$

$e^{-0.5(\frac{t}{T_2})^2}\cos(2\pi f_0 t)$

T_2

AMPLITUDE

TIME (SECS) $\times 10^3$

REAL F.T.

$\times \dfrac{1}{T_2\sqrt{\frac{\pi}{8}}}$

unit amplitude

$e^{-2\pi^2 T_2^2 (f-f_0)^2}$

$W = \dfrac{\sqrt{2 LN 2}}{\pi T_2}$

$AREA = \dfrac{W}{2}\sqrt{\dfrac{\pi}{LN 2}}$

-0.5

W

AMPLITUDE

IMAG F.T.

$\times \dfrac{0.78}{T_2\sqrt{\frac{\pi}{8}}}$

FREQ (HERTZ) $\times 10^{-2}$
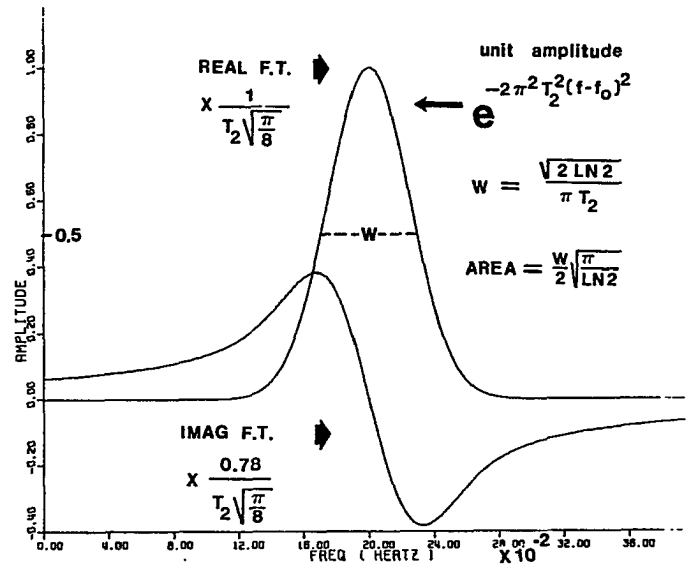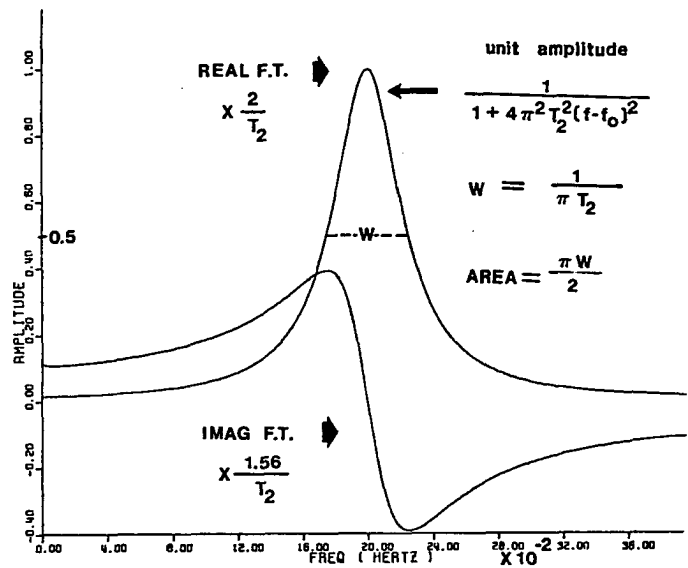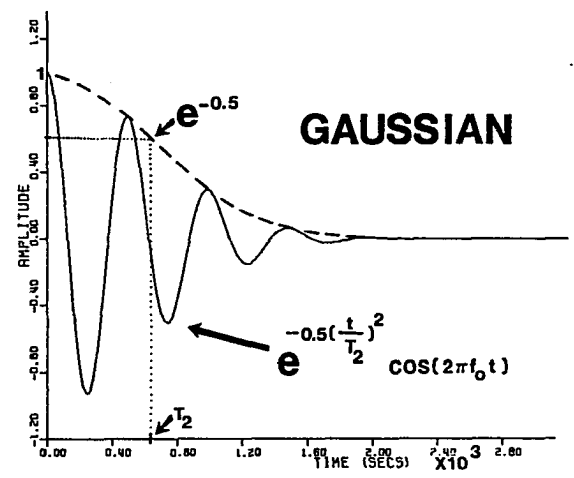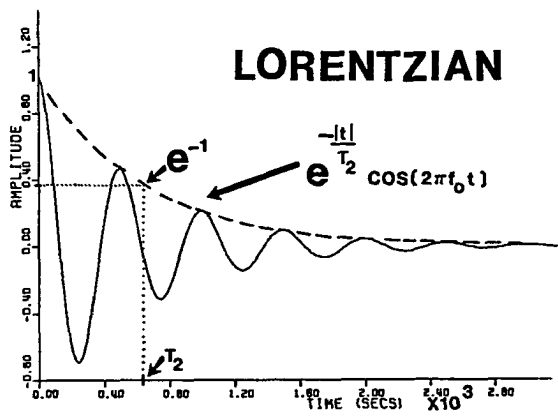
Figure 37.   The lineshapes of Lorentzians and Gaussians

Since the imaginary transform is always an odd function of frequency, it will make no contribution to the total area of the transform. Thus, only even time functions, which produce only real transform (absorptions), need be considered without loss of generality to all time functions.

The time, $t = 0$, can be selected by specifying $h(t)$ as a unit-area delta function:

$$h(t) = \delta(t) = \infty \quad t = 0 \qquad \int_{-\infty}^{\infty} \delta(t) = 1$$
$$= 0 \quad t \neq 0$$

The delta function can be assumed to be an even function about $t = 0$ without loss of generality for reasons discussed above. Its Fourier Transform, $H(f)$, will be a real constant, k, and equation 39 will reduce to:

$$g(0) = k\int_{-\infty}^{\infty} G(f) \, df \qquad (40)$$

Any causal (i.e. only $t \geq 0$ allowed) function, $g(t)$, can always be assumed an even function of time without loss of generality. Therefore, $G(f)$ will be a real transform (i.e. an absorption) and its area will be proportional to the initial value of the FID (free induction decay), $g(t)$. The constant, k, has the following values:

$$-\infty < t < \infty, \qquad k = 1 \text{ or}$$
$$0 \leq t < \infty, \qquad k = 2$$

A somewhat similar deduction can be made relating $G(0)$ to the integral of the function, $g(t)$.

It is interesting to note that, in general, processes which affect amplitudes in the time domain reflect themselves as processes which affect widths (or areas) in the frequency domain. The same argument can be said about processes which affect amplitudes in the frequency domain. This relationship can be generalized as a sort of width, inverse-width transform pair. An example of this phenomenon may be seen in the window function shown in Figure 36. As T approaches infinity, i.e., a horizontal increment, the real Fourier Transform approaches a delta function, i.e., a vertical increment.

C. Theoretical Lineshapes of Lorentzians and Gaussians

The lineshapes of Lorentzians and Gaussians have many uses in NMR analyses. Figure 37 shows the theoretical appearances of these lineshapes in the time and frequency domains. In the time domain they serve as models for NMR decays with the relaxation constant, T_2. In the frequency domain, these lineshapes can be used to resolve overlapping lines, to broaden the NMR powder pattern, to digitally filter a noisy data set, to model correlation functions, etc.

If the signal in the time domain is the response to a single-pulse excitation as shown in Figure 30, the lineshape is termed a FID. The real Fourier Transform is referred to as the absorption and the imaginary Transform, the dispersion. Figure 33 contains the mathematical forms of some representative lineshapes. The

relaxation constant, T_2, is defined in Figure 37. With the lineshapes represented by the mathematical forms of Figure 33 the area under each absorption $(0 \to \infty)$ is 1/4. However, the total area in each real Fourier Transform is 1/2 since each absorption is an even function of frequency. These areas are 1/2 the initial amplitudes of the FID since the Fourier Transform is one sided, i.e., $0.0 \leq t < \infty$. As expected from Parseval's Theorem discussed above, their areas are independent of T_2.

If a Gaussian and Lorentzian have the same initial amplitudes in the time domain, they will enclose the same areas in the frequency domain. Their maximum amplitudes and full widths (i.e. their shapes) will depend on T_2. For Gaussian and Lorentzian absorptions of the same maximum amplitudes and full widths at half height, the Gaussian's area will be $(\pi \ln 2)^{-1/2}$ or 67.8% of the Lorentzian's area. With an arbitrary amplitude the area of the absorption becomes proportional to both the amplitude and full width, W:

$$\text{Gaussian: Area} = W \cdot \text{amplitude} \cdot \frac{\sqrt{\frac{\pi}{\ln 2}}}{2} \qquad (41)$$

$$\text{Lorentzian: Area} = W \cdot \text{amplitude} \cdot \pi/2 \qquad (42)$$

D. Digital Filtering

1. Technique

The technique of digital filtering described in this Chapter is most conveniently applied to Fourier-Transformed data sets

(i.e., in the frequency domain). This technique also may be
applied to data sets in the time domain. The process of digital
filtering is graphically depicted in Figure 38 (frequency
domain) and Figure 39 (time domain).

In the frequency domain, the process involves the multiplication
of the raw data by a bandpass filter followed by convolution
with a broadening function (exponential filter). The equivalent
process in the time domain involves convolution of the raw data with
the inverse FT of the bandpass filter (sometimes termed its
impulse response) followed by multiplication by the inverse
Fourier Transform of the broadening function. The broadening
function is usually, but not necessarily, an exponential decay
in the time domain.

In order to prevent serious distortion of data, two criteria
are used. First, the center frequency, f_c, and width, W, of
the bandpass filter must be such that the appropriate spectral
region is selected. Second, the width of the broadening function
(exponential filter) must be such that absorptions are not
broadened to the point where overlapping occurs.

The simultaneous use of both a bandpass and exponential
filter has an important advantage over the widely used practice
of just exponential filtering. The bandpass filter will select
only the spectral region of interest. This feature is very
important when large transients and other noise lie close to
the spectral region one wishes to observe. These spurious
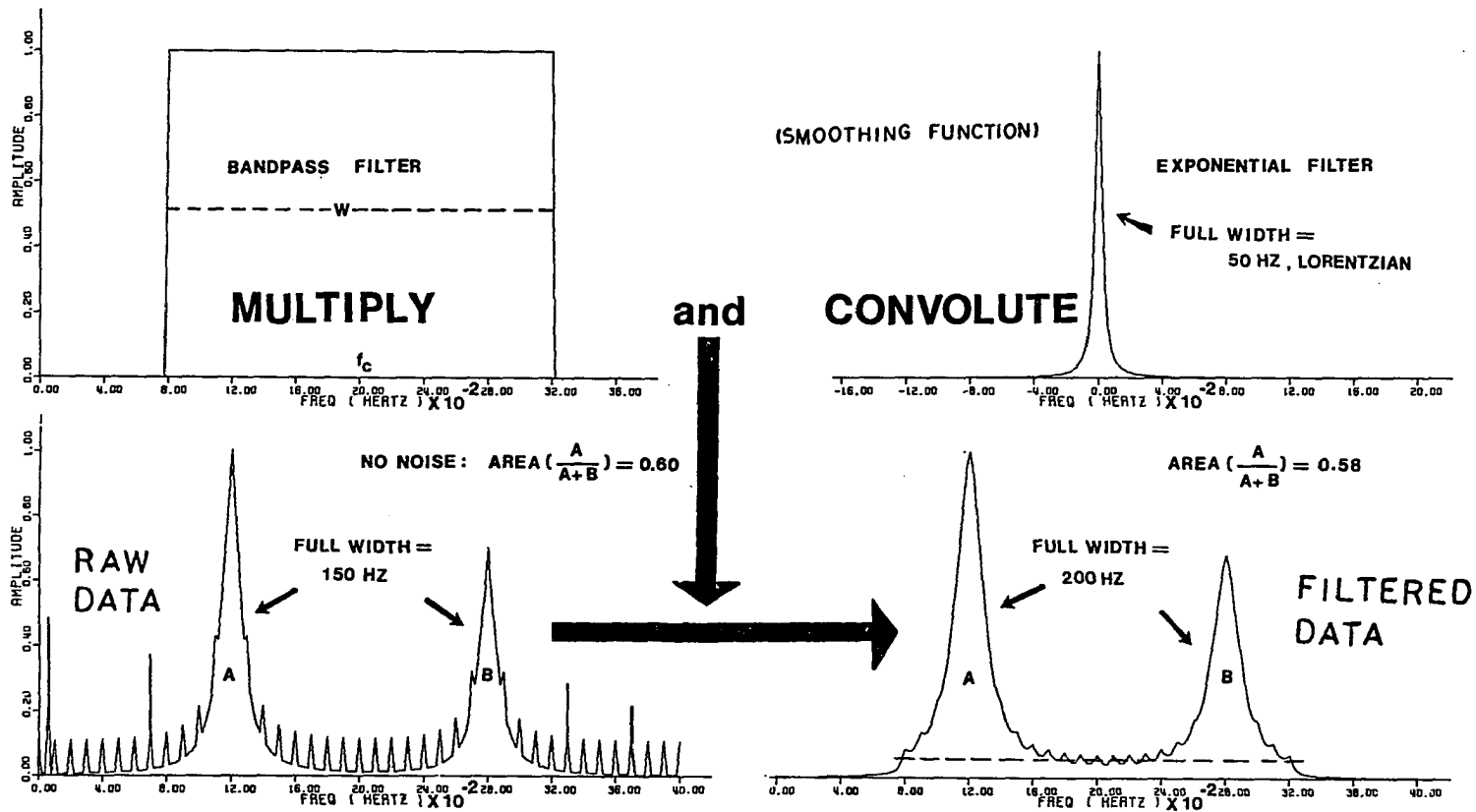
Figure 38. An example of digital filtering in the frequency domain

DIGITAL FILTERING: TIME

BANDPASS FILTER

0.8 — 3.2 KHZ

EXPONENTIAL FILTER

$T_2 = 6.37$ msec,

LORENTZIAN

CONVOLUTE   **and**   **MULTIPLY**

(SMOOTHING FUNCTION)

−0.56

NO NOISE, $T_2 = 2.12$ msec

$T_2 = 1.59$ msec

WITH SINUSOIDAL NOISE

RAW DATA

FILTERED DATA
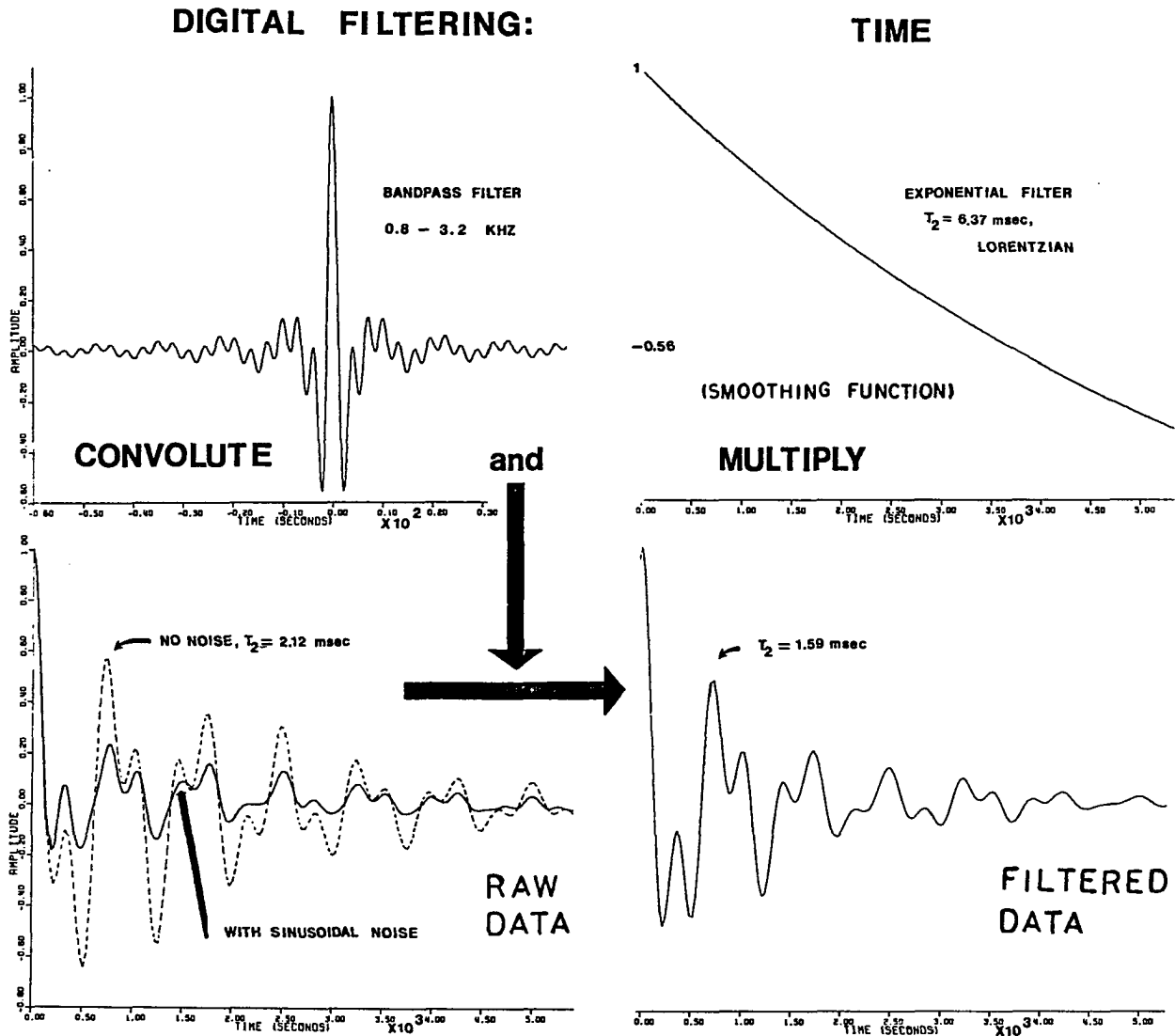
Figure 39.   An example of digital filtering in the time domain

artifacts may be removed from the spectrum and thus cannot lead to possible distortions following the application of the broadening function (exponential filter).

It should be particularly noted that every FT amplitude which results from the Fourier Transform of a time spectrum which has been multiplied by some non-constant function will now contain weighted contributions from all the original FT amplitudes. This phenomenon can be seen in the "mechanics" of convolution shown in Figure 33.

If there are large transients in the original time-data, there is a possibility of artifacts, such as sinusoidal baselines, in the frequency spectrum. Such a case is especially likely in solid state NMR where the shortest recovery times are needed and artifacts from RF ringdowns may be severe. For such data, it is convenient to perform the exponential filtering(smoothing) in the frequency domain (via convolution of a broadening function). A bandpass filter can be used to select only the spectral region of interest. Therefore, artificial contributions to integrated amplitudes will be minimized.

The concept of digital filtering is easy to visualize in terms of the widths of the absorption and noise. The noise is usually, but not necessarily, impulsive in the frequency domain and correlated over a small frequency interval. Convoluting with the broadening function is very similar to performing a weighted

smoothing over the entire spectral region; the width of the broadening function determines the weighting coefficients.

The process of convolution with a broadening function (or multiplication by an exponential in the time domain) will not change relative areas; however, it will broaden and thus alter amplitudes and widths. Useful filtering occurs when the width of the broadening function is much greater than the average width of the noise but much less than the width of the absorption. The noise will be smeared, leaving a slightly broadened absorption.

2. Applications

An example of the use of the digital filtering process is shown in Figure 40. In the frequency (or shift) domain, the application of a bandpass filter is a simple process--only data of interest are selected from the entire data set. The original, noisy data of Figure 40 is convoluted with a Lorentzian broadening function of half width, $W/2 = 150.0$ Hz. Besides attenuating and smoothing the impulsive noise, the filtering, more importantly, clearly establishes a base line for numerical integration. The proper base line is not at all apparent in the unfiltered data of Figure 40.

Figure 41 shows a filter-calibration graph. In this graph the relative area, f_a (called the fraction aromaticity), under the NMR absorption peak associated with the aromatic ^{13}C of a solid coal, is plotted vs. half width at half height for both Lorentzian
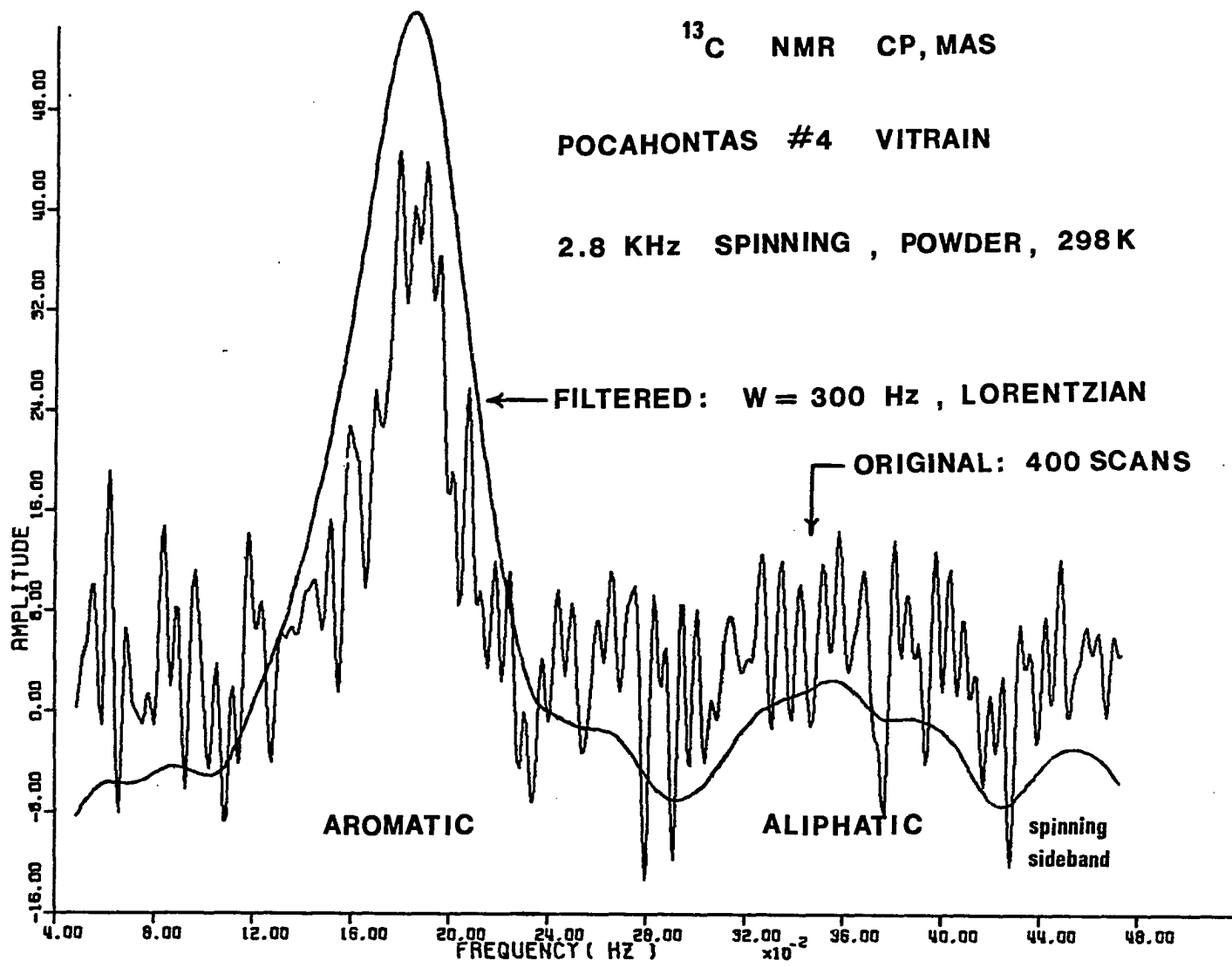
Figure 40. Digital filtering applied to the noisy ^{13}C absorption spectrum of a coal vitrain
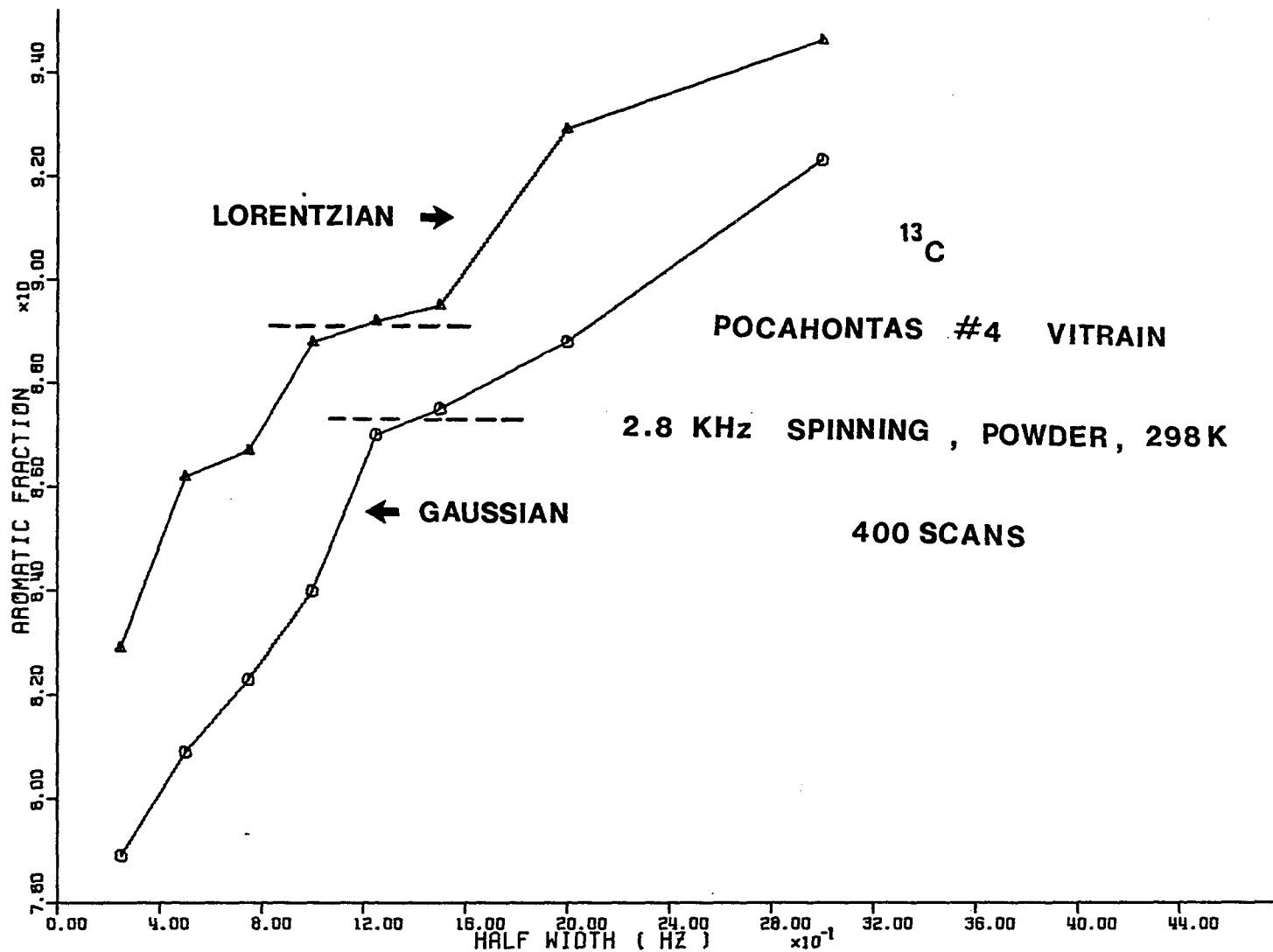
Figure 41. The effect of digital filtering on relative areas of the ^{13}C aromatic fraction

and Gaussian filters applied to the original, noisy data shown
in Figure 40. The concentrations of aromatic, ar, and aliphatic,
al, ^{13}C nuclear species are assumed proportional to the area
under the appropriate absorptions and

$$f_a = \text{concentration } (\frac{ar}{ar + al})$$
$$= \text{area } (\frac{ar}{ar + al}) \tag{43}$$

3. Behavior

The effect of the filtering process on the calculated absorption
areas can be separated into three cases. In the first case
(to the left of the dashed lines in Figure 41), the half widths
of the filters are too small. The noise contributions and
base-line uncertainties cause the area of the aliphatic peak to
be somewhat larger and thus the f_a's are lower. In the second
region (dashed lines of Figure 41), the half widths of the filters
are such that relatively constant areas and f_a's are calculated.
In the third region (to the right of the dashed lines of Figure 41),
the half widths of the filters are too large and the two peaks
begin to overlap--resulting in attenuation of the aliphatic
peak and higher f_a's.

The f_a values of the Lorentzian are consistently higher
than those of the Gaussian. The Lorentzian lineshape has longer
tails than the Gaussian and produces a slightly higher baseline.
Since the aliphatic absorption occupies less area, the higher
baseline will result in slightly less area for the aliphatic

absorption and consequently slightly higher f_a values. In
general, as the signal-to-noise improves the half width required
to reach the plateau (dashed lines of Figure 41) and constant
f_a decreases.

The digital filtering technique (frequency domain) is quite
general and can be applied to any type of sequential data. The
units of the axis are arbitrary since the theory may be formulated
for dimensionless axes such as a shift axis. A computer program
which performs this filtering along with numerical integration
has been described elsewhere (22).

E. Resolving an Absorption Spectrum into
Lorentzian and Gaussian Components

The absorption lineshapes of the Lorentzian and Gaussian
lines which are described in section C and displayed in Figure 37
are sometimes useful as models to resolve overlapping NMR
absorption-lines. Each lineshape is defined by three parameters:
an amplitude, A, a full width at half height, W, and a location,
f_o, on some axis (frequency or shift). Standard procedure involves
supplying initial guesses for the three parameters. A computer
program is used to statistically optimize these values via a
non-linear least-squares algorithm (Levenberg-Marquardt, for
example) until a specified convergence condition is established.

Useful information such as the T_2 of the FID and the area
under a given absorption can be deduced from the parameters A

and W of each resolved absorption. An example of the use of this technique is shown in Figure 42. This spectrum shows the current state-of-the-art resolution for solid state, ^{1}H NMR taken by L. M. Ryan of this laboratory.

Both Multiple Pulse (MP) (2, 3) to remove the static dipolar coupling, and Magic-Angle Spinning (MAS) (2, 3) to remove shift anisotropy, are combined to produce this relatively high resolution spectrum of protons in the solid state. The aromatic and aliphatic proton absorptions are not resolved in situ. However, they are completely resolved into the Lorentzian components shown super-imposed on the spectrum. The percent areas under these absorptions which are proportional to the number of a specific kind of proton to the total number of protons in the model compound are shown to agree quite closely with the theoretical values in parentheses. The computer program which performs this fitting and decomposition has been described elsewhere (22).
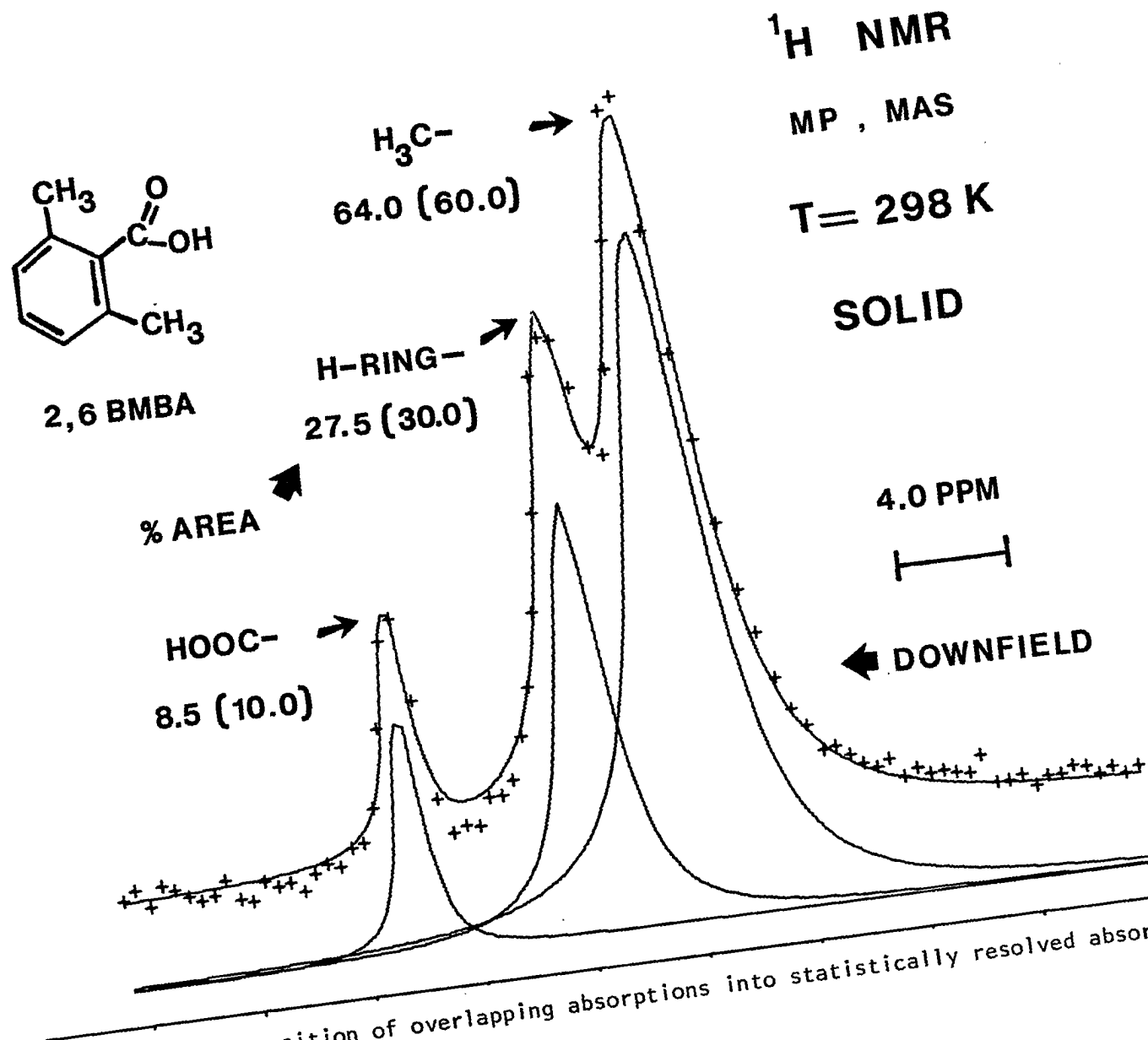
Figure 42. The decomposition of overlapping absorptions into statistically resolved absorptions

VI. THE LINESHAPE OF THE SHIELDING TENSOR

A. Introduction

In the absence of dipolar interactions, the NMR absorption spectrum of a spin = 1/2 nucleus, in a powdered solid sample, e.g. ^{13}C in CO(s) (27-29), results from the interaction: $H = -\overline{\overline{\sigma}} \cdot \overline{H}_o$ where $\overline{H}_o$ is a vector which represents both the magnitude and direction of the external magnetic field and $\overline{\overline{\sigma}}$ is a second-rank tensor called the shielding tensor. The spectrum under these conditions is usually called the "Powder Pattern" (27, 28, 2, 3).

In liquids, where isotropic molecular motion is rapid on a time scale compared to that of the dipolar interaction, dipolar interactions are averaged to zero and shielding anisotropies are averaged to yield a single line at the isotropic value of the shielding tensor. To illustrate these ideas, a comparison of lineshapes under conditions where: a) dipolar and shielding interactions are motionally averaged, b) dipolar interactions dominate, c) the shielding anisotropy dominates and d) both dipolar and shielding interactions are averaged to zero is shown in Figure 43.

For many nuclei in the solid state, static dipolar interactions, e.g. between ^1H and ^1H in $H_2O(s)$ or ^1H and ^{13}C in $C_6H_6(s)$ are much larger than shielding anisotropies. Broad, rather featureless NMR spectra result for such nuclei in powdered solids. Information
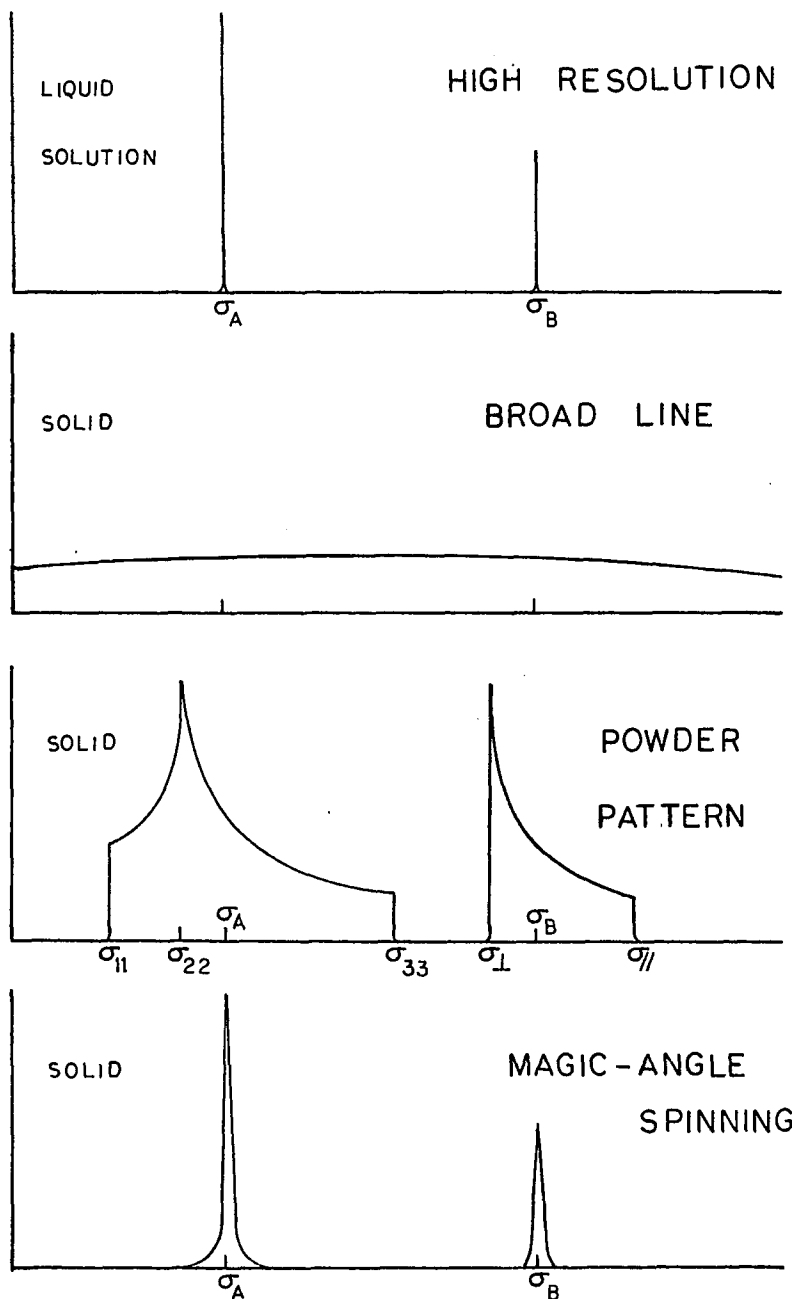
Figure 43. Typical lineshapes of NMR absorptions

about shielding anisotropies is not available from such systems without the use of some decoupling technique (2, 3, 28, 30-40).

Rare spins such as ^{13}C, ^{29}Si or ^{15}N only require a strong RF field applied to the abundant spins (e.g. ^{1}H) to decouple all heteronuclear neighbors. Since few homonuclear nearest neighbors are present, the lineshape of the Powder Pattern associated with shielding anisotropy is observed under these conditions. With the advent of Multiple-Pulse homonuclear decoupling experiments (2, 3, 28, 30-40), a laboratory-controlled manipulation of the homonuclear dipolar Hamiltonian can be achieved in such a way that the static homonuclear dipolar coupling is removed. This technique is discussed in Chapter VII. Thus, useful Powder Patterns are now being recorded for abundant spins such as ^{1}H and ^{19}F.

The origins of the shielding Powder Pattern have been well discussed in the literature (27, 28, 2, 3). It is characterized by three components: σ_{11}, σ_{22} and σ_{33}, which are called the principal components of the diagonalized shift (Knight or Chemical) tensor. Figure 44 shows the theoretical lineshapes for a non-symmetric tensor and an axially symmetric tensor for which two of the three components are equal (i.e. $\sigma_{\perp} = \sigma_{11} = \sigma_{22}$ and $\sigma_{\parallel} = \sigma_{33}$).

This Chapter will present a derivation of the theoretical lineshape of a Powder Pattern which was first derived by Bloembergen and Rowland (27) in 1953. Additionally, the concept

THEORETICAL
LINESHAPES
OF
SHIFT TENSORS

NON-SYMMETRIC

σ_{11} σ_{22} σ_{33}

AXIALLY
SYMMETRIC

$\sigma_{\perp}$ $\sigma_{\parallel}$
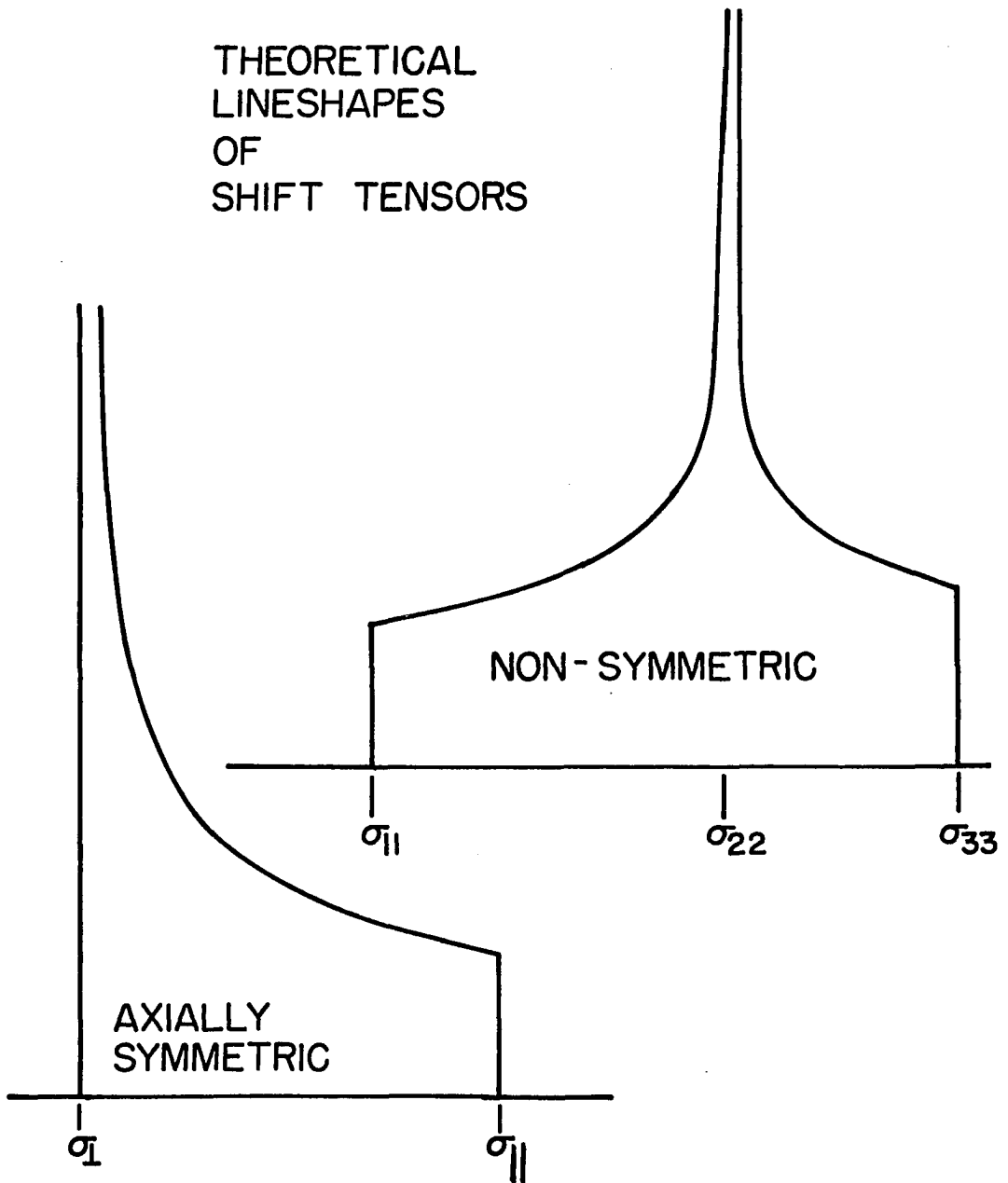
Figure 44.   The theoretical lineshapes of an axially symmetric
and non-symmetric shift tensor

of graphical convolution and its use to broaden the theoretical
lineshape is discussed. Also, the effect of assigning a finite
value to the discontinuity in the theoretical lineshape is
explored. This Chapter is a slightly modified version of a
D. O. E. report which describes the technique of computerized-
fitting of the Powder-Pattern lineshape to experimental data (41).
This technique is a very useful means of estimating the tensor
components when residual broadening is present. The shielding
anisotropies of the ^1H tensors in the hydrides of zirconium
halides (See Chapter VII) were inferred from computerized-fitting
(41) of the lineshape of the Powder Pattern. Also, the unsymmetric
properties of this lineshape make it a useful model to decompose
the overlapping lineshapes and estimate the aromatic fraction
of carbon in whole coals (See Chapter IX).

B. The Lineshape of the Powder Pattern

1. Calculation of the theoretical lineshape of the absorption

The observed frequency or shift, σ, of the NMR absorption
for a particular nucleus in a single crystal with axes X, Y, Z
oriented with spherical polar angles θ, ϕ to the external field,
H_o, is related (2, 28, 42) to the six components of a symmetric
shift tensor, $\overline{\overline{\sigma}}$, by the equation:

$$\sigma = \sigma_{33} \cos^2\theta + \frac{1}{2}(\sigma_{11} + \sigma_{11}) \sin^2\theta \qquad (44)$$

$$+ \frac{1}{2}(\sigma_{11} - \sigma_{22}) \sin^2\theta \cos 2\phi$$

$$+ \sigma_{12} \sin^2\theta \sin 2\phi$$

$$+ \sigma_{13} \sin\theta \cos\theta \cos\phi$$

$$+ 2 \sigma_{23} \sin\theta \cos\theta \sin\phi$$

The six quantities: σ_{11}, σ_{12}, σ_{13}, σ_{22}, σ_{23} and σ_{33}, are the Cartesian components of the second-rank shift tensor. Only the symmetric tensor (2) which produces non-symmetric, axially symmetric and isotropic lineshapes is considered. The pictoral definitions of these angles and the reference axes are shown in Figure 45.

A finely crushed powder can be considered a completely random orientation of very small crystallites (many, X. Y, Z axes). Of course, the orientation of the magnetic field, $\bar{H}_o$, will be different for each tiny crystallite. The orientation of the magnetic field, $\bar{H}_o$, with respect to the crystallographic axes of each (of the many) crystallites will determine the exact resonance (or shift) for the particular crystallite (equation 44).

It is convenient to define the spherical polar angles θ and ϕ to specify the orientation of the magnetic field with respect to the principal axes of the shift tensor of each crystallite as shown in Figure 45. Thus, the angles θ and ϕ
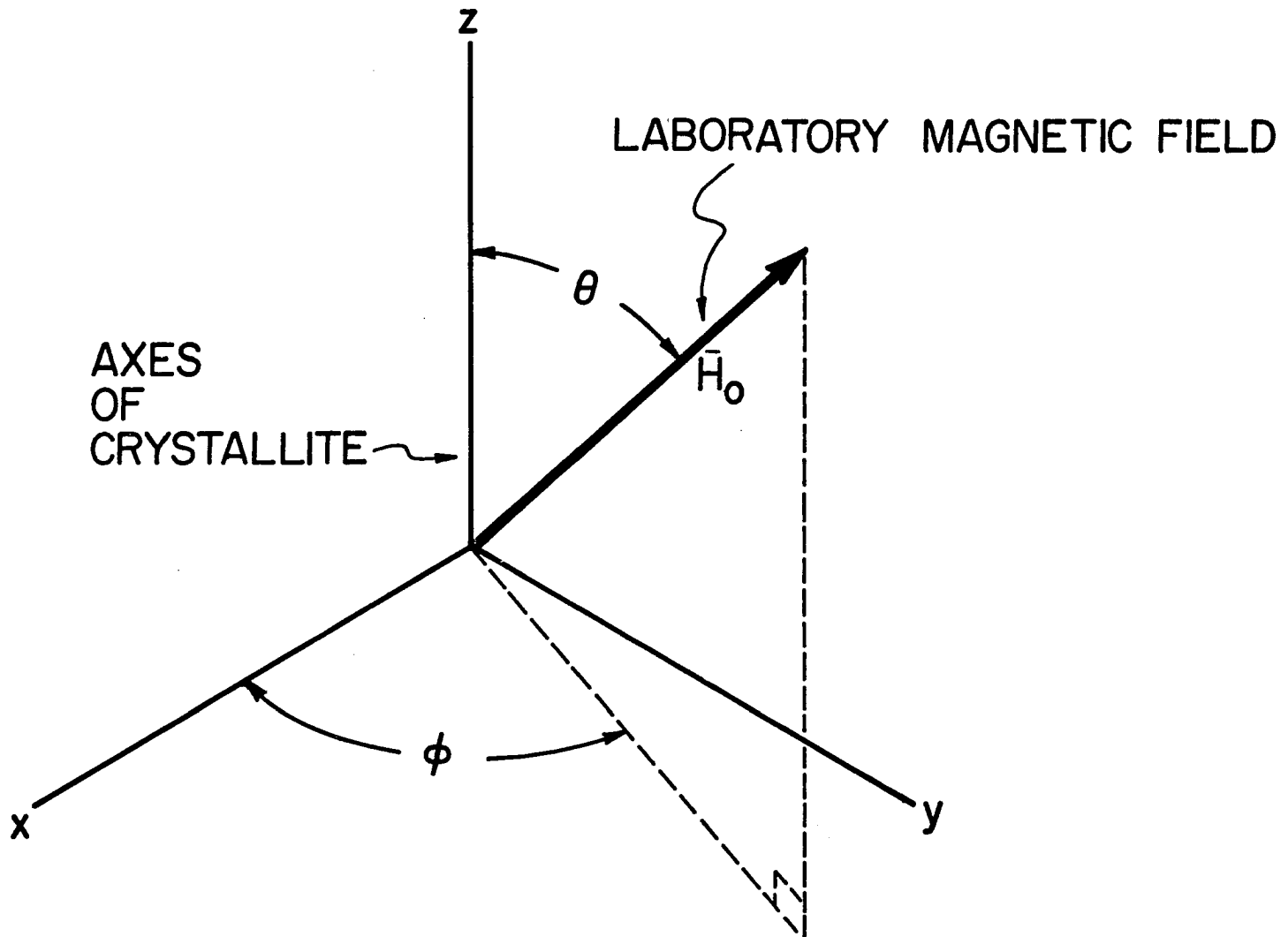
Figure 45.   The definition of the reference axes of a crystallite

are now assumed to be the appropriate angles which always specify orientations from the same reference frame inside of all crystallites. For instance, with this treatment, the location of the external field will occur at different locations in Figure 45 for crystallites with different orientations of their principal axes with respect to $\bar{H}_o$. In addition, non-diagonal tensor elements are identically zero for specification of θ and ϕ in this manner and equation 44 reduces to:

$$\sigma = \sigma_{33} \cos^2\theta + \frac{1}{2}(\sigma_{11} + \sigma_{22}) \sin^2\theta$$
$$+ \frac{1}{2}(\sigma_{11} - \sigma_{22}) \sin^2\theta\cos 2\phi \qquad (45)$$

This equation can be rearranged to:

$$\sigma = \sigma_{11} \sin^2\theta\cos^2\phi + \sigma_{22} \sin^2\theta \sin^2\phi$$
$$+ \sigma_{33} \cos^2\theta \qquad (46)$$

The lineshape of the Powder Pattern results from the weighted distribution of frequency (or shift) information. This information is stored in the inherent anisotropy (i.e. range of shifts for a given nucleus) which is the same for all crystallites. The angles (θ, ϕ) and the random orientation of crystallites are the weighting factors which spread this information between the largest value, σ_{33}, and the smallest values, σ_{11}. This distribution is displayed as the spectral amplitude vs. frequency (or shift) which is the lineshape of the Powder Pattern.

A completely random orientation of all crystallites is assumed such that all allowed values of θ and ϕ are equally

probable (i.e., $N(\theta, \phi)$ is a constant). With such a distribution one can use Calculus to show that the number of crystallites for which the external field, $\bar{H}_o$, is oriented between infinitesmal angles: θ, $\theta + d\theta$ and ϕ, $\phi + d\phi$ is proportional to $\sin\theta d\theta d\phi$. This number of crystallites will contribute to an infinitesmal element of area, $N(\sigma)d\sigma$, of the lineshape or:

$$N(\sigma)d\sigma \; \alpha \; \sin\theta d\theta d\phi \qquad (47)$$

In the following derivations, most equations will be written as proportions ("α") to signify the presence of some suitable normalization constant.

If θ is held fixed then:

$$N(\sigma)_\theta \; \alpha \; \left(\frac{d\sigma}{d\theta}\right)^{-1}$$

Equation 46 yields:

$$\left.\frac{d\sigma}{d\phi}\right|_\theta \; \alpha \; (\sigma_{22} - \sigma_{11}) \sin^2\theta \sin\phi \cos\phi \qquad (48a)$$

Also from equation 46:

$$\sin\phi = \frac{\pm 1}{\sin\theta} \left[\frac{\sigma - \sigma_{11}}{\sigma_{22} - \sigma_{11}} - \left(\frac{\sigma_{33} - \sigma_{11}}{\sigma_{22} - \sigma_{11}}\right) \cos^2\theta \right]^{\frac{1}{2}} \qquad (48b)$$

$$\cos\phi = \frac{\pm 1}{\sin\theta} \left[\frac{\sigma_{22} - \sigma}{\sigma_{22} - \sigma_{11}} + \left(\frac{\sigma_{33} - \sigma_{22}}{\sigma_{22} - \sigma_{11}}\right) \cos^2\theta \right]^{\frac{1}{2}} \qquad (48c)$$

Substitution of equations 48b and 48c into 48a yields:

$$N(\sigma)_\theta \; \alpha \left(\frac{d\sigma}{d\phi}\right)^{-1} \alpha \left[(\sigma - \sigma_{11}) - (\sigma_{33} - \sigma_{11}) \cos^2\theta \right]^{-\frac{1}{2}} \cdot \qquad (48d)$$

$$\left[(\sigma_{22} - \sigma) + (\sigma_{33} - \sigma_{22}) \cos^2\theta \right]^{-\frac{1}{2}}$$

Since $\cos^2\phi$ is bounded by the interval:

$$0 \le \cos^2\phi \le 1$$

then the following inequalities follow from equation 48c:

$$\frac{\sigma - \sigma_{11}}{\sigma_{33} - \sigma_{11}} \ge \cos^2\theta \ge \frac{\sigma - \sigma_{22}}{\sigma_{33} - \sigma_{22}} \qquad (48e)$$

Two cases must be considered. For:

$$\sigma_{11} \le \sigma < \sigma_{22},$$

$$\frac{\sigma - \sigma_{11}}{\sigma_{33} - \sigma_{11}} \ge \cos^2\theta \ge 0 \qquad (48f)$$

and for:

$$\sigma_{22} < \sigma \le \sigma_{33},$$

$$\frac{\sigma - \sigma_{11}}{\sigma_{33} - \sigma_{11}} \ge \cos^2\theta \ge \frac{\sigma - \sigma_{22}}{\sigma_{33} - \sigma_{22}} \qquad (48g)$$

with:

$$N(\sigma)_\theta \to \infty, \qquad \sigma = \sigma_{22}$$

and:

$$N(\sigma)_\theta = 0$$

outside of this interval.

The actual lineshape can be found by multiplying equation 48d by $\sin\theta$ and integrating over the permissible range of θ:

$$N(\sigma) \ \alpha \int N(\sigma)_\theta \ \sin\theta \ d\theta$$

This integral can be arranged into an elliptic integral of the first kind (43) in the following manner.

Beginning with $\sigma_{11} \le \sigma < \sigma_{22}$:

Let $t = \cos\theta$ and $dt = -\sin\theta d\theta$

then:

$$N(\sigma) \propto \int_0^{(\frac{\sigma - \sigma_{22}}{\sigma_{33} - \sigma_{11}})^{\frac{1}{2}}} [(\sigma - \sigma_{11}) - (\sigma_{33} - \sigma_{11})t^2]^{-\frac{1}{2}} \cdot [(\sigma_{22} - \sigma) + (\sigma_{33} - \sigma_{22})t^2]^{-\frac{1}{2}} dt \qquad (49)$$

Let $b = (\frac{\sigma - \sigma_{11}}{\sigma_{33} - \sigma_{11}})^{\frac{1}{2}}$ $a = (\frac{\sigma_{22} - \sigma}{\sigma_{33} - \sigma_{22}})^{\frac{1}{2}}$

then:

$$N(\sigma) \propto [(\sigma_{33} - \sigma_{11})(\sigma_{33} - \sigma_{22})]^{-\frac{1}{2}} \int_0^b (b^2 - t^2)^{-\frac{1}{2}} (a^2 + t^2)^{-\frac{1}{2}} dt \qquad (50)$$

This algebraic integral can be reduced to an elliptic integral of the first kind (43) in the following way.

$$\int_y^b [b^2 - t^2]^{-\frac{1}{2}} [a^2 + t^2]^{-\frac{1}{2}} dt = g \ F (\phi, k) \qquad (51)$$

$$g = [a^2 + b^2]^{-\frac{1}{2}} \qquad k^2 = \frac{b^2}{a^2 + b^2}$$

$$\phi = \cos^{-1}(Y/b) \qquad F(\phi, k) = \int_0^\phi [1 - k^2 \sin^2 X]^{-\frac{1}{2}} dX \qquad (52)$$

When $\phi = \pi/2$, equation 52 is referred to as a complete elliptic integral of the first kind.

The parameters: g, k and ϕ are related to the components of $\bar{\bar{\sigma}}$ as follows:

$$g = \left[\frac{(\sigma_{33} - \sigma_{22})(\sigma_{33} - \sigma_{11})}{(\sigma_{33} - \sigma)(\sigma_{22} - \sigma_{11})}\right]^{\frac{1}{2}}$$

$$k = \left[\frac{(\sigma - \sigma_{11})(\sigma_{33} - \sigma_{22})}{(\sigma_{33} - \sigma)(\sigma_{22} - \sigma_{11})}\right]^{\frac{1}{2}}$$

and $\phi = \cos^{-1}(0/b) = \pi/2$.

Equation 50 reduces as follows. For:

$$\sigma_{11} \leq \sigma < \sigma_{22},$$

we find:

$$N(\sigma) \propto \left[(\sigma_{33} - \sigma)(\sigma_{22} - \sigma_{11})\right]^{-\frac{1}{2}} \cdot \int_{0}^{\pi/2} [1 - k^2 \sin^2 X]^{-\frac{1}{2}} \, dX, \qquad (53)$$

A similar deduction can be made for $\sigma_{22} < \sigma \leq \sigma_{33}$

In this case:

$$k = \left[\frac{(\sigma_{33} - \sigma)(\sigma_{22} - \sigma_{11})}{(\sigma_{33} - \sigma_{22})(\sigma - \sigma_{11})}\right]^{\frac{1}{2}}$$

and:

$$N(\sigma) \propto \left[(\sigma_{33} - \sigma_{22})(\sigma - \sigma_{11})\right]^{-\frac{1}{2}} \cdot \int_{0}^{\pi/2} [1 - k^2 \sin^2 X]^{-\frac{1}{2}} \, dX \qquad (54)$$

and, of course,

$$N(\sigma) = 0 \text{ for } \sigma < \sigma_{11} \text{ and } \sigma > \sigma_{33}$$

It should be noted that the lineshape is discontinous at $\sigma = \sigma_{22}$.

2. The lineshape of an axially symmetric tensor

If two of the three components are equal, the tensor is said to be axially symmetric. Let $\sigma_{11} < \sigma_{22} = \sigma_{33}$, and $\sigma_{\parallel} = \sigma_{11}$, $\sigma_{\perp} = \sigma_{22} = \sigma_{33}$. The parameter k (in equation 52) will equal 0 for all σ and the value of the elliptic integral will become constant ($= \pi/2$) for all σ.

Equation 53 will then reduce to:

$$N(\sigma) \; \alpha \; [(\sigma_\perp - \sigma)(\sigma_\perp - \sigma_\parallel)]^{-\frac{1}{2}} \qquad (55)$$

which is the equation for the lineshape of an axially symmetric

tensor with $\sigma_\parallel < \sigma_\perp$.

Similarly, let $\sigma_{11} = \sigma_{22} < \sigma_{33}$ and let $\sigma_\perp = \sigma_{11} = \sigma_{22}$ and

$\sigma_\parallel = \sigma_{33}$. Equation 54 will reduce to:

$$N(\sigma) \; \alpha \; [(\sigma_\parallel - \sigma_\perp)(\sigma - \sigma_\perp)]^{-\frac{1}{2}} \qquad (56)$$

which is the equation for the lineshape of an axially symmetric

tensor with $\sigma_\perp < \sigma_\parallel$.

3. The lineshape of an isotropic tensor

If all three tensor components are equal, the tensor is

called isotropic. In this case:

$$\sigma_{iso} = \sigma_{11} = \sigma_{22} = \sigma_{33}$$

In such a case, the lineshape will have only one point and will

be discontinuous there--mathematically, a delta function.

Then:

$$N(\sigma) = \infty \quad \sigma = \sigma_{iso} \qquad (57)$$
$$N(\sigma) = 0 \quad \sigma \neq \sigma_{iso}$$

4. Broadening of the theoretical lineshapes and graphical convolution

The lineshapes predicted by equations 53-57 are ideal and

are not observed experimentally--simply because the time waveform

(Free Induction Decay, FID), whose Fourier Transform produces

the observed lineshape, must have a finite time duration. Some

phenomena that shorten the lifetime of the FID are the residual dipolar or quadrupolar relaxation mechanisms present in the chemical system, lifetime or T_1 broadening, magnetic field inhomogeneities, noise, etc.

These phenomena can be accounted for by multiplication of the ideal FID, which is the inverse Fourier Transform of the theoretical lineshape, by a decaying exponential. A first-order decay is called Lorentzian; a second-order decay, Gaussian. Multiplication of two functions in the time domain is identically equivalent to convolution (24) of the Fourier Transforms of the two functions in the frequency (or shift) domain. The broadening function of a Lorentzian line of full width at half height, W, may be written:

$$L(\sigma) \propto W(\frac{W^2}{4} + \sigma^2)^{-1} \tag{58}$$

Similarly for a Gaussian line of full width at half height, W, the broadening function may be written:

$$L(\sigma) \propto W^{-1} e^{-4\ln 2 (\frac{\sigma}{W})^2} \tag{59}$$

The convolution of theoretical lineshape, $N(\sigma)$, with the broadening function, $L(\sigma)$, may be written:

$$\int_{\sigma_{11}}^{\sigma_{33}} N(\sigma') L(\sigma - \sigma') d\sigma' = N(\sigma) * L(\sigma) \tag{60}$$

The convolution integral (equation 60), while sometimes very difficult to evaluate algebraically, is simple to evaluate

numerically on a computer (41). The numerical convolution
technique will allow the use of complicated broadening functions
which may be unsymmetric.

Graphical, or numerical, convolution can be regarded as a
"translating, multiplying and summing" process. An explicit
example of this technique is shown in Figures 34 and 35. The
function, $N(\sigma)$, may be considered a Powder-Pattern-like lineshape.
The function $L(\sigma)$ may be regarded as the lineshape of a broadening-
like function. $N(\sigma) * L(\sigma)$ is the graphical convolution of $N(\sigma)$
and $L(\sigma)$. The complete stepwise process of graphical convolution
similar to one described by Roden (24) is shown in Figure 35.

A brief description of the process follows. First, the
convoluting function $L(\sigma')$ is reflected $(-\sigma')$ through the
vertical axes. There will be no apparent change since $L(-\sigma')$
is symmetric about this axis. Next $L(\sigma - \sigma')$ is offset as a
function of the parameter, σ, until neither $N(\sigma')$ nor $L(\sigma - \sigma')$
overlap. Finally $L(\sigma - \sigma')$ is swept in the direction of increasing
σ' by increasing the value of σ. For each σ, the two functions
are multiplied and the area under the product curve is measured.
Each area value produces one point, as a function of σ, in the
convoluted function, $N(\sigma) * L(\sigma)$. The size of the increment
of σ can be made as small as required to produce enough points
to draw a smooth curve. The nine points generated by the graphical
convolution of Figure 35 are plotted as the convolution,
$N(\sigma) * L(\sigma)$, in Figure 34.

The technique of graphical convolution is relatively easy
to perform on a computer where $N(\sigma)$ and $L(\sigma)$ would be represented
as point-wise, continuous functions with a sufficient number of
points so that numerical integration (summing) techniques can
be used to calculate areas--resulting in very smooth, point-wise
convolutions.

An interesting result of convolution--which can be seen
in Figure 35--is that each frequency (or shift) in the convoluted
lineshape receives a weighted contribution from all frequencies
(or shifts) in the original lineshape, $N(\sigma)$. The broadening
function determines the weighting. Also, convolution results
in a smoothing of the "sharp corners" and "needle-like peaks"
of the theoretical lineshapes, $N(\sigma)$ and $L(\sigma)$.

The effects of increasing the full width of the broadening
function are shown in Figure 46 (non-symmetric tensor, Gaussian
broadening) and in Figure 47 (axially symmetric tensor, Lorentzian
broadening). The appearance of the lineshape is affected differently
by the imparted character of the convoluted broadening function.
For equivalent full widths, a Gaussian broadening function will
produce "rounded peaks" and "short tails"; whereas, a Lorentzian
broadening function will produce somewhat "more pointed peaks"
and "longer tails".

The anisotropy $(\sigma_{33} - \sigma_{11}$ or $\sigma_\perp - \sigma_{\parallel})$ of both tensors is
29 ppm (parts per million). For Curves A of Figures 46 and 47,
the full width of the broadening function is much less than the

CURVE	FULL WIDTH (PPM)	SCALE
A	0.70	X0.5
B	3.54	X1.0
C	7.10	X1.0
D	14.2	X1.0

NON-SYMMETRIC LINESHAPE

$\sigma_{11} = {}^-10 \qquad \sigma_{22} = 0.0 \qquad \sigma_{33} = 19.0$ PPM

vs.

FULL WIDTH OF GAUSSIAN BROADENING FUNCTION

DISCONTINUITY AT $\sigma_{22} \propto 1.5$

AMPLITUDE

SHIFT (PPM)
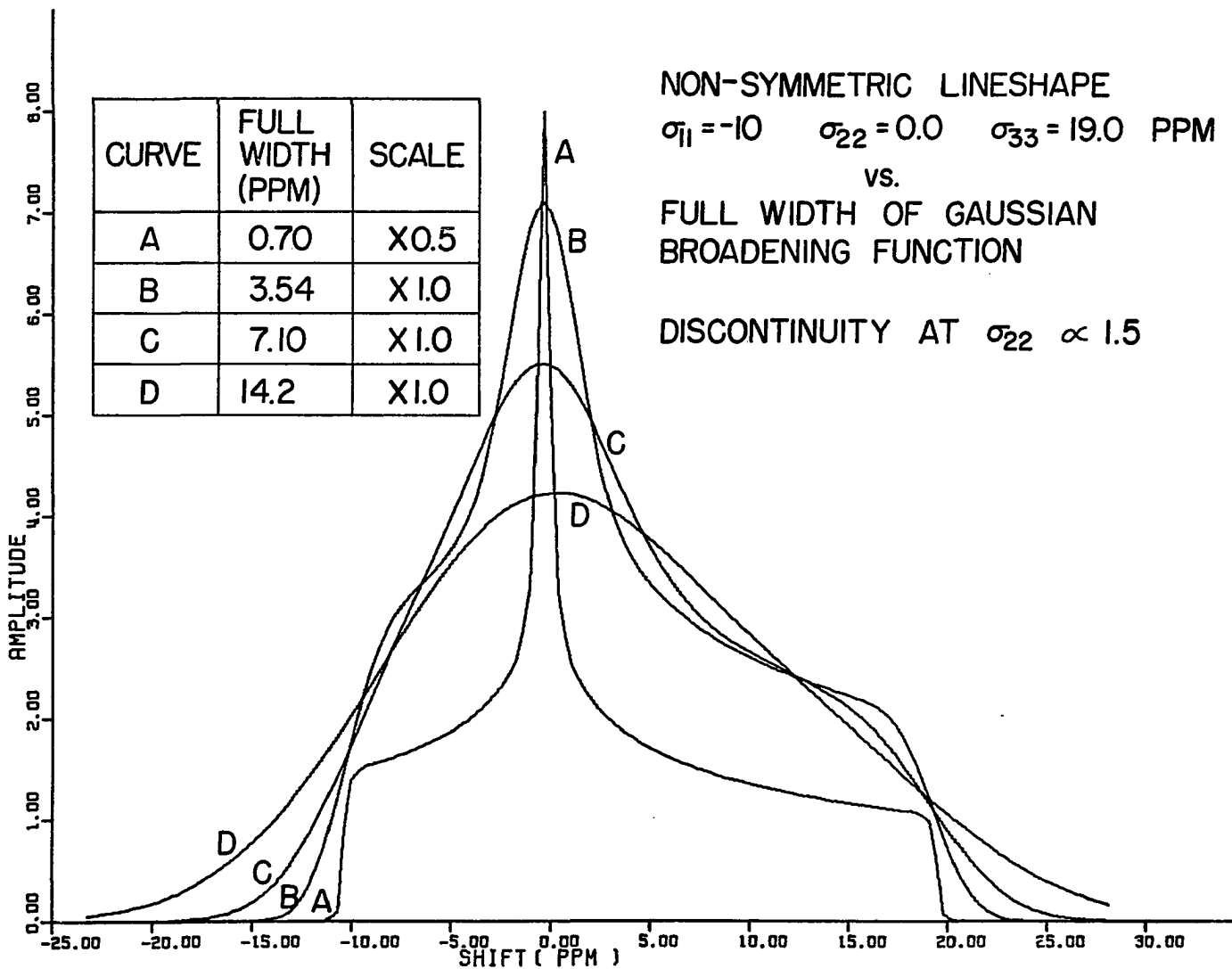
Figure 46. The lineshape of a non-symmetric shift tensor broadened by a Gaussian
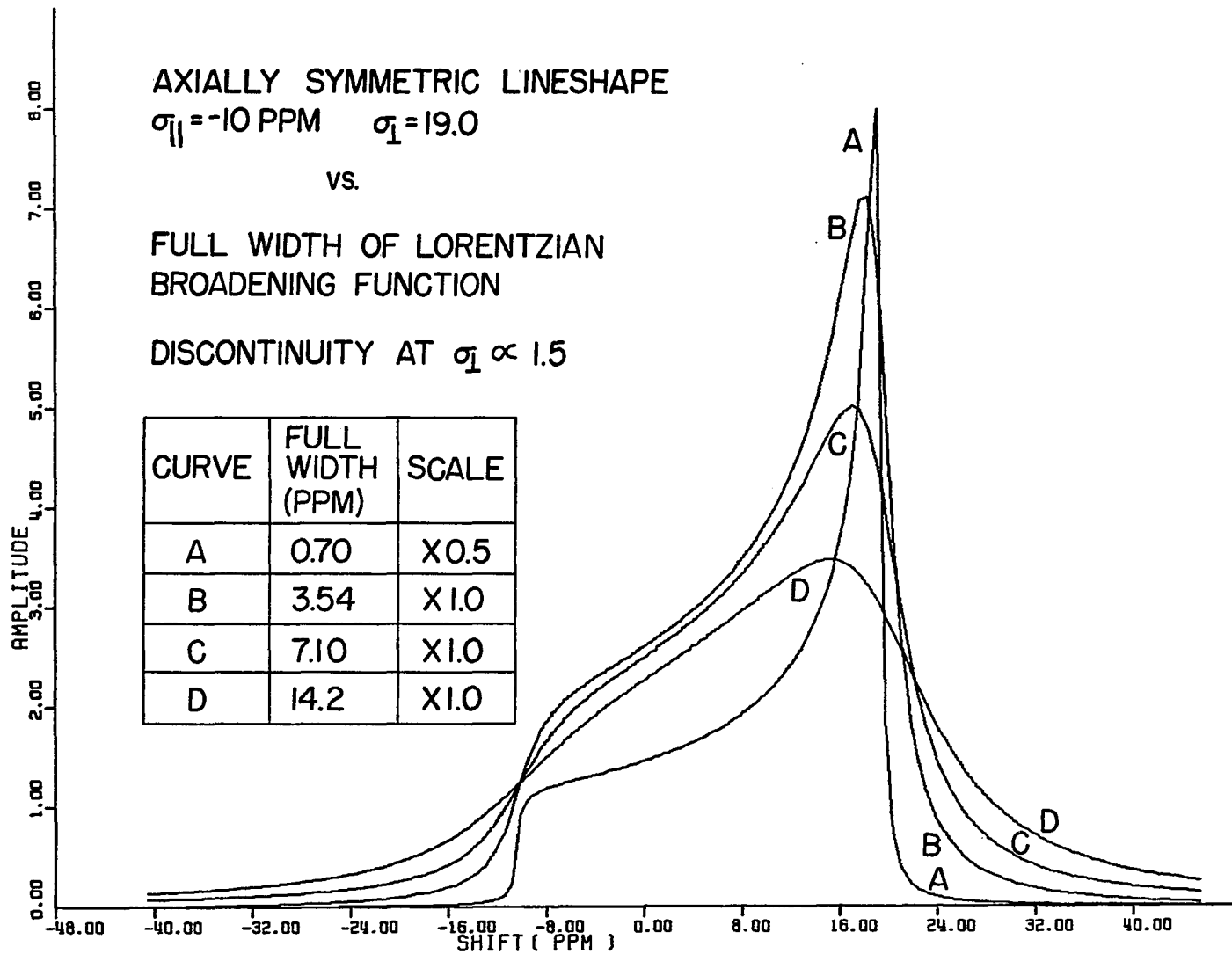
Figure 47. The lineshape of an axially symmetric shift tensor broadened by a Lorentzian

anisotropy (0.7 << 29 ppm) and the lineshapes look very much

like theoretical ones. However as the width of the broadening

function increases, the spectral features, "sharp peaks and

corners", associated with the tensor components begin to "smear

out". For curve D, the full width of the broadening function

is about one half of the anisotropy and already the lineshape

is starting to become "featureless".

A physical manifestation of this smearing process can be

seen in the lineshape of a solid where the static dipolar relaxation

mechanism is present. The observed lineshape can be regarded

as the convolution of the lineshapes of a theoretical tensor

and a broadening function, usually Gaussian, of enormously

large half width (10 or more times the anisotropy of the tensor).

The observed lineshape will be that of essentially a broad

Gaussian line with all tensor information being completely

"washed or smeared out".

In the case where the theoretical lineshape results from

an isotropic tensor (i.e. a "spike" or finite delta function),

convolution simply reduces to multiplying the broadening

function by a constant. The resulting lineshape will simply

be that of the convoluted broadening function.

5. The discontinuity in the theoretical lineshape

As has been shown above the theoretical lineshape is

discontinuous at σ_{22} (non-symmetric tensor), $\sigma_{\perp}$ (axially symmetric

tensor) and σ_{iso} (isotropic tensor). Of course, experimentally this discontinuity is never observed as other physical effects (3) cause the value at this shift to become finite. Figure 48 graphically reveals how assigning a finite value to this discontinuity effects the appearance of a theoretical non-symmetric lineshape convoluted with a Gaussian broadening function. A discontinuity equal to 1.0 means that the finite value of the discontinuity is approximately equal to the largest value of the points used to generate the theoretical lineshape before convolution with the broadening function. A discontinuity equal to 10.0 means that the finite value of the discontinuity is ten times the largest value of the points, etc.

As the value of the discontinuity increases, the theoretical lineshape will approach a delta function ("spike") so that the convoluted lineshape will take on the appearance of the broadening function--in this case, a Gaussian. For values such as 20.0 the lineshape begins to resemble two overlapping Gaussian peaks. For larger values only one Gaussian will predominate.

C. Fourier Transforms of Non-Quadrature Signals and Folding

The Powder Pattern is usually an unsymmetric lineshape. Its appearance in a frequency spectrum generated by a Fourier Transform is sensitive to the offset of the spectrometer when a non-quadrature signal is transformed.
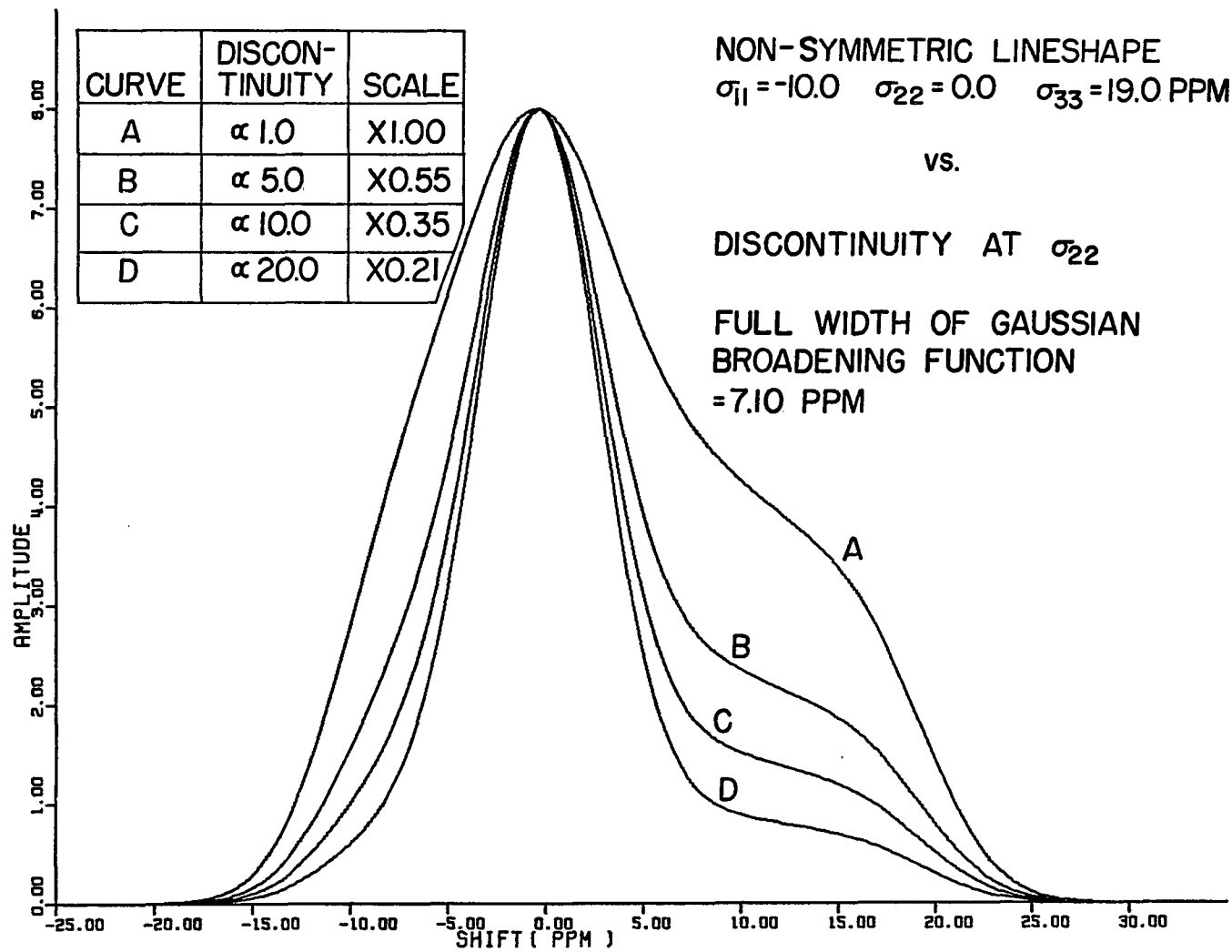
Figure 48. The effect of the discontinuity on the lineshape of a non-symmetric shift tensor

An example of a Fourier Transform performed on a quadrature signal is shown in Figure 49a. The transform was made via a computer with a Fast Fourier algorithm written by Bloomfield (26). It should be particularly noted that when a quadrature signal is transformed both positive and negative frequencies are unique. However, for non-quadrature signals (i.e. only a real or imaginary component), the sensitivity to the sign of the frequency is lost and all frequencies "fold over" with spectral amplitudes reduced by a factor of two.

This phenomenon results in a frequency spectrum which is an even function of frequency for an absorption (i.e. real FT) and an odd function of frequency for a dispersion (i.e. imaginary FT). The additional lines that would appear in the real FT are shown as dotted lines in Figure 49a. Of course, the ability to distinguish positive and negative frequencies is lost.

If a non-quadrature signal is to be transformed, the offset of the spectrometer must be carefully set so that all frequencies have the same sign. With a positive offset, all spectral information lies on the negative frequency axis, so it will "fold over" and show up on the "positive" frequency axis. For such an offset the "positive" axis is actually a negative axis which decreases in the direction of increasing magnitude.

No such folding will occur for a negative offset since all frequency information lies on the positive frequency axis.

FAST FOURIER TRANSFORM

TWO-COMPONENT DECAY
(GAUSSIANS)

	1st	2nd
AMPL.	5.0	3.0
FREQ.	-500.0	1000.0 Hz
PHASE	0.0	0.0°
T_2	3.9	3.9 mSEC

REAL TIME-DATA

QUADRATURE (COMPLEX) DATA

IMAG. TIME-DATA

F
F
T
4096
points

REAL FFT
X 138

- - - - ALIASES FOR
NON-QUADRATURE
TIME DATA

IMAG. FFT
X 138

ALIASES
NOT SHOWN
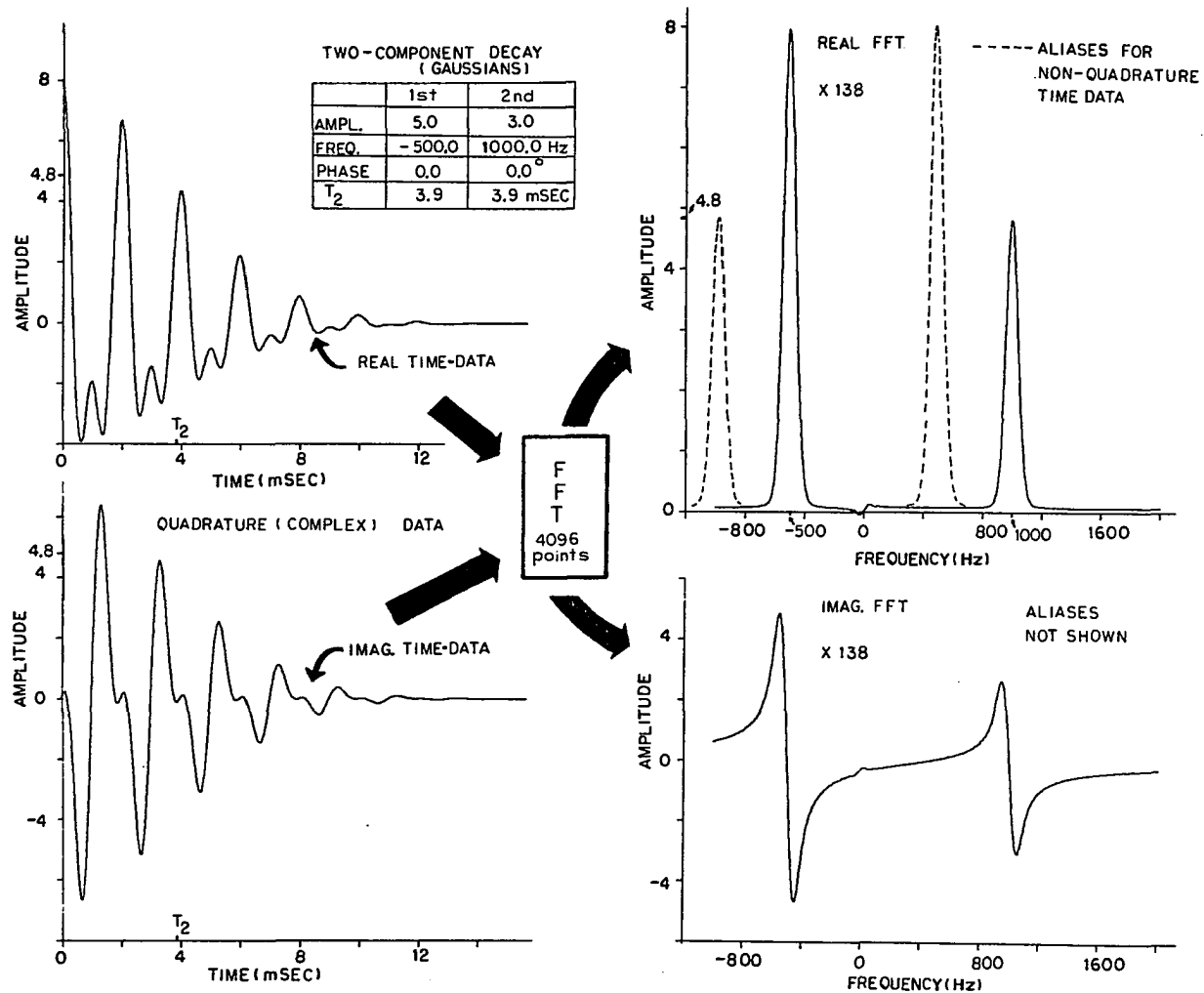
Figure 49a. An example of a Fourier Transform of a quadrature signal

Of course, noise will still "fold over". Figure 49b pictorally demonstrates the folding process for a Powder Pattern.

The above discussion on folding refers to folding which occurs from the loss of the sign of the frequency. The FID whose FT yields the Powder Pattern of Figure 49b is assumed to be sampled with an infinitesmal sampling time (or infinite sampling rate). Thus, the Nyquist frequency is infinite and no aliased Powder Patterns will appear from sampling-rate folding.

When "fold over" occurs, the Powder Pattern will reflect itself as its mirror image. This property is useful when "checking" that the lineshape's anisotropy is real and not an instrumental artifact. This technique was used to verify the authenticity of the large anisotropy of the Powder Pattern of ^1H in $ZrClH_{1.0}$ discussed in Chapter VII.

FOLDING

ABSOLUTE FREQ (MHz)

14.0000   14.0010   14.0020

negative
offset

RELATIVE FREQ (Hz)

0   1000.0   2000.0

positive
offset

fold-over

reversed
image

-800.0   -200.0   0   200.0   800.0   observed
RELATIVE FREQ (Hz)   (-200.0)   (-800.0)   actual
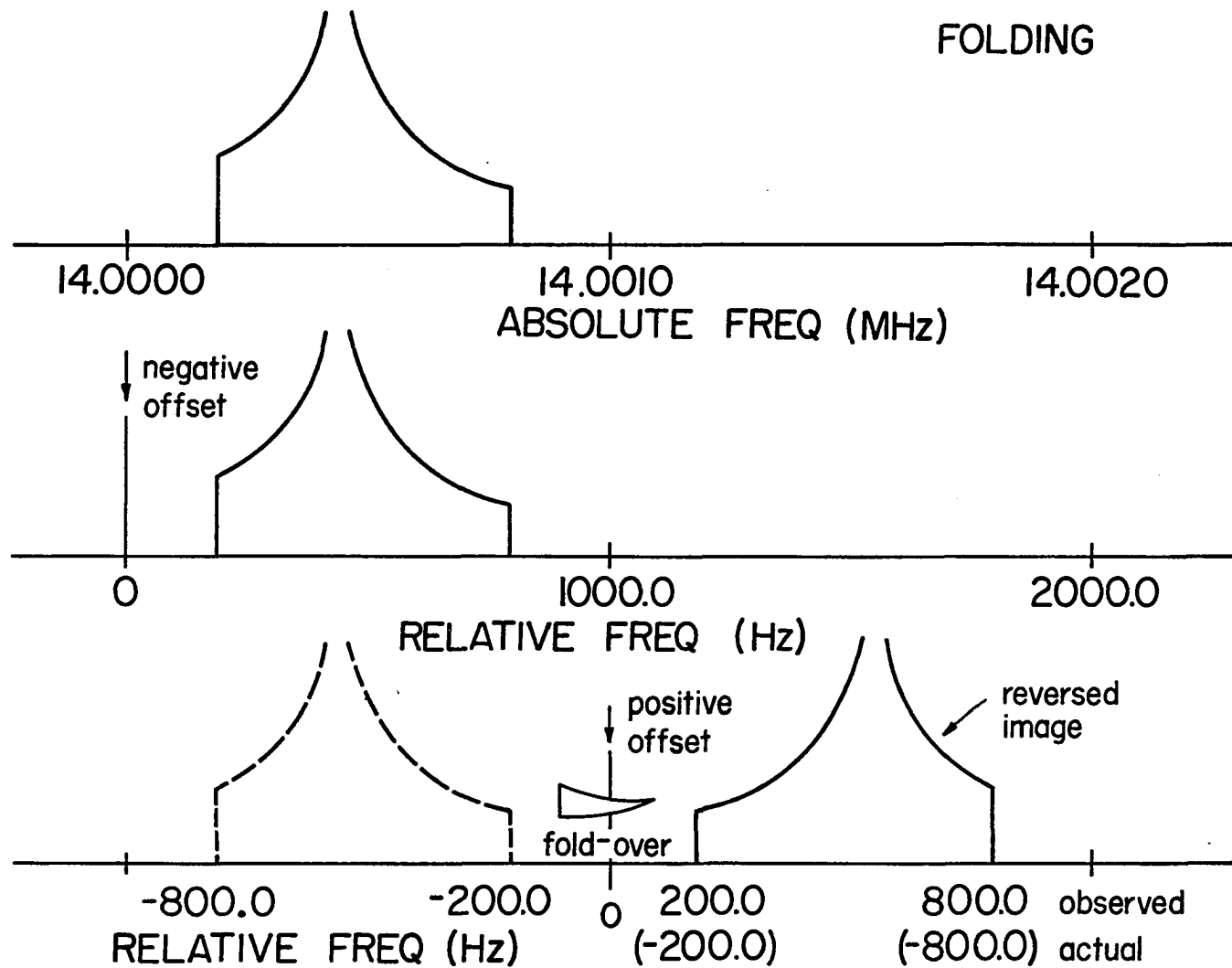
Figure 49b.   An example of folding and reversal of a Powder Pattern

131

VII. STUDIES OF ^{1}H IN ZIRCONIUM HALIDE HYDRIDES: NMR SHIELDING TENSORS

A. Introduction

The compounds: ZrCl and ZrBr (44-46) possess interesting physical and chemical properties. Both powders have high reflectivity and cleavage properties similar to graphite. These compounds are ductile and can be pressed to 97% of their X-ray densities of 4.68 g/cm^3 (ZrCl) and 5.71 g/cm^3 (ZrBr). These pellets have a low electrical resistance and hence these compounds are termed "metallic salts". This electrical behavior is consistent with the presence of a substantial density of occupied states at the Fermi level which indeed X-ray photoelectron spectra have established (44). The melting temperatures are in excess of 1100°C and are indicative of the strong metal-metal bonding character of these compounds.

The structures of ZrCl and ZrBr are indicated in Figure 50. The space groups are rhombohedral, R$\bar{3}$m (actually, trigonal indexed on hexagonal axes), and each structure consists of two dimensional, four-layered sandwiches made up of a double layer of zirconium with a sheet of halide above and below (see Figure 50). The metal-metal separation between the zirconium bilayers in the chloride is 3.09 Å and 3.42 Å within each close packed layer. In the bromide, the corresponding separations are 3.13 Å and 3.50 Å. The primary unit or building block for
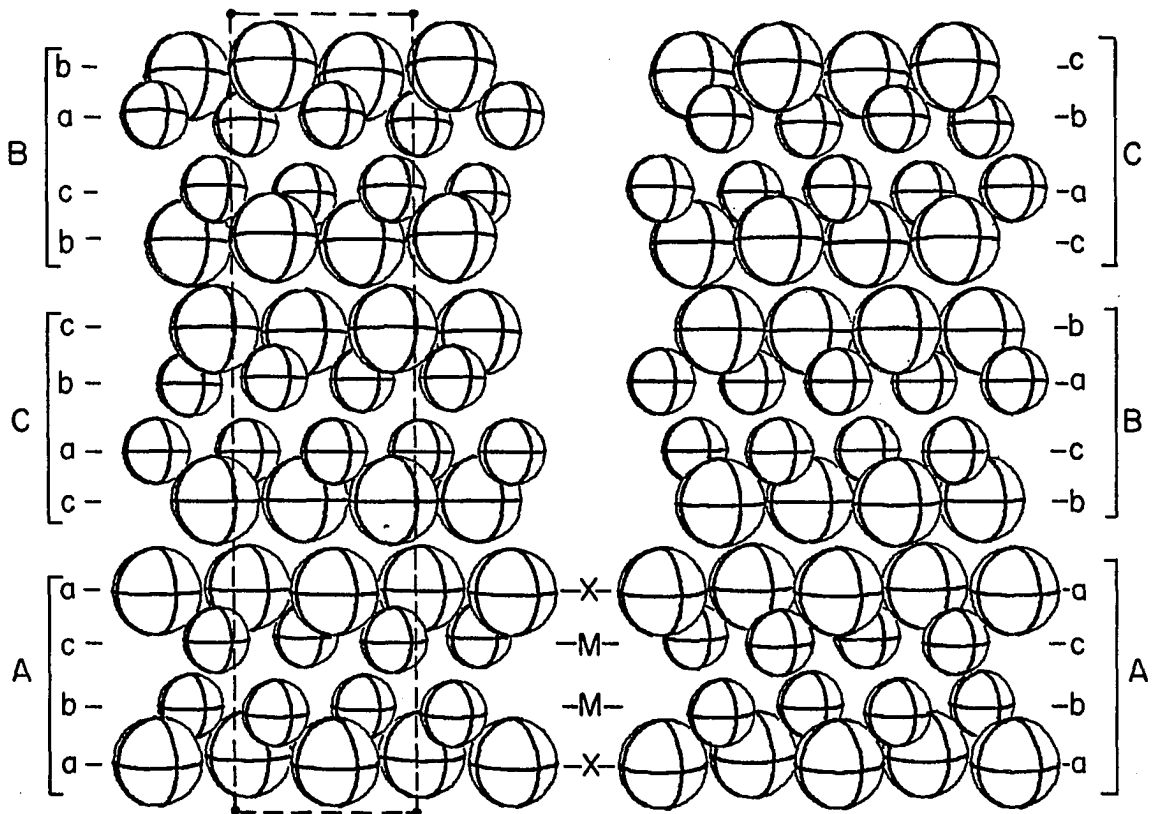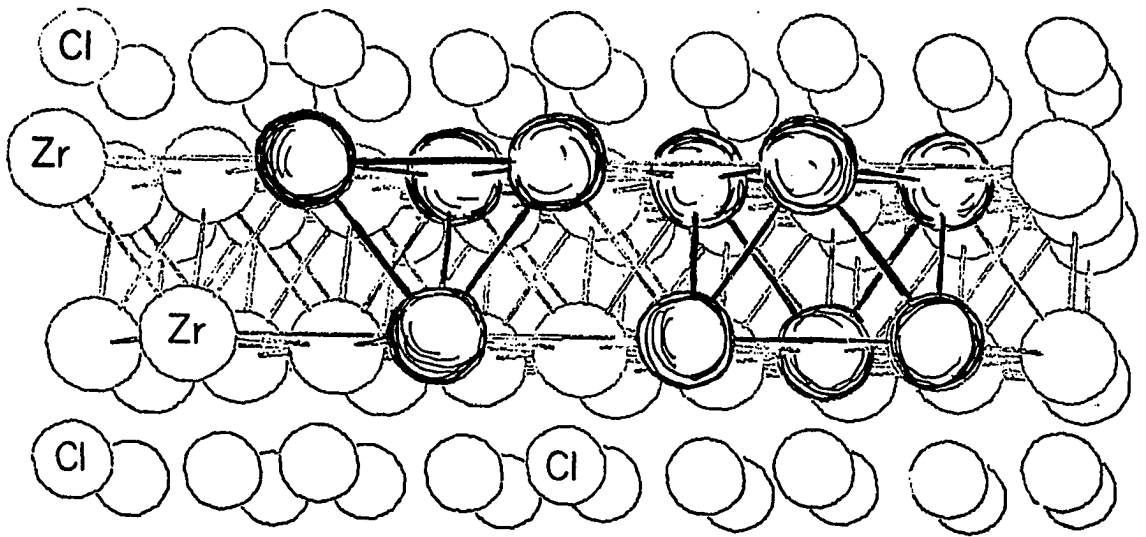
Figure 50.   The structure and stacking patterns of the zirconium halides

each crystal is the four-layered sandwich. Additionally, there is secondary order in the stacking of these sandwiches.

The presence of second nearest neighbor interactions between Br and Zr layers of the same orientation in adjoining slabs is believed responsible for the greater hardness and the absence of graphite-like structural damage which ZrCl exhibits. For this reason, these sandwiches are believed (44) stacked in an ACB pattern (ZrBr) and a ABC pattern (ZrCl) (See Figure 50). The zirconium halide, ZrX (X = Cl, Br), forms two hydrides, $ZrXH_y$ (y = 1.0, 0.5), which are stable with respect to disproportionation to $ZrH_2(s)$ and $ZrX_2(s)$ (or $Zr + ZrX_4(s)$). Upon hemi-hydride formation, the color changes to a darker grey. Upon full hydrogen absorption, the color changes from grey to brass (ZrCl) and grey to bronze (ZrBr).

The ^{1}H in $ZrXH_y$ is believed to insert into the metal-metal double layer from the following facts: thermodynamic measurements are characteristic of a compound or phase which has a Zr-H bonding strength comparable to the binary zirconium hydride, ZrH_2. The results of X-ray powder diffraction indicate little structural distortion after ^{1}H intercalation. Finally, the zirconium bilayers have electron-rich interstitial spaces which can be classified as either "octahedral-like" or "tetrahedral-like" (See Figure 50). There are 1/2 octahedral hole and 1 tetrahedral hole per XrCl unit.

Hwang et al. (47) have made broad line NMR measurements on ^{1}H in the ZrXH$_y$'s in the temperature range $77 \leq T \leq 450$K. At temperatures sufficient for motional narrowing, they have observed axially symmetric lineshapes for ZrClH$_{1.0}$ ($\Delta\sigma = 81.0$ ppm) and for ZrClH$_{0.5}$ ($\Delta\sigma = 75.1$ ppm). Furthermore, they reported a two stage behavior for the line narrowing in both hemi-hydrides. Second-moment calculations produce good agreement with experimental values if the protons are assumed to reside mainly in tetrahedral holes in ZrClH$_{1.0}$ (4% octahedral) and ZrBrH$_{1.0}$ (6% octahedral). Of course, no structural change upon ^{1}H intercalation is assumed. Unfortunately, the assignment of protons to specific sites in the hemi-hydrides was not completely unambiguous.

Hwang et al. (47) have proposed at least three models to explain the observed second moments in ZrBrH$_{0.5}$ and ZrCl$_{0.5}$. Model I assumes that alternate "strings" of tetrahedral holes are occupied with 5.6% octahedral occupation in the ZrBrH$_{0.5}$ and 2.5% octahedral occupation in the ZrClH$_{0.5}$. Model II assumes predominate occupation of tetrahedral holes with 5-7% of the octahedral sites occupied. Model III assumes predominate occupation of octahedral sites with about 12% of the tetrahedral sites occupied. All three models generate second moments which agree with experimental values.

The purpose of the present work is to investigate the shielding anisotropies of these compounds and the possible locations of ^{1}H species, particularly in the zirconium halide

hemi-hydrides, $ZrXH_{0.5}$. Multiple-Pulse techniques (33-36)
are used for homonuclear decoupling to remove static dipolar
broadening. Values of the shielding anisotropies thus obtained
are more amenable to direct interpretation than those obtained
in the temperature ranges where motion is sufficient to remove
dipolar broadening and to partially average the shielding
anisotropies.

The material in this Chapter is a slightly expanded version
of two publications (48, 49).

B. Discussion of Multiple-Pulse Homonuclear Decoupling

The repetitive cycles of Multiple-Pulse experiments are
designed (28, 32-37) such that in zeroth-order approximations,
the static dipolar and quadrupolar Hamiltonians are averaged to
zero while the chemical shift Hamiltonian is retained but
normally scaled (38). Additionally, the order and locations
of pulses are chosen to minimize extraneous errors introduced
by the RF pulses (36).

The techniques of Multiple-Pulse homonuclear decoupling
were originally introduced by Ostroff and Waugh (30) and pioneered by
Waugh et al. (32), Haeberlen and Waugh (37) and Rhim et al. (35, 36).
Three dipolar-decoupling pulse sequences have received the
most use: the WAHUHA-4 (32), the HW-8 (37) and the MREV-8
(33-36) . The MREV-8 has been shown (36, 2) to possess slightly
more favorable properties than both the WAHUHA-4 and HW-8.

The MREV-8 has been used to remove the static ^{1}H dipolar coupling in the experiments described in this Chapter.

Multiple-Pulse cycles are strange "beasts" indeed. Figure 51 shows the MREV-8 Pulse sequence. A preparation pulse is followed by a series of eight pulses which is repeated n times. All RF pulses are denoted by P_i and indicate a $\pi/2$ rotation about the i axis of the rotating frame. The series of RF pulses are specifically designed to manipulate the magnetic moment, M, in such a way that for cycle frequencies, $1/t_c$, which are fast compared to a given interaction, such as the static dipolar coupling and chemical shift, expressed in units of frequency, the moment will "see" only the cycle-average of these interactions.

The choice of spacings (i.e. τ) and phases of the RF pulses insures that the cycle-average of the static dipolar coupling is zero. Simultaneously, the chemical shift interaction is scaled by $\sqrt{2}/3$ (35, 36, 2). The restrictive condition which guaranties "effective" averaging (commonly called the Magnus Condition) is:

$$t_c \left\| H_{int} \right\| \ll 1 \tag{61}$$

$\left\| H_{int} \right\|$ signifies the appropriate interaction expressed in the units of Hertz. Since static dipolar interactions are typically of the order of 40 KHz, then cycle times less than 25 μ seconds are usually required. An additional restriction which arises from the Nyquist Sampling theorem (26) is

$$t_c \geq \frac{1}{2f_{max}} \tag{62}$$

MREV-8 PULSE
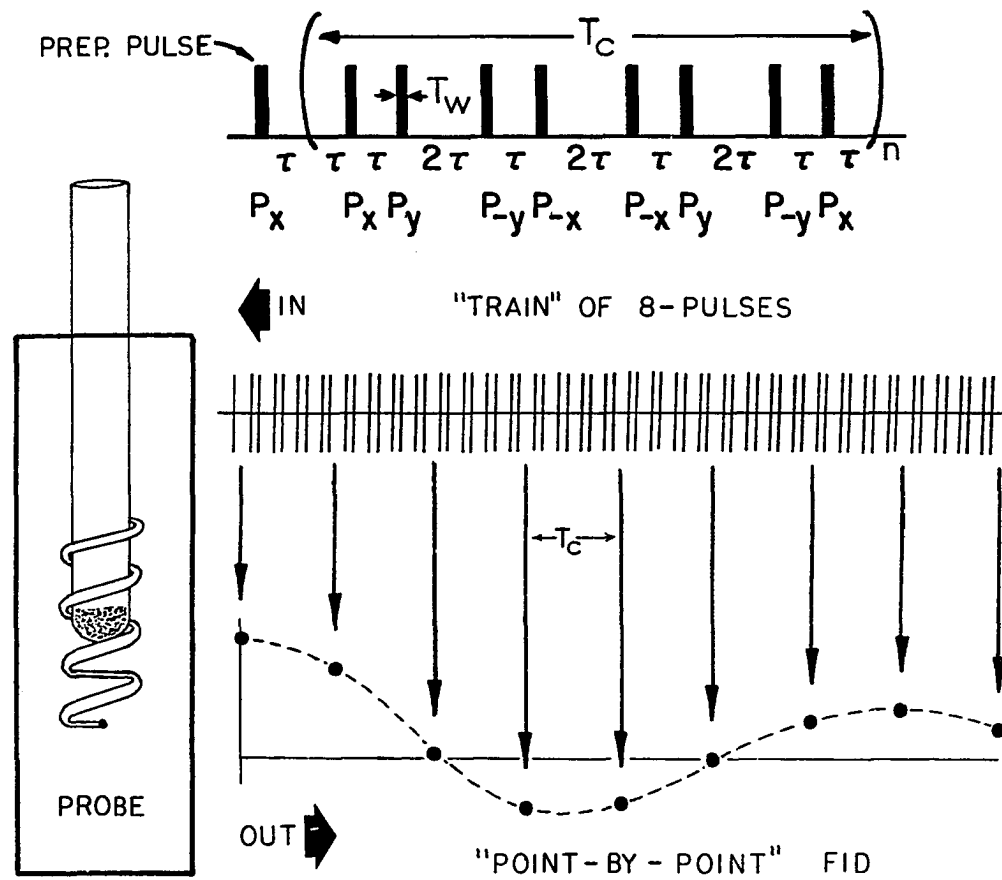
Figure 51. The MREV-8 pulse sequence and the synthetic, "point-by-point" FID

Here, f_{max} is the maximum frequency of the scaled chemical

shift and offset expressed in Hertz.

For cycle times of 25 μ seconds, the maximum allowable

offset is enormous, i.e. 20 KHz. However, for longer cycle

times, the allowable offset is reduced accordingly.

A large train of MREV-8 pulses irradiates the sample as

shown in Figure 51. Following each group of eight pulses, the

magnetization is sampled once along the Y phase to generate

one point of the "point-by-point" FID. This sampling is repeated

n times, such as n = 2048, to produce a data set which is

Fourier-Transformed into a typical Powder Pattern as discussed

in detail in Chapter VI. The time decay under Multiple-Pulse

experiments can be seen to originate in an entirely different

manner than the FID of a conventional single-pulse experiment

shown in Figure 30.

In-depth developments of the fundamental theories, such

as Coherent Averaging and Average Hamiltonian Theory, have

been presented by many authors (2, 28, 33-37, 39, 50-52).

Consequently, the repetition of such arguments will be avoided

in favor of an intuitive application of Average Hamiltonian

Theory using the MREV-8 pulse.

Figure 52 illustrates an application of Average Hamiltonian

Theory (AHT). The theory has been used to demonstrate that

$\bar{H}_{dip}^{(0)} = 0$ (also $\bar{H}_{dip}^{(1)} = 0$) and $\bar{H}_{shift}^{(0)} = \frac{\sqrt{2}}{3} I_{-101}$ for the MREV-8

STATIC HAMILTONIAN

$$H_z$$

MREV-8

$U_X H_Z U_{\bar{X}} = H_Y$ $U_X U_Y H_Z U_{\bar{Y}} U_{\bar{X}} = H_{\bar{X}}$ $U_X H_Z U_{\bar{X}} = H_Y$ $U_{\bar{X}} H_Z U_X = H_{\bar{Y}}$ $U_{\bar{X}} U_Y H_Z U_{\bar{Y}} U_X = H_{\bar{X}}$ $U_{\bar{X}} H_Z U_X = H_{\bar{Y}}$

"MOVING" HAMILTONIAN

| τH_Z | τH_Y | $2\tau H_{\bar{X}}$ | τH_Y | $2\tau H_Z$ | $\tau H_{\bar{Y}}$ | $2\tau H_{\bar{X}}$ | $\tau H_{\bar{Y}}$ | τH_Z |
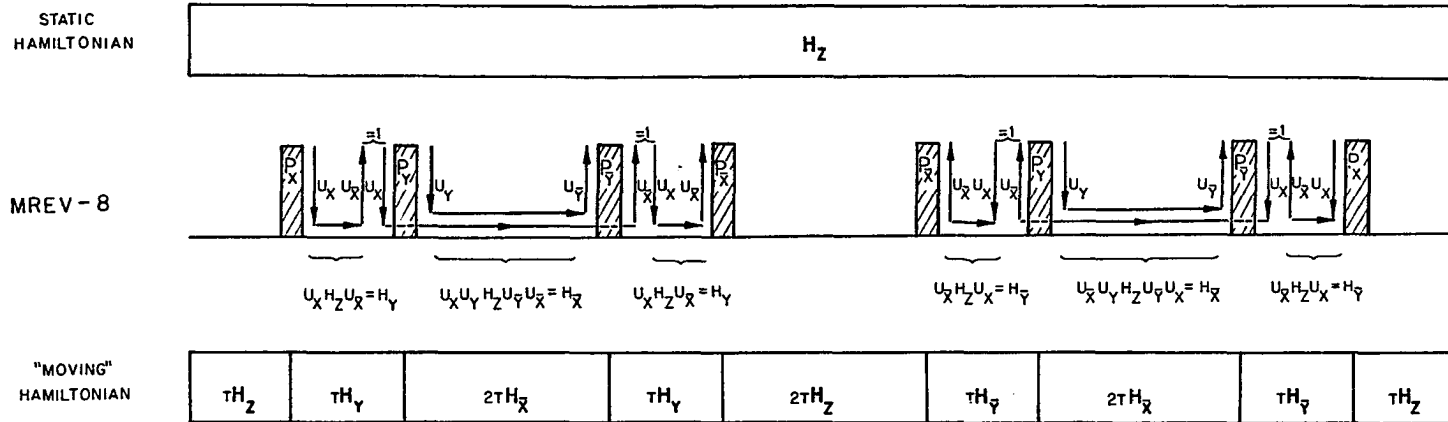
AVERAGE HAMILTONIAN

$$\bar{H}^{(0)} = \frac{1}{12\tau}\left[4\tau H_{\bar{X}} + 2\tau H_Y + 2\tau H_{\bar{Y}} + 4\tau H_Z \right]$$

AVERAGE HAMILTONIAN

THEORY

$$H_{dipolar} \propto \vec{I}_1 \cdot \vec{I}_2 - 3I_{z1}I_{z2}$$

$$H_{shift} \propto I_z$$

$$\bar{H}^{(0)}_{dipolar} \propto \frac{1}{12}\left[12\vec{I}_1\cdot\vec{I}_2 - 12I_{x1}I_{x2} - 6I_{Y1}I_{Y2} - 6I_{Y1}I_{Y2} - 12I_{z1}I_{z2} \right] = 0 \qquad \bar{H}^{(0)}_{shift} \propto \frac{1}{12}\left[-4I_X + 2I_Y - 2I_Y + 4I_z \right] = \frac{1}{3}\left[-I_X + I_z \right] = \frac{\sqrt{2}}{3}I_{\dashv 01}$$

Figure 52. An example of the use of Average Hamiltonian Theory applied to the MREV-8

when the magnetization is sampled at multiples of the cycle time, t_c. The reader is referred to discussions by Mehring (2) and Haeberlen (28) for the rigorous mathematical formalism of AHT. The crux of AHT is the ability to group RF pulses together so that they perform unitary transforms of the static Hamiltonian, H_i, yielding a transformed Hamiltonian, $\tilde{H}$. Such "manipulations" are only valid if cycle times, t_c, are such that the Magnus Condition (equation 61) is true.

The static Hamiltonian is assumed proportional to I_z and is written as H_z in Figure 52. A $\pi/2$ unitary transform which can be associated with a pair of $\pi/2$ RF pulse of the "a" and "ā" phases is written.

$$\tilde{H} = U_a H_z U_{\bar{a}} \tag{63a}$$

with

$$U_a = e^{-i\ \pi/2\ I_a} \tag{63b}$$

and

$$U_{\bar{a}} = e^{+i\ \pi/2\ I_a} \tag{63c}$$

The mathematical form of equation 63a results in a clockwise rotation of the Hamiltonian around the "a" axis, if one were to look down the "a" axis in the direction of decreasing "a". This is also equivalent to a counter-clockwise rotation of the Hamiltonian if one were to look in the direction of increasing "a".

For example, if $H_z \propto I_z$ and $a = y$, then the $\pi/2$ unitary transform of H_z, $\tilde{H} = U_y H_z U_{\bar{y}}$, would rotate I_z to the $\bar{x}$ axis.

The transformed Hamiltonian would now be written as $\tilde{H} \propto I_{\bar{x}} \propto H_{\bar{x}}$. Pulses must be grouped together into the form of equation 63a in order to perform "manipulations" of the Hamiltonian. Therefore, when required, identity transforms of the form:

$$U_a U_{\bar{a}} = 1 \qquad (63d)$$

may be strategically inserted into the pulse sequence to allow terms of the form of equation 63a to be written.

Such identity transforms are required at four places in applying AHT to the MREV-8 (See Figure 52). After insertion into the sequence, the identity transforms are usually regrouped such that forms of two rotations:

$$U_x U_y H_z U_{\bar{y}} U_{\bar{x}} = \tilde{H}_{\bar{x}} \qquad (63e)$$

are generated.

The static Hamiltonian is often referred to as being "switched" by such transformations (2, 28). It "spends" a period of τ or 2τ as an "effective" operator before it is switched into another form. Only the cycle-average $(1/12\tau)$ is felt (at appropriate sampling points) by the spins if the Magnus Condition is statisfied, i.e., switching is relatively rapid compared to the interaction caused by the static dipolar Hamiltonian. It should be noted that the operator $\bar{I}_1 \cdot \bar{I}_2$ is invariant to rotations and the operator $I_{a1} I_{a2}$, $a = x, y, z$, is invariant to the sign of rotation.

C. Experimental

^{1}H NMR measurements at $f_o = 56.020$ MHz were made using a
spectrometer sketched in Figure 53. The locations of RF phases
with respect to a sinusoidal waveform and in the rotating frame
are described in Figure 54. All samples were supplied by
Arthur Struss of the Ames Laboratory of D.O.E. Their preparation
(44, 45) has been previously reported. Approximately, 0.14 g
of each powder was sealed in a 5 mm o.d. thin walled NMR tube
at a pressure of less than 10^{-5} torr. The NMR probe used a
standard tapped series-tuned design (See Chapter II) with a
5 mm i.d.x15 mm coil. The coil was wound such that RF field
gradients were minimized in the central region of the coil
where the samples were located. Longitudinal relaxation times,
T_1's, of roughly 2 seconds, estimated by rapid $\pi/2$ pulsing,
agree with those previously measured for protons in ZrXH.

The effective transverse relaxations were well-fitted by
Gaussian decays. Figures 55, 56, 57 and 58 show graphs of
the natural log of the amplitude of the FID (Free Induction
Decay) vs. time squared with the linear least squares fitted
Gaussian superimposed. The values of T_2^* obtained from the
slopes of these lines ($T_2^* = (2 \times SLOPE)^{-1/2}$), as well as the
stoichiometries related to the initial amplitudes of these
lines, along with the stoichiometries measured by $H_{2(g)}$
absorption (45) are listed in Table 2.

MULTIPLE - PULSE   SPECTROMETER
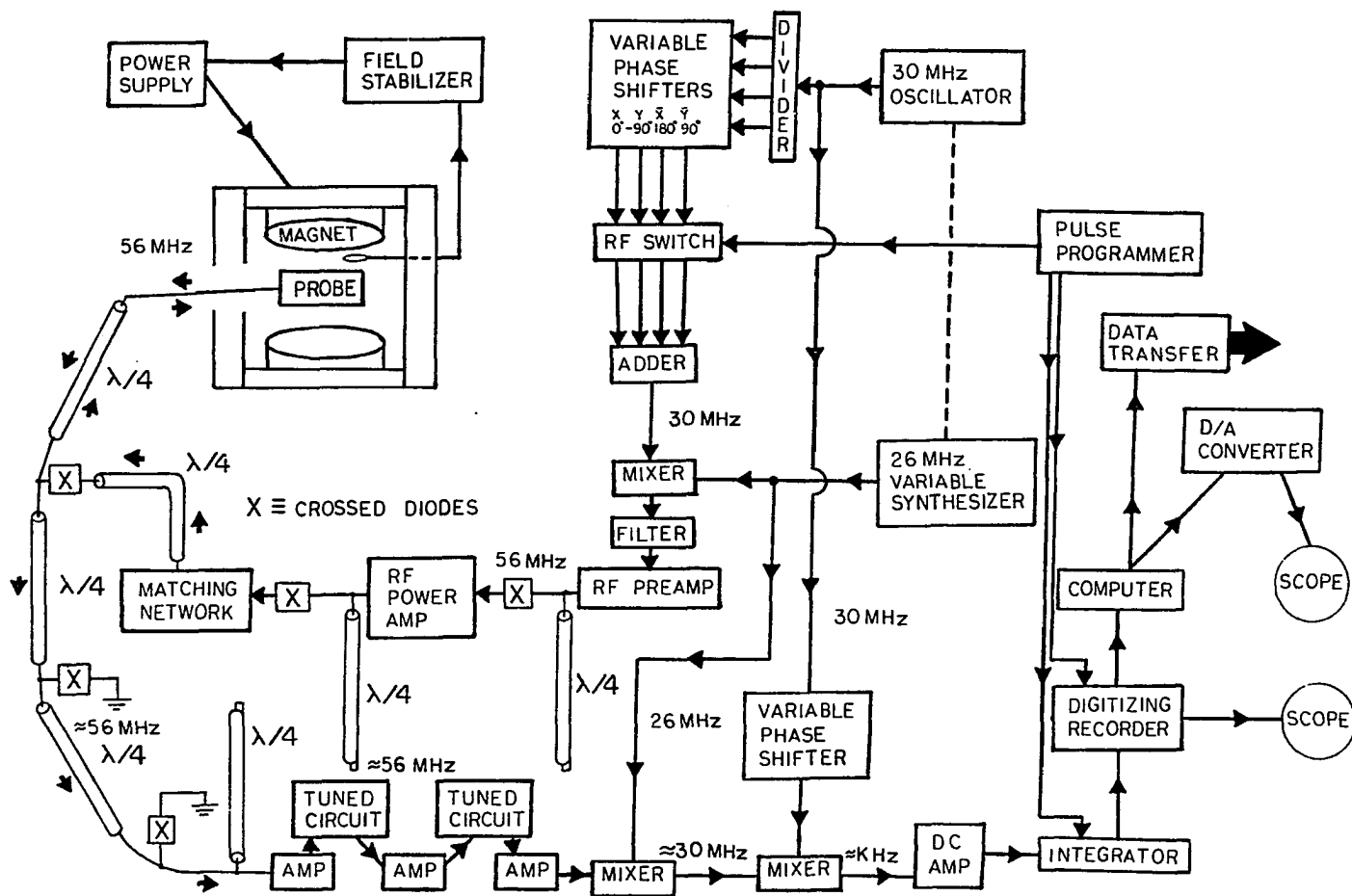
Figure 53.   A sketch of a ^{1}H Multiple-Pulse NMR spectrometer

X ← REFERENCE PHASE →

$2H_1$

CYCLE

ROTATING FRAME

Y PHASE

$\frac{1}{4}$ CYCLE DELAY

RF PHASES

$\pi/2$ RF PULSE

H_1

X PHASE

PROBE

FID

Y PHASE

MIXER + DC AMP

FID

"SCOPE"
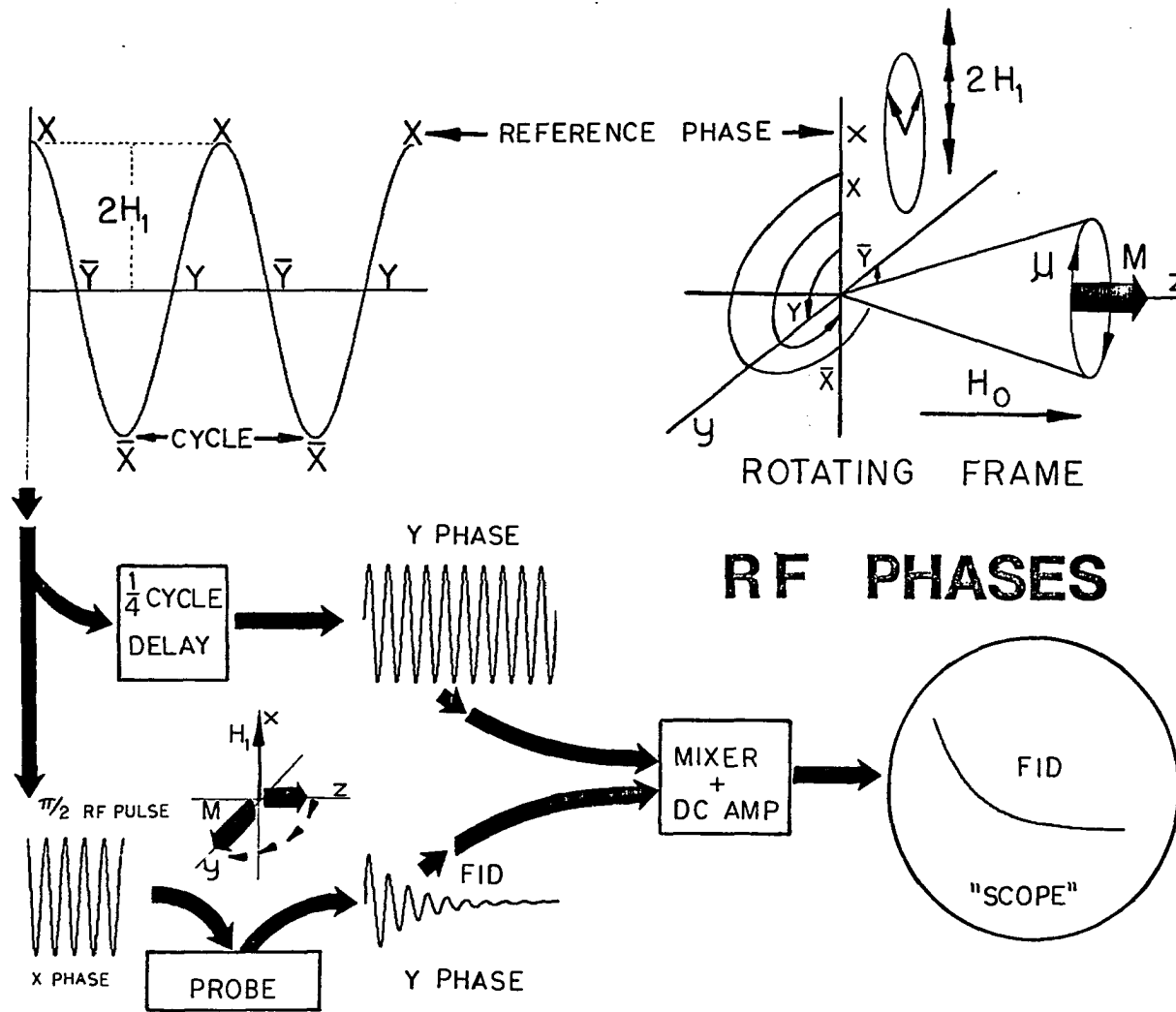
Figure 54. RF phases and mapping in the rotating frame
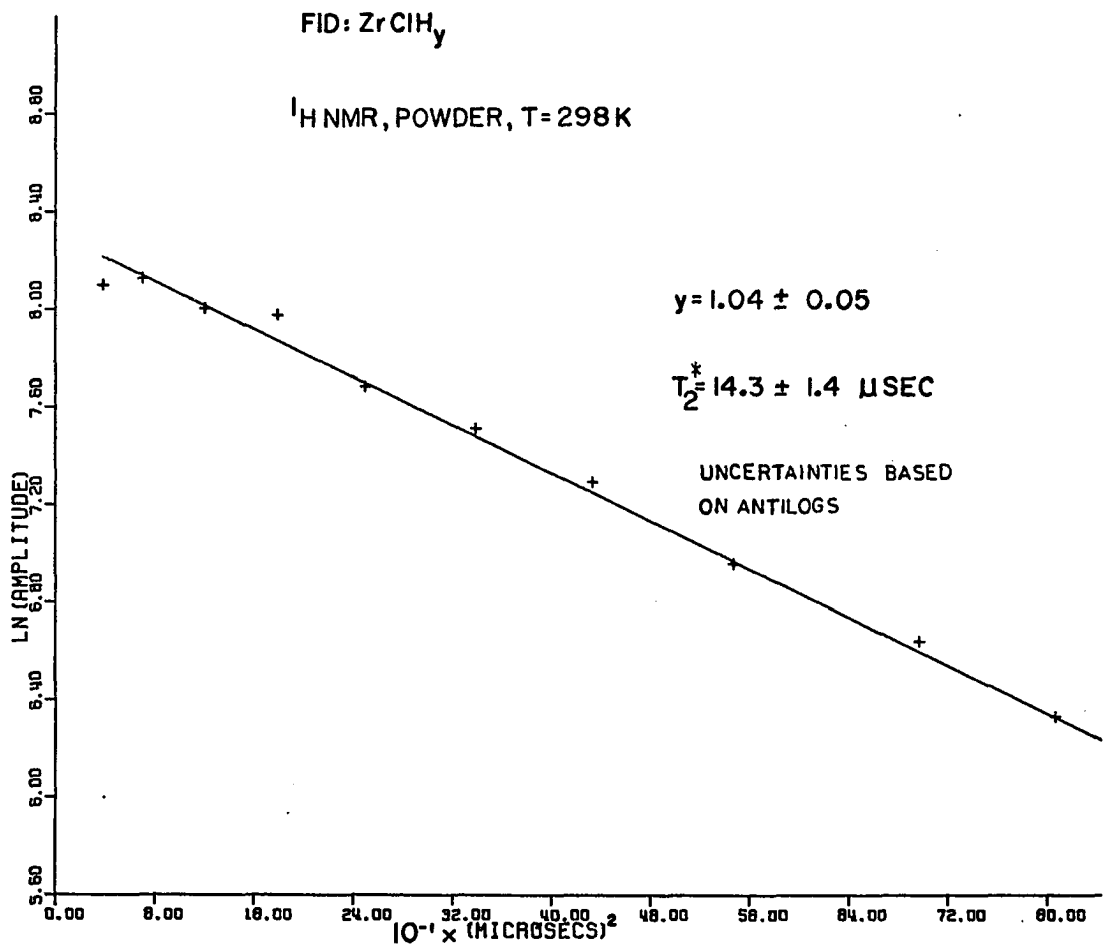
Figure 55. The natural log of the amplitude of the FID of
ZrClH$_{1.0}$ vs. time squared
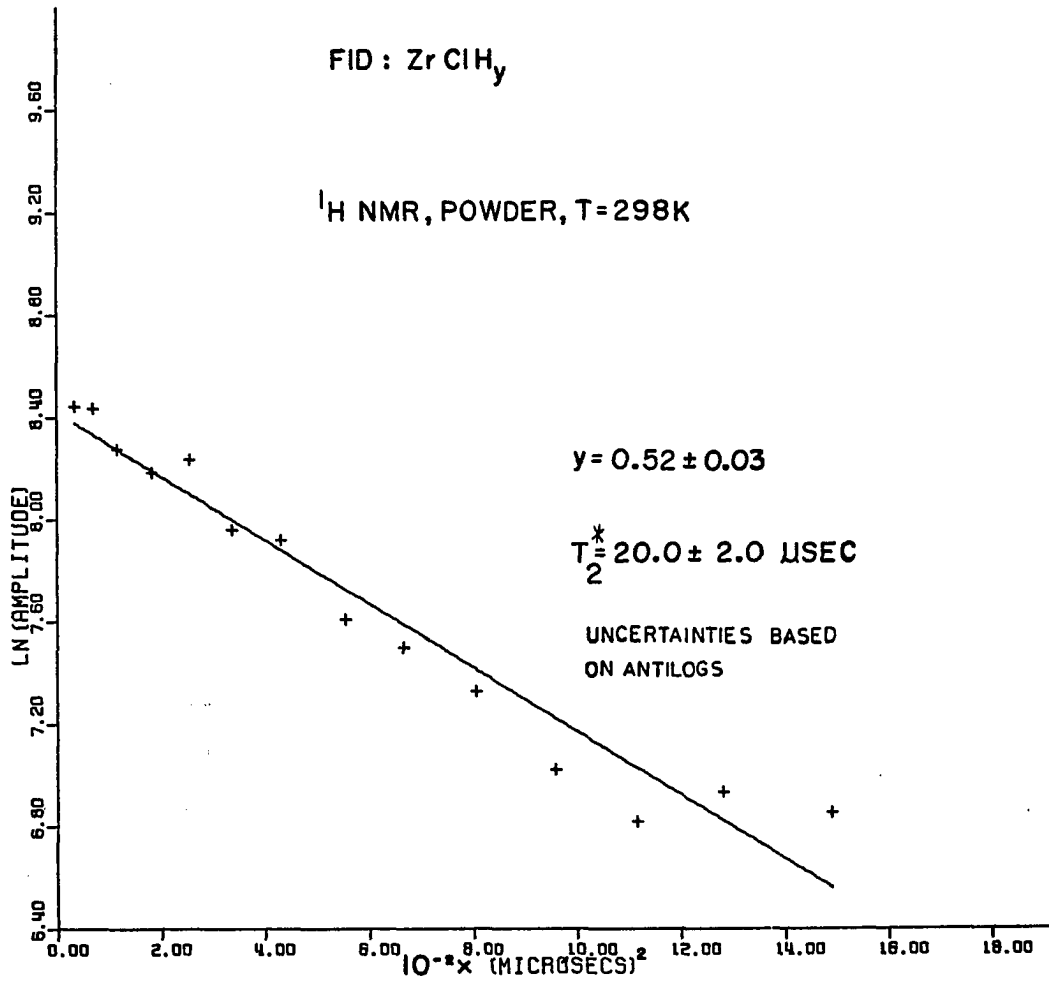
Figure 56. The natural log of the amplitude of the FID of ZrClH$_{0.5}$ vs. time squared
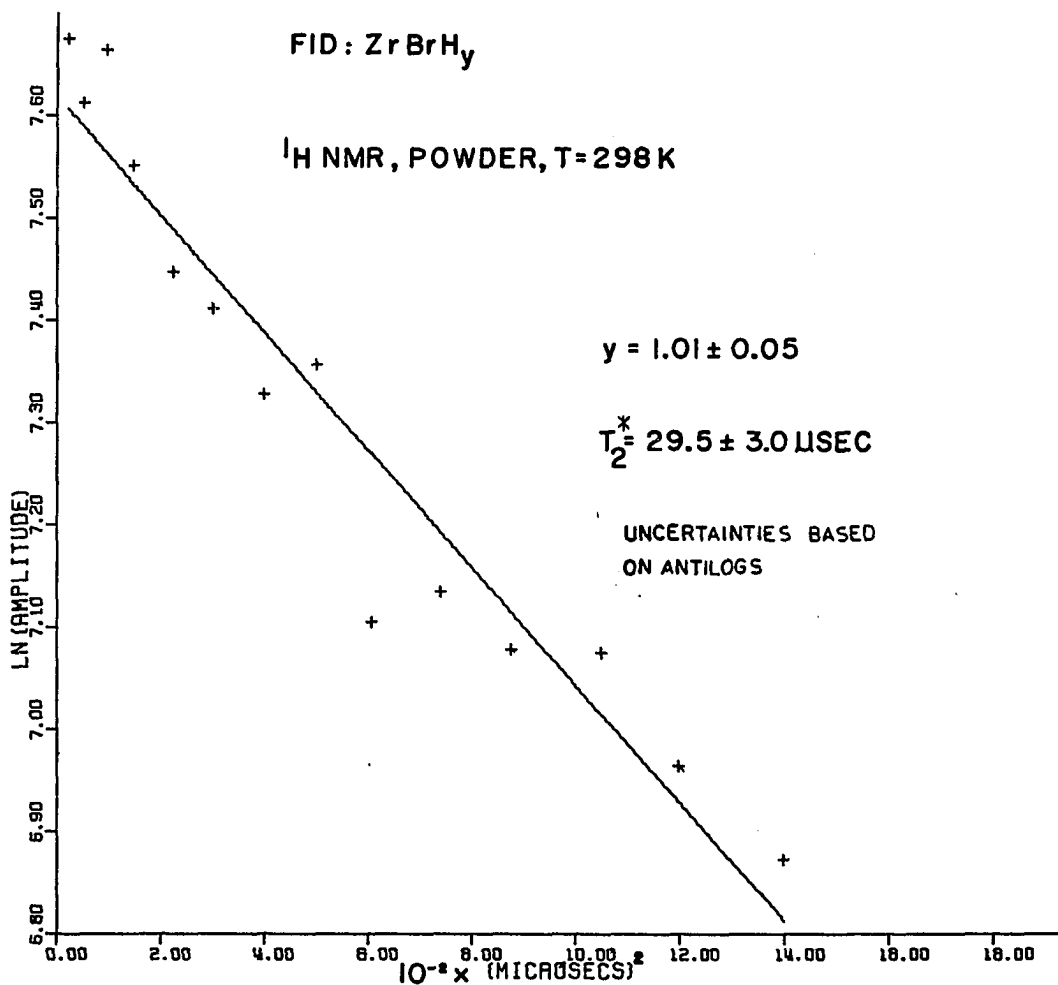
Figure 57. The natural log of the amplitude of the FID of
ZrBrH$_{1.0}$ vs. time squared
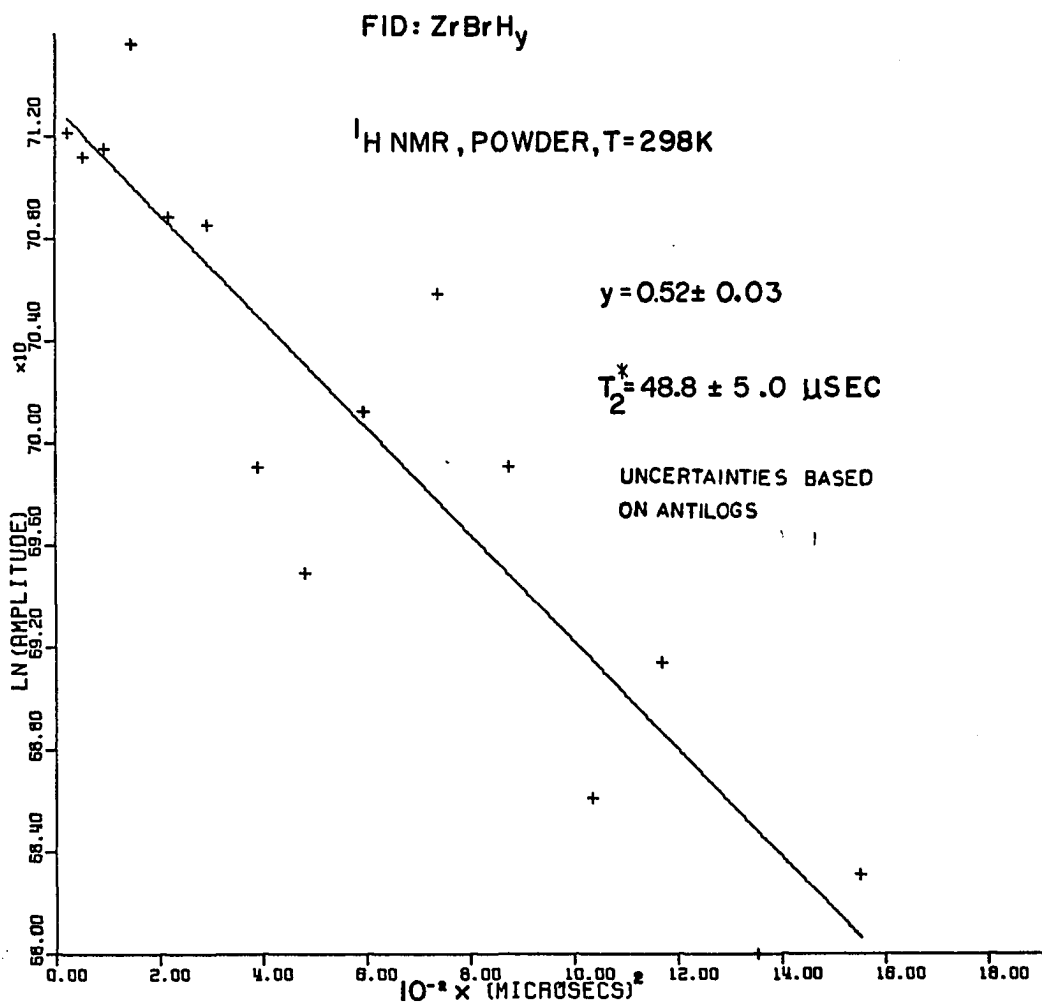
Figure 58. The natural log of the amplitude of the FID of ZrBrH$_{0.5}$ vs. time squared

Table 2. A list of the parameters for the ^1H shielding tensors of the $ZrXH_y$ family

[Negative shifts are downfield (i.e. less shielded).]

Compound	^1H spin count ±5%	^1H H_2 absorp.	$^2\mu$ sec ±10%	τ m sec	σ_{11} ppm ±5%	σ_{22} ppm ±5%	σ_{33} ppm ±5%	$\Delta\sigma$ ppm ±5%	σ_{ISO} ppm ±5%	W^a ppm ±5%
$ZrClH_{1.0}$	1.04	1.0	14.3	0.5	-23.1^b	-23.1	79.4	102.5	11.1	22.2^c
$ZrClH_{0.5}$	0.52	0.5-0.6	20.0	0.7						
A					-33.2^b	-33.2	67.2	100.4	0.3	20.3^c
B					-54.5	12.0	45.9	100.4	1.1	38.7^d
$ZrBrH_{1.0}$	1.01	1.0	29.5	0.3	-68.9^b	-68.9	-17.6	51.3	-51.8	34.7^c
$ZrBrH_{0.5}$	0.52	0.5-0.6	48.8	0.3	-56.6	-34.3	18.1	74.7	-24.3	26.1^c

[a] W = full width of broadening function

[b] axially symmetric: $\sigma_\perp = \sigma_{11} = \sigma_{22}$, $\sigma_\parallel = \sigma_{33}$

[c] Lorentzian

[d] Gaussian

The MREV-8 Multiple-Pulse sequence (33-36) was used for
homonuclear decoupling. The $\pi/2$ pulse widths were 1.5 μ sec
and cycle times, t_c = 25.2 usec and t_c = 30.0 usec were used
for $ZrClH_y$ and $ZrBrH_y$ measurements, respectively. Tuning was
critically adjusted such that phase glitch and tuning errors
were less than 200 Hz. Shifts are reported with respect to
an external H_2O reference of similar size to the $ZrXH_y$ samples
and precisely located in the same region of the coil. The
shifts have been corrected for bulk susceptibility effects
using the approximation of long cylindrical samples and
reference:

$$\sigma = \sigma_{obs} + (2\pi/3)(\chi_{vref} - \chi_v), \qquad (64)$$

where χ_v is the volume magnetic susceptibility. The molar
susceptibilities, $10^6\chi_m$ (corr) have been determined (46) to be
97 cm^3/mole (ZrCl) and 107 cm^3/mole (ZrBr) at room temperature.
A powder density of 1/2 the X-ray density is assumed. The
susceptibility correction to the shift is the same for all
compounds and is -5.3 ppm.

Because susceptibility and conduction electrons can affect
line positions, error limits are set at 10% which is ± 5 ppm
over the entire anisotropy range. Shifts have also been
corrected for scaling (33-36) under the Multiple-Pulse experiment.

D. Results and Discussion

The values of the various components of the shielding tensors as inferred by computerized fitting to the lineshape of the Powder Pattern (41) are listed in Table 2. The Powder Pattern of $ZrClH_{1.0}$ was measured for both positive and negative offsets of 6 KHz from the Larmor Frequency of 56.021 MHz. The shielding components for this compound are the average of the two measurements. All other spectra were recorded with a positive offset.

Values of parameters were extracted by non-linear least-squares fitting (41) the theoretical lineshapes to the experimental data. For $ZrXH_{1.0}$ and $ZrBrH_{0.5}$, the theoretical lineshapes were those of single shielding tensors convoluted with Lorentzian broadening functions. For $ZrClH_{0.5}$, the theoretical lineshape was that of two tensors convoluted with Lorentzian and Gaussian broadening functions. The resolution of any components is strongly limited by the full width of the broadening function. In general, the positions of the tensor components become less certain as the width of the broadening function increases. A possible source of broadening is dipolar coupling to the quadrupolar spin 3/2 species: ^{35}Cl and ^{37}Cl and spin 5/2 species ^{91}Zr.

The correlation time, τ, for the motion of the protons (50) can be obtained from the transverse relaxation constant, T_2^*,

and the second moment, M_2 (47). These values are listed in Table 2 and may be considered as order of magnitude estimates.

Before these measurements, the largest shielding anisotropy for ^1H was 44.8 ppm in KHF_2 (51). It is not surprising that large anisotropies are observed in the $ZrXH_y$ family. If the ^1H do indeed reside in holes within the metal-metal bilayer, the magnitude of the anisotropy might be expected to be large relative to other observed ^1H shielding anisotropies from a simple classical consideration of shielding expected for species within a single conducting metal sheet. The experimentally observed Powder Patterns, with the non-linear least-squares fitted Powder Patterns superimposed, are shown in Figures 59, 60, 61 and 62. Finally, the theoretical Powder Patterns which exhibit the 5 kinds of shielding tensors observed in this research are shown in Figure 63. It should be noted that the tensor of $ZrClH_{1.0}$ and tensor A of $ZrClH_{0.5}$ are very similar. All shift axes are drawn such that negative shifts (i.e. decreased shielding) are in the downfield direction.

Evidence is very strong that protons in $ZrClH_{1.0}$ and $ZrBrH_{1.0}$ mainly reside in tetrahedral-like holes. The values of the calculated second moments (47) are in good agreement with experimental values. The axial symmetry and large anisotropies of the shielding tensors are consistent with ^1H occupation in these slightly distorted tetrahedral holes within the metal-metal double layer. For these compounds, the NMR spectra would
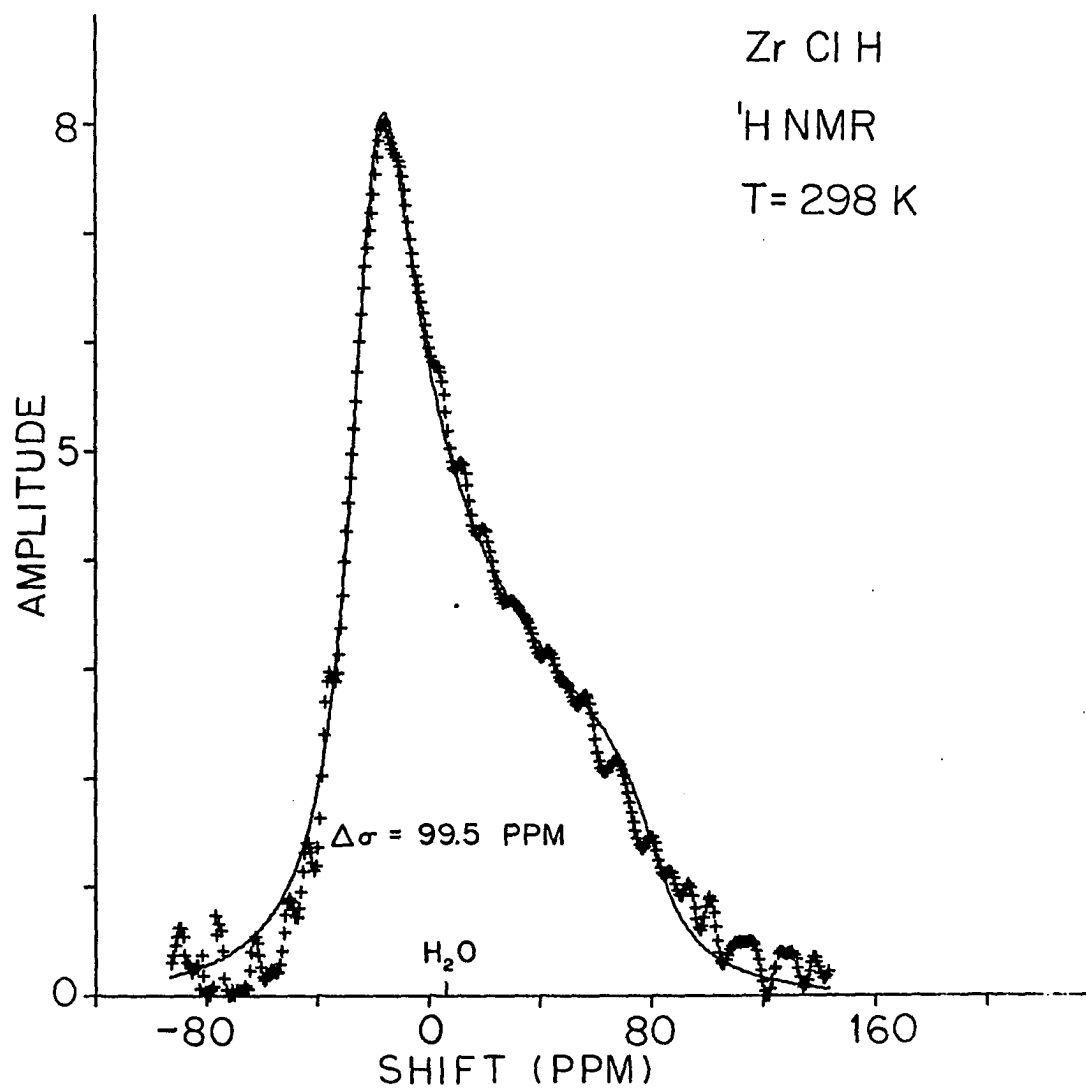
Figure 59. The ^{1}H NMR spectrum of powdered $ZrClH_{1.0}$
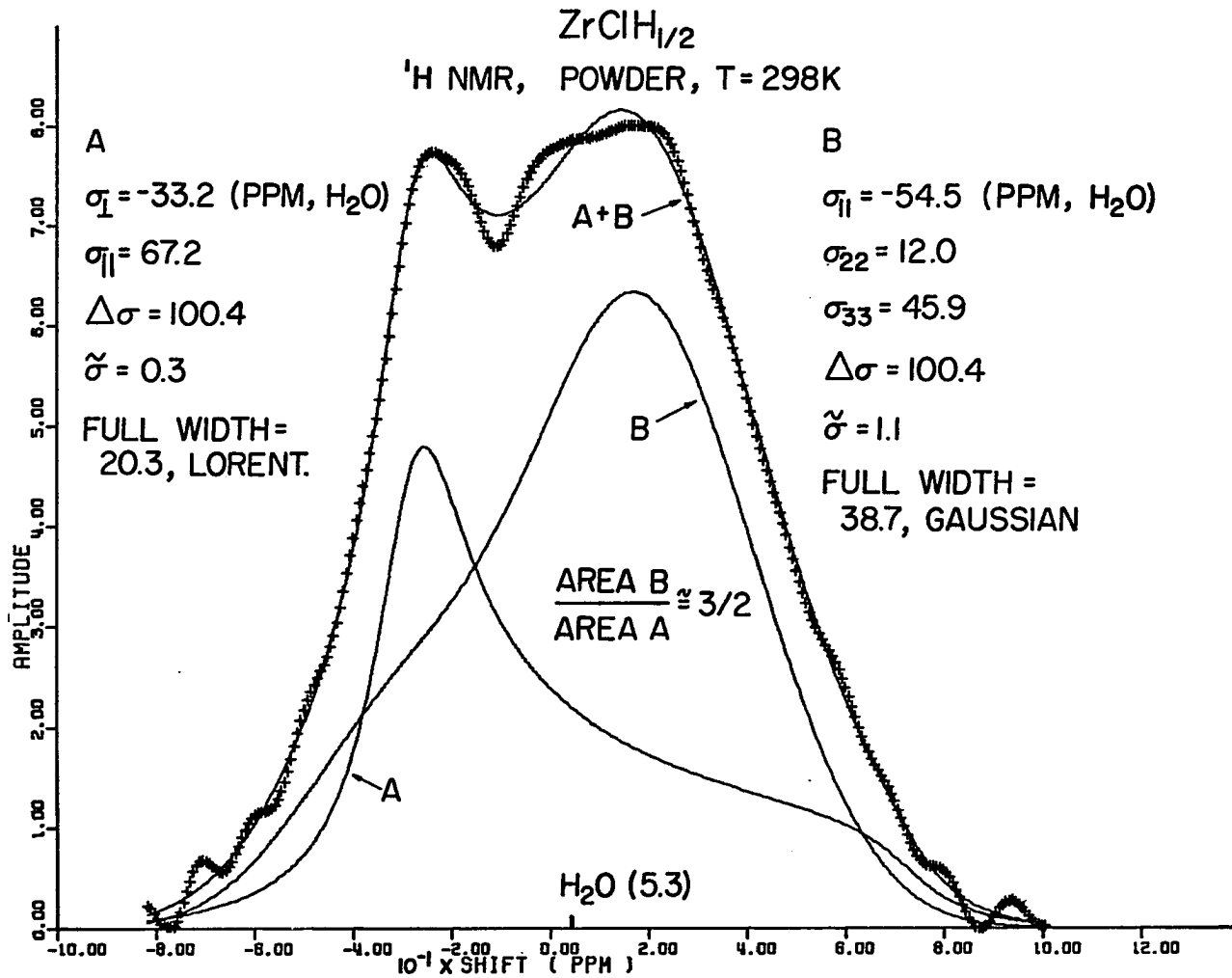
Figure 60. The ^1H NMR spectrum of powdered $ZrClH_{0.5}$

$ZrClH_{1/2}$

^1H NMR, POWDER, T = 298K

A

$\sigma_{\perp} = {}^-33.2$ (PPM, H_2O)

$\sigma_{\parallel} = 67.2$

$\triangle\sigma = 100.4$

$\tilde{\sigma} = 0.3$

FULL WIDTH = 20.3, LORENT.

B

$\sigma_{\parallel} = {}^-54.5$ (PPM, H_2O)

$\sigma_{22} = 12.0$

$\sigma_{33} = 45.9$

$\triangle\sigma = 100.4$

$\tilde{\sigma} = 1.1$

FULL WIDTH = 38.7, GAUSSIAN

A+B

B

A

$\dfrac{AREA\ B}{AREA\ A} \cong 3/2$

H_2O (5.3)

AMPLITUDE

10^{-1} X SHIFT (PPM)

155
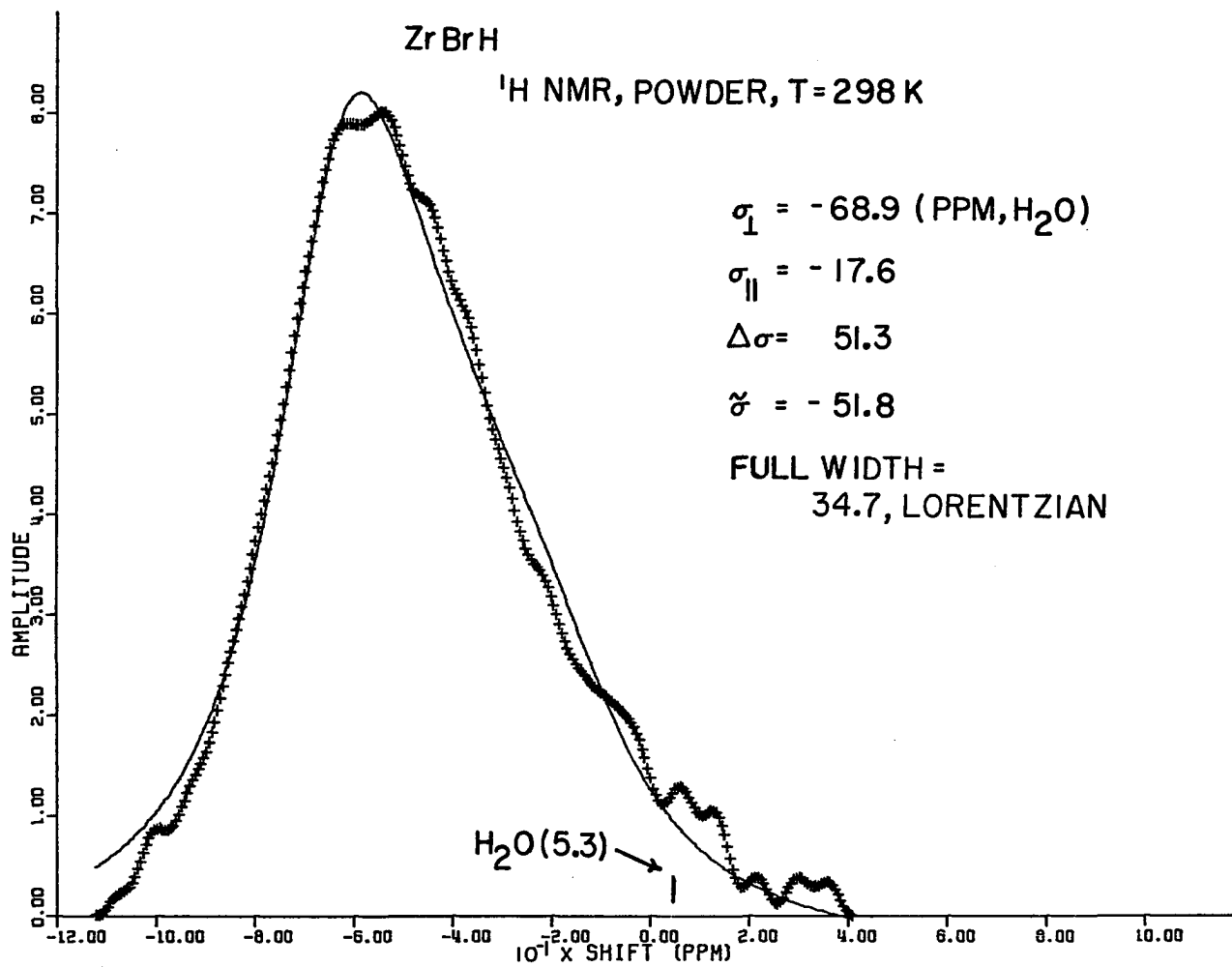
Figure 61. The ^{1}H NMR spectrum of powdered ZrBrH$_{1.0}$
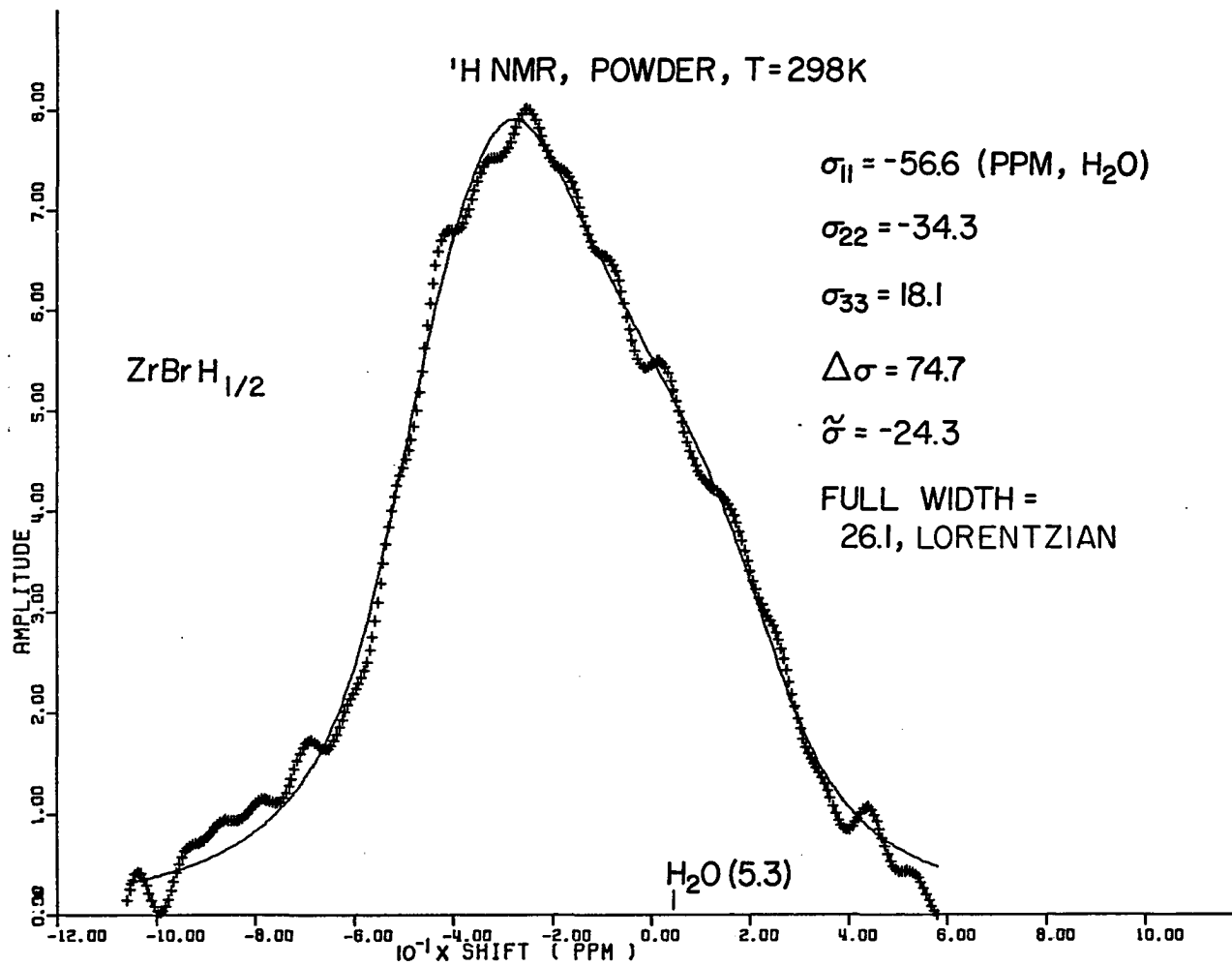
Figure 62. The ^{1}H NMR spectrum of powdered ZrBrH$_{0.5}$
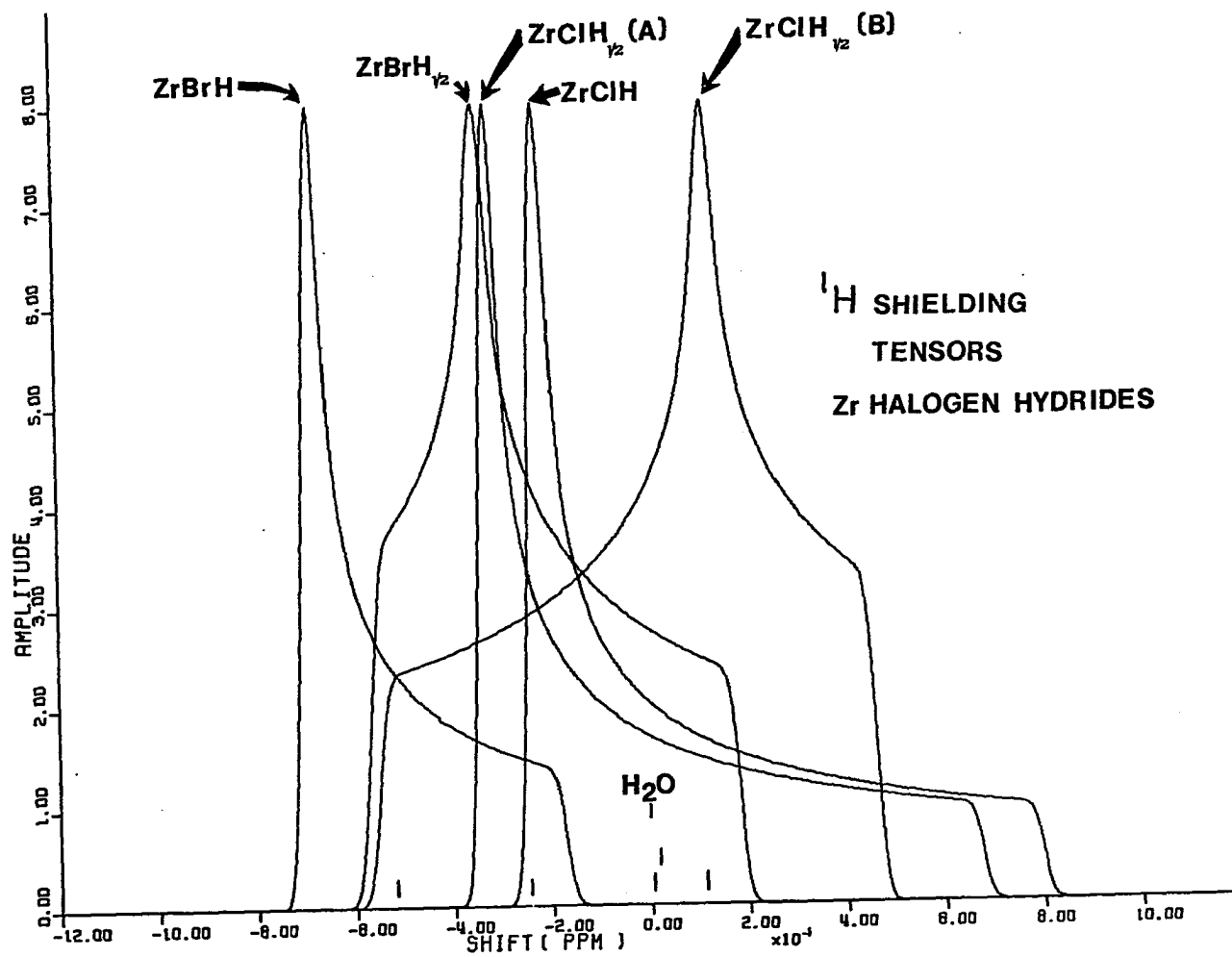
Figure 63. The five kinds of ^1H shielding tensors observed for the hydrides of ZrX

not be expected to show much contribution from occupation of octahedral holes (47) which is supposed less than 6%.

The NMR spectrum of $ZrClH_{0.5}$ (Figure 60) is very interesting as it is believed to result from the overlap of at least two inequivalent shielding tensors. The lineshape can be resolved into a tensor (A) of similar anisotropy and shielding to that found in $ZrClH_{1.0}$ and a second tensor (B). Tensor A is believed to result from the same shielding as found in $ZrClH_{1.0}$ and hence is assigned to occupation of tetrahedral holes. Tensor B is assigned to a second shielding--which may be due to ^1H occupation of octahedral holes. The large anisotropy of this tensor is a good indication that these protons reside in the metal-metal double layer but, of course, not in the hole which is assumed to be tetrahedral. The non-symmetric quality of this tensor may indicate some complicated or "string-like" (47) occupation as well.

From the ratio of the areas (assumed proportional to concentration) under these two proton lines, 40% of the protons appear to reside in the tetrahedral hole and the remaining 60% in a possibly complicated network of octahedral holes. Hwang et al. (47) do not propose any model of exactly this kind. Their Model III, which suggests octahedral occupation with 12% tetrahedral occupation, does seem to suggest these results if it were modified to account for a complicated octahedral-tetrahedral occupation.

Finally, the NMR spectrum of $ZrBrH_{0.5}$ (Figure 62) does not show any evidence of two Powder Patterns. The experimental data is well fitted by a single, non-symmetric tensor. The $ZrBrH_{0.5}$ tensor is non-symmetric and more shielded compared to that of $ZrBrH_{1.0}$. A somewhat similar relationship exists between the tensors of $ZrClH_{1.0}$ and $ZrClH_{0.5}$ (A) and that of $ZrClH_{0.5}$ (B). This relationship may be indicative of proton location in a region equivalent to that for the protons in $ZrClH_{0.5}$ (B). Possibly, this region is an octahedral hole. The presence of some occupation of tetrahedral holes cannot be ruled out; however, it must be small (< 10% or so) since there is little evidence of contributions from a second tensor. Since second-moment calculations (47) are in poor agreement for mainly octahedral occupation, Model III of Hwang et al. seems to be the most compatible. As with $ZrClH_{0.5}$, the site occupation of protons in $ZrBrH_{0.5}$ may be very complicated.

Daake and Corbett (46) have noted that the expected steric expansion in the plane of the four-layered sandwich is much less than expected in going from the chloride to the bromide (.08 instead of 0.42 Å). Expansion in the interlayer X-X distances is only slightly less than expected (0.24 instead of 0.30 Å). They suggest that these observations are consistent with a polarized, non-spherical bromide in ZrBr; whereas, a different anionic polarization is responsible for reducing

repulsion between anionic layers in ZrCl. Possible evidence of these phenomena may be reflected in the shielding tensors. The isotropic values of the shielding tensors for the zirconium bromide hydrides are considerably further downfield (less shielding) than those of the zirconium chloride hydrides. This strong deshielding may originate in the different halide polarization within the sandwiches and/or the different stacking of the sandwiches: (ACB in ZrBr and ABC in ZrCl).

VIII. STUDIES OF SILICON IN SILANES: $^1H-^{29}Si$

J CROSS POLARIZATION IN THE LIQUID STATE

A. Introduction

The technique of Cross Polarizing a rare-spin species, S, by an abundant-spin species, I, is well-known. In the early 1960's, Hartmann and Hahn (9) developed the theory of polarization transfer in liquids and solids via the coupling of two different nuclear species. They measured the $^1H-^{31}P$ coupling constant in hypophosphorous acid, $HP(OH)_2$, by observing the magnetization of the abundant spin, ^1H, and observed the Cross Polarization of ^{35}Cl by K^{39} in solid potassium chlorate, $KClO_3$. In the early 1970's, Pines, et al. (8) developed the Cross-Polarization technique with high-powered decoupling and rare-spin observation and recorded the first enhanced NMR spectra of rare spins in solids. Recently, Maudsley, et al. (53) and Bertrand, et al. (12) have utilized scalar coupling to Cross Polarize ^{13}C by ^1H in molecules in the liquid state, with observation of the ^{13}C magnetization.

The static dipolar coupling (2, 3, 8, 9) is the interaction used for polarization transfer between I and S spins in solids. In liquids, the static dipolar coupling is motionally averaged to zero. However, the indirect or scalar coupling which results from the hyperfine interactions of electrons and nuclei remains.

This indirect (or scalar, or J) coupling provides the means of polarization transfer in liquids (See below).

Cross Polarization, whenever possible, offers certain advantages in NMR studies of liquids. First, there is an enhancement in the magnetization of the rare spin, S, for suitable Cross-Polarization times, by a factor which can be as large as γ_I/γ_S. Second, the repetition period is determined by the longitudinal relaxation, T_1, of the abundant spin, I. The abundant spin's T_1 can be shortened through suitable "doping" with paramagnetic impurities and is usually much less than that of the rare spin.

The liquid J Cross-Polarization experiment notably differs from that on most solids in that the magnetization will oscillate between the abundant and rare spins. The equations which govern the behavior of the magnetization in the liquid state for the matched Hartmann-Hahn (H-H), on-resonance experiment have been previously reported by Hartmann and Hahn (9) and Bertrand, et al. (12). These equations are:

$$\text{S-I} \qquad M_S = M_I^* \sin^2\left(\frac{\pi J \tau}{2}\right) \tag{65}$$

$$\text{S-I}_2 \qquad M_S = M_I^{**} \sin^2\left(\frac{\pi J \tau}{\sqrt{2}}\right) \tag{66}$$

$$\text{S-I}_3 \qquad M_S = M_I^{**}\left(1/2\ \sin^2\left(\frac{\pi J \tau}{2}\right) + 1/2\ \sin^2\left(\frac{\pi J \tau \sqrt{3}}{2}\right) + 1/4\ \sin^2(\pi J \tau)\right) \tag{67}$$

In the above equations, S refers to the rare spin and I, to the abundant spins. Also, J refers to the scalar coupling constant between the S and I spins and is equivalent for all

S-1 bonds. The quantities M_I', M_I'' and M_I''' refer to the initial

magnetization of the abundant spins obtained by direct polarization.

When this relatively large magnetization is transferred to the

rare spin, the rare spin's magnetization is enhanced by a factor

which can be as large as γ_I/γ_S (ratio of gyromagnetic ratios)

times that obtained by direct polarization.

Furthermore, as can be seen in the above equations, the

magnitization is modulated as a function of Cross-Polarization

time by frequencies proportional to the spin coupling constant,

J.

Both Maudsley, et al. (53) and Bertrand, et al. (54) have

used the J Cross Polarization technique with rare-spin observation

to measure ^1H-^{13}C coupling constants. Recently, Bertrand et al.

(54) have also observed ^1H-^{15}N JCP. Maudsley, et al. (53) describe

techniques for the transfer of polarization by both oscillations

in the rotating frame and pulse-interrupted free precession.

The technique developed by Bertrand, et al. (12) relies on the

oscillatory transfer of polarization in the rotating frame.

Both Maudsley et al. (53) and Bertrand, et al. (12), use two-

dimensional Fourier Transforms to generate frequency spectra

from which the spin coupling constant, J can be inferred.

The present work uses the oscillatory transfer of

polarization in the rotating frame and reports the first use

of the J Cross-Polarization technique (12) on a ^1H-^{29}Si spin

system with rare spin observation. The method is used to

measure ^{1}H-^{29}Si spin coupling constants for three different

^{1}H coupling multiplicities in the compounds: triethylsilane,

$(CH_3CH_2)_3SiH$, diethylsilane, $(CH_3CH_2)_2SiH_2$, and phenylsilane

$C_6H_5SiH_3$. A lineshape-fitting technique is used to fit the

theoretical equations (65-67) to the experimental data. The

non-linear least-squares algorithm iterates a "best fit" to

the experimental data (modified Levenberg-Marquardt method

(55)) and yields the value of the spin coupling constant, J,

directly.

A dominant reason for the present work is the fact that

alkylated silanes are probes of the molecular environment of

oxygen in relatively complicated molecules (56). Since the

primary mechanism for Cross Polarization of ^{29}Si is by nearest

neighbor ^{1}H in liquids, the present work represents a basis

on which to enhance sensitivities of ^{29}Si NMR measurements in

studies of $(R)_n$-(SiH_{3-n})-O-R´ model compounds. The chemical

shifts of ^{29}Si in these -Si-O- model compounds will provide

a basis for understanding the structure of organic oxygen (in

the form of alkylated silyl-ethers) in much more complicated

systems such as derivatives of coals. A somewhat similar study

using ^{1}H NMR has been made by Schweighardt et al. (56).

The material of this Chapter is a slightly expanded version

of an article accepted for publication (57).

B. Theory of J Cross Polarization in an I-S System

The general sequences of RF pulses and phases for all Cross-Polarization (CP) experiments are shown in Figure 64. A brief description of the mechanics of Cross Polarization follows. The abundant, or I, spins are polarized by a $\pi/2$ pulse and then spin-locked along the direction of polarization. The amplitude, H_{1S}, of the CP pulse is now critically adjusted until the Hartmann-Hahn (H-H) condition:

$$\omega_S = \gamma_S H_{1S} = \gamma_I H_{1I} = \omega_I \qquad (68)$$

is satisfied. In the laboratory, the appearance of a rare-spin signal as the matching conditions are adjusted signifies proper H-H matching. The S spins are simultaneously decoupled from the abundant spins by H_{1I}, adjusted to be large compared to the magnitude of the spin-spin coupling.

The phase of the preparation pulse of the I spins is alternately inverted such that the rare-spin's magnetization is also inverted (58). By alternately adding and subtracting this FID from the data buffer, some base line and transient artifacts can be removed. The design of a single-coil double-resonance NMR probe has been described in Chapter III.

While the pulsing sequences are identical for JCP and regular CP, the magnitudes of the H_{1i} fields are usually different. In JCP, the size of H_{1S} is usually chosen such that ω_S is greater than any offset, $\Delta\omega_S$, and/or J. Such a choice

PHASE INVERTING C.P. PULSE SEQUENCES
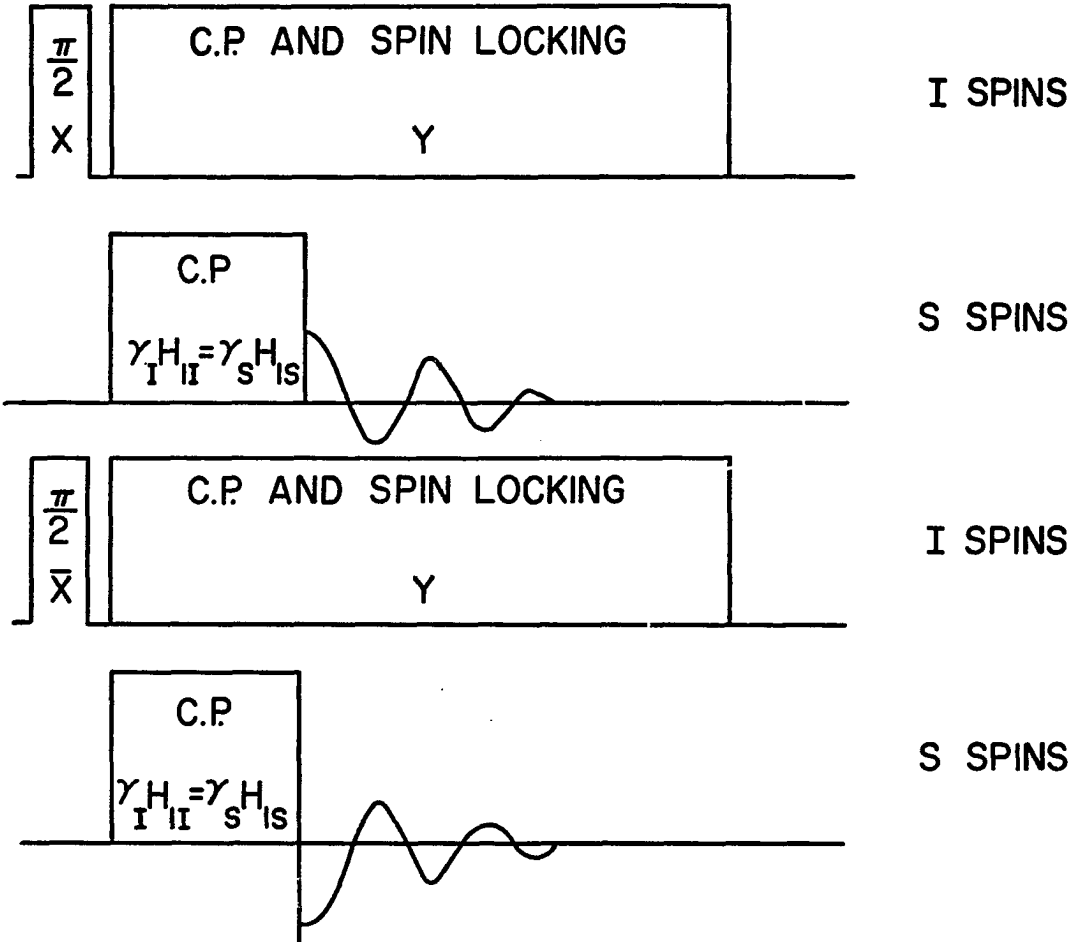
Figure 64. The phase-inverting pulse sequence used in Cross Polarization

will insure that the off-resonance H-H condition

$$\omega_S^- = [\Delta\omega_S^2 + (\gamma_S H_{1S})^2]^{1/2} = \gamma_I H_{1I} = \omega_I \qquad (69)$$

is satisfied. The required H_{1I} field will generally be more

than enough to decouple the I spins. Because of the weakness

of J-coupling as compared to the much stronger static dipolar

coupling, much more careful tuning is required to satisfy the

H-H condition in JCP than in regular CP.

In JCP, the initial magnetization imparted to the abundant,

or I, spins can be shown to oscillate between these spins and

the rare, or S, spins. The following discussion of this phenomenon

will rely on concepts originally stated by Hartmann and Hahn

(9) and will be applied to an I-S, spin = 1/2 system. In order

to remain consistent with the original H-H notation (9), the

abundant spins will now be assumed polarized and spin-locked

along the x axis. In the experiments described in this Chapter

and Chapter IX, the abundant spins were actually polarized and

spin-locked along the y axis as described above. However, the

expectation values are the same for derivations with respect

to any axis, but the form of the Hamiltonian will depend upon

the choice of the axis of spin-locking.

First Hartmann and Hahn showed that there exists a rotating

frame in which the I spin magnetization is constant in the

absence of an I-S interaction. This rotating frame is established

as the result of first transforming into the radiofrequency

(RF) rotating frame (rf) of both spins (abbreviated RFrf) and

next into the "spin-locked" rotating frame (SLrf) along the
x axis of the RFrf. They also showed that the Hamiltonian in
such a frame could be decomposed into two parts. One part,
H_{r0}, is always secular and the other part, H_{r1}, becomes secular
when the H-H condition, equation 69, is satisfied. The Hamiltonian,
H_{r1}, causes the double-resonance phenomenon to occur. In the
SL-RFrf, this Hamiltonian has the form:

$$H_{r1} = -1/2J(I_{zi}S_{zk} + I_{yi}S_{yk}) \tag{70}$$

where J is the scalar coupling constant, I and S are angular
momentum operators (42, 59, 60), and i, k indicate summation
over all pairs of heteronuclear spins.

In Quantum Mechanics (42, 59, 60) observable properties,
such as magnetization, M, are calculated via operators. The
magnetization of the I spins is then calculated from the relation
(8, 9, 42, 59, 60):

$$M_I = \hbar\gamma_I Tr(\rho I_x) \tag{71}$$

where ρ is the density matrix. An equation, similar to equation
71, is also used to calculate the magnetization of the S spins.
In addition to showing that H_{r1} is secular when the H-H condition
is established, Hartmann and Hahn also pointed out that

$$[I_x + S_x, H_r] = 0$$

where $H_r = H_{r0} + H_{r1}$. This commutator shows that the population
differences or the net magnetization (α aI_x + bS_x) will remain
constant.

Stoll (61) has discussed the behavior of a Hamiltonian of the form of equation 70 in great detail. This type of Hamiltonian always leads to an oscillatory transfer of magnetic polarization between the I and S spins. An important point in this regard is the distinction between oscillation and precession. The following derivation will calculate the frequency of this oscillation using time development of the density matrix for an I-S, spin = 1/2 system. Also, the S magnetization will be shown to be enhanced by γ_I/γ_S over its static field value. This deduction follows a similar pattern to that used by Stoll (61).

Initially a magnetization, M_{0I}, is established along the x axis of the SL-RFrf by $\pi/2$ rotation and spin-locking of the abundant, or I, spins. The rare, or S, spins are assumed to have no initial magnetization. Thus, the initial value of the density matrix (in the high-temperature approximation) is given by:

$$\rho(0) = Z^{-1}(1 + B'I_x) \qquad (72a)$$

or:

$$\rho(0) \propto BI_x \qquad (72b)$$

where B' is dimensionless constant:

$$B' = \frac{\hbar\gamma_I H_0}{kT} \qquad (73a)$$

and:

$$B = Z^{-1}B' \qquad (73b)$$

The quantity Z defined:

$$Z = \text{Tr}\{1\} = (2I + 1)^{N_I}(2S + 1)^{N_S}$$

is a constant which depends on the total number of spins,

$N_I + N_S$. This constant also can be considered to contain all

scale factors which insure that all future equations are valid.

The Hamiltonian of equation 70 will cause the density matrix

to develop in time according to the relation:

$$\rho(\tau) \propto e^{-iH_{r1}\tau} \rho(0) e^{iH_{r1}\tau} \tag{74}$$

Since $[I_z S_z, I_y S_y] = 0$, the exponential operator can be factored

into two separate exponential operators (42, 52) such that:

$$\rho(\tau) \propto B e^{i\frac{J\tau}{2}I_z S_z} e^{i\frac{J\tau}{2}I_y S_y} I_x e^{-i\frac{J\tau}{2}I_y S_y} e^{-i\frac{J\tau}{2}I_z S_z} \tag{75}$$

The following identities specific to spin 1/2 systems (42,

59, 60) are liberally used:

$$L_x^2 = L_y^2 = L_z^2 = 1/4 \tag{76a}$$

$$L_x L_y = -L_y L_x = 1/2 \, iL_z \tag{76b}$$

$$L_y L_z = -L_z L_y = 1/2 \, iL_x \tag{76c}$$

$$L_z L_x = -L_x L_z = 1/2 \, iL_y \tag{76d}$$

$$i = \sqrt{-1}$$

where $L_a = I_a$ or S_a, $a = x, y, z$. The following identity for

spin $= 1/2$ particles is also used (61):

$$e^{iDt I_a S_a} = \cos(\frac{Dt}{4}) + 4i \, \sin(\frac{Dt}{4}) I_a S_a \tag{77}$$

and $a = x, y, z$. Equation 77 is obtained by first performing

a Taylor-series expansion of the left hand side of this equation.

Terms of even powers are grouped together to form a Taylor

cosine-series while terms of odd powers are similarly grouped together to form a Taylor sine-series using equations 76a-d for spin = 1/2.

The application of the $I_y S_y$ operator leads to:

$$\rho(\tau) \propto B e^{i\frac{J\tau}{2}I_z S_z}[\cos(\frac{J\tau}{4})I_x + 2\sin(\frac{J\tau}{4})I_z S_y]e^{-i\frac{J\tau}{2}I_z S_z} \qquad (78)$$

Finally, $\rho(\tau)$ reduces to:

$$\rho(\tau) \propto B[\cos^2(\frac{J\tau}{4})I_x + \sin(\frac{J\tau}{2})(I_z S_y - I_y S_z) + \sin^2(\frac{J\tau}{4})S_x] \qquad (79)$$

Noting that $Tr(L_i L_j) = 1/2 \qquad i = j = x, y, z$

$$Tr(L_i L_j) = 0 \qquad i \neq j \qquad (80)$$

and including suitable constants, the magnetization of the abundant spins, M_I, will become:

$$M_I(\tau) = \hbar\gamma_I Tr(\rho I_x)$$

$$= M_{0I}\cos^2(\frac{J\tau}{4}) \qquad (81)$$

where:

$$M_{0I} = \frac{\hbar^2\gamma_I^2 H_0}{2\alpha kT}$$

Likewise, the magnetization of the rare spins is calculated:

$$M_S(\tau) = \hbar\gamma_S Tr(\rho S_x)$$

$$= \frac{\gamma_I}{\gamma_S} M_{0S}\sin^2(\frac{J\tau}{4}) \qquad (82)$$

where:

$$M_{0S} = \frac{\hbar^2\gamma_S^2 H_0}{2\alpha kT}$$

Both M_{0I} and M_{0S} represent magnetizations in terms of the Laboratory field, H_0.

The above derivations show that the magnetization of the abundant spin will oscillate with its maximum value being its initial value. The magnetization of the rare spin will likewise oscillate starting with zero amplitude (if no initial S magnetization is present) and will reach a maximum amplitude of γ_I/γ_S times its laboratory ralue, M_{0S}, which will result in an enhancement if $\gamma_I > \gamma_S$. The frequency of oscillation is $J/4$ radians $\sec^{-1}$, or $\frac{\pi J}{2}$ if J is expressed in Hertz and, of course, J is the heteronuclear J-coupling constant.

The net magnetization in the SL-RFrf can be shown to always remain constant when the H-H condition is matched. At any temperature T, the ratio of magnetizations of two different kinds of spins can be written:

$$\frac{M_{0S}}{M_{0I}} = \frac{\gamma_S^2 H_{1S}}{\gamma_I^2 H_{1I}}$$

and since $\gamma_S H_{1S} = \gamma_I H_{1I}$, then:

$$M_{0S} = \frac{\gamma_S}{\gamma_I} M_{0I} \tag{83}$$

Substituting the value of M_{0S} of equation 83 into equation 82, one arrives at:

$$M_S(\tau) = M_{0I} \sin^2\left(\frac{J\tau}{4}\right) \tag{84}$$

Since $M_I(\tau) + M_S(\tau) = M_{0I}$, the net magnetization is always constant and equals the initial value of the abundant spins.

This magnetization will oscillate between the abundant and rare spin, resulting in an enhancement of γ_I/γ_S in the observed magnetization of the rare spin as shown in equation 82.

An additional and important fact about the H-H condition is that the exact form is written:

$$\omega_S^- = [\Delta\omega_S^2 + \omega_S^2]^{1/2} = \omega_I \qquad (85)$$

where $\omega_i = \gamma_i H_{1i}$. If the amplitude of the H_{1S} field is chosen sufficiently large, then equation 85 will reduce to the normal H-H condition. However, the offset, $\Delta\omega_S$, cannot be "too large" or the Hamiltonian, H_{r1}, becomes non-secular and the interaction responsible for JCP will vanish. This Chapter describes experimental data in which the oscillatory transfer of magnetization is studied in ^{1}H-^{29}Si systems. Use of JCP is also shown to be potentially very valuable in measuring the chemical shifts of trace amounts of ^{29}Si in coal-derived liquids.

C. Experimental

The spectrometer used in these experiments was constructed in this laboratory and is described in Figure 65. Resonant frequencies for ^{1}H and ^{29}Si were 56.021 and 11.129 MHz, respectively. A single-coil probe doubly tuned at both frequencies (See Chapter III) was used. The NMR coil consisted of nineteen turns of #18 gold-plated copper wire, flattened to ribbon form in the central eleven turns to homogenize H_1. The coil was 5 mm i.d. x 29 mm long. The coil inductance was 0.38 μH.

CROSS - POLARIZATION   SPECTROMETER
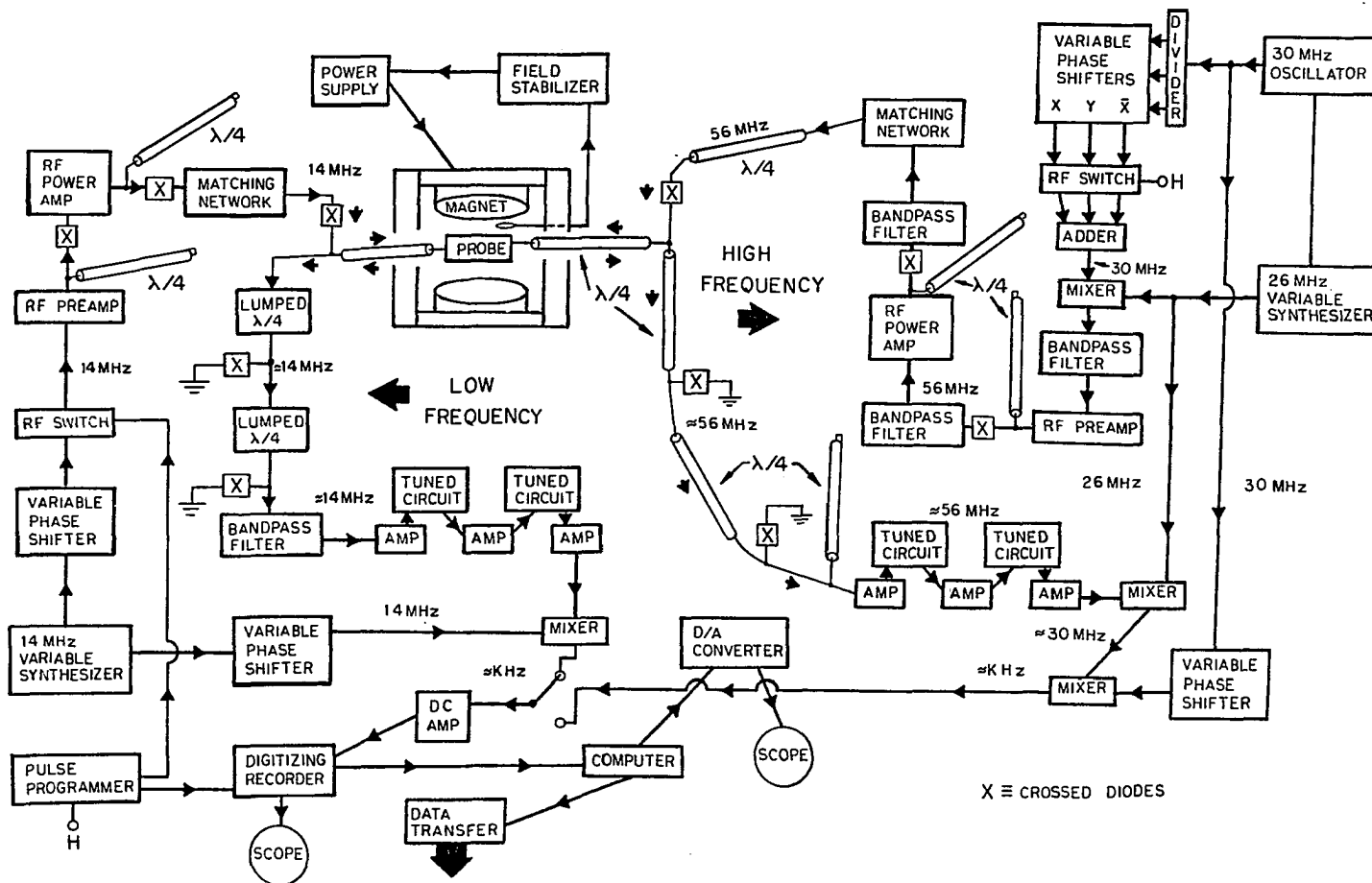
Figure 65.   A sketch of a Cross-Polarization NMR spectrometer

The design of the single-coil probe is shown in Figures 14 and 15. For highest Q, low-loss dielectric cable, RG-8U, and high Q Polyflon (15) capacitors (VC 25-6-26) were used. Capacitors C1H and C2H are used for high frequency (f_H) tuning. Cable D1 and capacitor C1L are used for low frequency (f_L) tuning. The use of high Q, low noise capacitors for C1H and C1L is essential for preventing the generation of broadband noise during the decoupling pulse.

When the H-H condition was matched, approximately 0.39 and 1.27 RMS Watts were required to achieve H_{1i}'s of 1 and 5 Gauss at frequencies of 56.021 and 11.129 MHz respectively. The $\pi/2$ pulse width of 62.5 μsec for protons was sufficiently short in insure uniform excitation of all frequencies of the ^{1}H multiplets by the preparation pulses.

Critical tuning (i.e. matching of RF power levels) is required to observe J Cross Polarization. A tuning procedure was followed which allowed fairly accurate matching (<70 Hz) of the H-H condition with the use of samples containing ^{29}Si in natural abundance. Initially, the $\pi/2$ pulses and RF phases are set on the I(^{1}H) channels at f_H = 56.021 MHz using water doped with ferric chloride. Next, the static magnetic field is lowered so ^{1}H resonance occurs at f_L = 11.129 MHz. The pulse width of the S(^{29}Si) Cross-Polarization channel, t_S, is set: $t_S = \dfrac{2\gamma_S t_I}{\gamma_I}$, where t_I is the $\pi/2$ pulse width of the I(^{1}H)

Cross-Polarization channel. For t_I = 62.5 µsec., t_S = 25 µsec. Now, the S channel RF power is adjusted for a π pulse (minimum signal) on the doped H_2O sample. This tuning procedure is sufficiently accurate to bring RF power levels to within 1 dB of those required for the H-H condition to be met.

The static magnetic field is returned to its normal value and a J-coupled sample such as ^{29}Si in triethylsilane is used for final tuning. The T-matching circuit of the S channel is varied slightly (match-mismatch) until the J Cross-Polarization FID [(S/N) ≈ 2] is a maximum. This tuning procedure has been found to result in accurate and reproducible, ^{29}Si-^1H matching and is potentially useful for other rare nuclei.

Figure 64 shows the pulse sequences used. A 180° phase-inverted, π/2 pulse was alternately applied to the ^1H spins, resulting in an alternating, 180° phase-inverted ^{29}Si FID. Every other FID was subtracted from the computer's memory buffer so that only magnetization from J Cross Polarization was observed. All measurements were made within 50 Hz of resonance. Sample spinning was not used.

D. Preparation of Dimethylsilyl-Ethers

These silyl derivatives were prepared from the corresponding alcohols by adding 0.40 moles of the alcohol to a 50 ml round bottom flask equipped with a reflux condenser, a heating mantle, and a magnetic stirrer. Liquid alcohols were added neat, but

solid alcohols were dissolved in a minimum amount of benzene

prior to addition. After purging the system with nitrogen,

0.20 moles of tetramethyldisilazane and one drop of

dimethylchlorosilane were added to the flask. The reaction

mixture was refluxed for 8 to 12 hours. The crude silyl-ethers

were separated from the reaction mixture by distillation through

a short path, microdistillation apparatus. Samples for ^{29}Si

NMR were purified by preparative gas chromatography on 5%

OV-101 or 10% carbowax 20 M. Infrared, mass spectral, and

^1H NMR analyses of purified dimethylsilyl-ethers were used

to confirm the authenticity of these materials.

E. Discussion

For 0.25 ml of doped triethylsilane (4×10^{19} ^{29}Si spins),

a bandwidth of 5 KHz and repetition rate of 3 seconds, a maximum

$(S + N)/N \simeq 2$ was obtained with one scan (See Figure 17). The

observed $(S + N)/N$ is consistent with an enhancement of $5(= \gamma_I/\gamma_S)$

over that obtained with a $\pi/2$ pulse. All $(S + N)/N$ ratios

refer to initial amplitudes of the FID.

Figures 66, 67 and 68 show the magnetization (arbitrary

units) of ^{29}Si as a function of Cross-Polarization time, τ.

The plotted values are the initial amplitudes of the FID following

the Cross-Polarization pulse. Each value is the average of two

measurements and the maximum value of each graph has been

normalized to 1.0. Superimposed on each graph is the lineshape
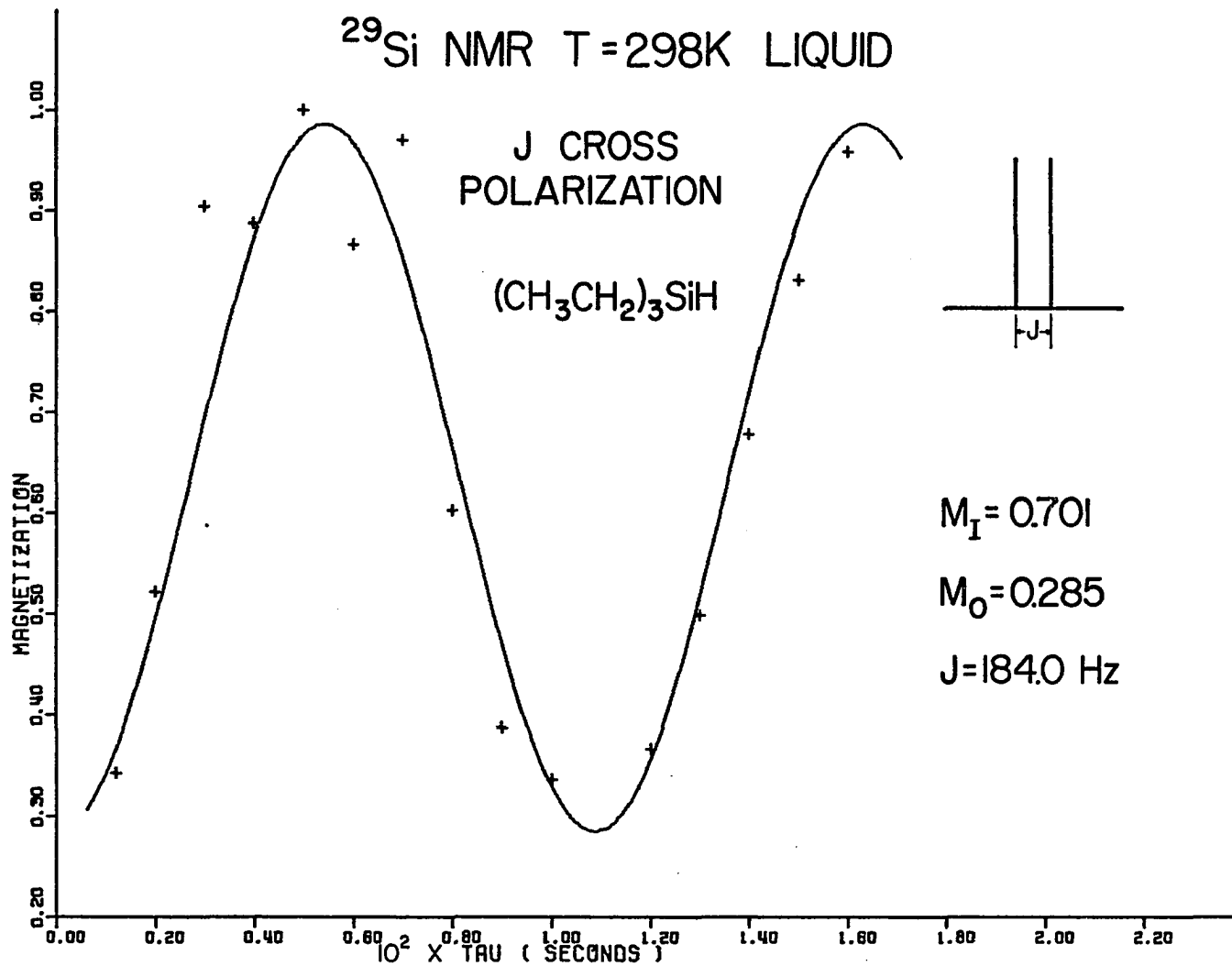
Figure 66. The ^{29}Si magnetization vs. Cross-Polarization time for triethylsilane
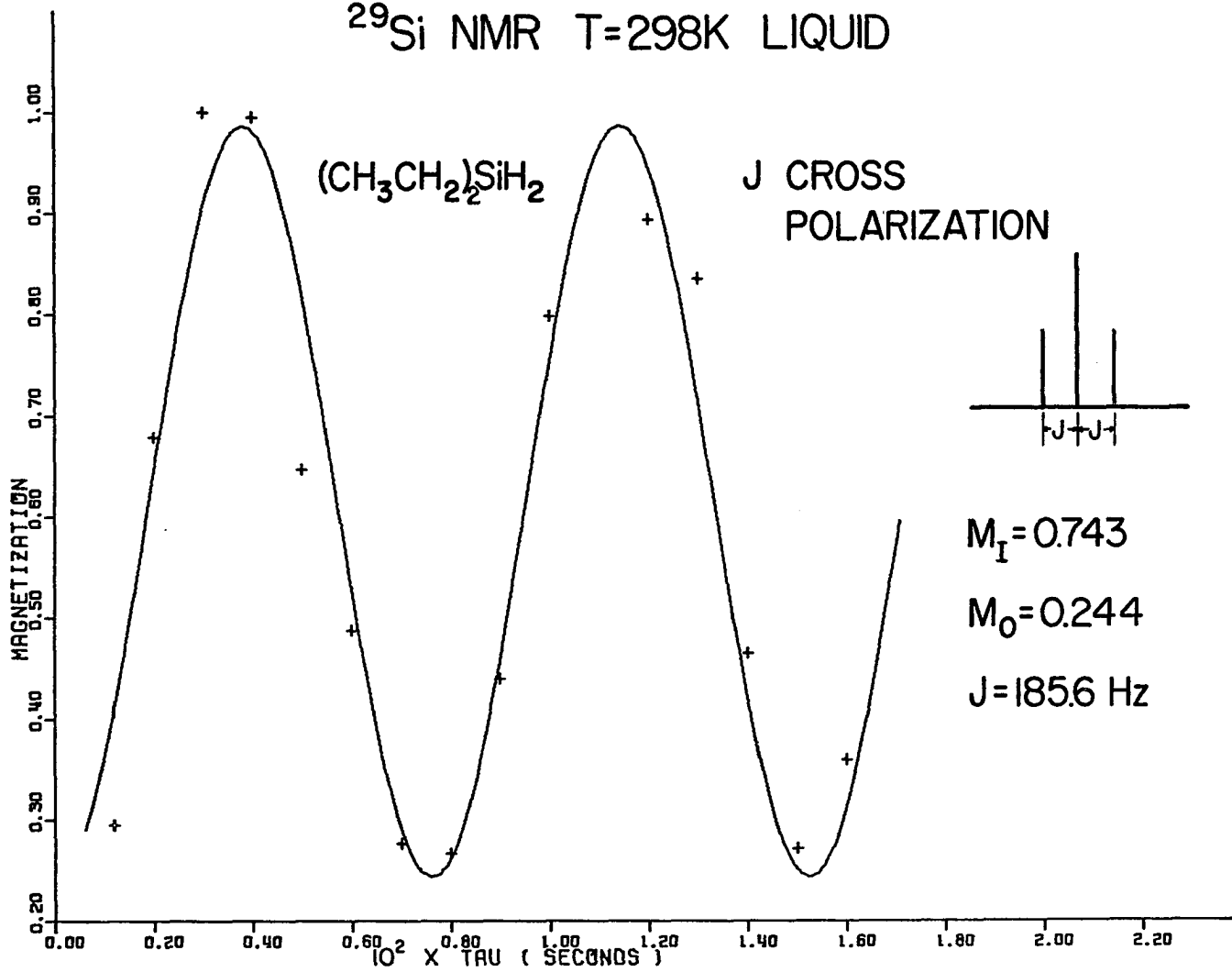
Figure 67.   The ^{29}Si magnetization vs. Cross-Polarization time for diethylsilane
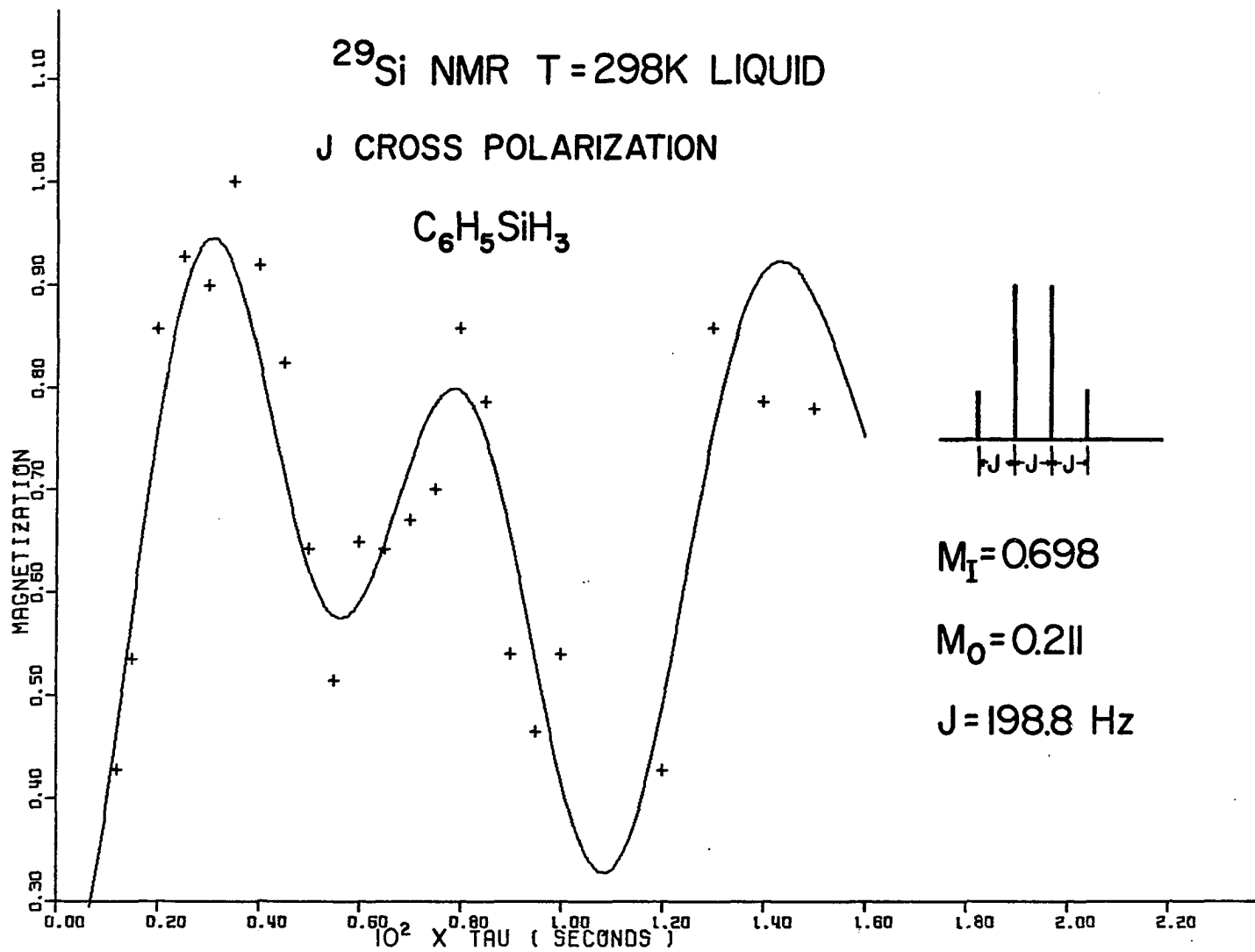
Figure 68.   The ^{29}Si magnetization vs. Cross-Polarization for phenylsilane

of the non-linear least-squares fit. A constant, M_o, was added

to each equation (65.- 67) to account for the experimental

artifact of D.C. offset. There are three parameters in each

fit: the amplitude of the abundant magnetization, M_I, the

base line constant, M_o, and the spin coupling constant, J.

The convergence condition for each fit was that the residual

sum of errors-squared changed by less than 0.001 for two

consecutive iterations of the parameters. Table 3 contains

the values of the parameters for each fit. Also included in

this table is the value of the spin coupling constant, $J_{\pi/2}$,

measured by the conventional method of $\pi/2$ excitation and

Fourier Transform. The quantity, $\Delta(\simeq |J^2_{\pi/2} - J^2|^{1/2})$ is an

estimate (53) of the mismatch in the H-H condition.

The spin coupling constants determined by this method

agree within experimental error with those of the conventional

method. The time evolution of the magnetization does appear

to follow the oscillatory behavior expressed in equations 66-67.

Of course, measurements of spin coupling constants via their

dependance on τ are time consuming. In fact, the amount of

time can be comparable to that of the conventional method--even

with shorter T_1's and signal enhancement. Clearly the most

rapid means of measuring J would be to use J Cross Polarization

for a suitable τ without abundant-spin decoupling. The coupling

Table 3. The parameters obtained by non-linear least-squares fitting of the JCP equations [M_I is the initial amplitude of the abundant-spin magnetization. M_o is the base-line constant. J is the value of the spin coupling constant obtained by J Cross Polarization while $J_{\pi/2}$ is that value obtained by excitation with a $\pi/2$ pulse. Δ is an estimate of the mismatch of the Hartmann-Hahn condition.]

Compound	M_I	M_o	J(Hz) ±10	J(Hz) $\pi/2$ ±5	Δ(Hz) ±12
$(CH_3CH_2)_3SiH$	.701	.285	184.0	195.4	66
$(CH_3CH_2)_2SiH_2$	.743	.244	185.6	195.4	61
$C_6H_5-SiH_3$	.698	.211	198.8	205.6	52

constant will modulate the FID and be directly measurable in the Fourier domain while the advantages of favorable T_1's and signal enhancement would be retained.

The choice of the Cross-Polarization time, τ, is important if the entire enhancement is to be realized. For chemical systems in which the approximate J values are known, equations 65-67 can be used to predict the optimum Cross-Polarization times. Also, this technique may be useful in resolving two

shifts that overlap--provided the overlapping lines have different spin coupling constants. A suitable τ is chosen such that a minimum magnetization occurs for one line, thereby producing a resolved spectra of the other line, and vice versa.

The origin of the large D.C. offset terms, M_o, is very interesting. Since the value of the D.C. term (or base line constant) is very similar in all three fits (Figures 66-68), its origin appears instrumental since all measurements were made using a virtually identical procedure.

Additional and subsequent measurements in this Laboratory have shown that the value of M_o is mainly determined by two factors: 1) the signal-to-noise of the initial point of the FID and 2) the accuracy of the RF phases. Furthermore, when larger data-averagings are used to improve $(S + N)/N$ and RF phases are critically adjusted, the value of this D.C. offset is reduced substantially.

Finally, Table 4 contains the ^{29}Si chemical shifts of silyl-ether model compounds and other compounds used in this research. Nuclei were excited via the JCP technique. The values of shifts are tabulated with respect to T.M.S. and negative shifts are downfield (i.e. less shielded).

Table 4. The ^{29}Si chemical shifts of silyl-ether model compounds [R = $(CH_3)_2HSi-O-$ for these compounds. Shifts are reported with respect to T.M.S. and negative shifts are downfield.]

Structure	Empirical formula	Shift (ppm) ±0.4
R - N butyl	$SiOC_6H_{16}$	-3.6
R - tert butyl	$SiOC_6H_{16}$	-0.5
R - N pentyl	$SiOC_7H_{18}$	-3.3
R - phenyl	$SiOC_8H_{12}$	-4.6
R - α naphthyl	$SiOC_{12}H_{14}$	-5.8
R - β naphthyl	$SiOC_{12}H_{14}$	-5.3
$(R - CH_2)_2$	$Si_2O_2C_6H_{18}$	-4.9
$((CH_3)_2HSi)_2NH$	$Si_2NC_4H_{15}$	+10.1
$(CH_3)_2HSiCl$	$SiClC_2H_7$	-11.1

IX. AROMATIC FRACTIONS OF CARBON IN COALS:

^{1}H-^{13}C CROSS POLARIZATION IN THE SOLID STATE

A. Introduction

This Chapter describes the measurements of the aromatic

fractions of ^{13}C (f_a) of whole coals. These determinations

were made using the combined techniques of ^{1}H-^{13}C Cross

Polarization (8, 2, 3) (described below) and Magic-Angle

Spinning (2, 62-64). The ^{13}C f_a values along with the ^{1}H f_a

values, presently being measured in this laboratory, can be

used to estimate the mysterious, average-condensed-polynuclear,

aromatic ring size in whole coals.

Prior to 1972 there was very little use of ^{13}C NMR for

solid-state studies of coals (65). In 1972, Retcofsky and

Friedel used broad-line ^{13}C NMR to study the chemical shifts

and anisotropies in four coals ranging from 83 to 96% carbon.

Based on comparisons of the locations of the broad peaks with

respect to those of the ^{13}C in diamond, assumed mainly aliphatic,

and in graphite, assumed mainly aromatic, they concluded that

f_a values appeared to increase with the "rank" of the coal

which is qualitatively related to the percent carbon in the

coal.

In 1976 Retcofsky (66) made an attempt to establish, once

and for all, that coals were highly aromatic. He attempted

to prove his point in several ways. 1) Both ^{13}C NMR studies

of carbon disulfide (CS_2) extracts and ^1H NMR studies of pyridine extracts of whole coals indicated these extracts to be highly aromatic. Also, the values of f_a increased with increasing rank for both extracts. The pyridine extracts, which represented a larger dissolved fraction of the whole coal, were consistently more aromatic than the CS_2 extracts. Thus, Retcofsky reasoned that whole coals should be very aromatic.

Retcofsky also made an attempt to estimate the average size of the condensed ring and average amount of ring substitution of the coal molecules in these extracts. However, many assumptions were used which make any extension of these results to whole coals questionable. 2) In collaboration with Vander Hart, Retcofsky also studied the ^1H-^{13}C Cross Polarization of whole coals. The f_a values are, more or less, directly obtained from the ^{13}C spectra with suitable data manipulation using their lineshape technique (67) described below. The f_a's were indeed higher than those of the extracts and again this study indicated that coals are highly aromatic. 3) Finally, infrared studies of whole coals combined with the results of the NMR studies seem to also suggest that coals were highly aromatic.

Two problems emerged from attempts to estimate f_a's of whole coals by extracts and a host of other techniques discussed by Retcofsky (66). First, f_a values were generally different for different techniques. Second, it was not clear what real

relation these f_a values had in describing whole coals. For meaningful results, f_a values would have to be measured on whole coals in the natural state.

Retcofsky (66) and Vander Hart and Retcofsky (67) were first to apply the ^1H-^{13}C Cross Polarization technique of Waugh (8, 2, 3) to studies of the ^{13}C of whole coals. Much greater ^{13}C sensitivity can be obtained than is possible with conventional methods. Again, f_a values were extracted via their lineshape technique (67) and these values seemed to be relatively constant as a function of experimental parameters.

Coals produce ^{13}C NMR spectra which are the sums of the many Powder Patterns generated by the inequivalent shifts and anisotropies of all ^{13}C with ^1H as nearest neighbors. An example of one such spectrum is shown in Figure 69. This spectrum contains two overlapping absorptions associated with aromatic and aliphatic species (66, 67).

Vander Hart and Retcofsky (67) used a technique of lineshape decomposition-synthesis to determine f_a. They measured the linear sum and difference of their two spectra and determined an average aromatic and aliphatic lineshape. Next, they re-synthesized each original spectrum by a linear combination of these two average lineshapes. From the relative areas of the two components, they were able to estimate f_a.

In order to check the accuracies of the f_a values obtained by Cross Polarization, they measured the f_a of a frozen "synthetic

STAR VITRAIN ^{13}C NMR, POWDER, T = 298 K

AROMATIC (AR)   ALIPHATIC (AL)

σ_{11} = -6.92 PPM σ_{11} = 102.2 PPM

σ_{22} = 48.5 σ_{22} = 166.4

σ_{33} = 194.1 σ_{33} = 176.8

$\triangle\sigma$ = 201.0 $\triangle\sigma$ = 74.6

$\tilde{\sigma}$ = 78.5 $\tilde{\sigma}$ = 148.5

FULL WIDTH   FULL WIDTH =
= 31.7,   35.8, LORENT.
LORENT.

AR + AL

AR

$\dfrac{\text{AREA AR}}{\text{AREA AL}} \cong 11/4$ F_a = 0.733 ± 0.03

AL

CS$_2$

AMPLITUDE

10^{-1} x SHIFT (PPM)

-8.00   -4.00   0.00   4.00   8.00   12.00   16.00   20.00   24.00   28.00   32.00   36.00

189
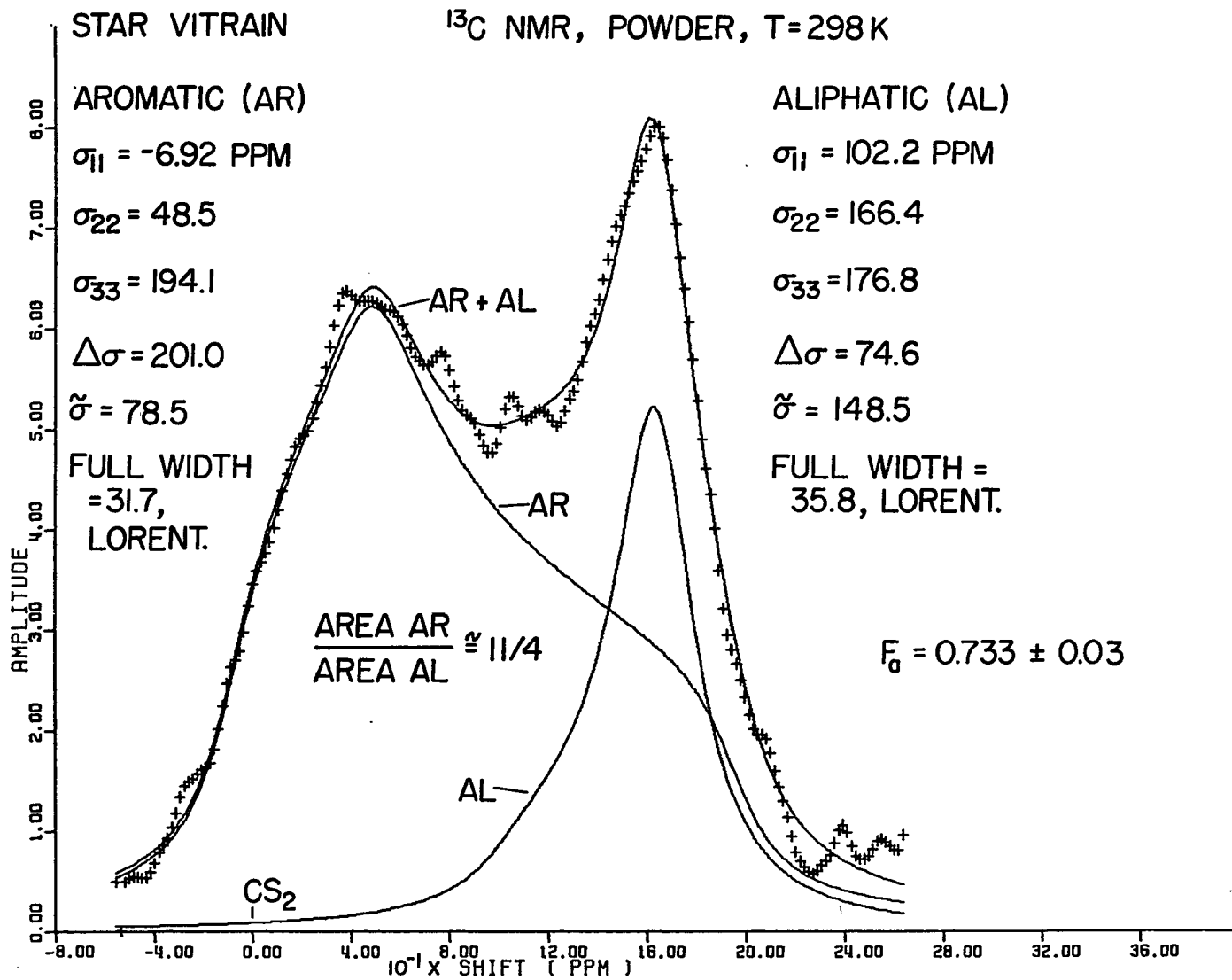
Figure 69. The ^{13}C NMR spectrum of a coal (non-spinning)

coal" whose exact f_a was measured by High Resolution NMR of the liquid. There was very good agreement between f_a's and it appeared that Cross Polarization produced valid f_a's. Retcofsky and Vander Hart (68) applied the same technique of lineshape analysis to the study of different macerals of a bituminous coal. They found, with one exception, that f_a increased with the % carbon. Furthermore, these f_a values were used to estimate the average-condensed-ring sizes in these macerals--although again, many assumptions were made.

Shortly after this work, the final technique for High Resolution in the solid state, Magic-Angle Spinning (MAS), was applied to coals (69), oil shales (69, 70) and kerogens (69, 70). Of course, MAS removes shift anisotropies and, for sufficiently fast spinning, the two classes of absorptions are resolved. Measurements of f_a are made directly from the relative area under the aromatic absorption.

Bartuska et al. (69) pointed out that f_a values, when the aromatic content is high such as for anthracite, can only be accurately measured with MAS. Such spinning is less important when the aliphatic content is high. Recently Maciel et al. (71) have extended CP-MAS measurements to ten additional coal samples. They have correlated f_a values with atomic (H/C) ratios and fuel values.

Based on this rich history of past achievement, the present
work applies Cross Polarization and Magic-Angle Spinning to
measure the ^{13}C f_a's of a range of coal vitrains.

B. Discussion of Cross Polarization

The polarization of a rare spin by abundant spins in the
solid state, or Cross Polarization (CP), was originally developed
by Hartmann and Hahn (9). As with J Cross Polarization on liquids,
they used an observation of the abundant, or I, spins to infer
the behavior of the rare, or S, spins. The development of the
technique of direct observation of the rare spins was pioneered
by Waugh in his PENIS (8) experiments. Today most CP experiments
(2), including JCP, are outgrowths of his initial work of the
early 1970's.

The pulse sequence which achieves Cross Polarization for
suitable matching of the Hartmann-Hahn condition (Equation
68 and/or 69) is the same as that for JCP and is shown in
Figure 64. Also, the aspects of abundant-spin preparation,
spin-locking, and Cross Polarization are identical to JCP and
and described in Chapter VIII.

The CP experiment on solids notably differs from the JCP
experiment in the strength of the H_{1i} fields and the lack of
oscillatory transfer of polarization for abundant spins when
such spins can be approximated as a heat bath (8, 72). Recently,
however, it has been shown that when the abundant spins are

decoupled using Multiple-Pulse homonuclear decoupling (The abundant spins no longer behave as a heat bath.), oscillatory phenomena are observed (73-75, 61).

Another notable difference between CP and JCP involves the use of abundant-spin decoupling during observation of the rare spin. In JCP, high resolution absorptions can usually be obtained even without abundant-spin decoupling since the indirect dipolar coupling is weak compared to chemical shifts. However in CP of solids, strong heteronuclear decoupling of the abundant spins must always be used. Finally, because of the broadness of static coupling when expressed in units of frequency, the matching of the H-H condition has a larger tolerance than is found for JCP which usually requires critical H-H tuning.

Both experiments are similar in that the magnetization of the rare spin is enhanced, and the time between signal accumulations is governed by the relatively short T_1 of the abundant spin.

In this Chapter, the technique of $^1H-^{13}C$ Cross Polarization has been applied to measurements of the relative ^{13}C aromatic content, f_a, of whole coals.

C. Experimental

The spectrometer used in these experiments was constructed in this laboratory and is sketched in Figure 65. Resonant

frequencies for ^{1}H and ^{13}C resonances were 56.021 and 14.087 MHz, respectively. A single-coil doubly-tuned probe designed by the author (13, 57) was used in these experiments. The design of the single-coil probe is shown in Figures 12 and 13. The construction of the probe has been described in Chapter III. The design of the spinning hardware has also been described in Chapter III.

A procedure for accurately setting the H_{1i} fields of the RF pulses has been described in Chapter VIII. With the H-H condition matched, approximately 80 and 250 RMS Watts at 56 and 14.1 MHz respectively, were required to achieve H_{1i}'s of 9.8 and 39.2 Gauss measured at the Magic Angle. The phase-inverted pulse sequence shown in Figure 64 and described in Chapter VIII was used to excite ^{1}H-^{13}C Cross Polarization. Rotor speeds ranging from 2.1 to 2.6 KHz were used to average shift anisotropies. Sample weights of roughly 0.3 grams were packed into the rotors described in Chapter III.

Offsets were 1.5 KHz above the Larmor freqeuncy of the aromatic ^{13}C absorption. The bandwidth of the DC amplifier was 17 KHz. Chemical shifts were measured with respect to an external reference of adamantane. Shift axes were drawn relative to ^{13}C in CS_2. Uncertainties in shifts are estimated at ±3 ppm. Cross-Polarization times of 1.5 msec were used and the pulsing sequence was repeated every 3 seconds.

The absorption spectra were digitally filtered by convolution with either a Lorentzian or Gaussian broadening function and are shown in Figures 70-73. This technique has been described in Chapter V. The full widths at half heights of the broadening functions were 21.3 ppm for the spectra of Figure 70 and 7.1 ppm for all other spectra shown in Figures 71-73. Areas under absorptions were calculated by numerical integration above the base line using Simpson's Rule (22). An example of a ^{13}C NMR spectra with the integration curve superimposed is shown in Figure 74.

The values of f_a are simply the relative area under the aromatic ^{13}C absorption which is centered around 65 ppm. All integrated areas are measured with respect to a base line of zero slope (or constant area). This base line is the initial value of the integration curve shown in Figure 74. The proper base line is that base line for which the integration curve shows constant area (i.e. zero slope) in regions where absorptions are not present. Uncertainties in f_a are estimated at ±3%.

D. Results and Discussion

The fraction aromaticities, f_a, along with elemental compositions of 18 coal vitrains are listed in Table 5. The absorption spectra are shown in Figures 70-73. A graph of f_a vs. atomic (H/C) ratio is presented in Figure 75. In general,

^1H - ^{13}C NMR: COAL VITRAINS

CROSS POLARIZATION WITH MAGIC-ANGLE SPINNING

SPEED: 2.4—2.6 KHz
FIELDS: 9.8 and 39.2 GAUSS
SAMPLES: 0.25g
SCANS: 20,000

AMPLITUDE

Vitrain	% Carbon	f_a (±0.03)
Pocahontas #4	90.3	0.862
Powellton	85.1	0.770
Star	77.0	0.713
Upper Mich	81.0	0.695
Lovilia	75.0	0.688

SHIFT (PPM)
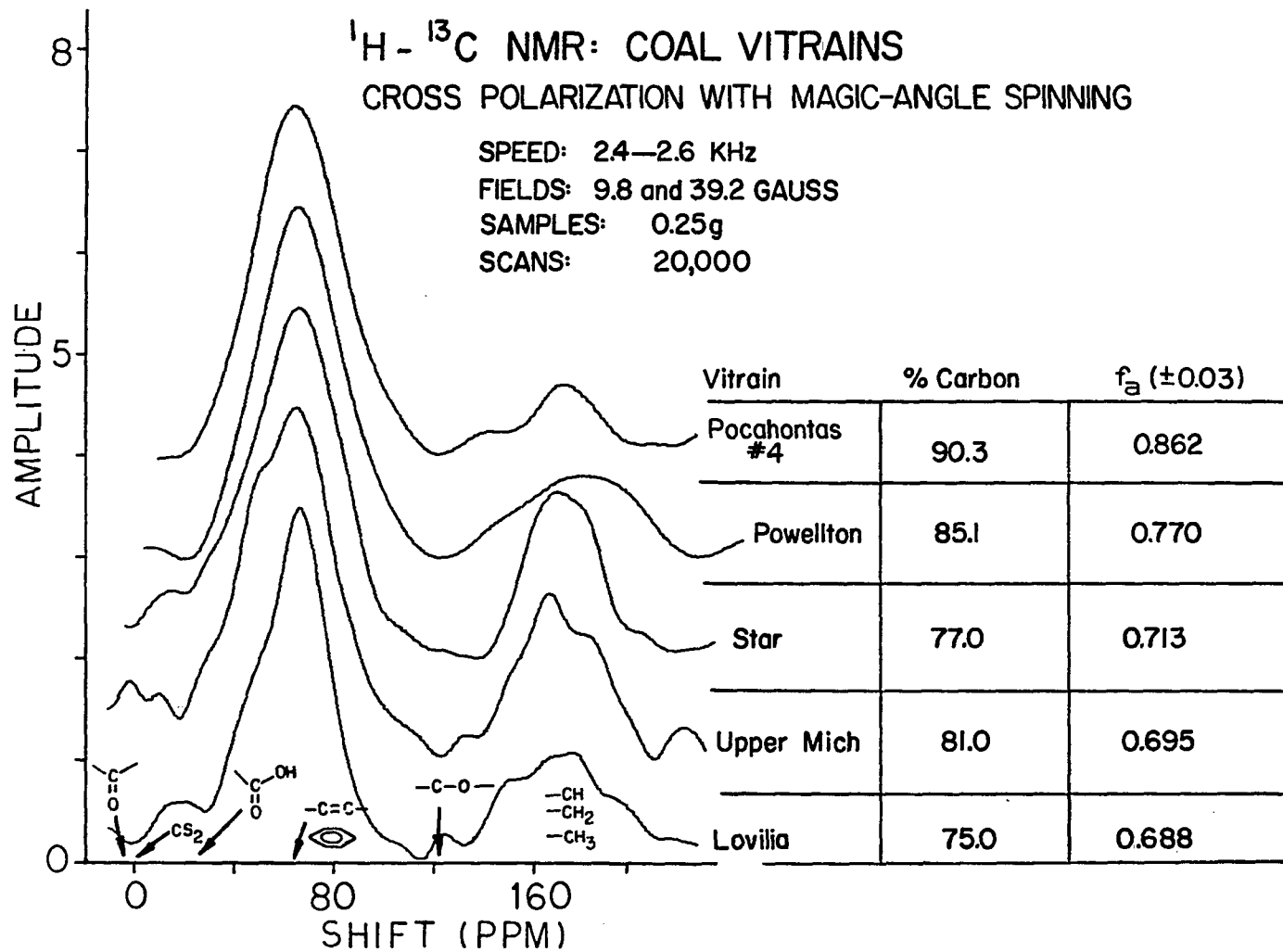
Figure 70. The ^{13}C NMR absorption spectra of coals

^{1}H - ^{13}C NMR: COAL VITRAINS

CROSS POLARIZATION WITH MAGIC-ANGLE SPINNING

SPEED: 2.1–2.5 KHz
FIELDS: 9.8 and 39.2 GAUSS
SAMPLES: 0.3 g
SCANS: 10,000

Vitrain	% Carbon	f_a (±0.03)
HAZARD #7 BUMIK 40660	81.3	0.77
LOWER CLARION PSOC-351	76.3	0.77
OHIO #5 PSOC-308	76.6	0.75
CANNEL PSOC-155	56.8	0.38

AMPLITUDE

SHIFT (PPM)
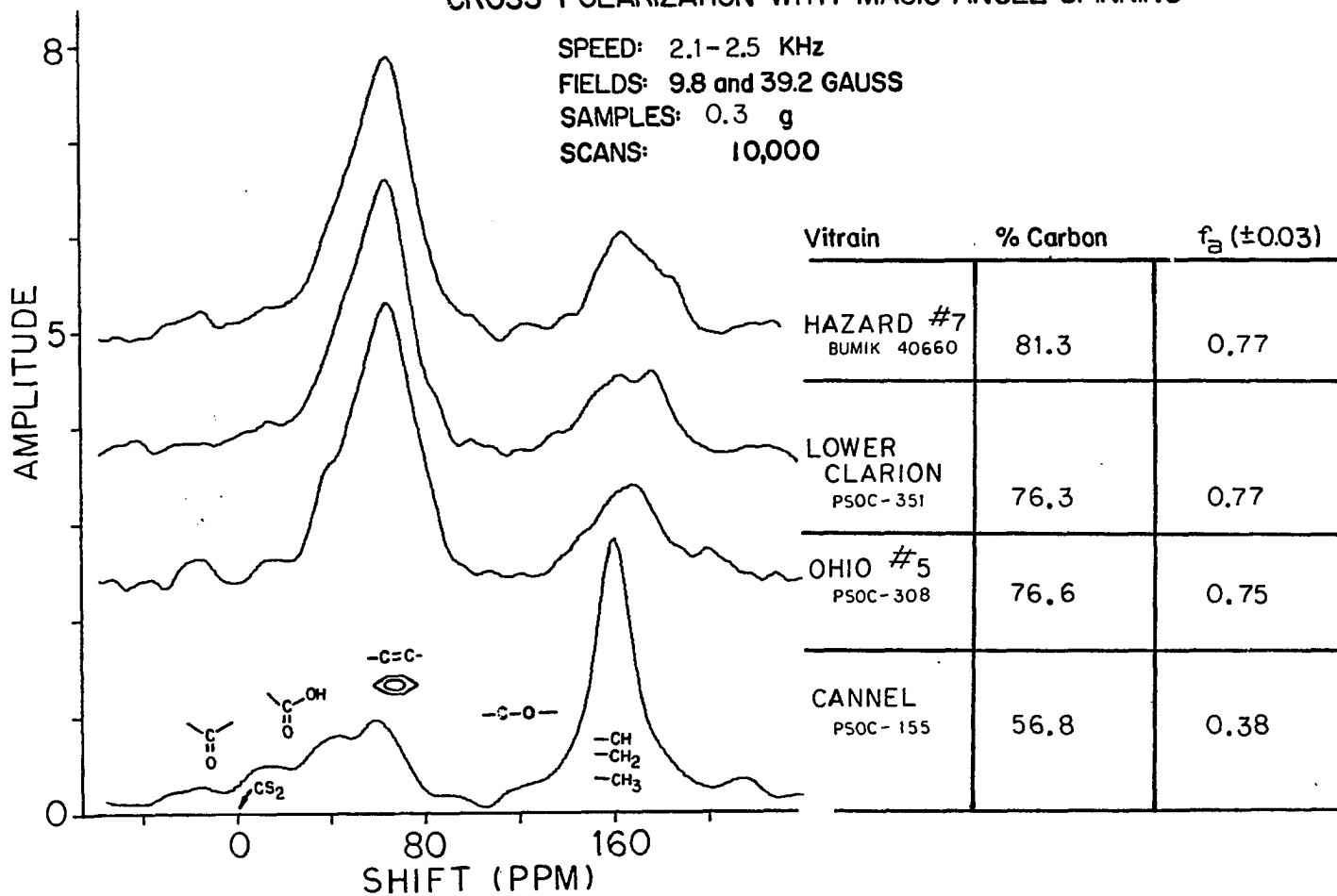
Figure 71. The ^{13}C NMR absorption spectra of coals
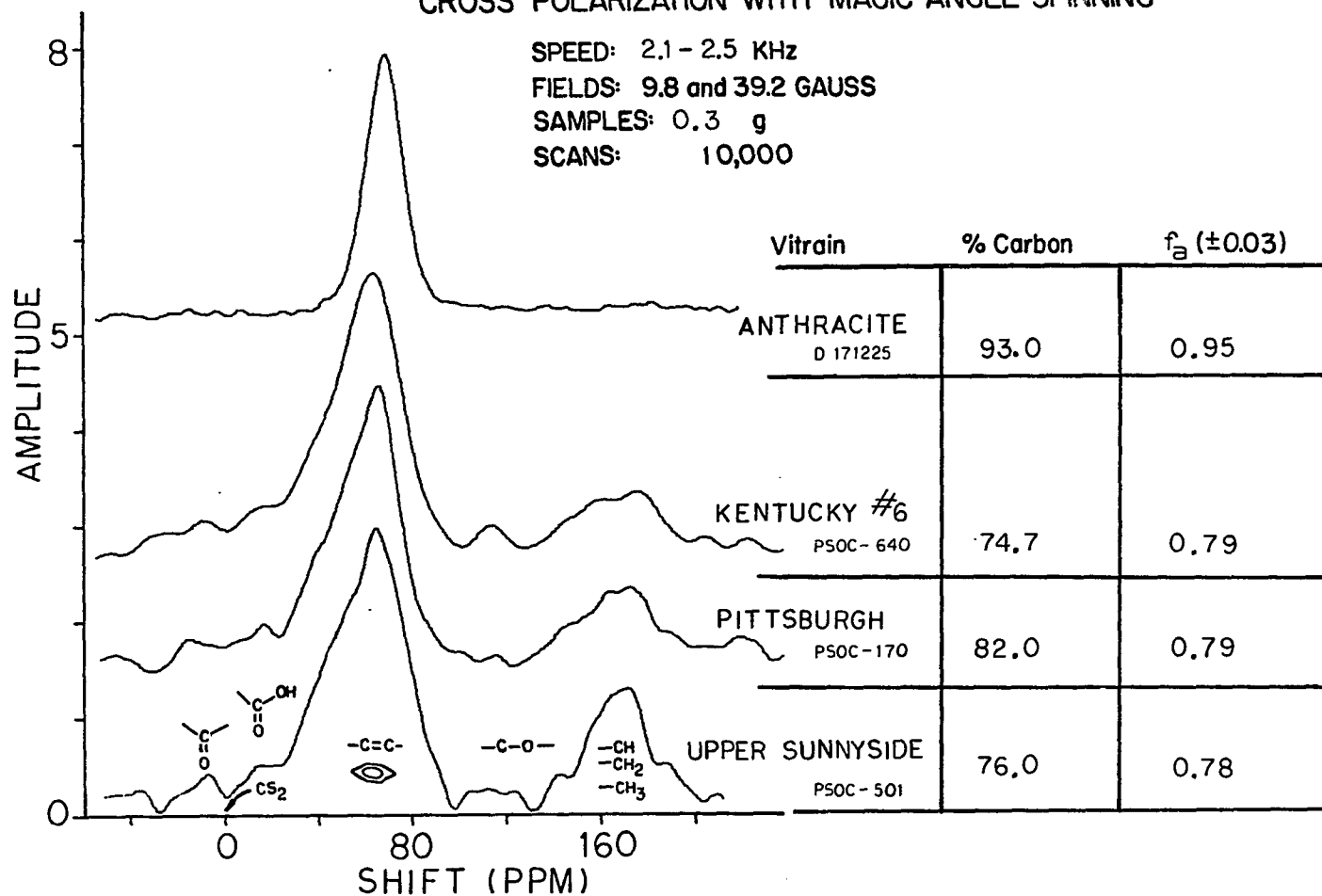
Figure 72. The ^{13}C NMR absorption spectra of coals
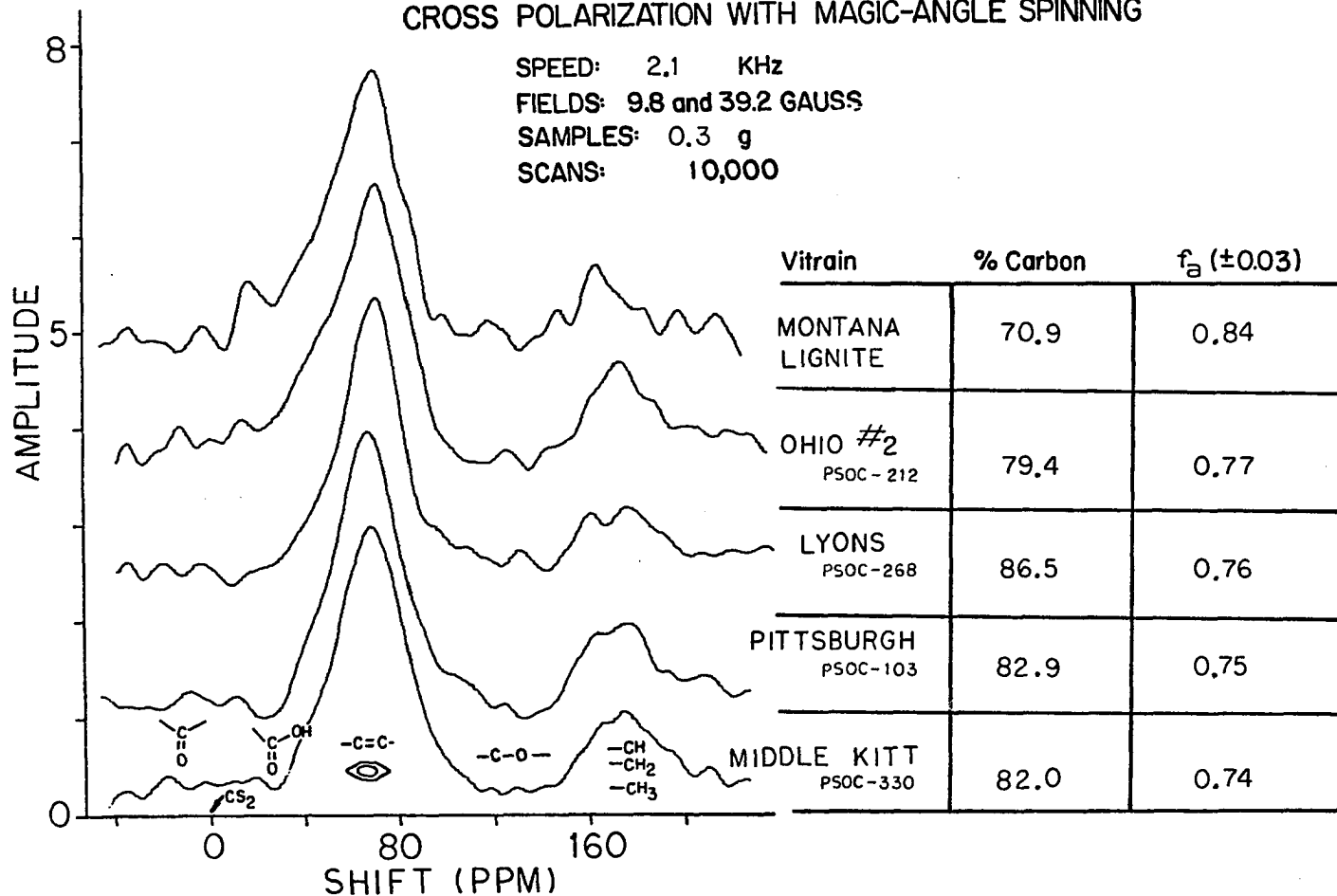
Figure 73. The ^{13}C NMR absorption spectra of coals

NUMERICAL INTEGRATION

^{13}C NMR   COAL VITRAIN   CP, MAS

NO CONTRIBUTIONS
FROM BASE LINE

$f_a = AREA(\dfrac{AR}{AR + AL})$

$= \dfrac{5.70}{5.70 + 1.73}$

$= 0.767$
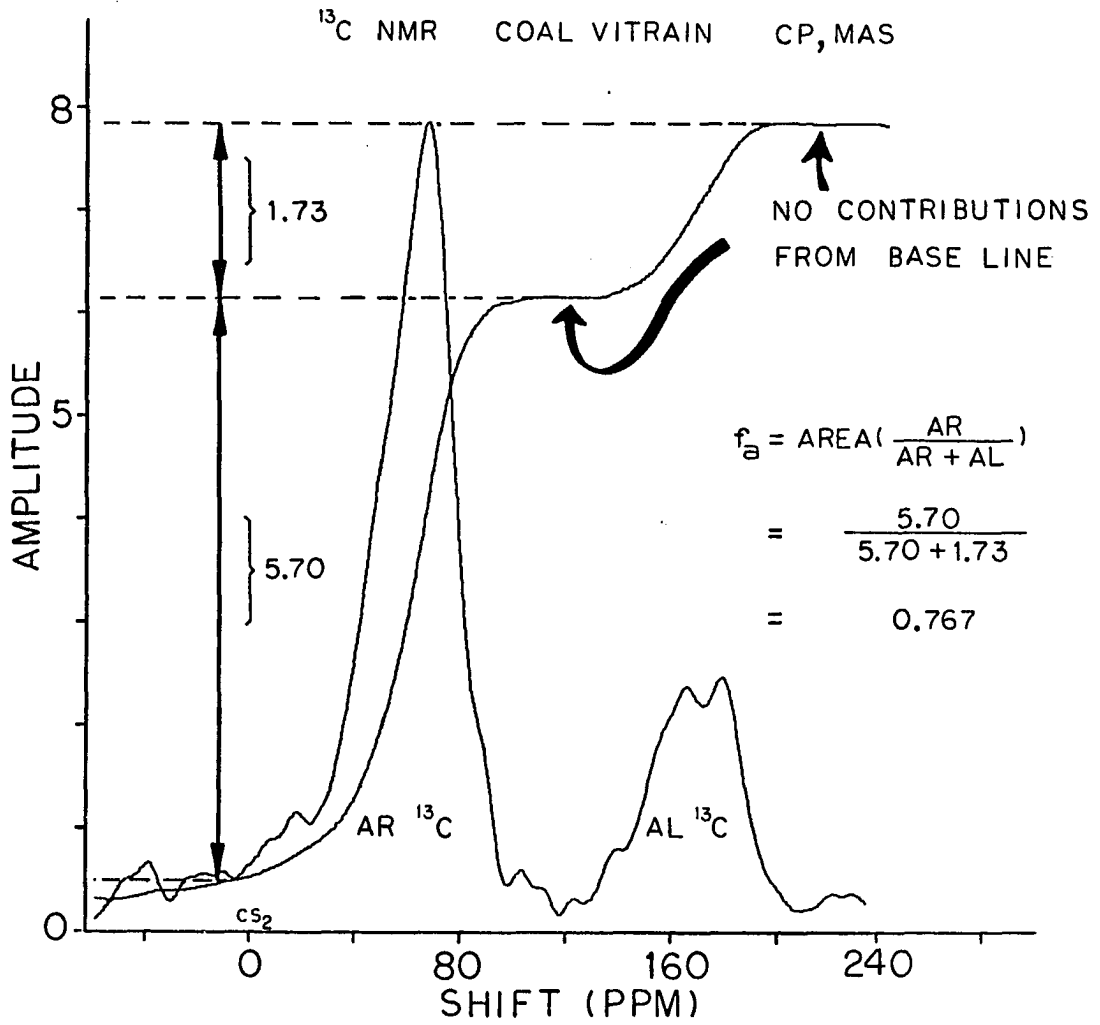
Figure 74.   An example of the technique of numerical integration
of an NMR absorption spectrum
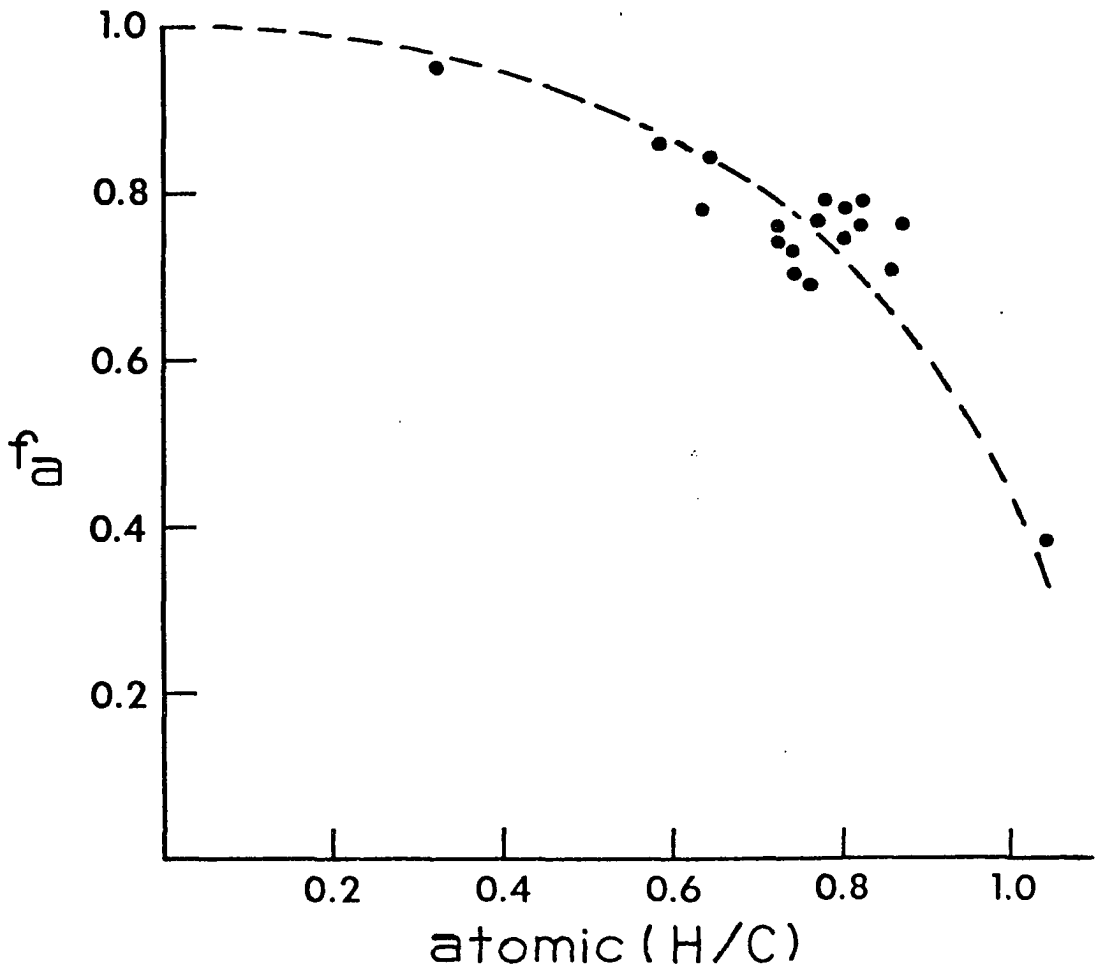
Figure 75. A graph of f_a vs. atomic (H/C) ratio of coals

Table 5. Fraction aromaticities and elemental composition of
the 18 coals studied in this research

VITRAIN	Composition[a]				Atomic[b]	f_a [c]
	%C	%O	%H	%N	H/C	
POCO. #4	90.3	5.0	4.4	1.3	.58	.86
POWELLTON	85.1	9.1	4.5	1.5	.63	.77
STAR	77.0	7.1	5.5	1.2	.85	.71
UPPER MICH	81.0	15.7	5.0	1.0	.73	.70
LOVILIA	75.0	13.6	4.8	1.4	.76	.69
ANTHRACITE	93.0?	-	2.5?	-	.32	.95
PSOC-640	74.7	8.0	5.1	1.3	.82	.79
PSOC-170	82.0	9.4	5.4	1.4	.78	.79
PSOC-501	76.0	8.2	5.1	1.3	.80	.78
BUMIK 40660	81.3	10.0	5.6	1.6	.82	.77
PSOC 351	76.3	6.6	5.6	1.6	.87	.77
PSOC 308	76.6	15.5	5.1	1.6	.79	.75
PSOC 155	56.8	9.3	5.0	1.1	1.05	.38
MONT. LIG.	70.9	23.5	3.9	1.1	.65	.84
PSOC-212	79.4	13.0	5.11	1.7	.77	.77
PSOC-268	86.5	5.8	5.3	1.5	.73	.76
PSOC-103	82.9	9.7	5.1	1.7	.73	.75
PSOC-330	82.0	10.8	5.1	1.6	.74	.74

[a]The remainder of the % is contributed by S and/or ash.

[b]atomic $(H/C) = \dfrac{12.01\ \%H}{1.01\ \%C}$

[c]f_a, fraction aromaticity of ^{13}C via ^1H-^{13}C CP.

f_a values are seen to decrease in a non-linear manner with increasing
content of hydrogen. This behavior is similar to that reported
by Maciel et al. (71).

It is believed (65-71) that coals are highly aromatic materials.
Also, as coals metamorphose (or age and increase their rank or
%C), both the size and number of condensed aromatic ring structures
increase at the expense of non-aromatic material. In coals
of very high rank, the aromatic structures are believed to become
graphite-like (65-66). Within experimental error, the behavior
of the f_a values of the 18 vitrains are, more or less, consistent
with the above interpretation, i.e., f_a increases with decreasing
atomic (H/C) ratio or with increasing rank.

Finally, Table 6 lists f_a values extracted from the non-
spinning Powder Patterns of five coals by numerical techniques
(See Figure 69). Also listed for comparison are f_a values
obtained with Magic-Angle Spinning (MAS). A typical ^{13}C NMR
spectra of a coal vitrain without spinning is shown in Figure
69. The appearance of this spectrum is attributed to the
overlap of many Powder Patterns, but mainly, of two different
classes: 1) aromatic ^{13}C centered around 40 ppm and 2) aliphatic
^{13}C centered around 165 ppm.

Each spectra was decomposed into two optimized lineshapes of
overlapping Powder Patterns via non-linear least-squares techniques
(41, Also, see Chapter VII). An example of such a fit is shown
in Figure 69. The f_a's were measured as the area of the "aromatic"
Powder Pattern to the total area of both Powder Patterns. Areas
were determined by numerical integration via Simpson's Rule.

Table 6. Comparison of fraction aromaticities of coals obtained
from non-spinning and Magic-Angle spinning experiments

Coal	$f_a{}^a$ non-spin ±0.03	$f_a{}^a$ MAS ±0.03
POCO. #4	0.78	0.86
POWELLTON	0.82	0.77
STAR	0.73	0.71
UPPER MICH	0.68	0.70
LOVILIA	0.67	0.69

$^a f_a$, fraction aromaticity of ^{13}C via ^1H-^{13}C CP.

As can be seen by comparison of the non-spinning f_a's
to the MAS f_a's tabulated in Table 6, agreement is good for
low f_a's. However at higher f_a's, the lineshape technique
appears to slightly favor the aliphatics and results in lower
f_a's.

X. REFERENCES

1. R. J. Myers, Molecular Magnetism and Magnetic Resonance (Prentice-Hall, Inc., New Jersey, 1973).

2. M. Mehring, High Resolution NMR Spectroscopy in Solids (Springer-Verlag, Berlin, 1976).

3. L. Van Gerven, Editor, Nuclear Magnetic Resonance in Solids (Plenum Press, New York, 1977).

4. T. C. Farrar and E. D. Becker, Pulse and Fourier Transform NMR (Academic Press, New York, 1971).

5. U. H. Hayt, Jr. and J. E. Kemmerly, Engineering Circuit Analysis (McGraw-Hill, New York, 1971).

6. R. G. Brown, R. A. Sharpe, W. L. Hughes and R. E. Post, Lines, Waves and Antennas (Ronald, New York, 1973).

7. P. D. Murphy and B. C. Gerstein, U.S.D.O.E. Report No. IS-4436 (unpublished).

8. A. Pines, M. G. Gibby and J. S. Waugh, J. Chem. Phys. 59, 569 (1973).

9. S. R. Hartmann and E. L. Hahn, Phys. Rev. 128, 2042 (1962).

10. J. R. Cross, R. K. Hester and J. S. Waugh, Rev. Sci. Instrum. 47, 107 (1976).

11. M. E. Stoll, A. J. Vega and R. W. Vaughan, Rev. Sci. Instrum. 48, 800 (1977).

12. R. D. Bertrand, W. B. Moniz, A. N. Garroway and G. C. Chingas, J. Am. Chem. Soc. 100, 5227 (1978).

13. P. D. Murphy and B. C. Gerstein, U.S.D.O.E. Report No. IS-4388 (unpublished).

14. R. G. Pembleton, L. M. Ryan and B. C. Gerstein, Rev. Sci. Instrum. 48, 1286 (1977).

15. Capacitors available from Polyflon Corporation, 35 River Street, New Rochelle, NY, 10801

16. Capacitors available from American Technical Ceramics, One Norden Lane, Huntington Station, New York, 11746.

17. R. J. Bertini, 73 Magazine 134, 57 (1971).

18. The Radio Amateur's Handbook, 49th ed. (ARRL, Newington, CN, 1972).

19. P. D. Murphy and B. C. Gerstein, U.S.D.O.E. Report No. IS-4596 (unpublished).

20. Power supply available from Heath Company, Benton Harbor, MI, 49022.

21. Boxes available from ITT Pomona Electronics, 1500 E Ninth Street, P.O. Box 2767, Pomona, CA, 91766.

22. P. D. Murphy and B. C. Gerstein, U.S.D.O.E. Report No. IS-4620 (unpublished).

23. G. R. Cooper and C. D. McGillem, Probabilistic Methods of Signal and System Analysis (Holt, Rinehart and Winston, New York, 1971).

24. M. S. Roden, Introduction to Communication Theory (Pergamon Press, New York, 1972).

25. D. C. Champeney, Fourier Transforms and Their Physical Applications (Academic Press, New York, 1973).

26. P. Bloomfield, Fourier Analysis of Time Series: An Introduction (Wiley, New York, 1976).

27. N. Bloembergen and J. A. Rowland, Acta Met. 1, 731 (1953).

28. U. Haeberlen, High Resolution in Solids. Selective Averaging (Academic Press, New York, 1976).

29. A. A. V. Gibson, T. A. Scott and Eüchi Fukushema, J. Mag. Res. 27, 29 (1977).

30. E. D. Ostroff and J. S. Waugh, Phys. Rev. Letters 16, 1097 (1966).

31. P. Mansfield and D. Ware, Phys. Letters 22, 133 (1966).

32. J. S. Waugh, L. M. Huber and U. Haeberlen, Phys. Rev. Letters 20, 180 (1968).

33. P. Mansfield, Solid State Phys. 4, 1444 (1971).

34. P. Mansfield, M. J. Orchard, D. C. Stalker and K. H. B. Richards, Phys. Rev. B7, 90 (1973).

35. W-K. Rhim, D. D. Elleman, and R. W. Vaughan, J. Chem. Phys. 58, 1772 (1973); 59, 3740 (1974).

36. W-K. Rhim, D. D. Elleman, L. B. Schreiber and R. W. Vaughan, J. Chem. Phys. 60, 4595 (1974).

37. U. Haeberlen and J. S. Waugh, Phys. Rev. 175, 453 (1968).

38. J. D. Ellet and J. S. Waugh, J. Chem. Phys. 51, 2581 (1969).

39. R. G. Pembleton, Ph.D. thesis, Iowa State University, 1978 (unpublished).

40. M. Mehring and J. S. Waugh, Phys. Rev. B5, 3459 (1972).

41. P. D. Murphy and B. C. Gerstein, U.S.D.O.E. Report No. IS-4516 Rev (unpublished).

42. A. Abragam, Principles of Nuclear Magnetic Resonance (Clarendon Press, Oxford, 1961).

43. R. F. Byrd and M. F. Friedman, Handbook of Elliptic Integrals for Engineers and Scientists (Springer-Verlag, Berlin, 1971).

44. D. G. Adolphson and J. D. Corbett, Inorg. Chem. 15, 1820 (1976).

45. A. W. Struss and J. D. Corbett, Inorg. Chem. 16, 360 (1977).

46. R. L. Daake and J. D. Corbett, Inorg. Chem. 16, 2029 (1977).

47. T. Y. Hwang, D. R. Torgeson, and R. G. Barnes, Phys. Letters A 66A, 137 (1978).

48. P. D. Murphy and B. C. Gerstein, J. Mag. Res. (May, 1979).

49. P. D. Murphy and B. C. Gerstein, J. Chem. Phys. (in press).

50. K. F. Lau, R. W. Vaughan and C. B. Satterthwaite, Phys. Rev. B 15, 2449 (1977).

51. P. Van Hecke, H. W. Spiess, and U. Haeberlen, J. Mag. Res. 22, 103-116 (1976).

52. B. C. Gerstein and C. R. Dybowski, An Introduction to the Theory and Practice of Pulse Techniques in Nuclear Magnetic Resonance (in preparation).

53. A. A. Maudsley, L. Müller and R. R. Ernst, J. Mag. Res. 28, 463 (1977).

54. R. D. Bertrand, W. B. Moniz, A. N. Garroway and G. C. Chingas, J. Mag. Res. (in press).

55. The subroutine ZXSSQ from the IMSL library was used. IMSL Library Reference Manual, IMSL LIB1-0006, revised: July, 1977. IMSL: International Mathematical and Statistical Libraries, Inc., Sixth floor--GNB Bldg., 7500 Bellaire, Houston, TX, 77036.

56. F. T. Schweighardt, H. L. Retcofsky, S. Friedman and M. Hough, Anal. Chem. 50, 368 (1978).

57. P. D. Murphy, T. Taki, T. Sogabe, R. Metzler, T. G. Squires and B. C. Gerstein, J. Am. Chem. Soc. (in press).

58. E. O. Stejskal and J. Schaefer, J. Mag. Res. 18, 560 (1975).

59. I. N. Levine, Quantum Chemistry (Allyn and Bacon, Boston, 1974).

60. E. Merzbacher, Quantum Mechanics (Wiley, New York, 1970).

61. M. E. Stoll, Ph.D. thesis, The California Institute of Technology, 1977 (unpublished).

62. E. R. Andrew and R. G. Eades, Proc. Roy. Soc. (London) A216, 398 (1953).

63. I. J. Lowe, Phys. Rev. Letters 2, 285 (1959).

64. K. W. Zilm, D. W. Alderman and D. M. Grant, J. Mag. Res. 30, 563 (1978).

65. H. L. Retcofsky and R. A. Friedel, J. Chem. Phys. 77, 68 (1973).

66. H. L. Retcofsky, Appl. Spect. 31, 116 (1977).

67. D. L. Vander Hart and H. L. Retcofsky, Fuel 55, 202 (1976).

68. H. L. Retcofsky and D. L. Vander Hart, Fuel 57, 421 (1978).

69. V. J. Bartuska, G. E. Maciel, J. Schafer and E. O. Stejskal, Fuel 56, 354 (1977).

70. H. A. Resing, A. N. Garroway and R. N. Hazlett, Fuel 57, 450 (1978).

71. G. E. Maciel, V. J. Bartuska and F. P. Miknis, Fuel (in press).

72. M. Goldman, Spin Temperature and Nuclear Magnetic Resonance in Solids (Oxford, London, 1970).

73. R. K. Hester, J. L. Ackerman, V. R. Cross and J. S. Waugh, Phys. Rev. Letters $\underline{34}$, 993 (1975).

74. R. K. Hester, V. R. Cross, J. L. Ackerman and J. S. Waugh, J. Chem. Phys. $\underline{63}$, 3606 (1975).

75. M. E. Stoll, A. J. Vega and R. W. Vaughan, J. Chem. Phys. $\underline{65}$, 4093 (1976).

XI. ACKNOWLEDGMENTS

I would like to thank the following people:

1. Dr. John Basart who reviewed the original Ames Lab Reports which were the basis for the material of Chapters II and III.

2. Dr. Robert Lambert who derived the imaginary transform of the Gaussian shown in Figure 33.

3. Larry Ryan who supplied and analyzed the experimental data shown in Figure 42.

4. Bob Taylor who supplied the original derivation of the equations of the Powder Pattern discussed in Chapter VI.

5. Dr. John Corbett who supplied the zirconium halide hydrides and reviewed the original material of Chapter VII.

6. Dr. Richard Barnes who also reviewed the original material of Chapter VII.

7. Dr. Toshihiko Taki who collected and analyzed experimental data of Chapter VIII and Chapter IX.

8. Taka Sogabe who assisted Dr. Taki and also reviewed Chapter VI.

9. Dr. Thomas Squires who reviewed the material of Chapter VIII.

10. Bob Metzler who synthesized the silyl-ether compounds discussed in Chapter VIII.

11. Dr. Peter Solomon of United Technologies Research Center who supplied coals used in Chapter IX.

12. Dr. Peter Given of Pennsylvania State University who supplied coals used in Chapter IX.

13. Dr. Herbert Retcofsky of the Pittsburgh Energy Research Center who supplied coals used in Chapter IX.

14. Dr. Donald Biggs who supplied coals used in Chapter IX.

15. The members of my thesis committee: John P. Basart, Bernard C. Gerstein, Robert S. Hansen, Jack Horowitz and Gerald J. Small.

16. Doug Adduci and the Instrumentation Group who designed and serviced equipment used in my research.

17. Tom Kelly and the Graphics Art Group who drew figures used in this thesis.

18. Denny Sailsbury and the Photographic Group who did all of the photographic work in this thesis.

19. Shirley Standley who typed the original Ames Lab reports from which the material of Chapters II, IV, V and VI was derived:

20. Marie Robbins who typed this thesis.

Finally, I would like to sincerely thank Dr. Bernard C. Gerstein, my thesis director, who suggested my research projects which he enthusiastically supported and criticized.